UNIVERSITA' DEGLI STUDI DI MILANO

Facoltà di Scienze Matematiche, Fisiche e Naturali

Dipartimento di Fisica

Istituto Nazionale di Fisica Nucleare, sez. Milano

Laboratorio Acceleratori e Superconduttività Applicata (LASA)

CORSO DI DOTTORATO DI RICERCA IN FISICA, ASTROFISICA E FISICA APPLICATA, CICLO XX

FAST FREQUENCY TUNER FOR HIGH GRADIENT SC CAVITIES FOR ILC AND XFEL

Tesi di Dottorato di Ricerca di:

Rocco Paparella

Matricola N. R06118

FIS/01 FISICA SPERIMENTALE

Tutore: Prof. C. Pagani

Direttore: Prof. G. Bellini

Anno Accademico 2006/2007

Submitted in fulfillment of the requirements for the degree of PhD

Supervisors Committee:

Tutor: Prof. C. Pagani

Co-Tutor: Prof. A. Pullia

Referee: Prof. M. Napolitano

Supervisor: Prof. N. Schiavoni

Coordinator: Prof. G. Bellini

TABLE OF CONTENTS

LIST OF FIGURES

LIST OF TABLES

ACKNOWLEDGMENTS

The last three years of activity for this PhD thesis allowed me to directly experience the gratification of doing scientific research within a truly international collaboration. As a consequence, I'm now grateful to several people from different laboratories who gave a significant contribution to the presented results and, with their kindness and abilities, helped me improving my knowledge, not only in the field of particle accelerators, and my pleasure in doing physics.

Firstly, I would like to warmly thank all the group of colleagues and friends at the LASA laboratory, starting from Angelo Bosotti, Paolo Michelato, Laura Monaco, Carlo Pagani, Nicola Panzeri, Paolo Pierini and Daniele Sertore because without their everyday support and collaboration, since I was a student, this dissertation would not even exist. I need to thank also Serena Barbanotti, Massimo Fusetti, Massimo Bonezzi, Gianpietro Spada and Carlo Uva, whose prompt help never missed for all my frequent questions and problems.

Among various collaboration, the core role for the entire activity presented in this dissertation is played by DESY, Hamburg, where all major experimental measurements have been performed. I would like firstly to sincerely thank Lutz Lilje that has been my reference in DESY since my first time there, and whose support has been always fundamental for every experimental test. I owe him an huge contribution to the results and analyses presented in this dissertation, moreover I always enjoyed my frequent stays in Hamburg also thanks to his friendliness and enthusiasm, during our piezo tests as well as after work. Many thanks also to Rolf Lange, Clemens Albrecht, Denis Kostin, Kay Jensch and all the DESY Halle III cryogenic group for their inestimable and qualified support during our tests, especially during the Blade Tuner cold test at CHECHIA that wouldn't have been possible without them. I would like to acknowledge also Stefan Simrock and all the people at DESY afferent at the LLRF group. Particular thanks to Waldemar Koprek that constantly and kindly support me during my activity on the SIMCON, answering all my questions and introducing me to the LLRF topics, and to Konrad Prygoda for our positive and interesting cooperation on the piezo controller code development and test.

Then, I would like to thank Przemyslaw Sekalski from Technical University of Lodz, Poland, a quite old date friend and a qualified colleague since the beginning of my activity in the field of fast frequency tuners. I also acknowledge Mohammed Fouaidy from Orsay, Paris, for our productive collaboration on piezoelectric actuators characterization and Alexander Brandt from DESY for kindly helping me with his cavity detuning computation routines that we then used for CMTB and CHECHIA tests.

In conclusion, I must say that I'm most of all grateful to my family, Chiara and all my closer friends for their outstanding, even surprising but always encouraging confidence in my abilities.

I wish also to acknowledge the support of the European Community-Research Infrastructure Activity under the FP6 "Structuring the European Research Area" programme (CARE, contract number RII3-CT-2003-506395), within which this Ph.D. activity has been partially conducted.

1 INTRODUCTION

1.1 THE TERASCALE REGION

"• What is the universe? How did it begin?

• What are matter and energy? What are space and time?

Throughout human history, scientific theories and experiments of increasing power and sophistication have addressed these basic questions about the universe. The resulting knowledge has revolutionized our view of the world around us, transforming our society and advancing our civilization. Everyday phenomena are governed by universal laws and principles whose natural realm is at scales of time and distance far removed from our direct experience. Particle physics is a primary avenue of inquiry into these most basic workings of the universe. Experiments using particle accelerators convert matter into energy and back to matter again, exploiting the insights summarized by the equation $E = mc^2$*. Other experiments exploit naturally occurring particles, such as neutrinos from the Sun or cosmic rays striking Earth's atmosphere. Many experiments use exquisitely sensitive detectors to search for rare phenomena or exotic particles. Physicists combine astrophysical observations with results from laboratory experiments, pushing towards a great intellectual synthesis of the laws of the large with laws of the small."* [1]

Successes of the whole particle physics of the 20th century are summarized in the development of the Standard Model and the confirmation of many of its aspects. Through experimental investigation, particles constituting the ordinary matter have been revealed, and the four forces that hold matter together and transform it identified. Particle interactions were found to obey precise laws of relativity and quantum theory. Remarkable features of quantum physics were observed, including the real effects of "virtual" particles on the visible world. Starting from this successful model, particle physicists are now able to address even more fundamental and deeper questions. How can we solve the mystery of dark energy, dark matter and antimatter? Are there extra dimensions of space? Do all the forces become one? What are neutrinos telling us?

A worldwide program of particle physics investigations, using multiple approaches, is already underway to search for a breakthrough impact on many of these fundamental questions through exploring the undiscovered landscape of the Terascale energies (Tev region). The Standard Model in fact clearly hypothesizes a new form of Terascale energy, called the Higgs field, that permeates the entire universe. Interaction of particles with this field leads to acquisitions of particle mass, and the Higgs field also breaks a fundamental electroweak force into electromagnetic and weak forces, which are experimentally observed in very different forms. So far, there is no direct experimental evidence for a Higgs field or the Higgs particle that should accompany it. Furthermore, quantum effects of the type already observed in experiments should destabilize the Higgs boson of the Standard Model, preventing its operation at Terascale energies. The proposed antidotes for this quantum instability mostly involve dramatic phenomena at the Terascale: new forces, a new principle of nature called supersymmetry, or even extra dimensions of space. Thus for particle physicists the Higgs boson is at the center of a much broader program of

discovery, taking off from a long list of questions. Are there really Higgs bosons? If not, what are the mechanisms that give mass to particles and break the electroweak force? If Higgs bosons exist, do they differ from the hypothetical Higgs of the Standard Model? What are the new phenomena that stabilize the Higgs boson at the Terascale? What properties of Higgs boson inform us about these new phenomena?

Moreover, another unprecedented opportunity for the investigation of the Terascale energies region is related to dark side of the universe. Astrophysical data shows that dark matter dominates over visible matter, and that almost all of this dark matter cannot be composed of known particles. This data, combined with the concordance model of Big Bang cosmology, suggests that dark matter is comprised of new particles that interact weakly with ordinary matter and have Terascale masses. It is truly remarkable that astrophysics and cosmology, completely independently of the particle physics considerations reviewed above, point to new phenomena at the Terascale.

Finally, additional goals for the international programs of particle physics investigations at the Terascale are present. Particle physics data already suggests that three of the fundamental forces originated from a single "grand" unified force in the first instant of the Big Bang. Theoretical models to explain the properties of neutrinos, and account for the mysterious dominance of matter over antimatter, also posit unification at high energies. Therefore experiments could provide evidences of this original Einstein's vision of an ultimate unified theory. While the realm of unification is almost certainly beyond the direct reach of experiments, different unification models predict different patterns of new phenomena at Terascale energies so it possible to aim to distinguish among these patterns, effectively providing a telescopic view of ultimate unification.

1.2 THE TEV SCALE ACCELERATORS

Since the ADA "proof of principle" experiment in Frascati [2], colliding beams have been used to reach and advance the energy frontier in particle physics. With respect to the fixed target experiments, colliding two elementary particles with the same energy has the great advantage to let available in the center of mass (c.m.) all the energy transferred by the particle accelerator to them. Conversely, when a fixed target is used, relativity associates just one fraction of the beam energy to the moving center of mass. The drawback of this concept is that the collision probability for the interacting particles is quite small because of the beam low density. Luminosity[1] is then the quality parameter that is required for a collider to produce a sufficient event rate of a given cross section. In principle higher energy demands higher luminosity, but for the same beam quality luminosity is inversely proportional to the beam energy. In spite of this issue, for more than two decades, from ADONE in 1969 [3] to LEPII [4] and TEVATRON [5], the discovery energy frontier had an exponential grow, following the so called "Livingston Plot".

[1] Luminosity [$cm^{-2}\ s^{-1}$] is the measure of the number of particles per unit area and unit time.

From the accelerator side, the reference machine of all colliders has been a synchrotron based storage ring. Once accelerated to the nominal energy, the two beams are stored and used for collision for billions of times. In a synchrotron the maximum energy is proportional to both the ring radius and the average magnetic field. In parallel to the magnetic field improvement, machine size and cost are naturally associated with the radius increase. With increasing energies, the energy lost by synchrotron radiation become the main issue for leptons. The factor 2000 in the relativistic γ, together with the γ^4 dependence of the energy lost per turn, leads to impossibility to realize lepton synchrotrons above the c.m. energy of the about 200 GeV successfully reached by LEPII [4], in its 27 km ring. Scaling LEPII to 1 TeV with a luminosity of about 10^{34} cm^{-2} s^{-1} would for instance require a circular machine close to 1000 km in length and consuming an unbearable amount of electrical power.

Conversely, the Large Hadron Collider (LHC) [6] has been planned at CERN since 1994 to make use of the existing LEP tunnel in order to reach to first direct look at the Terascale physics. LHC synchrotron will reach this with its baseline design of two colliding proton beams, 7 TeV each. As of today, LHC is concluding its commissioning phase and it will be ready to operate in middle 2008. If the Higgs particle exists, it is almost certainly to be found in the ATLAS or CMS experiments of LHC. Anyway each of the possible LHC outcomes, concerning the existence or the absence of the Higgs boson, whether it is consistent with the Standard Model or not, would lead to the need for an additional experimental tool to uncover or move forward the understanding of the Higgs mechanism. A wide agreement among particle physicists is present on the choice of a linear electron-positron collider of a comparable TeV scale as the correct one. The two machines would finally allow to perform combined analyses and exploit the possibility of exciting interplay between different experiments and observations.

The idea of a linear collider to avoid the synchrotron radiation limit was firstly proposed in 1965 by Maury Tigner, but almost 40 years of research have been spent to demonstrate its practical feasibility. The two major problems of a linear collider are the luminosity and the efficiency to economically transfer the energy to the beams. While in a storage ring collider as LHC the same particles are circulating 10^4 times in a second, contributing 10^4 times to the beam current and resulting in a beam power close to 4 TW, in a linear collider each accelerated particle is given a single chance to collide before being dumped. Therefore the goal for such a linac is to preserve, once a low normalized emittance[2] beam has been generated in a damping ring, the highest possible luminosity value all along the acceleration up to the interaction point. For a linear collider, 10 MW is a reference value for the power of each beam, should the linac technology being able to transform plug power into beam power with unprecedented conversion efficiency.

Since the Eighties a large number of ideas and conceptual scheme emerged, so that finally in 1994 an International panel, the ILC-TRC, has been constituted by the Inter-Laboratory Collaboration for R&D toward TeV-Scale Electron-Positron Linear Colliders. This panel produced its first report which for the first time gathered in one document the

[2] The emittance is defined as the beam phase-space volume.

current status of eight major e^+/e^- linear collider designs in the world by the end of 1995. Among those, a prominent proposal was the idea of investigating the use of superconducting accelerating structure as the basic technology for a future Linear Collider, called TESLA[3] [7]. This idea was firstly discussed in a small workshop held at Cornell in July 1990, organized by Ugo Amaldi and Hasan Padamsee. Two years later the TESLA Collaboration was set up at DESY (Deutsches Elektronen-Synchrotron in Hamburg, Germany) for the development of a SRF-based TeV e^+-e^- Linear Collider. The baseline idea was simply that pushing to the limit the niobium SRF technology, accelerating field up to 50 MV/m could be conceived, with efficiency from plug to beam power much higher than any other normal conducting (NC) linac. Due to the lower frequency and larger beam apertures, a better beam quality preservation could be expected. The combination of these two effects would have produced an higher luminosity for a cold machine, if compared to the same plug power and beam quality. Several years of R&D activities in the frame of TESLA collaboration finally resulted in the publication, in March 2001, of the TESLA Technical Design Report for a Superconducting linear collider with c.m. energy of 500 GeV, upgradeable to 800 GeV. A key document that included a full machine costing based on specific industrial studies of all the major components, whose critical parts had been meanwhile developed and tested, in view of the required mass production.

The growing interest of the scientific community for the foreseen synergies between LHC and the lepton collider pushed to find a way to concentrate the worldwide efforts on a single design, concluding the now expensive technology competition. By the end of 2003, twelve "Wise Persons"[4] were selected to form the International Technology Recommendation Panel (ITRP), the aim being to produce a globally accepted choice between the two remaining competitors: the "warm" JLC-X/NLC [8][9] and the "cold" TESLA. The ITRP, completed the recommendation process in eight months, through documentation, presentations, visits and discussions, the three project leaders (Kaoru Yokoya for JLC-X, David Burke for NLC and Carlo Pagani for TESLA,) being invited to participate to all the process as the "technology experts". Finally, the ITRP recommendation for the "cold" TESLA technology was unanimously indorsed in Beijing in August 2004, starting the process towards the International Linear Collider, ILC.

1.3 THE INTERNATIONAL LINEAR COLLIDER

As of today, the ILC global collaboration achieved a milestone in its course with the release, in August 2007, of the International Linear Collider Reference Design Report [1]. The reference design provides the first detailed technical snapshot of the ILC machine, defining in detail the technical parameters and components that make up each section of the 31 km length machine. It provides guidelines for the worldwide R&D programs,

[3] TeV Energy Superconducting Linear Accelerator.

[4] Asia: G.S. Lee, A. Masaike, K. Oide H. Sugawara; Europe: J-E Augustin, G. Bellettini, G. Kalmus, V. Soergel; America: J. Bagger, B. Barish, P. Grannis, N. Holtkamp. Chaired by Barry Barish.

engineering and costing for the industrialization phase and in view of the final mass production.

The International Linear Collider (ILC) [10] is a 200 to 500 GeV center-of-mass high-luminosity linear electron-positron collider, based on the 1.3 GHz superconducting radio-frequency (SCRF) accelerating technology that was pioneered by the TESLA collaboration. The TESLA technology, currently in charge to the TESLA Technology Collaboration (TTC) [11], is based on niobium elliptical multi-cell RF cavity designed to operate at about 2 K temperature to drastically lower RF losses through cavity walls. A detailed analysis of this cold acceleration technology, the underlying physics and the actual 1.3 GHz resonators for ILC is presented in the following chap. 2.

The ILC design has been developed to achieve the following physics performance goals:

- a continuous center-of-mass energy range between 200 GeV and 500 GeV.
- a peak luminosity of about $2 \cdot 10^{34}$ $cm^{-2}s^{-1}$, and an availability (75%) consistent with producing 500 fb^{-1} in the first four years of operation.
- 80% electron polarization at the Interaction Point (IP).
- an energy stability and precision of $\leq 0.1\%$.
- an option for 60% positron polarization.
- options for e^--e^- and γ–γ collisions.

In addition, the machine must be upgradeable to a center-of-mass energy of 1 TeV. These goals guarantee a rich and varied program of physics. The energy of the ILC will be sufficient to produce a very large number of top-antitop pairs, which will allow top-quark physics to be studied with unprecedented precision. The energy range of the ILC spans all predictions for the mass of a Standard Model Higgs boson based on the precision electroweak data. Any supersymmetric particles found by LHC will lead to a rich harvest of new phenomena at ILC; in addition, the ILC has its own unique discovery capabilities which will be the only way to produce a full picture of any of the new physics that might exist at the TeV energies scale. Basic parameters for the ILC baseline design at 500 GeV c.m. energy are summarized in Tab. 1.1.

Parameter	Value	Unit
Center-of-mass energy range	200 – 500	GeV
Peak luminosity	$2 \cdot 10^{34}$	$cm^{-2}s^{-1}$
Average beam current in pulse	9.0	mA
Pulse rate	5	Hz
Pulse length (beam)	~1	ms
Number of bunches per pulse	1000 - 5400	
Charge per bunch	1.6 – 3.2	nC
Accelerating gradient	31.5	MV/m
RF pulse length	1.6	ms
Beam power (per beam)	10.8	MW
Typical beam size at IP	640 x 5.7	nm
Total AC Power consumption	230	MW

Tab. 1.1 – 500 GeV c.m. energy baseline design parameters [1]

The current ILC baseline assumes an average accelerating gradient of 31.5 MV/m in the cavities to achieve a center-of-mass energy of 500 GeV. The high luminosity requires the use of high power and small emittance beams. The choice of 1.3 GHz SCRF is well suited to the requirements, primarily because the very low power loss in the SCRF cavity walls allows the use of long RF pulses, relaxing the requirements on the peak power generation, and ultimately leading to high wall-plug to beam transfer efficiency. The primary cost drivers are the SCRF Main Linac technology and the Conventional Facilities (including civil engineering). The choice of gradient is a key cost and performance parameter, since it dictates the length of the linacs, while the cavity quality factor Q_0 (see par. 2.1.1) relates to the required cryogenic cooling power. The achievement of 31.5 MV/m as the baseline average operational accelerating gradient will be achieved through the request of a minimum performance of 35 MV/m during cavity mass-production acceptance testing and it represents the primary challenge to the global ILC R&D.

The schematic view of the overall layout of the ILC, indicating the location of the major sub-systems, is shown in Fig. 1.1.

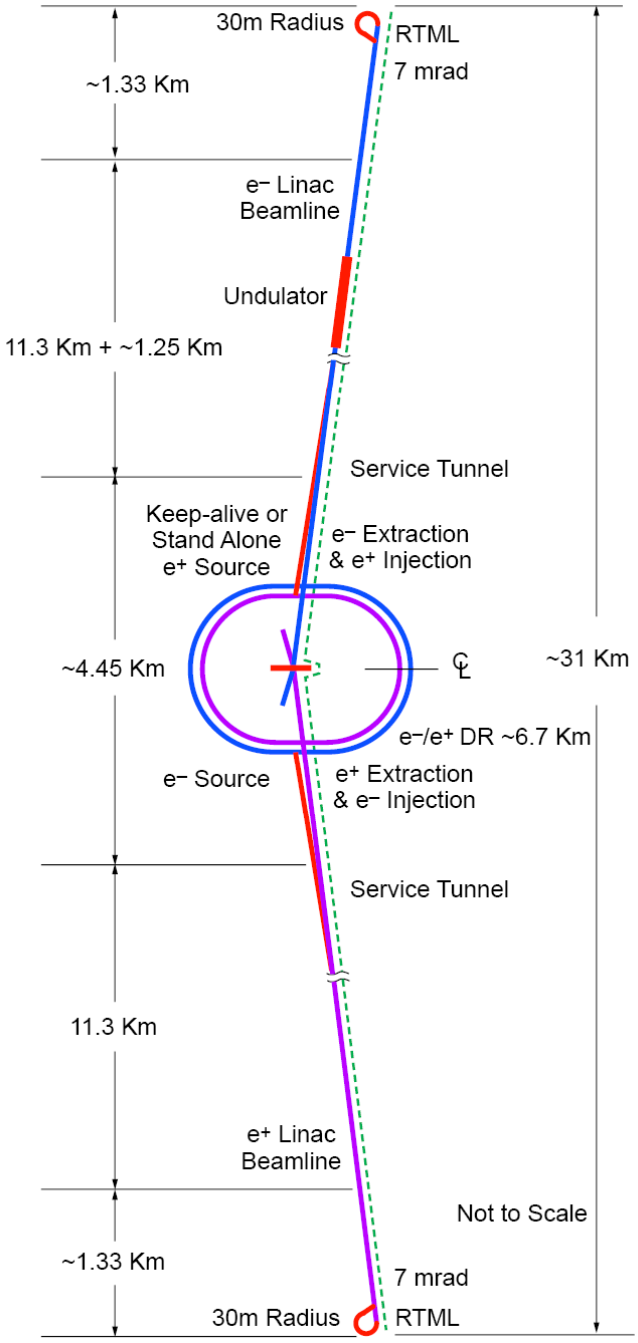

Fig. 1.1 – schematic layout of the ILC complex for the 500 GeV c.m. energy baseline [1]

Each subsystem layout is described in details in the Reference Design Report document [1]. An overview of main ones is here given with particular focus on the linac subsystem that is directly involved in this PhD thesis work. Here follows a summary of main components (refer to Fig. 1.1):

- a polarized electron source based on a laser illuminating a photocathode in a DC gun. It is required to generate the bunch train of electrons with the goal polarization, capture and accelerate the beam up to 5 GeV before the injection in the electron dumping ring.
- an undulator-based positron source. A 150 GeV main electron beam is diverted, transported through a helical undulator then returned to electron linac. The resulting multi MeV photons beam is directed to a rotating metal target for positron production. The e^- beam is then captured and accelerated to 5 GeV prior injection to the positron dumping ring.
- 5 GeV electron and positron damping rings (DR) with a circumference of 6.7 km, housed in a common tunnel at the center of the ILC complex. DR accept beams with large transverse and longitudinal emittance and dump them to low emittance, low jitter and high stability beams for downstream systems, within the 200 ms time between subsequent pulses.
- beam transport lines from the damping rings to the main linacs, also named as RTML (Ring To Main Linac). This subsystem is mainly composed of a about 15 km long 5 GeV transport line, RTML also perform additional beam operations as 180 deg turn-around, beam stabilization and spin rotations. Finally a two-stage bunch compressor system compresses the beam before the injection into the main linac, from several millimeters to few hundred microns bunch length.
- a 4.5 km long beam delivery system or BDS, which brings the two beams into collision with a 14 mrad crossing angle, at a single interaction point which can be shared by two detectors. BDS also focuses beams to the sizes required to meet ILC luminosity goals using strong compact superconducting quadrupoles and, after IP, transport spent beams to main high-powered water-cooled dumps.
- two main linacs, based on 1.3 GHz SCRF cavities with an average gradient of 31.5 MV/m. They accelerate the electron and positron beams from the injected energy of 15 GeV to the final 250 GeV, over a combined length of 23 km. Linacs are required to perform acceleration while preserving the small injection emittance, avoiding any additional transverse or longitudinal jitter, and to maintain the beam energy spread within the requirement of about 1 % at the IP. Each linac is composed of modular RF units, 278 for e^+ linac and 282 for e^-, including three contiguous SCRF modules for a total number of 26 cavities. A schematic representation of this layout is given in Fig. 1.2.

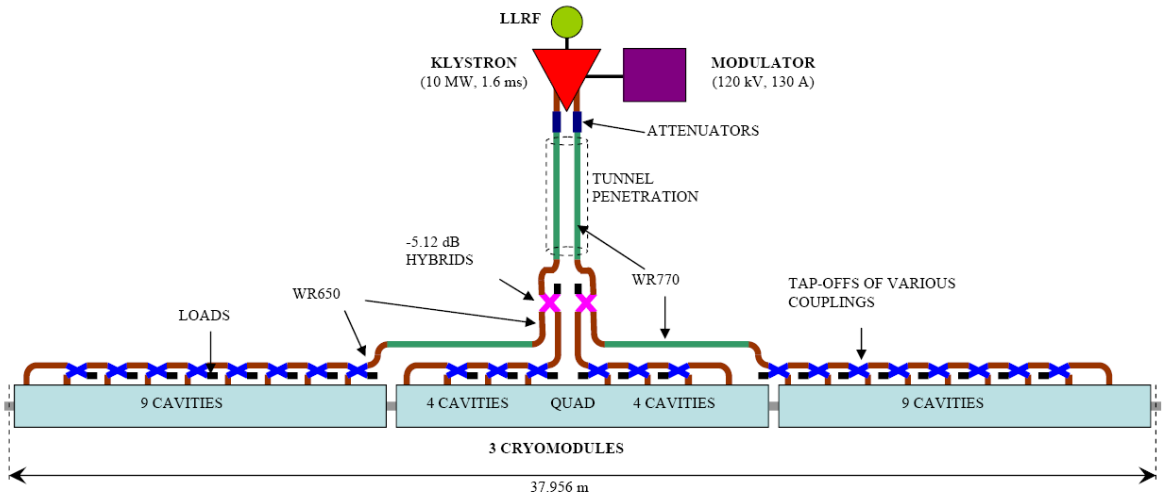

Fig. 1.2 – layout of a modular RF unit for ILC

Each RF unit has a stand-alone RF source, which includes a conventional pulse-transformer type high-voltage (120 kV) modulator, a 10 MW multi-beam klystron RF power amplifier, and a waveguide system that distributes the RF power to the cavities. It also includes the low-level RF (LLRF) system to regulate the cavity field levels (see par. 4.2.1), interlock systems to protect the source components, and the power supplies and support electronics associated with the operation of the source. The cryomodule design is a modification of the Type-3 version developed and used at DESY TTF [12][13]. The layout of a TTF cryomodule cross section is presented in Fig. 1.3, a CAD picture of the outer and the inner part of an ILC cryomodule with the focusing quadrupole in the center is instead given in Fig. 1.4. In addition an actual FLASH type-3 module, the ACC6, is visible in the picture of Fig. 1.7.

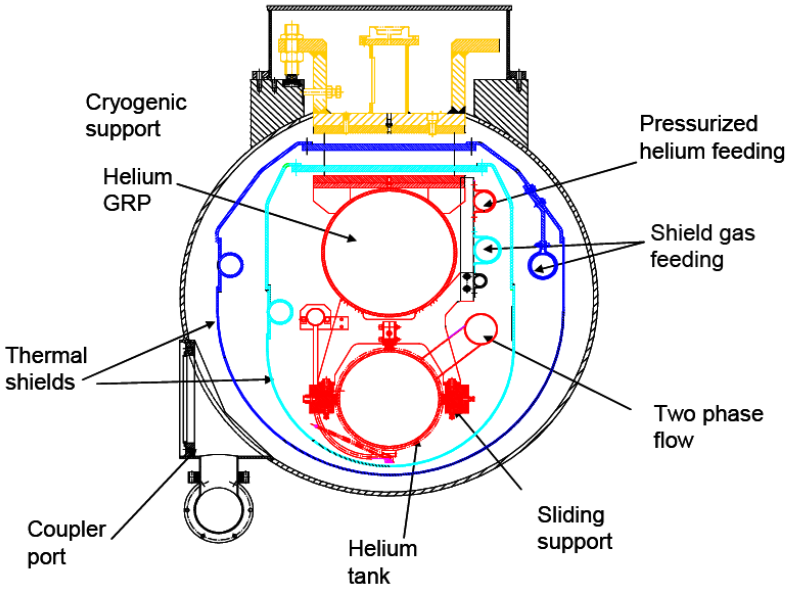

Fig. 1.3 – cross section view of a TTF cryomodule [12]

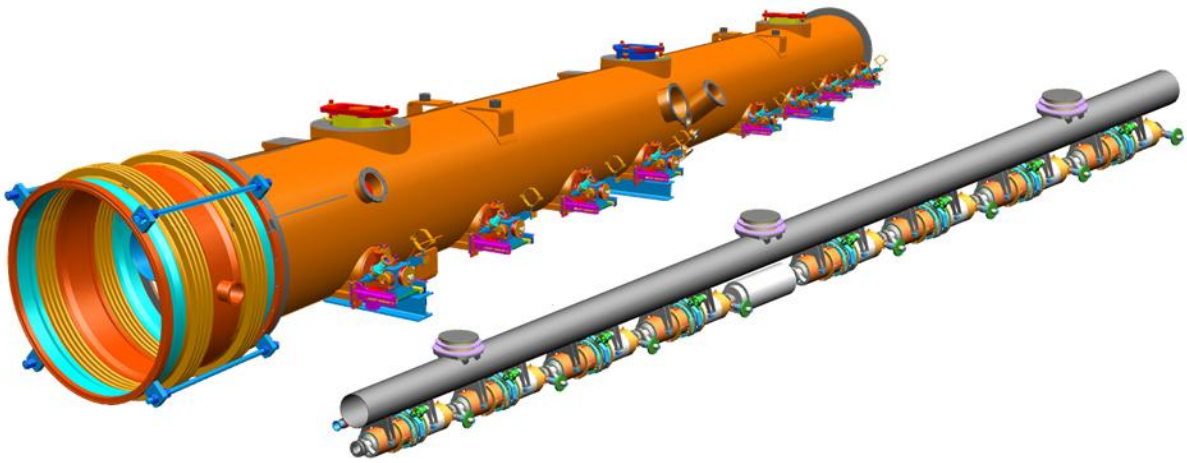

Fig. 1.4 – 3C CAD view of an ILC cryomodule, both outer vacuum vessel (left) and inner cold mass string (right). Gas return pipe, 8 cavities and the central focusing quadrupole are visible in the latter.

Within the cryomodules, a 300 mm diameter helium gas return pipe serves as a support for the cavities and other beam line components. The middle cryomodule in each RF unit contains a quad package that includes a superconducting quadrupole magnet at the center, a cavity BPM, and superconducting horizontal and vertical corrector magnets. To operate the cavities at 2 K, they are immersed in a saturated He II bath (see par. 2.2), and helium gas-cooled shields intercept thermal radiation and thermal conduction at 5-8 K and at 40-80 K. The estimated static and dynamic cryogenic heat loads per RF unit at 2 K are 5.1 W and 29 W, respectively. Liquid

helium for the main linacs and the RTML is supplied from 10 large cryogenic plants, each of which has an installed equivalent cooling power of about 20 kW at 4.5 K. The main linacs follow the average Earth's curvature to simplify the liquid helium transport. Finally, as of today the main challenges for the linac ILC subsection are achieving the design average accelerating gradient of 31.5 MV/m, that is higher than that typically achievable today, and control of the beam energy spread.

Finally, the total ILC machine footprint is about 31 km. The electron source, the damping rings, and the positron auxiliary (`keep-alive') source are centrally located around the interaction region (IR). The plane of the damping rings is elevated by about 10 m above that of the BDS to avoid interference. To upgrade the machine c.m. energy to 1 TeV, the linacs and the beam transport lines from the damping rings would be extended by additional 11 km each.

The technical design and cost estimate for the ILC is based on two decades of world-wide Linear Collider R&D, beginning with the construction and operation of the SLAC Linear Collider (SLC) [14]. The SLC is acknowledged as a proof-of-principle machine for the linear collider concept. The competing design work on a normal conducting collider (NLC with X-band [9] and GLC with X- or C-Band [15]), has advanced the design concepts for the ILC injectors, Damping Rings (DR) and Beam Delivery System (BDS), as well as addressing overall operations, machine protection and availability issues. The X and C-band R&D has led to concepts for RF power sources that may eventually produce either cost and/or performance benefits. Finally, the European XFEL [16] to be constructed at DESY, Hamburg, Germany, will make use of the TESLA linac technology, and represents a significant on-going R&D effort of great benefit for the ILC.

With the completion of the RDR, the GDE will begin an engineering design study, closely coupled with a prioritized R&D program. The goal is to produce an Engineering Design Report (EDR) by 2010, presenting the matured technology, design and construction plan for the ILC, allowing the world High Energy Physics community to seek government-level project approvals, followed by start of construction in 2012. When combined with the seven year construction phase that is assumed in studies presented in RDR, this timeline will allow operations to begin in 2019. This is consistent with a technically driven schedule for this international project.

1.4 LABORATORIES AND TEST FACILITIES

In this paragraph a brief description of the several test facilities that will be reported in this thesis work is given. A surely prominent role is assumed by the different installation present at DESY Hamburg related to the R&D on TESLA superconducting cavities. Since 1992, when the TESLA Collaboration was set up at DESY, the realization of a demonstrative prototype of electron linear accelerator was decided to demonstrate the feasibility of a SCRF-based TeV e^+-e^- Linear Collider at competitive costs and performances. The prototype SC linac at DESY was the TTF, TESLA Test Facility,

e^- linac completed in 1995, that used superconducting cryomodules hosting 8 TESLA 1.3 GHz niobium 9-cell cavities. From the initial 100 m long layout at 250 MeV of TTF I, the linac was successively further developed with the TTF II stage, and in 2004 has been finally extended to a 260 m long 1 GeV linac with 6 SCRF cryomodules and converted to FLASH (Free electron LASer in Hamburg, formerly VUV-FEL). FLASH, based on the SASE-FEL[5] principle to provide VUV to soft X-rays radiation beams to a user facility, covering a wavelength range from 6.5 nm to 50 nm with GW peak power and pulse durations between 10 fs and 50 fs. A schematic layout of the whole FLASH machine is presented in Fig. 1.5 while a detailed view of the current cryomodules outline of the FLASH SCRF linac section is given in Fig. 1.6. Highlighted modules in Fig. 1.6, #5*, #6 and #7 have been installed in the beam line during recent FLASH linac upgrade in spring 2007 (module #6 was new and assembled in 2006).

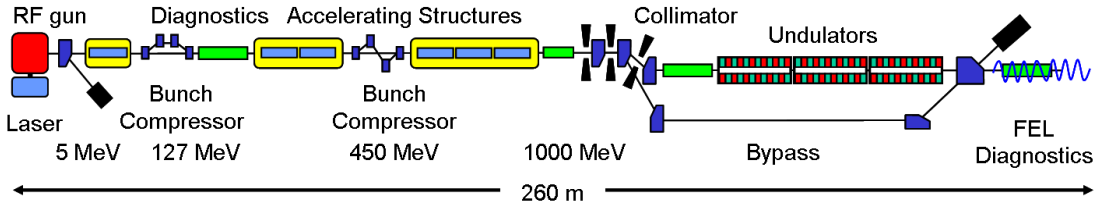

Fig. 1.5 – schematic layout of FLASH

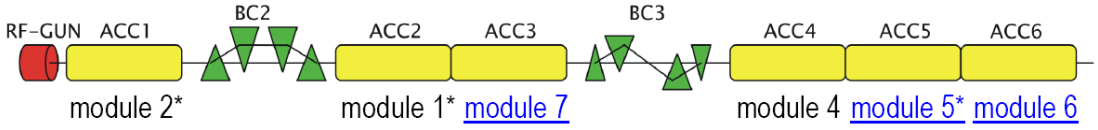

Fig. 1.6 – FLASH linac cryomodules outline after upgrade in spring 2007

FLASH linac represents the basis also for the incoming European XFEL project [16] for a 3.4 km long X-rays source facility based on the same TESLA accelerating SCRF technology. XFEL construction is due to begin in spring 2008 and commissioning will start at the end of 2013. Therefore, in addition, both FLASH and XFEL linacs will lay the foundation for the future ILC.

In order to perform experimental tests on assembled cryomodules independently from the main FLASH linac operations, a Cryo Module Test Bench facility (CMTB) has been built at DESY close to the TTF site. The CMTB facility host a single complete FLASH cryomodule for validation tests, including RF cavities and coupler processing, cryogenics tests as well as component repairs or test of new features. The CMTB facility has been commissioned at the end of 2006 and the recently assembled type III cryomodule #6 (or ACC6) for FLASH has been firstly installed in October 2006 (see Fig. 1.7) for a repetitive test cycle (see chap. 5).

[5] Self-Amplified Spontaneous Emission Free Electron Laser. It refers to the exponential growth of the FEL pulse energy as a function of the length traveled in the undulator [132].

Fig. 1.7 – FLASH module #6 (ACC6) during installation in the CMTB facility

CMTB represents an unique resource for these testing purposes and in view of the huge effort required by the ILC it will be soon replied by similar facilities as the SMTF at Fermi National Laboratory (FNAL), US, and STF at KEK, Japan.

In addition to the shown facilities, the TTF site includes several smaller test benches in use for standard cavity testing program. Among these facilities, a noteworthy role is given to the single cavity horizontal cryostat named CHECHIA (Cryostat Horizontal d'Essai de Cavités Habillées et de l'Instrumentation Associée) installed at the Halle III building at DESY. CHECHIA hosts a complete TESLA cavity setup and allows to perform processing, RF power tests and tuner tests, it has been used in particular for the coaxial Blade Tuner cold test reported together with additional CHECHIA features and pictures in chap. 6.

Beside these crucial test facilities available at DESY, both cryogenic and RF test equipments have been installed at the LASA (Accelerators and Applied Superconductivity Laboratory) INFN[6] laboratory [17] in order to perform minor in house experimental validations. A facility for cryogenic test of small components as piezo actuators or force sensors has been realized. It relies on a small 2 K vertical cryostat from Criotec[7]. The facility is described in par. 4.4.3 together with the report of a life-time test of piezo actuators performed [18]. A test bench for RF measurements and coaxial tuner test has been also realized, it is based on a niobium TESLA single cell cavity. The equipment is presented in Fig. 6.32 concerning the room temperature test of the revised design coaxial tuners (par. 6.6), it has been also used during past years for piezo-to-RF transfer function

[6] The Italian National Institute for Nuclear Physics

[7] Italian cryogenic plants manufacturer from Turin [141]

measurements and analysis (see app. A) and for microphonic detuning active compensation studies [19].

2 SUPERCONDUCTING RF RESONATORS FOR ACCELERATORS

Electromagnetic cavities resonating at microwave frequency are key components of modern particle accelerators, as the devices that impart energy to the charged particles. Basic properties and figures of merit of radiofrequency (RF) cavity are firstly reviewed. Benefits of RF superconductivity are exploited in this frame in order to achieve, among other features, larger mean accelerating gradient and electric power efficiency. Later in this chapter, basics of superconductivity effect and its application to RF resonators for particle accelerators will be shown[8]. Large emphasis will be given to niobium material and its superconductive features since, thanks to its more favorable properties, it is widely used for all existing large scale installation of SC cavities. Finally, the multi-cell niobium elliptical cavity developed in the frame of the TESLA Technology Collaboration (TTC) [11] will be introduced and described in details[9]. Performances and specifications of this object, further on named as TESLA cavity, are fundamental for this thesis topics.

2.1 BASICS OF RF RESONATORS

According to a broad definition, an RF cavity can be simply described as a given volume of space in which an electromagnetic (EM) energy is stored, as it is given, for instance, by a perfect dielectric surrounded by metallic boundaries. In order to achieve an analytical treatment of the EM fields inside the cavity, simplified geometries are assumed [20]. Firstly, for instance, the spatial and temporal variations of the RF fields in a infinite wave guide along z axis, of uniform cross-section and bounded by a perfect conductor, are assumed as

$$\begin{aligned} \mathbf{E}(x,t) &= \mathbf{E}(\rho,\varphi)e^{ikz-i\omega t} \\ \mathbf{H}(x,t) &= \mathbf{H}(\rho,\varphi)e^{ikz-i\omega t} \end{aligned} \tag{2.1}$$

where ω is the angular frequency and k the wave number. Maxwell's equations for EM fields near a perfect conductor require to express boundary conditions as

$$\hat{n} \times \mathbf{E} = 0\,, \qquad \hat{n} \cdot \mathbf{H} = 0 \tag{2.2}$$

where n is the unit vector normal to the surface of the conductor. Combining Maxwell's equations according to assumptions in (2.1) and (2.2) results in the wave equation

[8] A detailed and exhaustive introduction to RF superconductivity for accelerators can be found in [20].
[9] The reference sources for TESLA resonator description are found in [45] [1].

$$\nabla_{\perp}^2 + \left(\frac{\omega^2}{c^2} - k^2\right)\begin{Bmatrix}\mathbf{E}\\ \mathbf{H}\end{Bmatrix} = 0 \tag{2.3}$$

where

$$\nabla_{\perp}^2 = \nabla^2 - \frac{\partial^2}{\partial z^2} \tag{2.4}$$

The solutions to the eigenvalue equation (2.3) form an orthogonal set with eigenvalues

$$\gamma^2 = \frac{\omega^2}{c^2} - k^2 \tag{2.5}$$

The different boundary conditions imposed on E_z and H_z, components along the waveguide axis z and the fact that they are independent, finally generate two sets of modes with different eigenvalues. These two families are named as transverse magnetic (TM) modes, where the magnetic field is always transverse to the cavity symmetry axis, and conversely the transverse electric (TE) modes. This waveguide model can be easily converted into a cavity introducing conducting surfaces at z = 0 and z = d. When the new spatial and temporal form of fields is considered, including the stationary wave now obtained after reflections on opposite surfaces, and substituted in (2.3) the cavity fields $\psi(\rho,\varphi)$ (ρ and φ are the polar coordinates in the transverse plane) result to be solutions of the eigenvalue equation

$$\left(\nabla_{\perp}^2 + \gamma_j^2\right)\psi(\rho,\phi) = 0 \tag{2.6}$$

where

$$\gamma_j^2 = \left(\frac{\omega_j}{c}\right)^2 - \left(\frac{p\pi}{d}\right)^2 \tag{2.7}$$

is the j^{th} eigenvalue and p is the integer indicating the TE or TM mode number.

These derived fields equations can be for example analytically solved for a simple cavity design, a cylindrical "pill-box" cavity of length l and radius R. solutions to (2.6) are in this case Bessel functions. Cavity modes are usually classified in the literature as TM_{mnp}, where integer indices indicate the number of sign changes of E_z in the φ, ρ and z directions respectively (similarly for TE). Anyway, only TM_{0np} modes have a non-vanishing longitudinal electric field on axis and can therefore be used for charged particle accelerations, in particular the TM_{010} mode is usually chosen since it has the lowest eigenfrequency. For instance the pill-box TM_{010} mode[10] is given by

$$E_z = E_0 J_0\left(\frac{2.405\rho}{R}\right)e^{-i\omega t} \tag{2.8}$$

[10] The complete list of pill-box modes can be found is [20].

$$H_\phi = -i\frac{E_0}{\eta} J_1\left(\frac{2.405\rho}{R}\right) e^{-i\omega t}$$

and its resonance frequency is

$$\omega_{010} = \frac{2.405c}{R} \tag{2.9}$$

A broader result is underlying the formula in (2.9): it is actually always confirmed that the cavity mode spectrum is inversely proportional to the cavity linear size.

The shape of actual cavities differs from the one of the pill-box example, first of all to allow the beam to pass through the cavity, beam pipes are added at both ends and they are chosen so that their cutoff frequency is above the frequency of the accelerating mode: in this way cavity field cannot propagate out of the cavity. Anyway, the length of each cell is always chosen so that the time needed to the particle to pass through it equals one half of the RF period T_{010}. Therefore, to accomplish the acceleration of a charged particle it must be verified that:

$$\frac{d}{c\beta} = \frac{T_{010}}{2} = \frac{\pi}{\omega_{010}} \tag{2.10}$$

where c is the velocity of light and β is the normalized particle velocity[11] v/c. As an indication, a schematic representation of the electric and magnetic fields inside a single cell with beam tubes excited with the TM_{010} mode is presented in Fig. 2.1.

[11] Therefore, typically, cavities for e^- or e^+ acceleration are designated as $\beta = 1$ cavities. Lower β structures ($\beta < 0.3$) for heavier particles have very different geometry than these considered here. For an overview of existing cavities refer to [131]

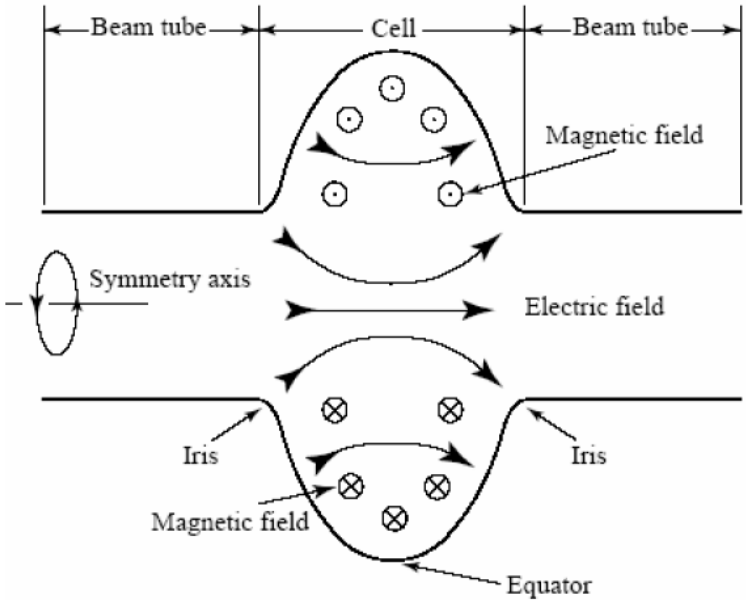

Fig. 2.1 – schematic representation of a single cell cavity excited in the TM010 mode [21]

Real cavity design is optimized using numerical simulations with computer codes to obtain the field distributions. One of the most commonly used 2-D codes is SUPERFISH [22], while HFSS [23] and MAFIA [24] are popular 3-D codes.

In order to efficiently accelerate the beam, multi-cell resonators are often used, as for the TESLA cavity (see par. 2.4). A multi-cell cavity is realized by periodically repeating a single cell resonating structure and by providing coupling between successive cells. The simplest coupling is represented by the electric field itself through the beam hole, in order to form a capacitive coupling[12]. As for any other set of coupled oscillators, there are multiple modes of oscillation of the full structure for a given cell excitation mode, as the TM_{010} for example. The multi-cell cavity can therefore be simply modeled as a lumped electrical circuit as shown in Fig. 2.2, provided that only the accelerating mode is considered.

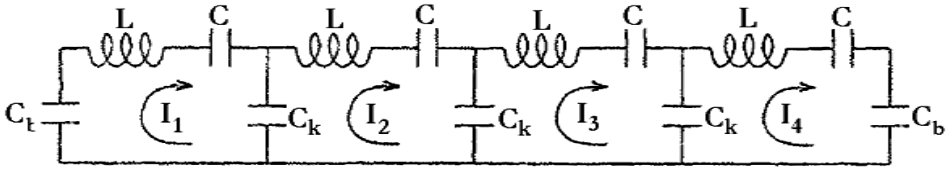

Fig. 2.2 – lumped circuit model of a multi-cell cavity with capacitive coupling [20]

[12] Capacitive coupling is widely used for β about 1 cavities. Low β structures more often use inductive coupling[51].

L and C are the characteristic equivalent inductance and capacitance for each cell and the cell-to-cell coupling is done capacitively via C_k. The beam tubes are modeled as C_b and, since the quality factor Q_0 is expected to be significantly high, the circuit resistance is taken as zero. The circuit model can be solved applying the Kirchhoff's voltage rule to each mesh. The final result [20] shows that the multi-cell cavity made up by N coupled cells each resonating, for instance, at frequency ω_{010}, can oscillate in N normal eigenmodes with eigenfrequencies close to ω_{010}. The different multi-cell cavity modes are expressed by

$$\omega_n = \omega_0 \sqrt{1 + k\left[1 - \cos\left(\frac{n\pi}{N}\right)\right]} \tag{2.11}$$

Where k_{cell} is the coupling coefficient that determines the mode spacing in the cavity spectrum. Each mode is usually designated by its corresponding phase advance per cell, that is $^{n\pi}/_{N}$ (2.11). The mode used to accelerate the beam is then the π mode so that the synchronism between accelerated particle and the RF field is preserved thanks to the 180 deg phase shift between adjacent cells. In particular a "flat" π mode is wanted, so that the accelerating field amplitude is the same in each cell. This compensation (named as beam tube compensation) can be accomplished by correctly choosing the cavity-to-beam tube coupling strength via the C/C_b ratio [20].

2.1.1 CAVITY FIGURES OF MERIT

During the transit through the cavity longitudinal axis z, a single charged particle sees a time varying electric field, but provided that it enters when the field change sign and that the time needed to traverse the cavity equals one half of the chosen RF period, it sees an accelerating field pointing in the same direction. The *accelerating voltage* V_c of a cavity can be therefore defined as

$$V_c = \left|\frac{1}{e} \times \text{maximum energy gain possible during transit}\right| \tag{2.12}$$

and it is related to the line integral of E_z as seen by the electron

$$V_c = \left|\int_0^d E_z(\rho = 0, z) e^{i\omega_0 z/c} dz\right| \tag{2.13}$$

Consider, for example, the pill box cavity resonating in the TM_{010} mode. Using the field expressions in (2.8) it is found that:

$$V_c = dE_0 \frac{\sin\left(\frac{\omega_0 d}{2c}\right)}{\frac{\omega_0 d}{2c}} = dE_0 T \tag{2.14}$$

where the quantity T is known as the *transit factor*. Provided that (2.10) is satisfied, $T = 2/\pi$ for the pill-box cavity TM_{010} mode. The *accelerating field* E_{acc} during the whole transit d through the cavity finally evaluates to

$$E_{acc} = \frac{V_c}{d} = TE_0 \tag{2.15}$$

For a given EM field distribution inside the cavity, as for the TM_{010} previously considered, two additional parameters are considered in order to determine how large the field amplitude E_0 can be: the peak surface magnetic field H_{pk} and the peak surface electric field E_{pk}. The former one is mainly related to operation of SC resonators since a superconductor will quench (see par. 2.2.2) above a critical magnetic field H_c^{rf}, the latter is instead important because of the danger of field emission in high electric field cavity regions. To maximize the accelerating field is therefore important to minimize the *ratios of the peak fields to the accelerating field*. For instance, in the pill-box case both E_{pk} and H_{pk} lie on the end faces of the cavity and corresponding ratios evaluate to

$$\begin{aligned} \frac{E_{pk}}{E_{acc}} &= \frac{\pi}{2} = 1.6 \\ \frac{H_{pk}}{E_{acc}} &= 2430 \frac{A/m}{MV/m} = 3.05 \frac{mT}{MV/m} \end{aligned} \tag{2.16}$$

In order to support the EM fields inside the cavity, currents flow within a thin surface layer of the walls. Therefore, cavity ohmic *surface resistance* R_s, that even for a superconductor is not zero for RF frequencies, determines the energy dissipated through the cavity walls. Typically, R_s is from few $n\Omega$ to few tens of $n\Omega$ for niobium superconducting surface, whereas in the $m\Omega$ range for the copper ones.

A fundamental figure of merit for accelerating cavities is the *quality factor* Q_0, which is related to the power dissipation and it is defined as

$$Q_0 = \frac{\omega_0 U}{P_c} \tag{2.17}$$

where U is the EM energy stored in the cavity and P_c is the power dissipated in the cavity walls. Q_0 can be roughly considered as the number of RF cycles it takes to dissipate the stored energy. The total energy in the cavity can be expressed as

$$U = \frac{1}{2}\mu_0 \int_V |\mathbf{H}|^2 dv = \frac{1}{2}\varepsilon_0 \int_V |\mathbf{E}|^2 dv \tag{2.18}$$

where the integral is taken over the volume of the cavity, and accordingly the dissipated power

$$P_c = \frac{1}{2} R_s \int_S |\mathbf{H}|^2 ds \tag{2.19}$$

this time integrating over the interior cavity surface[13]. Thus finally, for the quality factor Q_0 it is found:

$$Q_0 = \frac{\omega_0 \mu_0 \int_V |\mathbf{H}|^2 dv}{R_s \int_S |\mathbf{H}|^2 ds} \tag{2.20}$$

Q_0 factor is often expressed as

$$Q_0 = \frac{G}{R_s} \tag{2.21}$$

$$G = \frac{\omega_0 \mu_0 \int_V |\mathbf{H}|^2 dv}{\int_S |\mathbf{H}|^2 ds} \tag{2.22}$$

where G is the *geometry constant*, a parameter that depends only on the cavity shape and not on its size, different therefore from the quality factor that varies with cavity size due to the frequency dependence of R_s [20].

Another important quantity used to characterize the losses in a cavity is the *shunt impedance* R_a. It is defined, in unit of Ω per cell, according to ("accelerator" definition, see [20])

$$R_a = \frac{V_c^2}{P_c} \tag{2.23}$$

Moreover the ratio

$$\frac{R_a}{Q_0} = \frac{V_c^2}{\omega_0 U} \tag{2.24}$$

is noteworthy since it is independent of the surface resistance and therefore of the cavity size. It is frequently quoted as a figure of merit of cavity design and it also used for determining the level of mode excitation by charges passing through the cavity (see par. 2.3). As a reference for further cavity analyses, figures of merit for the pill-box cavity can be analytically computed and they are reported in Tab. 2. [20]

[13] In the assumption that the surface resistance is not varying over the cavity surface

Quantity	Pill-box cavity	Unity
T	$2/\pi$	
G	257	Ω
R_a/Q_0	196	Ω/cell
E_{pk}/E_{acc}	1.6	
H_{pk}/E_{acc}	3.05	mT/(MV/m)

Tab. 2.1 – pill-box cavity figures of merit [20]

In conclusion, it is desirable to achieve for the chosen cavity accelerating mode (TM_{010} typically) the highest possible values for G and R_a/Q_0, and simultaneously the lowest possible values for peak to accelerating fields ratios. Additional considerations anyway apply. For instance, for normal conducting (NC) cavities, where power dissipation in the walls is the major issue, it is mandatory to maximize accelerating mode R_a/Q_0 ratio by using a small beam hole. This anyway tends to increase the same parameter also for higher order modes, different from the one chosen for acceleration, causing degradation of beam quality. This scenario drastically change for a superconducting resonator since R_s is drastically lowered in this case and the dissipated power is no longer a critical issue. Thanks to the high Q_0, SC cavities can sustain large beam hole and the consequent penalty in the R_a/Q_0 value for the accelerating mode, moreover the reduced R_a/Q_0 ratio for higher order modes positively affects beam quality. These issues together with additional dividends and disadvantages of superconducting cavities will be described in details in par. 2.3.

2.1.2 CAVITY MODEL

Resonant modes in a cavity can be modeled by means of lumped LCR circuit, although some simplifications must be included in comparison to a real cavity [25]. Values of L and C lumped elements are respectively related to the magnetic and electric energy stored in the cavity and they both determine the actual resonant frequency ω_0 according to

$$\omega_0 = \frac{1}{\sqrt{LC}} \tag{2.25}$$

Lumped resistance R is instead the expression of losses in the cavity and is directly related to the accelerator definition of the shunt resistance R_a by

$$R = \frac{1}{2} R_a \quad [14] \tag{2.26}$$

[14] The factor ½ depends on the actual definition chosen for Ra and in this case comes from the time average.

Both the excitation of the resonator by the RF generator and the accelerated beam can be described as current sources, I_g and I_b respectively. In particular for relativistic particles ($\beta \sim 1$) since the corresponding beam current is constant during the acceleration in the cavity; this is no more true for non-relativistic heavier particles with low β. In view of its application to relativistic electron acceleration, only the former case is here considered. The resulting circuital model is presented in Fig. 2.3.

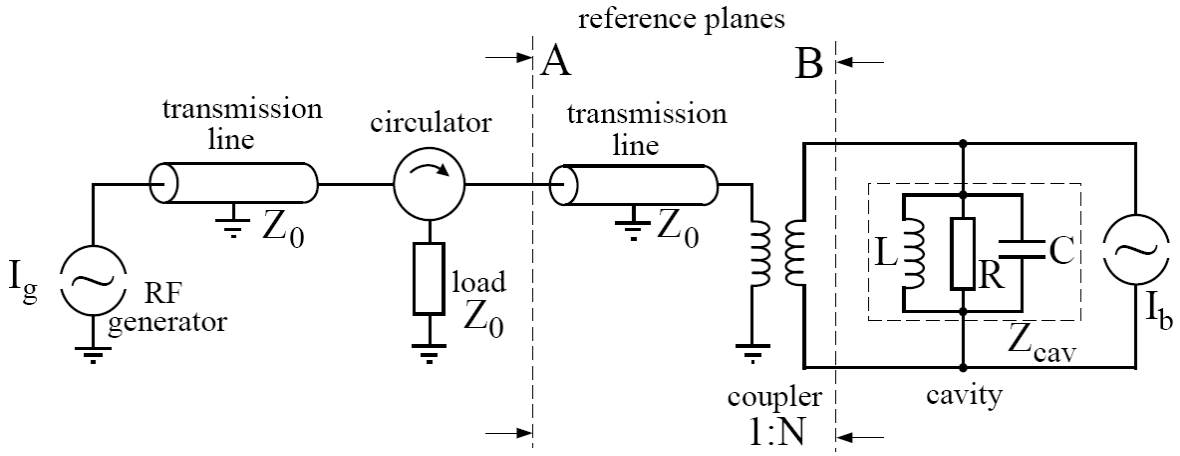

Fig. 2.3 – circuital model of a cavity coupled to RF generator through coupler and transmission lines [26]

All elements in the RF path are supposed to be correctly matched to the impedance value Z_0. A circulator is also included as a protection, it is used to deviate RF power reflected by the cavity to a matched load instead of reaching the klystron generator. The power coupler is modeled as an ideal transformer with a transforming ratio of 1:N, therefore the cavity equivalent impedance Z_{cav} is seen by the RF transmission line as

$$Z'_{cav} = \frac{1}{N^2} Z_{cav} \tag{2.27}$$

The presented model can be further simplified by expressing all needed quantities as they are seen from cavity side, that means from the right side of reference plane B in Fig. 2.3. This results in the model shown in Fig. 2.4.

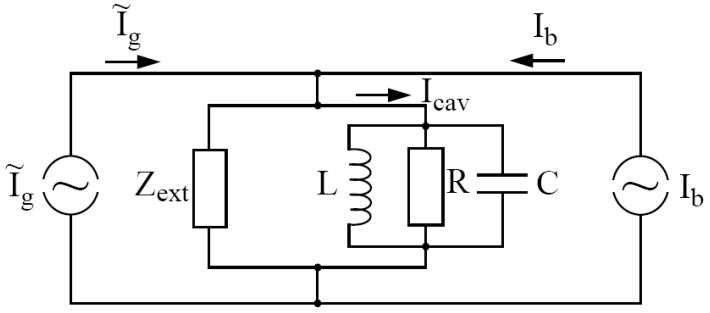

Fig. 2.4 – RF circuital model as seen by cavity point of view [26]

The transmission line, which is terminated by the load Z_0, acts as a parallel load to the cavity resistor R. All other eventual losses are included in the load Z_{ext}. In this equivalent model the generator current I_g is related to the true current from the klystron by:

$$I'_{gen} = \frac{2}{N} I_{gen} \tag{2.28}$$

Taking into account basic formulas from circuit theory it is possible to relate cavity figures of merit to circuital lumped parameters [25]. The resonator quality factor Q_0, referring to formula (2.17), can be then expressed as

$$Q_0 = \frac{2\pi}{T} \cdot \frac{\frac{1}{2} CV^2}{\frac{1}{2}\frac{V^2}{R}} = \omega_0 RC = \frac{R}{L\omega_0} \tag{2.29}$$

where V is the amplitude of the oscillating voltage and T the time period of an RF cycle. Beside the power dissipated in the cavity walls, also the power coupled to the external probes (including the power coupler) must be considered. For this reason the *external quality factor* Q_{ext} is introduced and accordingly defined as

$$Q_{ext} = \frac{\omega_0 U}{P_{ext}} \tag{2.30}$$

where P_{ext} is the power dissipated in each external device and U the energy stored in the cavity. And finally the *loaded quality factor* Q_L is defined as

$$Q_L = \frac{\omega_0 U}{P_{tot}} \tag{2.31}$$

Energy conservation requires

$$P_{tot} = P_c + \sum P_{ext} \tag{2.32}$$

and this leads to

$$\frac{1}{Q_L} = \frac{1}{Q_0} + \sum \frac{1}{Q_{ext}} \tag{2.33}$$

For instance, when superconducting resonators are considered (see par. 2.3), the unloaded Q_0 is typically several orders of magnitude larger than the Q_{ext}, so $Q_L \sim Q_{ext}$. The final complex impedance of the model in Fig. 2.4 can be easily computed as a function of the Laplace transform complex variable s using basic circuital conventions:

$$Z(s) = \frac{V(s)}{I(s)} = \frac{sR_L L}{R_L LCs^2 + Ls + R_L}, \qquad R_L = \frac{RR_{ext}}{R + R_{ext}} \tag{2.34}$$

Then, according to the rules of the inverse Laplace transform, the differential equation that describes the circuital model is found and it is given by

$$\frac{d^2V(t)}{dt} + \left(\frac{1}{R} + \frac{1}{Z_{ext}}\right)\frac{1}{C}\frac{dV(t)}{dt} + \frac{1}{LC}V(t) = \frac{1}{C}\frac{dI(t)}{dt}, \qquad I = I_b + I_g \tag{2.35}$$

or even, using Q_L and ω_0 in replacement,

$$\frac{d^2V(t)}{dt} + \frac{\omega_0}{Q_L}\frac{dV(t)}{dt} + \omega_0^2 V(t) = \frac{\omega_0 R_L}{Q_L}\frac{dI(t)}{dt} \tag{2.36}$$

The stationary solution of (2.36) can be found assuming an harmonic input current. The resulting cavity parallel voltage V is then given by

$$V(t) = \hat{V} \cdot \sin(\omega t + \psi) \tag{2.37}$$

where both amplitude and phase can be again expressed as a function of Q_L and ω_0 achieving the expressions

$$\begin{aligned} \tan\psi &= Q_L\left(\frac{\omega_0}{\omega} - \frac{\omega}{\omega_0}\right) \\ \hat{V} &= \frac{R_L \hat{I}_0}{\sqrt{1 + \tan^2\psi}} \end{aligned} \tag{2.38}$$

Corresponding plots for amplitude and phase of cavity voltage are shown in Fig. 2.5.

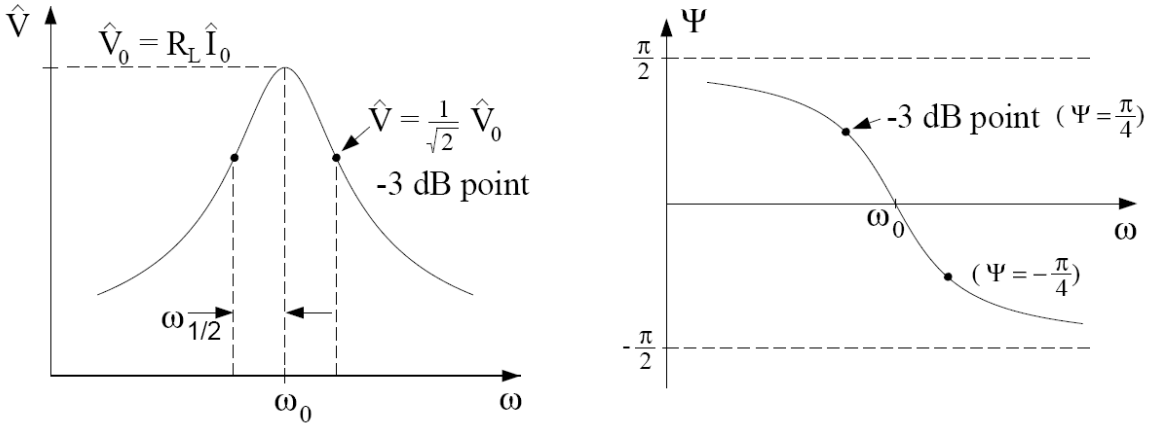

Fig. 2.5 – resonance curves for both amplitude and phase of cavity voltage [26].

As visible in the amplitude plot, the cavity bandwidth $\omega_{1/2}$ is operatively defined as the frequency bandwidth where the voltage drops to $1/\sqrt{2}$ of its maximum value (-2 dB). Substituting in equations (2.38) the expression for $\omega_{1/2}$ is obtained:

$$\omega_{1/2} = \frac{\omega_0}{2Q_L} = \frac{1}{\tau} \tag{2.39}$$

where τ is the *filling time* of the cavity. Energy stored in the cavity correspondingly drops to half the peak value.

From the same cavity model, described by equation (2.36), the transient behavior description can be deduced, thus obtaining the relations that describe the pulsed operation of the resonator. Provided that the following assumptions are verified:

- the beam and the RF generator current are turned on for a long time compared to characteristic filling time of the cavity τ, determined by its quality factor according to (2.39)
- the cavity is weakly damped ($1/Q_L << 1$) so that the peak frequency ω_{pk} given by:

$$\omega_{res} = \omega_0 \sqrt{1 - \frac{1}{4Q_{load}^2}} \tag{2.40}$$

  can be considered as equal to ω_0.
- the second order time derivatives could be neglected.

the dynamic system can be described by the following state-space (see par. 4.1) [27] equation [28]:

$$\underbrace{\frac{d}{dt}\begin{pmatrix} V_{re} \\ V_{img} \end{pmatrix}}_{\dot{x}} = \underbrace{\begin{pmatrix} -\omega_{1/2} & \Delta\omega \\ \Delta\omega & -\omega_{1/2} \end{pmatrix}}_{A} \underbrace{\begin{pmatrix} V_{re} \\ V_{img} \end{pmatrix}}_{x} + \underbrace{\begin{pmatrix} R_L\omega_{1/2} & 0 \\ 0 & R_L\omega_{1/2} \end{pmatrix}}_{B} \underbrace{\begin{pmatrix} I_{re} \\ I_{img} \end{pmatrix}}_{u} \tag{2.41}$$

where

$$\begin{aligned} V(t) &= \left(V_{re}(t) + iV_{img}(t)\right)e^{i\omega t} \\ I(t) &= \left(I_{re}(t) + iI_{img}(t)\right)e^{i\omega t} \end{aligned} \tag{2.42}$$

represents the complex vector. Beside cavity bandwidth $\omega_{1/2}$, the detuning parameter $\Delta\omega$, defined as ω_0-ω, appears.

2.2 BASICS OF SUPERCONDUCTIVITY

2.2.1 INTRODUCTION AND LENGTH SCALES

Superconductivity was discovered in 1911 by Kammerlingh-Omnes [29] when the vanishing of ohmic resistance of a mercury sample was found when below a critical temperature T_c. Several elements and compounds, mainly alloys and ceramics, have been found showing this behavior below a wide range of critical temperatures (see Tab. 2.2).

	T_c [K]		**T_c [K]**
Al	1.2	Nb	9.3
In	3.4	Ta-Nb	6.3
Sn	3.7	NbN	16
Hg	4.2	Nb_3Sn	18
Ta	4.5	MGB_2	39
Pb	7.2	$Y_1Ba_2Cu_3O_{7-\delta}$	90 [15]

Tab. 2.2 - Critical temperatures of some elements, alloys and metallic compounds.

In addition, any external magnetic field up to a critical field B_c is expelled, this magnetic field expulsion is called the Meissner-Ochsenfeld effect [30]. This behavior significantly differs from the properties of an ideal conductor where the field would be trapped inside the material. Even if the field is switched off, an ideal conductor would keep the magnetic field and become a permanent magnet as the currents induced by the field will continue to flow. Experimentally, B_c can be determined as the area below the magnetization curve of

[15] This compound with $T_c > \sim 30$ K is called a "high-temperature superconductor" and the exact value of the critical temperature depends on the precise stechiometry.

the material and, as reported in Fig. 2.6 this highlighted the existence of two different types of superconductors, usually named as type-I and type-II.

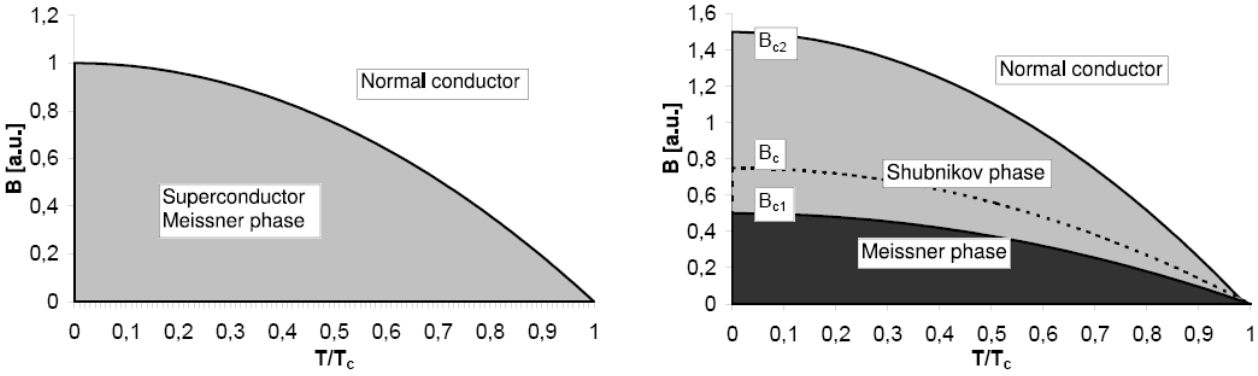

Fig. 2.6 – phase diagrams for superconductors of type-I (left) and type-II (right) [31]

If the field exceeds a critical value B_c in a superconductors of type I the superconductivity breaks down and the normal conducting state is restored. This critical field depends on the critical temperature:

$$B_c(T) = B_c(0)\left[1 - \left(\frac{T}{T_c}\right)^2\right] \tag{2.43}$$

For the second type of superconductor the magnetic field will start to penetrate the material above the lower critical field B_{c1}. Magnetic fluxons [30] enter the material and their number increases with increasing field. If one raises the field further to a value of B_{c2} the material becomes normalconducting. The temperature dependence of the critical magnetic fields B_{c1} and B_{c2} is the same as for the B_c of a type I superconductor. This is also shown in Fig. 2.6.

For classical superconductors like lead or tin, a very successful microscopic theory was developed by Bardeen, Cooper and Schrieffer which is called BCS theory [32]. They assumed that electrons begin to condense below T_c to pairs of electrons, the so called Cooper pairs. The two electrons in a pair have opposite momentum and spin. They experience an attractive force mediated via quantized lattice vibrations called phonons. This bound state of the two electrons is energetically favorable. As the overall spin of these two paired electrons is zero, many of these pairs can co-exist coherently, just like other bosons. The coherence length ξ_0 describes the distance over which the electrons are correlated. It is given by:

$$\xi_0 = \frac{\hbar v_F}{\Delta} \tag{2.44}$$

where v_F is the velocity of the electrons near the Fermi energy and 2Δ is the energy necessary to break up a Cooper pair. Relating the coherence length to the size of a Cooper pair it is meaningful the fact that it spans over many lattice constants of the

superconductive material. Within the BCS theory the energy gap can be calculated and it evaluates to:

$$\Delta = 1.76 k_B T_c \tag{2.45}$$

The exact value of Δ is material dependent and, for niobium, higher value of $\Delta = 1.9\ k_B T_c$ is found. The number of Cooper pairs $n_{cooper} = n_s/2$ is temperature dependent and only at T = 0 K all conduction electrons are condensed into Cooper pairs. The superconducting electrons co-exist with their normalconducting counterparts. The number of normalconducting electrons is instead given by the Boltzmann factor:

$$n_e(T \to 0) \approx n_s(0) \exp\left(\frac{\Delta(T)}{k_B T}\right) \tag{2.46}$$

Even in a type-I superconductor the magnetic field is not completely expelled, but penetrates into the material over a small distance, as otherwise the shielding current density would have to be infinitely large. The so-called London penetration depth λ_L is given by the characteristic length of the exponential decay of the magnetic field into the superconductor. Its value is

$$\lambda_L = \sqrt{\frac{m}{\mu_0 n_s e^2}} \tag{2.47}$$

where e is the charge of an electron, m its mass and n_s the number of superconducting charge carriers per unit volume. The theory did not allow neither for impurities in the material nor for a temperature dependence of the penetration depth. Gorter and Casimir [33] introduced the two-fluid model where a coexistence of a normal and superconducting fluid of charge carriers is postulated. A temperature dependence of the superconducting charge carriers component is also suggested, according to

$$n_c = n_n + n_s\ , \qquad n_s(T) = n_s(0)\left[1 - \left(\frac{T}{T_c}\right)^4\right] \tag{2.48}$$

Combining (2.47) and (2.48) the penetration depth shows the following temperature dependence

$$\lambda_L(T) = \lambda(0)\left[1 - \left(\frac{T}{T_c}\right)^4\right]^{-\frac{1}{2}} \tag{2.49}$$

where the Ginzburg-Landau [34] parameter κ, defined as

$$\kappa = \frac{\lambda_L}{\xi_0} \tag{2.50}$$

allow to distinguish between the two types of superconductor. κ is below $1/\sqrt{2}$ for type-I materials while it is above $1/\sqrt{2}$ for type-II.

In this frame, the role of impurities in the superconductive material is based on the evidence that the penetration depth depends on the *mean free path* l of the electrons in the material [35], the former increases when the latter is reduced. In the limit of very impure or "dirty" superconductor, the coherence length ξ is significantly reduced from its characteristic value ξ_0 and it becomes $\xi = l << \xi_0$ [36]. Actually the shielding mechanism of a static magnetic field in a superconductor is analogous to the shielding of a microwave field in a normal metal. If a microwave frequency is incident on a metal surface one can show that the field is decaying over a characteristic distance, the skin depth δ [20].

In niobium, for instance, l is strongly influenced by interstitial impurities like oxygen, nitrogen and carbon. This has a relevant impact on the final cavity quality factor and its dependence on the accelerating field [31]. Experimental evaluations for main superconducting properties of the polycrystalline high-purity niobium are reported in Tab. 2.3.

Experimental values	
Nb, type-II superconductor	
T_c	9.3 K
Coherence length ξ_0	39 nm
London penetration depth λ_L	30 nm
GL parameter κ	0.8

Tab. 2.3 – main superconducting properties of the polycrystalline high-purity niobium [31][37][20]

2.2.2 RF CRITICAL MAGNETIC FIELD

The above mentioned description of the critical magnetic field applies for the DC case. For microwaves in the GHz regime the situation is actually more complicated. Calculations have shown that the Meissner state can persist beyond B_{c1}. If no nucleation centers are available the possibility of a metastable state exists and therefore a delayed entry of the magnetic field, the so-called *superheated state,* might occur. Possible nucleation centers for magnetic flux are surface defects like protrusions or normalconducting inclusions. Therefore the surface condition and roughness are very important to achieve the superheating state.

The superheated field has been calculated on the basis of the Ginzburg-Landau equations [38]. The superheating field is given for different κ in [39]:

$$\begin{aligned} B_{sh} &= 0.75 B_c \text{ for } \kappa \gg 1 \\ B_{sh} &= 1.2 B_c \text{ for } \kappa \approx 1 \\ B_{sh} &= \frac{1}{\sqrt{\kappa}} B_c \text{ for } \kappa \ll 1 \end{aligned} \tag{2.51}$$

A superheating field has been observed in type-I when a defect-free surface was used [40]. Measurements on type-I and type-II superconductors at various frequencies indicate that the superheating field indeed exists at temperatures close to the critical temperature. This was confirmed in more recent measurements where on 1.3 GHz niobium cavities it was shown that the superheating state can be achieved if the temperature is close to T_c [20]. Anyway at temperatures of 4.2 K or 2 K the superheated state has not yet been established probably because other effects limit the maximum field gradient. These are for example local defects, which limit the maximum achievable field due to thermal breakdown [31].

Expected and measured performances of TESLA cavities in terms of critical magnetic fields are reported in Tab. 2.4. This confirms that the actual maximum field achieved at 2 K is in the order of B_{c1}, still some margin exist toward the superheating field limit of about 240 mT, corresponding to an eventual maximum accelerating gradient higher than 50 MV/m.

property	**Experimental data [mT] at 4.2 K**	**Calculated field [mT]**		**Eacc [MV/m] at 2 K**
		at 0 K	**at 2 K**	
B_{c1}	130	164	156	37
B_c	158	200	190	45
B_{sh}	190	240	230	54
B_{c2}	248	312	297	62

Tab. 2.4 – critical magnetic fields of high purity niobium together with the corresponding theoretical accelerating gradient for a TESLA cavity [31][41][42]

2.2.3 SURFACE RESISTANCE

For a direct current (DC) or low frequency alternating currents the superconducting electrons shield the normalconducting electrons from the electromagnetic field so that no power is dissipated. For alternating currents at microwave frequencies this is not true anymore. The inertia of the Cooper pairs prohibits them to follow the changing electromagnetic fields immediately, the shielding is not perfect anymore. The NC electrons start to flow and dissipate power. This gives rise to a resistance which depends on the number of normalconducting electrons and the frequency of the alternating current. For

temperatures $T < T_c/2$ and an energy of the microwave photons of $hf << \Delta$ the surface resistance can be approximated by:

$$R_{BCS}(T,f) = A\frac{f^2}{T}\exp\left(\frac{-\Delta}{k_B T}\right) \tag{2.52}$$

The factor A depends on material parameters like coherence length, electron mean free path, Fermi velocity and penetration depth. For niobium it is about $9\cdot10^{-5}$ $\Omega K/(GHz)^2$. Therefore the BCS resistance at 1.3 GHz is about 600 nΩ at 4.2 K and about 1 nΩ at 2 K. The exponential temperature dependence is the reason that operation at 1.8 – 2 K is essential for achieving high accelerating gradients in combination with very high quality factors. Superfluid helium is moreover an excellent coolant owing to its high heat conductivity. Exact result derived for R_{BCS} from the two-fluid model is [43]:

$$R_{BCS}(T,f) = C\sigma_{nc}\lambda_{eff}^3\frac{f^2}{T}\exp\left(\frac{-\Delta}{k_B T}\right) \tag{2.53}$$

C is a constant, which does not depend on the material properties. σ_{nc} is the conductivity in the normalconducting state. The dependence of R_{BCS} on the mean free path l is therefore [44]:

$$R_{BCS}(l) \propto \left(1+\frac{\xi_0}{l}\right)^{\frac{3}{2}}\cdot l \tag{2.54}$$

The total surface resistance contains in addition a temperature independent part, which is called residual resistance R_{res}. The residual resistance is usually dominated by lattice imperfections, chemical impurities, adsorbed gases and trapped magnetic field. Well prepared niobium surfaces show a residual resistance of a few nΩ (Fig. 2.7).

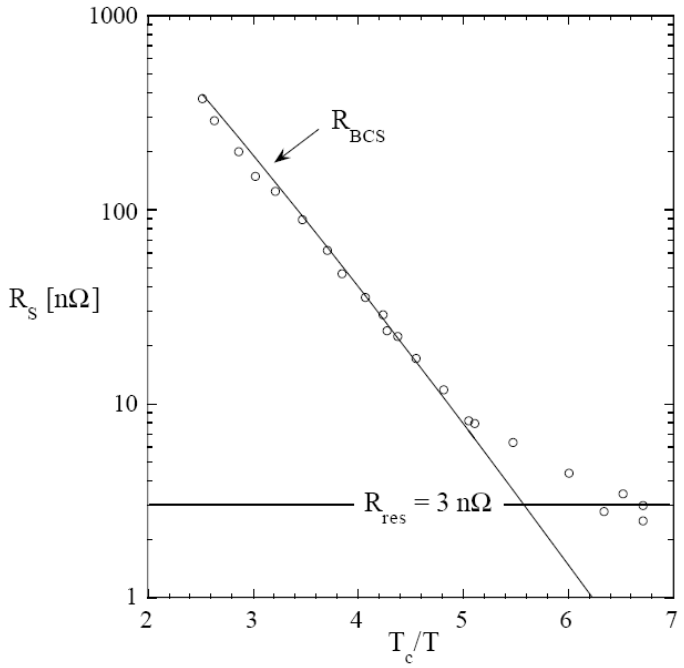

Fig. 2.7 - The surface resistance of a 9-cell TESLA cavity plotted as a function of T_c/T. [45]

Absorbed gases can lead to a high residual resistance [46]. The dielectric properties of N_2 and O_2 are the reason for this behavior. If a cavity is not shielded from the earth magnetic field its surface resistance is also increased since, in practice, weak magnetic DC fields are not expelled upon cooldown but remain trapped in the niobium and each flux line contains a normalconducting core. Any contamination of the surface with metallic parts (from screws, gaskets, etc.) or dielectric remnant from the surface treatment has to be avoided since it can enhance the residual RF losses to an intolerable level.

2.3 SUPERCONDUCTING CAVITIES

In view of large accelerator installations as ILC or XFEL the reduction of investments and operations costs become an increasingly demanding problem. For this reason the benefits of superconductivity are exploited. After magnets, accelerating RF cavities are currently the existing larger scale applications.

The fundamental advantage of superconducting cavities is the extremely low surface resistance as seen in the previous paragraph, in the nΩ region at 2 K temperature. The typical quality factors of normal conducting cavities are 10^4 - 10^5 while for sc cavities they may exceed 10^{10}, thereby reducing the RF power losses by 5 to 6 orders of magnitude according to (2.17). Only a tiny fraction of the incident RF power is dissipated in the cavity walls, most of it is either transferred to the beam or reflected into a load. The effective

final power efficiency must take anyway into account that this small power must be dissipated at cryogenic temperature, typically 2 K or 4.2 K when using liquid He as a cooler. In spite of the low corresponding refrigeration efficiency, a net reduction factor of several hundred in the power losses is still there, if compared to the normal conducting case[16]. Superconductivity benefits therefore become evident specially for application demanding high CW (Continuous Wave) accelerating gradient or aiming to an high duty cycle. In the latter case, SC cavities typically allow duty cycles in the order of 1 % or more. For lower duty factors applications, copper cavities take an advantage for what strictly concerns the accelerating gradient that can be up to 100 MV/m. This is anyway sustainable only for few μs and peak power needed are enormous.

Apart from the general advantages of reduced RF capital and operating costs, superconductivity offers certain special advantages that stem from the low cavity wall losses. Normalconducting cavities design were largely driven by the need to search for the maximum shunt resistance of the accelerating mode. This for instance led to small beam holes and a cavity shape focused mostly on dissipated power removal optimization. Instead SC cavities are designed mainly to achieve low surface peak electric and magnetic fields, issues related to shunt resistance are of minor importance since it is sufficiently large thanks to the lower surface resistance, according to (2.23). This afford to make the beam hole of a superconducting cavity much larger than for a normal conducting cavity. The large beam hole substantially reduces the beam cavity interaction, reducing coupling to higher order modes, allowing better beam quality and higher current for improving the precision and reaction rates of physics experiments.

For what concerns niobium cavity performances, it has been previously shown that the physical limitation of a SC resonator is given by the requirement that the RF magnetic field at the inner surface has to stay below the superheating field limit of the superconductor of about 240 mT, and for TESLA cavities this implies a maximum theoretical accelerating field close to 50 MV/m (par. 2.2.2). In principle, the quality factor should stay roughly constant when approaching this fundamental superconductor limit, but in practice the "excitation curve" Q_0 vs. E_{acc} ends at considerably lower values, often accompanied with a strong decrease of Q_0 towards the highest gradient reached in the cavity.

The reasons for this performance degradation have been identified and deeply studied over past years in the frame of TESLA collaboration, leading to a notable improvement in cavity results. These reasons are excessive heating at impurities on the inner surface, field emission of electrons, and multipacting (cavity performances limitations are discussed at much greater detail in [20] and [31]).

The former limitation of the maximum field in a superconducting cavity is related to thermal instability. Temperature mapping at the outer cavity walls usually reveals that the heating by RF losses is not uniform over the whole surface but that certain spots exhibit larger temperature rises, often beyond the critical temperature of the superconductor. Hence the cavity becomes partially normal conducting, associated with strongly enhanced

[16] A direct verification of the influence of superconductivity on cavity power efficiency comes from LEP operations with both NC and SC cavities, refer to [135] for results.

power dissipation. Because of the exponential increase of surface resistance with temperature, this may result in a runaway effect and eventually a quench of the entire cavity. Analytical models as well as numerical simulations are available to describe such an avalanche effect. The tolerable defect size depends on the RRR[17] of the material and the desired field level. As a typical number, the diameter of a normalconducting spot must exceed 50 μm to be able to initiate a thermal instability at 25 MV/m for RRR > 200. There have been many attempts to identify defects which were localized by temperature mapping. Examples of defects are drying spots, fibers from tissues, foreign material inclusions, weld splatter, and cracks in the welds. Both preparing and cleaning the cavity surface with extreme care and increasing the thermal conductivity of the superconductor material result in a reduction of the danger of thermal instability.

Field emission of electrons from sharp tips is the most severe limitation in high-gradient superconducting cavities. In field-emission loaded cavities, the quality factor drops exponentially above a certain threshold and X rays are observed. The field emission current density is given by the Fowler-Nordheim equation [47]

$$j_{FE} = c_1 E_{loc}^{2.5} \exp\left(-\frac{c_2}{\beta E_{loc}}\right) \tag{2.55}$$

where E_{loc} is the local electric field, β is a so-called field enhancement factor, and c_1 and c_2 are constants. There is experimental evidence that small particles on the cavity surface (e.g. dust) act as field emitters. Therefore, perfect cleaning, for example by high-pressure water rinsing (HPR), is the most effective remedy against field emission.

"Multipacting" is a commonly used abbreviation for "multiple impacting" and designates the resonant multiplication of field emitted electrons which gain energy in the RF electromagnetic field and impact on the cavity surface where they induce secondary electron emission. Depending on the secondary electron emission coefficient (SEEC) which typically shows an energy dependence, the number of new electrons can be larger than 1. These particles are accelerated in the electromagnetic field and hit eventually the wall again. If this process takes place in resonance to the RF phase, an avalanche of electrons will occur and cause the cavity to breakdown. When the electrons travel forth and back between two points on the cavity surface, this is called two-point multipacting. A typical place for two-point multipacting to occur is the equator region of elliptical cavities. Usually, multipacting barriers can be passed within a few minutes. This means that the electrons in the avalanche force gases to be desorbed. In this way the surface can be cleaned and the SEEC will drop below 1. This process is usually called "Conditioning" or "Processing".

In conclusion, in considering SCRF applications, the shown advantages must be balanced against the added cost and technology of the refrigerator and cryogenic distribution system, as well as the demands for clean surface preparation. Another factor

[17] RRR is the Residual Resistivity Ratio and it is defined as the ratio of the resistivity at room temperature and at liquid helium temperature in normal state. The low temperature resistivity is measured either just above Tc or at 4.2 K, applying a magnetic field to assure the normal state.

to keep in mind is that the useful length to active length ratio ranges from 50 - 75% due to the filling factor of cavities in the cryostat as well as to the need for other accelerator components (such as higher mode couplers) in the beam line.

As of today, niobium superconducting resonators are the choice for all the existing large scale installations of sc cavities. Beside some cases of a thin niobium layer sputtered onto the inner surface of a copper cavity, as in particular at CERN for LEP, cavities are fabricated from solid niobium sheets as at Cornell (CESR), KEK (TRISTAN), DESY (PETRA, HERA), Darmstadt (SDALINAC), Jefferson Lab (CEBAF) and finally DESY for TTF and following linacs.

2.4 THE TESLA CAVITY

The accelerating gradient in the ILC main linac will be supplied by over 16000 9-cell superconducting RF cavities, grouped into approximately 12.6 m long cryomodules. Another about 1200 9-cell cavities provide acceleration in the sources and bunch compressors. The baseline cavities use the TESLA design developed at DESY over the past 10 years. The TESLA 9-cell superconducting cavity was chosen as the baseline design because it has achieved the highest qualification gradients to date for multi-cell cavities, approximately within the range required for ILC. There is significant operational experience with these cavities and it has been demonstrated with beam that accelerating gradients of greater than 30 MV/m are possible after full installation in a cryomodule. ILC cavities will be required for qualification at 35 MV/m gradient in a vertical test in order to finally operate at an average gradient of 31.5 MV/m.

The TESLA resonator design is firstly illustrated in the following paragraph, including the choice of the final EM frequency, as well as mechanical and electromagnetic parameters of interest for the thesis activity. In conclusion, cavity fabrication procedures and treatments up to its installation are described.

2.4.1 TESLA CAVITY DESIGN

The TTF cavity is a 9-cell standing wave structure of about 1 m length whose lowest TM mode resonates at 1300 MHz. A photograph is shown in Fig. 2.8.

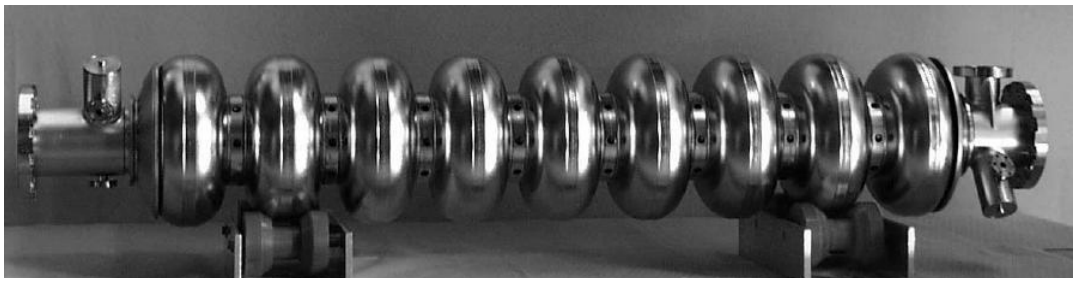

Fig. 2.8 – superconducting 9-cell 1.3 GHz TESLA cavity

The cavity is made from solid niobium and is cooled by superfluid helium at 2 K. Each 9-cell cavity is equipped with its own titanium helium tank, a tuning system driven by a stepper motor, a coaxial RF power coupler capable of transmitting more than 200 kW, a pickup probe, and two higher-order mode (HOM) couplers. To reduce the cost for cryogenic installations, eight cavities and a superconducting quadrupole are mounted in a common vacuum vessel and constitute the so-called cryomodule of the TTF linac (see par. 1.4). Within the module the cavity beam pipes are joined by stainless steel bellows and flanges with metallic gaskets. The cavities are attached to a rigid 300 mm diameter helium supply tube which provides position accuracy of the cavity axes of better than 0.5 mm. Invar rods ensure that the distance between adjacent cavities remains constant during cooldown. Radiation shields at 5 and 60 K together with 30 layers of super-insulation limit the static heat load on the 2 K level to less than 3 W for the 12 m long module.

The losses in a microwave cavity are proportional to the product of conductor area and surface resistance according to (2.19). For a given length of a multi-cell resonator, the area scales with $1/f$ while the surface resistance of a superconducting cavity scales with f^2 for $R_{BCS} >> R_{res}$ and is independent of f for $R_{BCS} << R_{res}$ (par. 2.2.3). At an operating temperature T = 2 K, the BCS term dominates above 3 GHz and, hence, the losses grow linearly with frequency, whereas, for frequencies below 300 MHz, the residual resistance dominates and the losses grow with $1/f$. In order to minimize the dissipation in the cavity wall cavity frequency is usually chosen in the range 300 MHz to 3 GHz. Cavities in the 350 to 500 MHz regime are in use in electron-positron storage rings. Their large size is advantageous to suppress wake field effects and higher-order mode losses. However, for a linac of several km length the niobium and cryostat costs for these bulky cavities would be prohibitive, hence an higher frequency has to be chosen. Considering material costs, f about 3 GHz might appear the optimum, but there are compelling arguments for choosing about half this frequency. For instance, beside the availability of high power klystrons for 1.3 GHz,:

- The wake field losses scale with the second to third power of the frequency [20]. Beam emittance growth and beam-induced cryogenic losses are therefore much higher at 3 GHz.
- The f^2 dependence of the BCS resistance sets an upper limit of about 30 MV/m at 3 GHz, hence not compatible with ILC requirements.

A multi-cell resonator is advantageous for maximizing the active acceleration length in a linac of a given size. With the increasing number of cells per cavity, however, difficulties arise from trapped modes, uneven field distribution in the cells, and too high power requirements on the input coupler. Extrapolating from the experience with 4-cell and 5-cell cavities, a 9-cell structure appeared manageable. A side view of the TTF cavity with the beam tube sections and the coupler ports is given in Fig. 2.9.

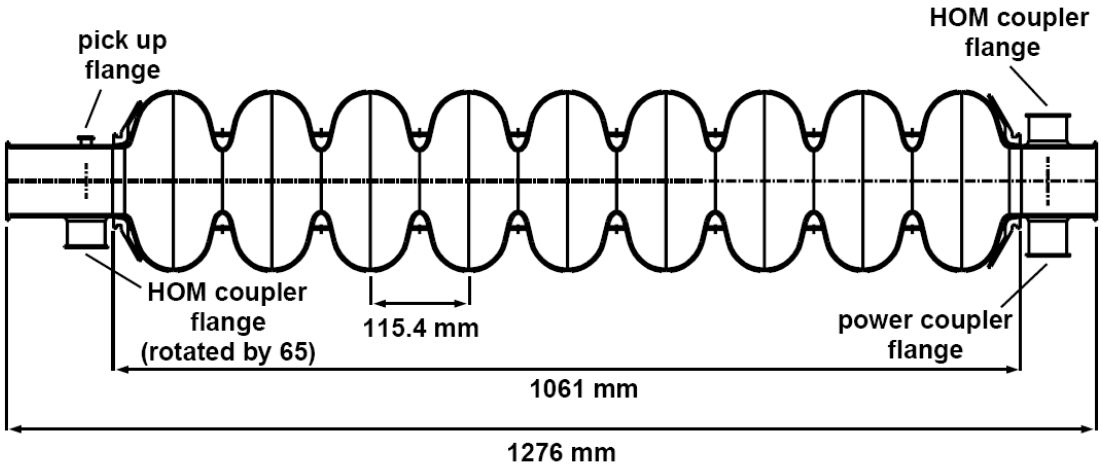

Fig. 2.9 - Side view of the 9-cell TESLA cavity with ports for the main power coupler and two HOM couplers.

The design of the cell shape was guided by the following considerations:

- a spherical contour near the equator with low sensitivity for multipacting.
- minimization of electric and magnetic fields at the cavity wall to reduce the danger of field emission and thermal breakdown.
- a large iris radius to reduce wake field effects.

The shape of the cell was optimized using the code URMEL [48]. The resonator is operated in the π mode with 180° phase difference between adjacent cells. The longitudinal dimensions are determined by the condition that the electric field has to be inverted in the time a relativistic particle needs to travel from one cell to the next. The separation between two irises is therefore $c/(2f)$. The iris radius R_{iris} influences the cell-to-cell coupling k_{cell}, the excitation of higher-order modes, and other important cavity parameters, such as the ratio of the peak electric (magnetic) field at the cavity wall to the accelerating field and the ratio R_a/Q_0. The final contour of a half-cell is shown in Fig. 2.10 and all the corresponding dimensions are reported in Tab. 2.5.

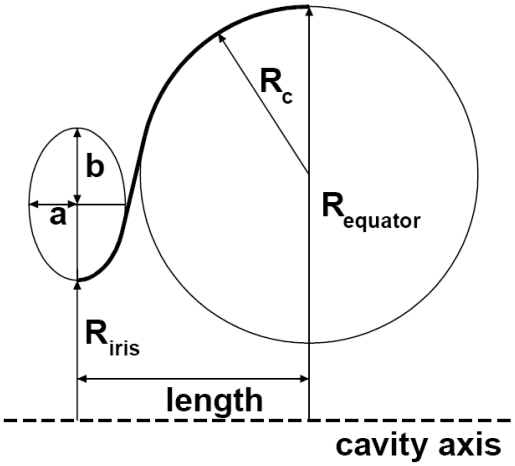

Fig. 2.10 – schematic contour of a TESLA half cell

Cavity shape parameter	Midcup [mm]	Endcup 1 [mm]	Endcup 2 [mm]
Equator radius R_{equat}	103.3	103.3	103.3
Iris radius R_{iris}	35	39	39
Radius R_{arc} of circular arc	42	40.3	42
Horizontal half axis a	12	10	9
Vertical half axis b	19	13.5	12.8
Length l	57.7	56	57

Tab. 2.5 – TESLA half-cell shape parameters

It is composed of a circular arc around the equator region and an elliptical section near the iris. The half-cells at the end of the 9-cell resonator need a slightly different shape to compensate the beam tube and ensure equal field amplitudes in all 9 cells. In addition, there is a slight asymmetry between the left and right end cell which prevents trapping of higher-order modes.

2.4.2 MAIN PARAMETERS AND PERFORMANCES

All TESLA cavity mechanical and electromagnetic design parameters are summarized in Tab. 2.6.

Parameter	Value
Structure type	Standing wave
Accelerating mode	TM_{010}, π mode
Fundamental frequency	1.300 GHz
Average installed gradient for ILC	31.5 MV/m
Qualification gradient for ILC	35 MV/m
Installed quality factor for ILC	$\geq 1 \cdot 10^{10}$
Qualification quality factor for ILC	$\geq 0.8 \cdot 10^{10}$
Active length	1.038 m
Number of cells	9
Cell to cell coupling k_{cell}	1.87 %
Iris diameter	70 mm
R_a/Q_0	1036 Ω
Geometry factor G	270 Ω
E_{pk}/E_{acc}	2.0
B_{pk}/E_{acc}	4.26 mT MV^{-1} m^{-1}
Tuning range	± 300 kHz
$\Delta f/\Delta l$	315 kHz/mm
Number of HOM couplers	2
Q_{ext}	$3.5 \cdot 10^6$
Cavity bandwidth with $Q = Q_{ext}$	370 Hz FWHM

Tab. 2.6 – TESLA 9-cell SC niobium cavity for ILC design parameters [1][7]

The cavity is then enclosed in a special vessel, usually referred as the helium tank, that contains the superfluid helium needed for cooling and serves at the same time as a mechanical support of the cavity and as a part of the tuning mechanism. The He tank is made from titanium whose differential thermal contraction relative to niobium is 20 times smaller than for stainless steel.

The ambient magnetic field must be, as introduced in par. 2.2.2, shielded to a level of about a mT to reduce the magnetic surface resistance to a few nΩ. This is accomplished with a two-stage passive shielding, provided by both the conventional steel vacuum vessel of the cryomodule and a high-permeability cylinder around each cavity. The magnetic shielding cylinders of the cavities are made from Cryoperm[18] μ-metal which retains an high permeability when cooled to liquid helium temperature.

The power input coupler provide the transfer of RF power from the klystron generator to the cavity and hence to the beam. It must provide the correct match between the generator impedance and the combined impedance of the cavity-beam system. Different coaxial couplers have been developed for TESLA cavity [49], consisting of a "cold part," which is mounted on the cavity in the clean room and closed by a ceramic

[18] Cryoperm is made by Vacuumschmelze Hanau, Germany.

window, and a "warm part," which is assembled after installation of the cavity in the cryomodule. The warm section also contains the transition from waveguide to coaxial line. The couplers allow for some longitudinal motion inside the 12 m long cryomodule when the cavities are cooled down from room temperature to 2 K [19]. For this reason, bellows in the inner and outer conductors of the coaxial line are provided and by moving the inner conductor of the coaxial line, Q_{ext} can be varied in the range $1 \cdot 10^6$ to $9 \cdot 10^6$ to allow not only for different beam loading conditions but also to ease in situ high power processing of the cavities.

The intense electron bunches excite eigenmodes of higher frequency in the resonator which must be damped to avoid multi-bunch instabilities and beam breakup. This is accomplished by extracting the stored energy via HOM (High Order Modes) couplers mounted on the beam pipe sections of the 9-cell resonator. HOM are welded to the cavity, the good cooling of the superconducting inner conductor by two stubs makes the design insensitive to γ radiation and electron bombardment. A tunable 1.3 GHz notch filter is incorporated to prevent energy extraction from the accelerating mode when mounted on the cavity.

For a direct reference, Fig. 2.11 shows results from excitation curve, Q_0 vs. E_{acc}, for the best vertical test performance for individual cavity structures at DESY.

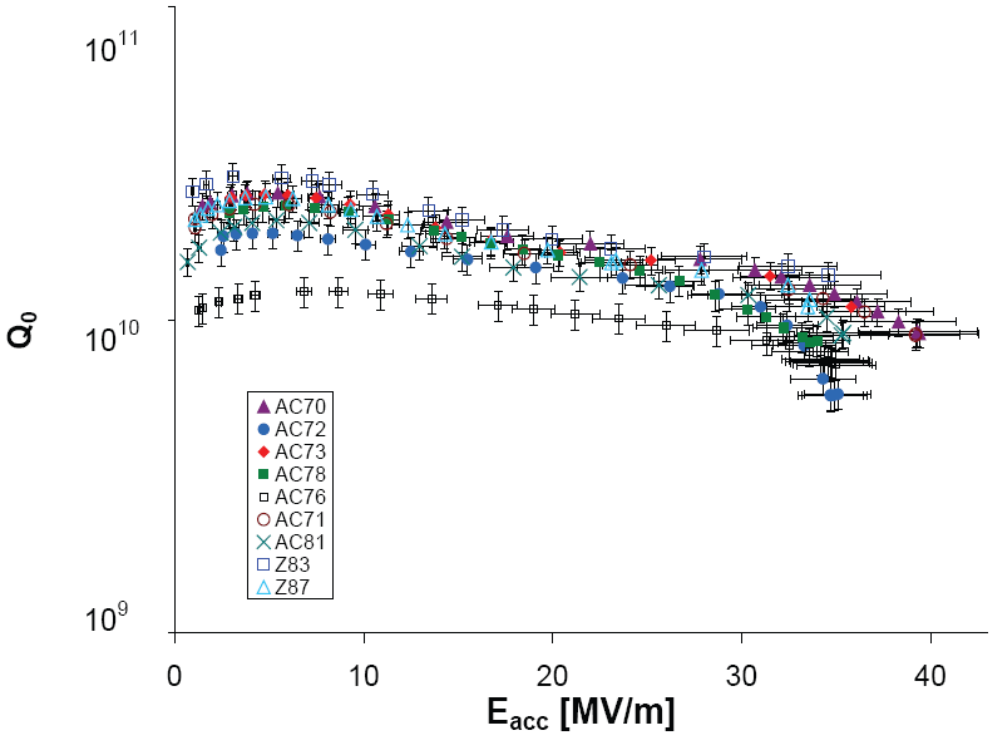

Fig. 2.11 - Q_0 vs. E_{acc} curves for the best 9 Cell vertical qualification tests at DESY [1]

[19] The motion of the coupler ports is up to 15 mm in the first cryomodules but has been reduced to about 1 mm in the most recent cryostat design by fixing the distance between neighboring cavities with invar rods.

Further recent data about TESLA cavity performances, referring to several different cavities and two FLASH cryomodule (#6 and #7), are reported in the frame of the experimental measurements presented in this thesis work, in chap. 4, 5 and 6.

2.4.3 CAVITY FABRICATION AND TREATMENTS

The fabrication of high quality superconducting cavities starts with high quality niobium materials. The analysis of RF superconductivity features, shown in previous paragraphs, clearly highlighted how crucial is the role of cavity wall niobium surface properties in determining overall performances. The RRR (Residual Resistivity Ratio) value indirectly indicates the purity of the bulk metal as well as interstitial contamination that can affect the performance of the superconducting properties. An RRR value of 300 is considered as desirable. The transition joints to the helium vessel are fabricated from a lower grade niobium sheet with a RRR value of around 40. The cavity flanges and transitions to the helium vessel are made from bar or round stock niobium alloy, typically NbTi55. The alloy is harder and stronger, and it prevents deformation near the vacuum seals and provides strong transition joints at the cavity connections.

As a final quality assurance check prior to use, the cell material is sometimes eddy-current scanned to a depth of 0.5 mm into the surface of the sheet material. Cavity cells are traditionally formed by deep drawing or hydro-forming methods where the sheets are pressed into dies to form the necessary shapes. These fabrication methods require machining of surfaces to form the weld joints. All cavity subcomponents are joined by electron beam welding in a vacuum chamber. This reduces the contamination at the welds and is considered the cleanest form of joining metals together. Prior to electron beam welding, all subcomponents are inspected, degreased then prepared typically by mechanical polishing of surfaces to be welded, as necessary. The welded components are degreased and chemically etched and rinsed to remove inclusions and surface contamination from the machining and welding steps. The two primary issues with cavity fabrication are therefore quality assurance on the niobium materials and on the electron beam welds. Niobium materials must be scanned to detect and eliminate surface defects, and then protected with care throughout the manufacturing process.

The current technology for preparing cavity surfaces consists of a series of different processes [50]:

- Mechanical Inspection: The cavity is mechanically measured with a coordinate measuring machine to compare dimensional measurements against mechanical tolerances identified on design drawings.
- RF Inspection: The cavity fundamental frequency is measured. A bead is pulled through the beam axis of the cavity to determine and record the stored energy of

each cell. The bead disturbs the fields in each cell as it passes through and changes the frequency by an amount equal to the stored energy in that cell [51].

- Bulk Chemistry: Both the internal and external surfaces of the cavity are ultrasonically treated in hot de-ionized water to remove grease from the handling and surface particulates that have been collected since fabrication. The cavity is then internally chemically etched with electro-polishing [52] to remove 150-250 μm of material.
- Heat treatment: After bulk chemistry the cavity is cleaned and dried before inserting into a vacuum furnace for heat treatment. The chamber is evacuated to about 10^{-7} mbar and the bare cavity is heated to 800 °C and soaked at that temperature to remove any excess hydrogen gained during the chemistry. This additional hydrogen, if not removed, lowers the cavity Q_0 value due to formation of a niobium hydride during cool-down, that adds surface losses.
- RF Tuning: The cavity is tuned to the correct warm frequency and the stored energy (field flatness, FF) in each cell equalized. The cells are measured with a bead pull and then plastically deformed by pulling or squeezing in a mechanical tuner. The cavity is mechanically adjusted to correct any alignment errors that would affect tuning for field flatness.
- Final Chemistry: The final internal chemistry refreshes the niobium surface by electro-polishing removal of 10-30 μm of material. The processing steps are the same as for the bulk chemistry although the processing time is much shorter.
- High Pressure Rinsing: The cavity is inserted vertically into the high pressure rinse (HPR) [53] system where a wand is moved slowly through the beam axis of the cavity and the cavity is rotated. The head of the wand has small diameter nozzles tilted at angles through which high pressure ultra pure water is sprayed. A water pressure to the wand of 80-100 bar produces up to 40 N of force on the surface at impact. The wand is repeatedly moved up and down spraying all surfaces of the cavity with water to remove surface particulates which are attached on the cavity interior. The HPR process is considered the most effective cleaning method to remove surface contamination.
- First Assembly: Assembly takes place in a Class 10 clean room, where the cavity has been left open to air dry over night. Once the cavity has dried, cleaned subcomponents are carefully attached to the cavity by hand. Each flange connection is sealed using a diamond shaped aluminum alloy gasket that is crushed between flange faces with high line loading forces. High strength bolts and nuts with washers provide the force necessary to crush the seal. All subcomponents are assembled to the cavity except the bottom beam-line flange to allow for the second high pressure rinse.

These cavity treatment stage are performed according to the presented sequence, followed by a second HPR and a second assembly needed to connect beam line flanges.

Finally, the cavity is evacuated and vacuum is forced in the beam pipe typically using a turbo-molecular pump. Then the cavity is ready for first cold RF qualification and acceptance tests to be performed in a vertical cryostat.

As of today, only two manufacturer in the world are fully qualified for the production of TESLA cavity: Zanon from Italy [54] and Accel from Germany [55]. Some cavities have been formerly produced also by Cerca [56] from France[20]. In the meanwhile other manufacturers in different countries emerged (as AES [57] in US) and started to be involved, therefore additional manufacturing resources are expected for the future in view of the needed ILC large scale production.

Full details concerning how the application of all these techniques and treatments, combined with an extremely careful handling of the cavities in a clean-room environment, has led to a significant increase in cavity performances can be found in [31] and [45].

[20] Cerca has currently discontinued its activity on the TESLA cavity.

3 CAVITY DETUNING AND TUNERS

The physical elements that lead to the detuning of the superconducting cavity during operations are presented in this chapter for what concern TESLA type resonators. The theory for the main sources of static and dynamic detuning will be presented together with solutions adopted to achieve their experimental characterization. Two different scenarios were considered, continuous wave (CW) and the final pulsed mode, the former being mainly used during preliminary R&D phase for detuning and tuners characterization, even for CW accelerating machine based on TESLA SC technology as the BESSY FEL linac [58].

Basics principles of cavity tuning via resonator length change are then presented together with the first cavity tuner, the TTF tuner, realized for the TESLA test facility linac.

Finally, the latest solution for dynamic detuning acquisition has been further developed by the author and used for the characterization of the Lorentz force detuning effect during the measurements performed on module #6 and #7 (ACC6 and ACC7) in CMTB (see par 1.4).

3.1 STATIC DETUNING AND CW MEASUREMENTS

A general analytical approach has been firstly introduced by J. C. Slater [59] for the resonance frequency shift of a resonator with perturbed boundaries, as in the case of a displacement of its geometrical shape from the nominal one. Assuming an infinitesimal deformation of the original cavity volume so that a perturbative analysis can be performed, the following notable formula is deduced:

$$\omega^2 = \omega_a^2 \left(1 + \int (H_a^2 - E_a^2) dv\right) \tag{3.1}$$

where the perturbed resonant frequency ω, resulting from an original resonance mode ω_a, is given in terms of an expression of the unperturbed fields H_a and E_a that is integrated over the volume which is removed by the volume of the resonant cavity by the perturbation of the surface. As a consequence, the direction of the induced frequency shift is related to the specific part of the resonator involved in the perturbation. Generally, when a resonator surface is pressed in (i.e. a volume is removed) the frequency increases if the magnetic field is strong at the perturbed part of the surface, and is decreased if the electric field is strong there.

The reduced thickness of walls and the high quality factor gained thanks to the superconductivity (see par. 2.3) make TESLA cavities extremely sensitive to mechanical perturbations, even on the micrometer level. As a reference, if relation (3.1) is applied by means of a proper finite element modeling (FEM) code for EM fields (see chap. 6 and appendix B), for a 1 mm length displacement on the cavity axis of a TESLA resonator geometry, a frequency shift of 315 Hz is found [1]; a value that is higher than the resonator half-bandwidth of about 190 Hz. This result is often referred as the tuning factor of TESLA cavities and it couples the longitudinal length variation of the resonator to the shift in its resonant frequency, provided that the variation is within a small range of few hundreds of μm (1 mm maximum displacement for a warm cavity before plastic deformations occur). Namely:

$$\frac{\partial f}{\partial z} = 315\ {}^{\mathrm{kHz}}/_{\mathrm{mm}} \tag{3.2}$$

Once in the final operating conditions, slowly varying drifts in the temperature of the cavity or in the pressure of the He bath surrounding the resonator contribute to generate a quasi-static detuning.

A general scheme for the experimental measurements of cavity detuning is now introduced. For the cavity in CW stationary condition the detuning information can be easily obtained through phase detection according to the scheme represented in Fig. 3.1.

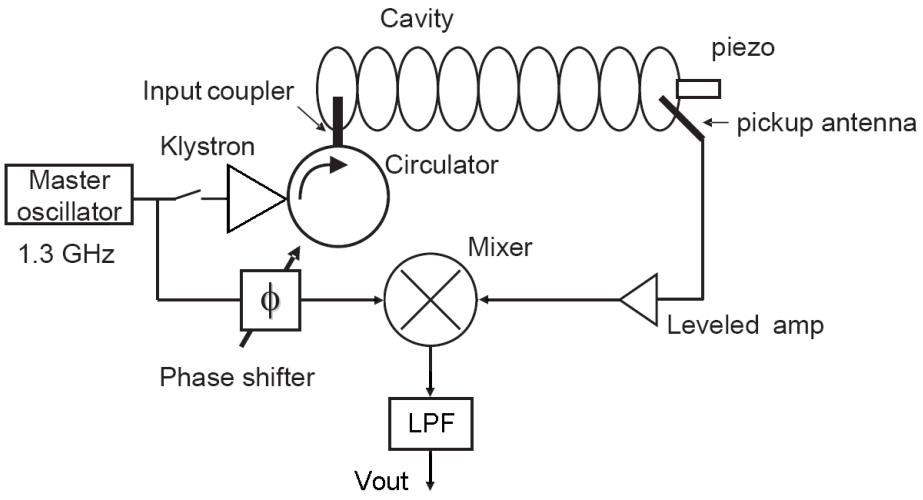

Fig. 3.1 – phase detection based detuning measurement scheme

A phase detector device compares the phase of the signal from cavity pick-up antenna with the phase of the reference RF signal (from Local Oscillator or LO), the latter being assumed as the reference cavity phase. Phase detection is realized by means of a RF mixer followed by a low-pass filter to clear the mixer output signal by the intermodulation products and therefore output only V_{out} , the part of the signal that is directly related to phase difference $\Delta\varphi$, according to (3.3):

$$V_{out} = K_C K_{PD} \cos(\Delta\varphi) \tag{3.3}$$

RF delay lines are used to set the phase detector working point, in order to obtain a quasi-linear response from the detector around phase of $\pi/2$ and multiples. This scheme is very common and widely used, especially in the frame of Phase Locked Loops (PLL) [60]. The phase detector can then be calibrated exciting it with two signals with slightly different known frequencies or even directly through the coefficient K_C during operations, by properly detuning the cavity of a known amount while reading the phase detector output. Alternatively, the loop can be closed realizing a VCO (Voltage Controlled Oscillator) with the V_{out} signal, so to phase-lock the local oscillator to the cavity instant frequency (exactly a PLL).

3.2 TUNING PRINCIPLES AND THE TTF TUNER

To ensure the correct cavity tuning for beam acceleration, resonators are provided with a tuning mechanism that usually relies on an electro-magnetic coupling or on a mechanical action on the cavity itself. For the TESLA type resonators the cavity tuning is accomplished by a mechanical device that modify the cavity length driven by a stepper motor, according to a solution formerly designed for TTF linac. This tuning assembly, further on named as TTF tuner, is installed at the helium tank side opposite to the power coupler and exploits the high longitudinal tuning sensitivity of this resonators, as seen in (3.2). The original design of the leverage is shown in Fig. 3.2. It has been initially introduced by M. Maurier and P. Leconte, based on the MACSE tuner design [61].

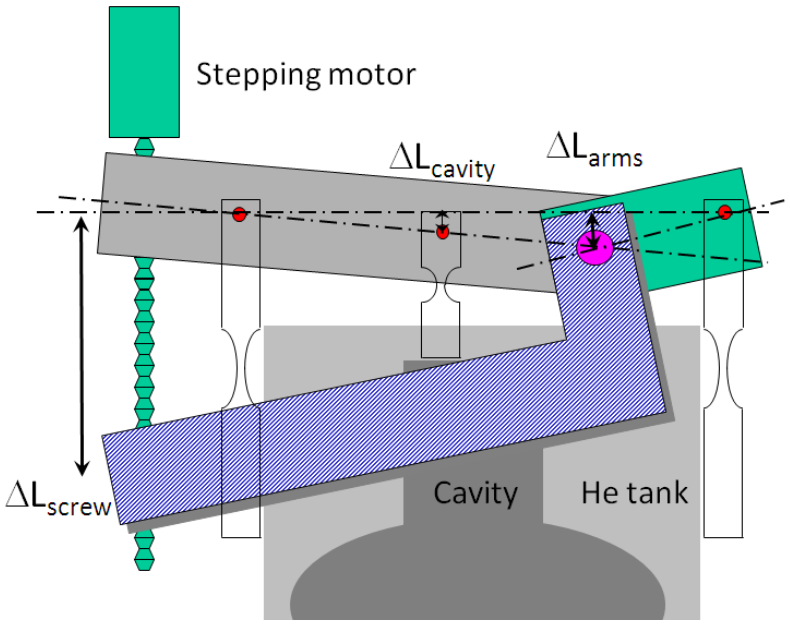

Fig. 3.2 – schematic representation of the TTF tuner working principles

The leverage system is designed in order to provide a sufficient demultiplication factor, around 1/25, to reduce stresses on the stepper motor and to enhance sensitivity . The motor, according to the reference TTF scheme, is driving a copper-beryllium alloy (CuBe) screw through an harmonic drive gear box[21] leading to a final sensitivity below 1Hz /step and to a total static tuning range higher than 800 kHz. Several assemblies of this kind have been so far installed, both in TTF and in FLASH linacs, performing satisfactory reliability and life-time even in cryogenic operations. As an example, a typical TTF tuner installation is presented in Fig. 3.3 where a part of the cold mass cavity string of a TTF cryomodule is visible. The harmonic drive housing is also visible, connecting the stepper motor and the CuBe screw that drives the mechanical leverage.

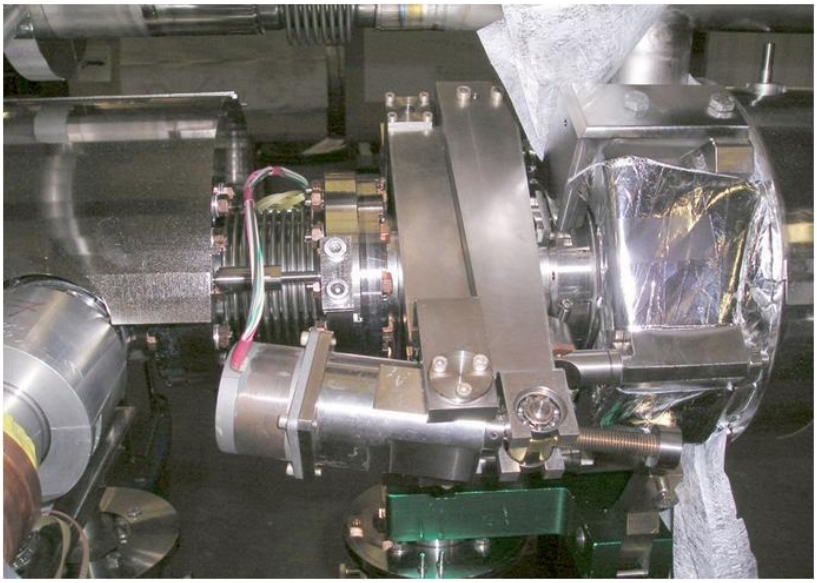

Fig. 3.3 – the TTF tuner

The tuner is installed across a bellow that is placed at the corresponding helium tank edge between the vessel and the cavity end dish, in order to allow the tuner longitudinal tuning action. The final stiffness of the whole assembly is about 100 kN/mm and the hysteresis over the tuning range is below the cavity typical bandwidth.

Once TESLA cavities achieved performances allowed higher accelerating gradients than first TTF installation, the issues related to dynamic detuning, described in detail in the following paragraph, started to be critical. This former design of the TTF tuner has then been modified, introducing fast actuators to counteract dynamic detuning. This solution, although not specifically designed for this feature and therefore significantly limited, has been anyway repetitively and successfully operated at gradient up to 36 MV/m. In the next par. 4.4.4 the integration of fast actuators up to the present modified design of the TTF tuner is described.

[21] Harmonic drive refers to the special design of the de-multiplication gear box, for further information refer to [137].

3.3 DYNAMIC DETUNING SOURCES

3.3.1 MICROPHONICS

The high sensitivity to mechanical deformations of TESLA superconducting cavities has been already underlined. External mechanical vibrations can be transferred to the cavities via the supporting system of the cryostat, the beam pipes and the helium bath. Even a nonlinear flow of liquid He itself might disturb the geometry of the cavity. Outer sources of disturbances can eventually contribute as human activity above the tunnel, civil works, or seismic movement of ground. The excited vibrations of the cavity therefore induce stochastic modulations of the resonance frequency of the cavity leading to the so called microphonic detuning or microphonics. This corresponds to an amplitude and phase jitter of the accelerating field, which has to be suppressed by the Low Level RF control (see par. 4.2.1).

Experimental characterization of the microphonics source of dynamic detuning make use of the CW operation measurements that are currently performed on TESLA cavities. For instance, in the frame of the FEL linac that will be installed in BESSY, based on TESLA cavities operated in CW, microphonics are the dominant error source for field stability. Microphonics measurements are usually performed using the same scheme illustrated in Fig. 3.1, although it is strictly verified for static detuning. Actually, as far as the dumping time of the cavity own TM_{010} π mode, that is excited by the microphonics dynamic detuning, is significantly lower than the typical period of the cavity mechanical disturbances the assumption of stationary state is preserved. Therefore, correspondingly, the cavity resonance quality factor actually determines the maximum achievable bandwidth of this measurement. Up to 2 kHz bandwidth is generally allowed but even more for room temperature cavities. According to this scheme, an experimental verification of microphonic detuning has been performed in the CHECHIA test cryostat [62] and results are here presented in Fig. 3.4 and Fig. 3.5. The latter represents the detuning spectrum as the Fast Fourier Transform or FFT of the acquired time data.

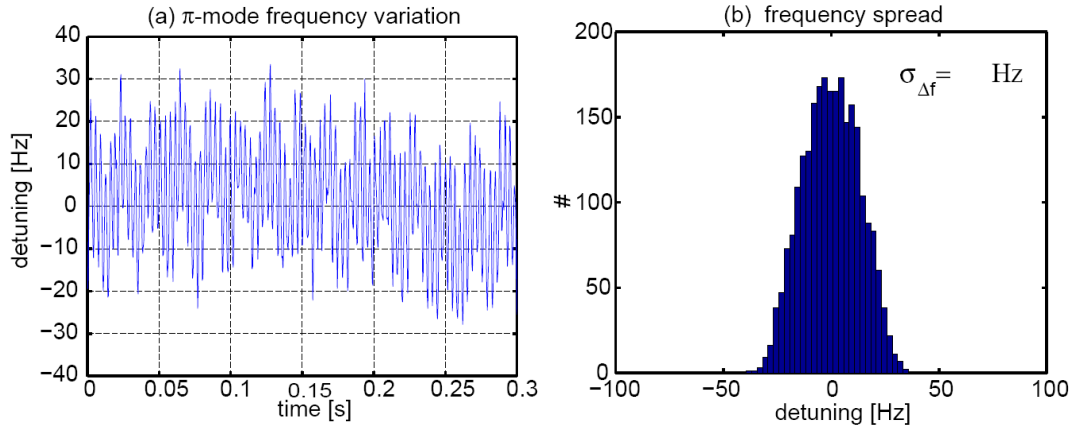

Fig. 3.4 – fluctuations of the cavity frequency, plotted against time (left) and frequency spread (right) [62]

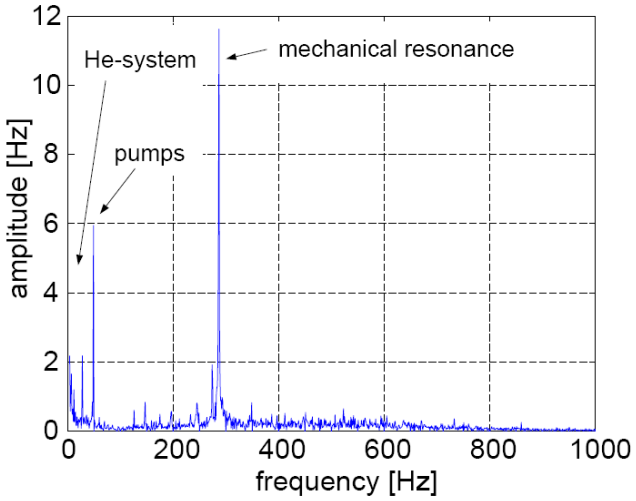

Fig. 3.5 – spectrum of microphonics detuning showed in Fig. 3.4 [62]

The frequency has a Gaussian distribution, and the spectrum of the microphonics confirms that the fluctuations are dominated by few low frequencies, which are vibration frequencies of the vacuum pumps and the helium compressors as well as resonance frequencies of mechanical cavity modes. A mechanical resonance at 287 Hz shows the strongest excitation, this value can correspond to the cavity main longitudinal mode (see par 5.3.1) The frequencies of the excited mechanical vibrations are well below 1 kHz. Accordingly, in pulsed cavity operation (1.6 ms pulse length for ILC) it is expected that microphonics mainly modulate the electrical resonance frequency from pulse to pulse, but not within the pulses. Further measurements performed (with a different procedure, see par 3.4) at the FLASH site (TTF linac at that time) confirmed a microphonics level below 10 Hz rms [26], which is small for the superconducting cavity operations foreseen for ILC.

As a reference, an additional measure for microphonics characterization has been performed at BESSY on a CW driven TESLA cavity [63][64]. Results, in Fig. 3.6, show a significant correlation between the cavity frequency oscillations and the pressure of the He bath thus revealing that the main contribution to the microphonics can be expected coming from the cooling medium itself. A change in Helium pressure was measured to lead to a detuning of 55 Hz/mbar. Fig. 3.6 shows the microphonics recorded over a period of 30 seconds in correlation with the He-bath pressure.

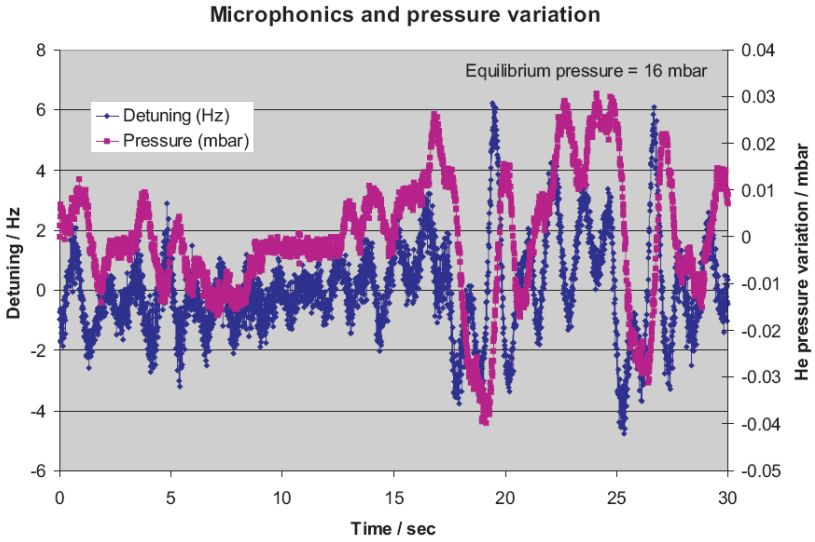

Fig. 3.6 – microphonics correlation to the He bath pressure difference [64]

It must be finally considered that, as will be outlined later on in par. 5.3, the choice to install and mechanically couple to the cavity one or more piezoelectric actuators lead to an alternative possibility to evaluate detuning. This refers to the possibility to make use of the sensor feature of the piezo stack to record cavity deformations as an induced piezoelectric voltage over time. This is an indirect method, as the mechanical influence from cavity and tank on the frequency response does not necessarily lead to a linear relationship between cavity (and detuning) and piezo position. Some experimental results related to this peculiar mechanical analyses of the cavity have been performed by the author and are presented in par. 5.3.

3.3.2 LORENTZ FORCE DETUNING

The electromagnetic fields inside the cavity during the RF pulse exert 'radiation pressure' on the cavity walls. Application of the 'right hand rule' of the Lorentz force between magnetic field in the cavity and its induced shielding current results in an outward directed force on this current and thus also on the wall. For the electric field, the induced surface charges are attracted by the electric field, thus creating a force pulling the wall inside. The final force per unit area (i.e. the pressure) is given by [65]:

$$P_R = \frac{1}{4}(\mu_0|\mathbf{H}|^2 - \varepsilon_0|\mathbf{E}|^2) \tag{3.4}$$

where H and E denote the magnetic and electric fields distribution on the walls. As a reference, the Lorentz forces in the case of an elliptical resonator as the TESLA cavity point inward in the iris region dominated by electric field, therefore tending to contract the

cells, while they tend outward at the equator, dominated by the magnetic field, trying to increase the radius of the cell (see Fig. 3.7).

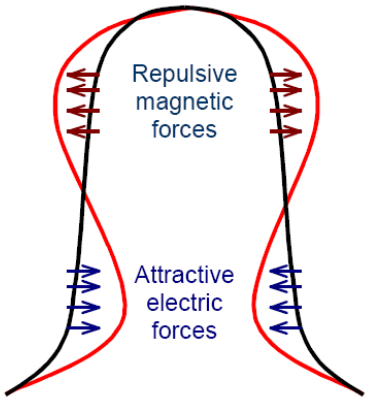

Fig. 3.7 – schematic view of the Lorentz forces inside a TESLA shaped cell

For TESLA cavities this electromagnetic pressure results to be about 1 N/cm^2, a small but anyway important value due to cavity extreme sensitivity to mechanical deformations. The resulting deformation of the cavity shape shifts the resonance frequency of the accelerating mode from its nominal value according to formula (3.1) previously introduced. Since both surface charges and currents as well as electrical and magnetic field are proportional to the RF field, the resulting force is proportional to the square of the excitation amplitude. As a result, assuming that the cavity volume changes linearly with the pressure and its change is small so that the H and E fields of the unperturbed cavity can be considered in formula (3.1), the steady-state Lorentz force induced frequency shift Δf (Lorentz force detuning or LFD) is, for CW and constant gradient condition, proportional to the square of the accelerating gradient E_{acc}.

$$\Delta f = K_L \cdot E_{acc}^2 \tag{3.5}$$

The parameter K_L, called the static Lorentz force coefficient, is always negative since the final effect of both electrical and magnetic fields in the resonator does not lead to a cancellation of the induced cavity detuning, but always a decrease of resonance frequency. This can be understood from a lumped circuit model of the resonator: increase of the magnetic volume means a larger inductance with lower frequency, decrease of the electric volume means increasing the capacitor (smaller gap), thus also a lower frequency [66]. TESLA cavities were initially designed aiming to a reference value for K_L of -1 $Hz/(MV/m)^2$.

K_L value is first of all strongly dependant on resonator stiffness k_c As a consequence an additional cavity stiffening has been provided. This could have eventually been achieved increasing the thickness of cavity walls but this option has been discarded for several reasons: Nb material costs, thermal conductivity needs and cavity reaction force during

tuning. Finally, stiffening rings, welded in between adjacent cells, have been used and are visible in Fig. 3.8 where the TESLA cavity end group is reported (see also Fig. 2.9).

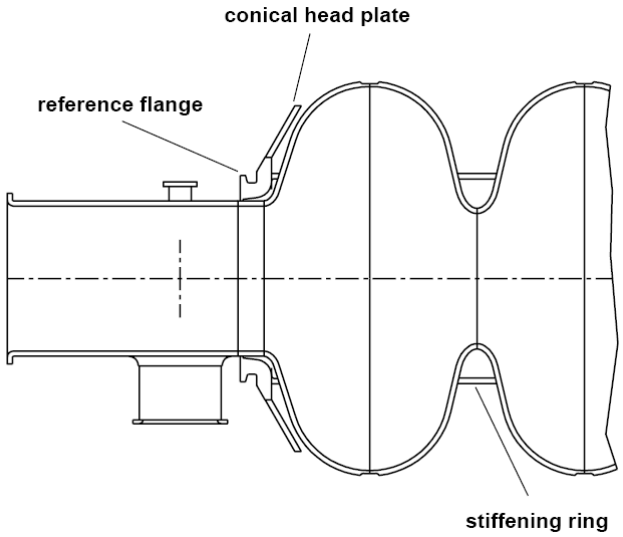

Fig. 3.8 – detail of the end group of a TESLA cavity [45]

Welded rings significantly reduces cavity deformations close to iris region and simultaneously preserve cavity elasticity that is dominated by the equator region of each cell. Final resulting resonator longitudinal stiffness is 3.023 kN/mm (see par. 2.4).

Additionally, the K_L coefficient is drastically dependant on the external stiffness k_{ext}, defined as the longitudinal stiffness of the mechanism that constraints the cavity. According to an analytical model originally developed for TRASCO proton cavities [67], overall cavity behavior under Lorentz forces can be assumed as a linear superposition of two effects:

- a pressure acting on the length-constrained cavity and therefore inducing only a shape distortion. This results in a frequency variation Δf^{∞} and in a longitudinal reaction force at the cavity boundary of F^{∞}.

- a cavity constraint of arbitrary longitudinal stiffness k_{ext}.

As a consequence, the resulting static Lorentz force induced detuning Δf for the arbitrary external boundary condition and at a given gradient accelerating value, are given by:

$$\Delta f = \Delta f^{\infty} + \frac{\partial f}{\partial z}\frac{F^{\infty}}{k_c + k_{ext}} \tag{3.6}$$

And therefore the corresponding K_L coefficient can be assumed as composed by two parts, K_L^{∞} and K_L^{ext} both having dimensions of $Hz/(MV/m)^2$, according to:

$$K_L = K_L{}^{\infty} + K_L^{ext}\left(\frac{1}{1+{k_{ext}}/{k_c}}\right) \tag{3.7}$$

where while $K_L{}^{\infty}$ is , as said, mainly a function of the cavity stiffness k_c, the parameter $K_L{}^{ext}$ is instead given by:

$$K_L^{ext} = \frac{\partial f}{\partial z}\frac{F^{\infty}}{k_c} \tag{3.8}$$

The validity of this assumption has been proved successfully comparing the formula with ANSYS[22] FEM calculations (see appendix B) where a "weak" boundary condition, characterized by an external stiffness k_{ext}, has been taken into account [67]. This semi-analytical model shown actually allows to evaluate any boundary condition by performing only two load cases of the structural simulations: the one needed to assess the longitudinal frequency sensitivity and cavity spring constant, and the Lorentz force calculation for the constrained cavity. The final behavior of the static Lorentz force sensitivity coefficient can be evaluated through the plot in Fig. 3.9 that shows the general trend of K_L according to formula (3.7).

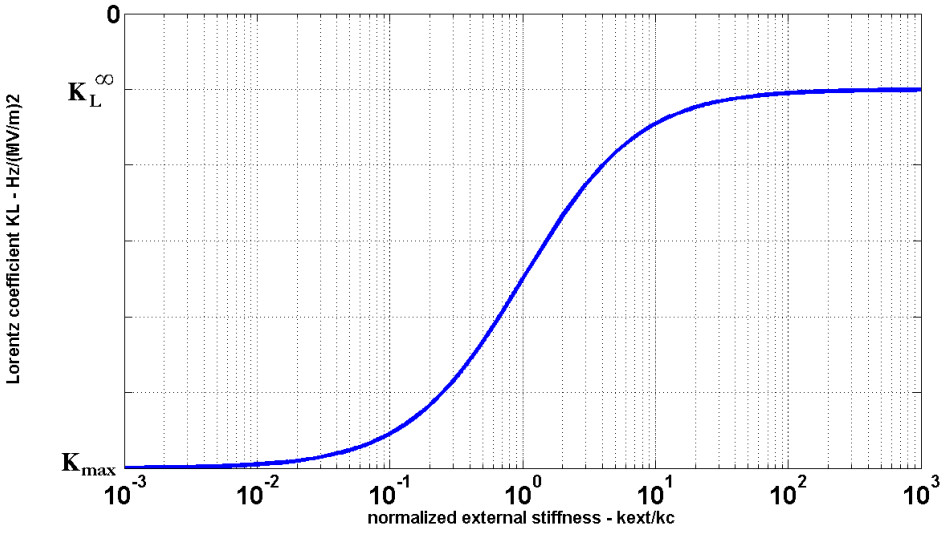

Fig. 3.9 - Lorentz force detuning coefficient as a function of the external longitudinal boundary condition.

According to this models, it is therefore possible to conclude that the use of stiffening rings between adjacent cells actually allowed to minimize only the $K_L{}^{\infty}$ value. Then assuming this cavity design as definitive, any eventual further improvement for the final

[22] Finite Element Modeling (FEM) software from Ansys inc. [138]

sensitivity to Lorentz forces must be found in K_L^{ext} only, through an increasing of the stiffness of cavity constraining mechanism.

Direct measurement of the static Lorentz force detuning coefficient, done at CHECHIA facility at DESY with a CW driven TTF cavity [26] confirmed expectations (see Fig. 3.10).

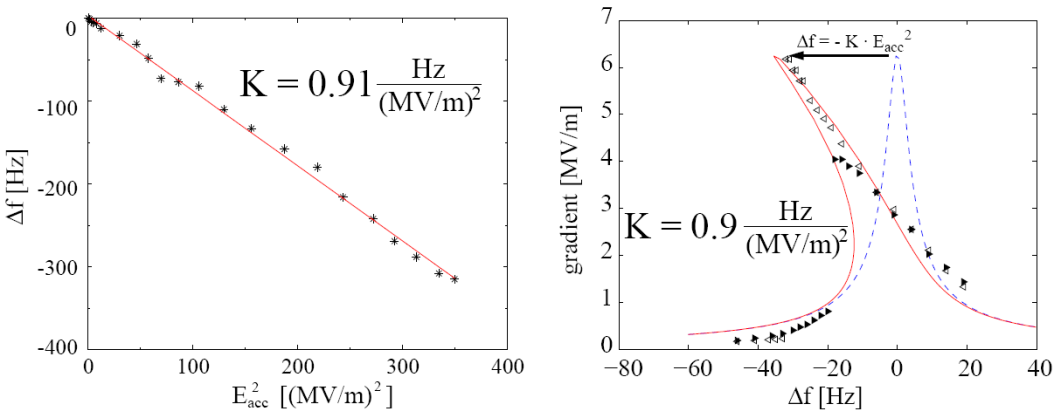

Fig. 3.10 – static LFD coefficient measure (left) and comparison between ideal and LFD affected resonance curve (right) [26]

For ILC and XFEL linacs (as it is for FLASH presently), cavities will be anyway operated in pulsed mode. This means that steady-state conditions do not apply while gradient is varying with time according the RF pulse specifications (see par. 4.2.1). Cavity is powered only for a limited time window, 1.3 ms currently at FLASH and 1.6 ms for ILC, at a repetition rate of 10 Hz and 5 Hz respectively. As a consequence time varying Lorentz forces interact with cavity own inertia and mechanical modes to determine the final time varying detuning.

To account for the different behavior of the Lorentz force during pulsed cavity operations, a different parameter is introduced: the dynamic Lorentz force detuning coefficient K_L'. It is defined as the total amount of frequency shift (also in this case named as LFD) induced by the time varying Lorentz forces only during the time window of the pulse flat-top (see par. 4.2.1). First reference measurements of dynamic LFD [62], were performed in the CHECHIA facility on a cavity equipped with a TTF tuner and operated with 0.8 ms flat-top RF pulse at 10 Hz. Results, shown in Fig. 3.11, revealed that LFD is reproduced very accurately from pulse to pulse and only small modulations are overlapped due to microphonics. K_L' has then been estimated to be around -0.414 Hz/(MV/m)^2.

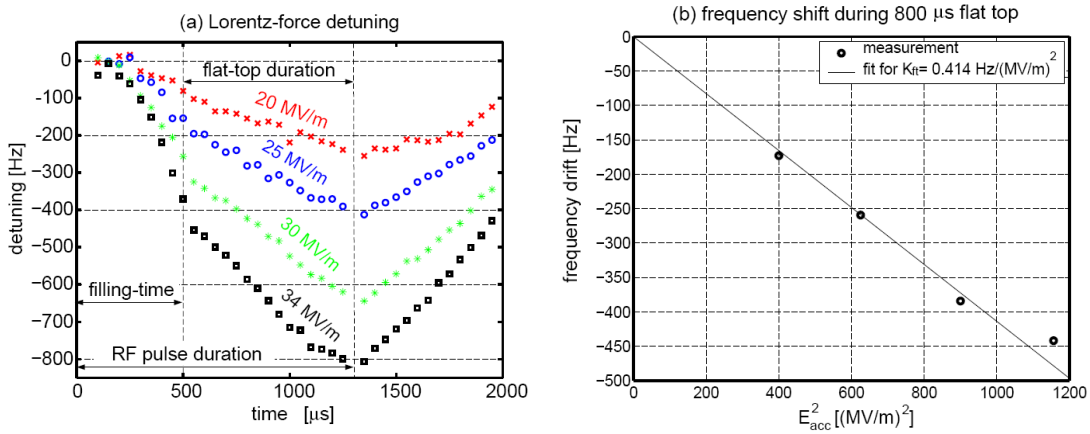

Fig. 3.11 – measurements of the dynamic LFD coefficient for CHECHIA pulsed operation (left) and estimation of the corresponding coefficient [62]

Experimental results confirmed that, even with some significant differences from cavity to cavity, several hundreds of Hz of detuning are expected even only during the flat-top phase when gradients of 25 MV/m or more are achieved. This makes the Lorentz force detuning (LFD) the major and critical source of dynamic detuning for TESLA cavities.

The dynamic behavior of the LFD during the RF pulse, visible in Fig. 3.11, has been fully understood introducing the dynamic mechanical properties of the cavity. These can be described in terms of cavity mechanical eigenmodes that are excited by the Lorentz forces during the RF pulse. Although even a 1st order differential model has been proved to partially describe the dynamic LFD [26], the optimum result and a correct estimation of the K_L' coefficient has been obtained through a 2nd order differential model. Each one of the major cavity resonances (up to 3 for the recent development of the LLRF control system, see par. 4.2) can be modeled as an harmonic oscillator for the variable Δf, this therefore leads to a set of 2nd order differential equations:

$$\frac{d^2\Delta f_k^{acc}}{dt^2} + \frac{\omega_k}{Q_k}\frac{d\Delta f_k^{acc}}{dt} + \omega_k^2\Delta f_k^{acc} = -\omega_k^2 K_k \cdot E_{acc}^2 \ , \qquad k = 1,2,\dots \tag{3.9}$$

Where Δf_k is the contribution to the final detuning Δf of the given eigenmode k, each completely described by w_k, Q_k and $K_{L\,k}$' parameters, the frequency, the quality factor and the dynamic Lorentz force coefficient respectively. Correct interpolation of experimental data (as those in Fig. 3.11) are possible even considering only the main cavity mode (see par. 5.3.1), and this led to an analytical confirmation for the K_L' to be about -0.4 – -0.5 $Hz/(MV/m)^2$ [68], close to experimental results.

It's important to underline that the same semi-analytical approach previously presented for the static LFD still holds for the dynamic detuning. Provided that K_L' is considered instead of K_L and its definition is fixed and redefined as the detuning over the flat-top time window, the same model can be applied. Therefore also in this case two contributions can

be assumed and described via the infinitely rigid length constrained coefficient K_L^{∞}' and via the purely longitudinal variation one, K_L^{ext}', according to:

$$K_L' = K_L^{\infty\prime} + K_L^{ext\prime}\left(\frac{1}{1+{}^{k_{ext}}/_{k_c}}\right) \tag{3.10}$$

Finally, for a fixed resonator design and so for a constant K_L^{∞}', also in this case a reduction of the sensitivity of the cavity to dynamic LFD must be searched increasing the stiffness of cavity constraining mechanism and consequently lower K_L^{ext}'. Assuming with confidence the plot in Fig. 3.9 as valid for K_L' , its trend shows that, when the external support structure stiffness approaches the cavity longitudinal stiffness k_c , K_L' and therefore the induced frequency displacement is reduced and then reaches a constant minimum value when cavity stiffness becomes negligible with respect to the external stiffening. The minimum K_L' ("constrained" cavity behavior, $K_L' = K_L^{\infty}$') is almost achieved once the longitudinal stiffness of the supporting structure of the cavity, mainly composed by cavity end dishes, helium tank and the tuning mechanism, is about 10 times greater than the cavity one, therefore around 30 kN/mm.

Furthermore, the author had the opportunity to directly cooperate with colleagues from DESY and Technical University of Lodz (TUL) [142], Poland, in performing several additional measurements of the dynamic Lorentz force detuning on TESLA cavities on two cryomodules assembled for the FLASH linac at DESY, the ACC6 and ACC7. Detuning measurement techniques used and experimental results are presented in the next paragraph of this thesis work.

3.4 DYNAMIC DETUNING MEASUREMENTS

3.4.1 MEASUREMENTS TECNIQUES IN PULSED OPERATIONS

When cavity operations are far from a stationary CW RF condition, as it is verified when it is driven by a 1.6 ms length, 5 Hz rate ILC RF pulse, the phase locked loop detuning measurement technique cannot be applied. Two alternative solutions have been developed over past years to address this task according to signal and instruments actually available in the cavity environment during operations.

The former [26] was proposed and used for the first measurements on dynamic detuning, among these, the ones reported in Fig. 3.11. It relies on the behavior of the cavity itself at the end an RF pulse. According to ILC specifications after 1.6 ms the RF forward power is abruptly switched off at the end of the flat-top region, when this incident power is removed the RF fields stored in the cavity decays exponentially with the frequency of the detuned cavity. The frequency shift is revealed as the phase difference

between the cavity field and the reference master oscillator. The initial slope of the phase, starting from the switch-off time, is therefore proportional to the detuning according to:

$$\frac{\partial \varphi}{\partial t} = \Delta\omega = 2\pi \cdot \Delta f \tag{3.11}$$

In order to measure the detuning during the whole pulse, several pulses with different time length are needed, typically around 100 pulses from the shortest to the nominal one. Each time the detuning is measured as the phase slope at the end of the pulse. This method is actually invasive and cannot be used during the normal cavity operations.

A different method was later developed in order to obtain a single pulse and non perturbing method for detuning measurement [69][28], it is based on the cavity model presented in par. 2.1.2 (lumped circuit model). Rewriting equation (2.36) for the detuning $\Delta\omega$ as $\omega - \omega_0$, it is possible to determine the relation between the detuning itself and the amplitude and phase of signal from RF power probes. The resulting formula is:

$$\Delta\omega = -\frac{1}{2\pi}\left(\frac{d\phi_{probe}}{dt} - 2\omega_{1/2}\frac{|U_{for}|}{|U_{probe}|}\sin\left(\phi_{for} - \phi_{probe}\right)\right) \tag{3.12}$$

where U_{for}, U_{probe}, ϕ_{for} and ϕ_{probe} are the magnitude and phase of forward and probe (inside the cavity) power signal respectively. In order to perform tests on FLASH and CMTB cavities, this formula has been implemented as a Matlab script for an off-line computation relying on digital data from power and directional couplers available within DOOCS system trough the DAQ modules (2 ms buffer, 1 MHz sampling). The developed algorithm also performed the calibration of each power probe readouts in order to take care of cross-talk effects and finite directional coupler directivity (for further details refer to [69]). A major advantage of this algorithm is that it is implementable in VHDL code for FPGA chips [70]. Extremely low latency in case of FPGA implementation allows to realize a truly real-time cavity detuning monitor. This latter issue is currently and successfully under development, refer to par. 4.5.2 for the status of this activity and the contributions of the author in this topic. Finally, the main disadvantage for this method is related to the dependence from the derivative of the phase. This causes the algorithm to be very sensitive to rapid changes of signal and this typically appear as two glitches in the beginning and in the end of the flat top (see Fig. 3.12 for reference). Even the simple option of a smoothing filter must be carefully taken into account due to the eventual additional computation delay .

For the specific case of the CMTB (ACC6, ACC7) and CHECHIA (Blade Tuner) tests, presented by the author and reported in chap. 5 and 6, the existing MATLAB routine has been modified by the author in order to access the proper CMTB data stream from DOOCS and to use the correct parameters of the module ACC6 RF pulse. Moreover, to accomplish different test requirements, different ancillary scripts, based on the original routine, were made. To save computational time for example, the calibration routine, the most time-demanding one, was then performed just once for each cavity and eventually refreshed from time to time. The corresponding calibration coefficients were saved and

just quickly recalled when needed. In this way quick scripts were made available that continuously plot both detuning and power probes data, thus realizing a pseudo real-time detuning scope. It was therefore possible to have a direct and almost immediate feedback of the effect of any action made on the cavity, both with slow and fast actuators.

3.4.2 LORENTZ FORCE DETUNING MEASUREMENTS IN FLASH ACC6 AND ACC7

The modified MATLAB routine previously described has been used by the author to acquire the dynamic detuning for each cavity of FLASH module #6 (ACC6) after its installation in the CMTB facility (see par. 1.4). Later on, additional measurements have been performed with the same scripts also on the module #7 (ACC7) in the same facility on April 2007. Collected data and analysis are reported in this paragraph.

ACC6 has been assembled to be the most advanced cryomodule in operation. It is a FLASH Type-III cryomodule, equipped with 8 out of the most performing cavities (4 from ACCEL, 4 from ZANON firms, see par. 2.1.2) each equipped with a TTF tuner with 2 of the latest generation piezo actuator (see par. 4.4) aiming to achieve a final average accelerating gradient of 30 MV/m. ACC6 has been the first cryomodule to be installed in the recently build CMTB facility and the reference goal has been chosen to be the analysis of the effect, on every module component, of several successive thermal cycles (cooldown or CD and warm-up or WU). 11 complete thermal cycles have been finally performed. In particular, after the 7^{th} cooldown, once stable 10 Hz repetition rate conditions were achieved, the detuning over the flat-top for each cavity for different values of the accelerating field has been measured, up to the quench limit of each cavity (Tab. 3.).

ACC6 Cavity #	**Quench limit – MV/m**
1	36
2	24
3	36
4	35
5	21
6	21
7	30
8	24

Tab. 3.1 –quench limits for ACC6 cavities

During measurements, in order to preserve lower performances cavities from quenching, they have been significantly detuned when high forward power values were used to feed the other cavities. Moreover a safety margin of about 1 MV/m apart from the limit has been considered during tests. Finally, the average gradient for ACC6 of 27

MV/m actually do not fully met expectations mainly due to a critical limit drop in cavity #5 and #6 in comparison to their own horizontal test in CHECHIA [71].

All the detuning curve collected for each cavity at its maximum safe gradient (i.e. reasonably far from quench) are presented in Fig. 3.12. Corresponding data have been computed using the modified MATLAB algorithm described in the previous paragraph. The overall result is, for each cavity, perfectly coherent with the Lorentz force detuning expectations, as presented in par. 3.3.2. A proper static pre-detuning has been set for each cavity in order to minimize power requirements (see par. 4.3): the stepper motor has been used to set the detuning in the flat-top region as close as possible (and symmetrical) to zero.

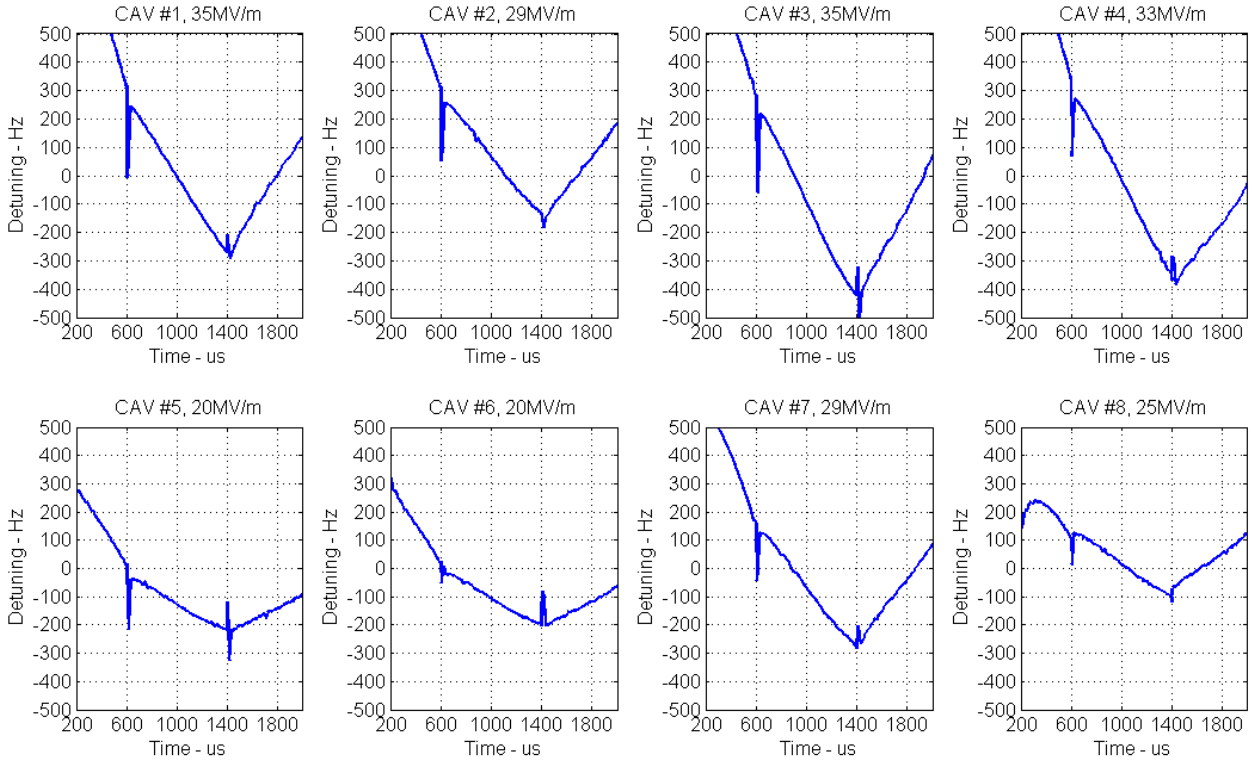

Fig. 3.12 – collection of detuning plots from cavities of ACC6 at their maximum safe gradient

For the analysis, only the Lorentz force detuning shown by each cavity over the duration of the flat-top time has been considered. The flat-top region is starting 600 μs after the beginning of the RF pulse (100 μs delay was set before fill-time) and lasts 800 μs. The procedure here proposed for the extrapolation of the detuning value is based on the acquisition of a number (typically 10) of successive detuning curve with identical settings. Then, collected data for the flat-top are averaged and interpolated over time with a 3rd order polynomial fit. Finally the fitting polynomial is evaluated in the flat-top time window and the absolute difference between its maximum and minimum value is assumed as the final LFD value. If compared to a linear interpolation of the flat-top data, this

method allows to take into account the small deviations from linearity shown by collected LFD curves and avoid a significant overestimation for low gradient data (moreover piezo compensated measurements typically show deviation from linearity). Final results are summarized in Fig. 3.13 where data from LFD in each cavity is plotted as a function of the squared value of the accelerating gradient so to highlight the dynamic Lorentz coefficient K_L'. The quadratic dependence expected from theory for K_L', corresponding to a linear trend in the case of this plot, is confirmed.

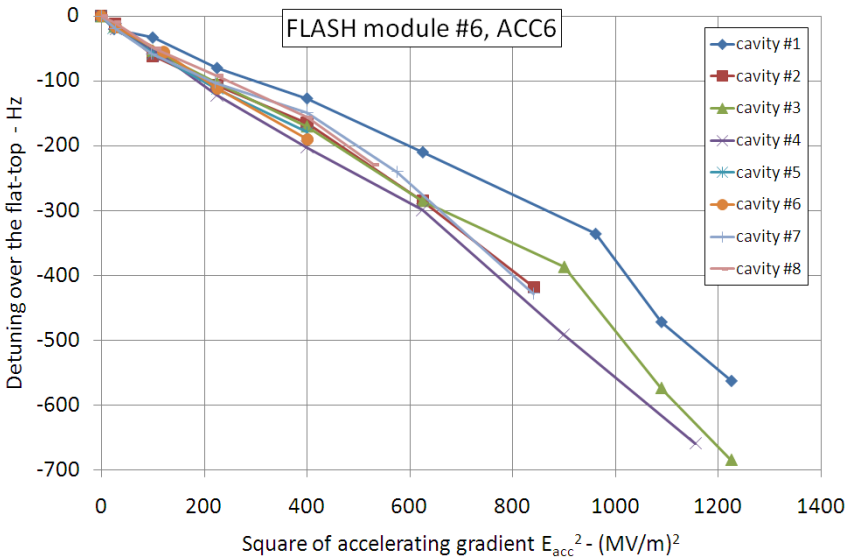

Fig. 3.13 – LFD showed during the flat-top for ACC6 cavities, plotted vs. the square of accelerating field

Curves in Fig. 3.13 have been linearly interpolated and K_L' coefficients are collected in Tab. 3.2 together with average K_L' value for the whole ACC6 module.

ACC6 Cavity #	K_L' [Hz/(MV/m)²]	Interp. r^2
1	-0.410	0.967
2	-0.475	0.991
3	-0.508	0.977
4	-0.546	0.993
5	-0.465	0.988
6	-0.479	0.999
7	-0.466	0.973
8	-0.418	0.994
Avg.	**-0.471 ± 0.044**	**0.985**

Tab. 3.2 –flat-top dynamic Lorentz coefficients for ACC6 cavities

Data substantially agree with expected trend, even if clear differences are visible from cavity to cavity. A contribution to the differences visible in the K_L' values is certainly

determined by the intrinsic variations in the cavity stiffness from cavity to cavity, since K_L' is very sensitive to the external stiffness value(par. 3.3.2). Small differences in the total effect given by the various chemical, thermal and mechanical treatments to which cavity surface is subjected can eventually bring to a different final stiffness.

Later on, ACC6 has been moved to FLASH linac and the recently completed ACC7 instead installed in the CMTB for qualification tests. ACC7 is a FLASH Type-II cryomodule that has been re-assembled from the former M3* module (ACC3). The cold string has been equipped with 8 recent cavities (3 from ZANON, 4 from CERCA, 1 from ACCEL) so to achieve notable performances in line with the previous ACC6. TTF tuners are installed for each cavity similarly to ACC6 but including only 1 piezo actuator (see par. 4.4). A LFD measurement and analysis have been conducted on ACC7 using the same detuning computation routine and the same subsequent data managing as for ACC6. LFD as a function of the square of the accelerating gradient is shown for each cavity in Fig. 3.14. Then, resulting linear interpolating coefficients, K_L', are summarized in Tab. 3.3.

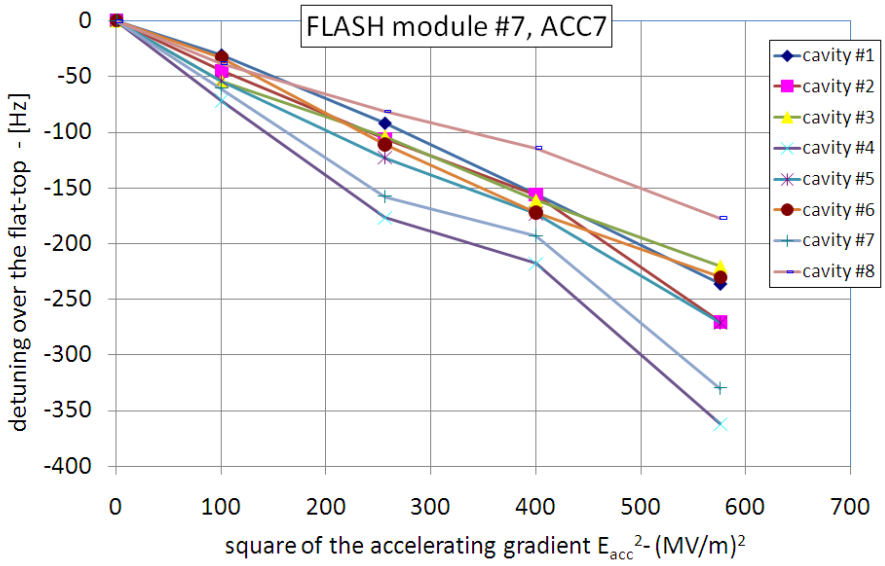

Fig. 3.14 - LFD showed during the flat-top for ACC7 cavities, plotted vs. the square of accelerating field

ACC7 Cavity #	K_L' [Hz/(MV/m)^2]	Interp. r^2
1	-0.396	0.993
2	-0.439	0.983
3	-0.393	0.99
4	-0.613	0.982
5	-0.462	0.994
6	-0.41	0.994
7	-0.553	0.981
8	-0.303	0.993
Avg.	**-0.446 ± 0.098**	**0.989**

Tab. 3.3 - flat-top dynamic Lorentz coefficients for ACC7 cavities

ACC7 performed an average accelerating field in the CTMB tests of 29 MV/m and it has been later on installed along FLASH linac working with a conservative gradient set-point of 25 MV/m.

These measurements allowed to observe that for the two latest TESLA technology based cryomodules, ACC6 and ACC7, the average strength of the Lorentz force detuning, expressed by the K_L' coefficient as -0.471 and -0.446 Hz/(MV/m)^2 respectively, is close to but anyway slightly higher than the reference value for the ILC of -0.414 Hz/(MV/m)^2 [1]. An estimation of the consequences of the difference among these values is found in par. 4.3, where expectations and issues concerning the RF power requirements are presented.

As already underlined in par. 3.3.2, achieving an higher cavity external stiffness is mandatory to improve the current LFD performances and lower the average K_L' coefficient. Besides, this will also lead to several benefits even for what concerns fast actuating efficiency and cavity mechanical stability. More details concerning possible current solutions to approach this goal are presented in chap. 6, devoted to the coaxial Blade Tuner.

4 CONTROL OF CAVITY DETUNING

The experimental approach to the detuning active compensation must be regarded as the first step toward the development of a complete detuning control system that would take control of installed fast and slow actuators and ensure the best compensation of both repetitive and stochastic dynamic detuning. The design of this control system should grant the feasibility of integration with existing control systems, as low level RF control, both from the hardware and software point of view.

In this chapter the main topics related to the detuning controller will be developed. Firstly an overview is given in the first paragraph, about the fundamental concepts of control theory that are widely used or mentioned. Then the primary control of the EM fields inside cavities, the Low Level RF control (LLRF), will be introduced. Lastly, the activity related to the choice and characterization of the fast actuator and the used electronic equipment will be reported, together with first results from experimental validation tests of realized parts of the controller code.

4.1 BASICS OF SYSTEMS AND CONTROL THEORY

In order to achieve an analytical modeling of the active control of the detuning in a superconducting cavity, different fundamental concepts of the automatic control and systems theories have been used[23].

Firstly, it will be widely assumed in the following that each element of interest, both electrical (as filter, amplifier etc.) and mechanical (as cavity, piezo etc.), could be always described in terms of a linear system. This means that the principle of effects superposition always applies. The resulting linear system is also assumed to be oriented and completely described by a finite number of inputs and outputs and by the functional relation among them. The final system is therefore realized as an interconnection of simpler blocks and its features are ultimately related to its topology (series, parallel, loop etc.) and its sub-systems (algebraic nodes, junctions etc.). In order to describe the behavior of each block a transfer functions is defined in the frequency domain and, since linearity is assumed for the whole system, the transfer function is expressed in terms of the Laplace transform [72]. As a result, each block or sub-system is completely described by an analytical function of the complex variable $s = a + j\omega$. A schematic representation of a generic linear system is therefore given in Fig. 4.1.

[23] Only basic concepts are here presented, for a detailed introduction of systems and control theories refer to [27]

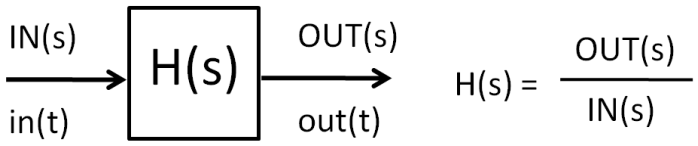

Fig. 4.1 – transfer functions corresponding to a linear and oriented system representation

where IN(s) and OUT(s) represent the Laplace transformed signals in(t) and out(t) respectively. The transfer function H(s) is represented throughout the thesis by separate plots corresponding to its amplitude and frequency as a function of frequency[24]. A direct evaluation of the transfer function is achieved via three elements: the DC gain of the system given by H(s→0), roots of H(s) numerator named *zeros* and roots of H(s) denominator named *poles*. Poles and zeros lead to fundamental and symmetrical contributes in the shape of transfer function amplitude and phase. Consider for instance the presence of a complex conjugate poles pair in H(s) as

$$H(s) = \frac{\omega^2}{s^2 + a\omega s + \omega^2} \tag{4.1}$$

The H(s) form shown in (4.1) is widely used as the transfer function of a system characterized by a single resonating frequency. The corresponding amplitude and phase are shown in Fig. 4.2.

[24] Amplitude and phase values corresponding to each given frequency represent the amplitude gain and the phase difference induced by the system on a sinusoidal input signal of that frequency.

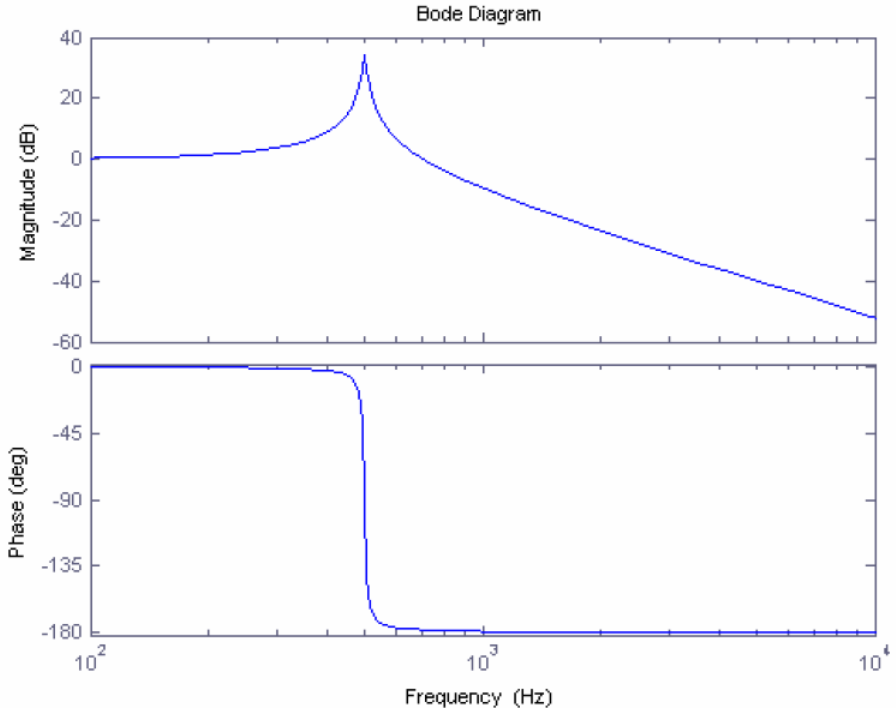

Fig. 4.2 – amplitude and phase of a transfer function with a complex conjugate poles pair (w=2·π·500 , a = 0.01)

According to the reference scheme in Fig. 4.3, in a feedback loop, the output of system (i.e. the *plant*) to be controlled, the *controlled variable* y(t), is forced to follow a given input set-point, by the *control variable* u(t) and the corresponding *error variable* e(t) defined as the instantaneous difference between the former one and the set-point (*negative* feedback).

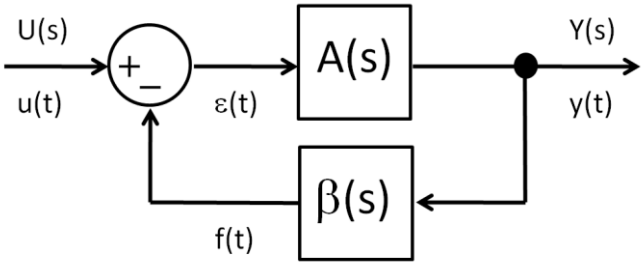

Fig. 4.3 – reference scheme for a feedback control of system A(s)

According to the Laplace transform formalism (U(s) and Y(s) are as before the Laplace transformed u and y) the transfer function of the whole feedback stage can be expressed as a function of the complex variable s as [72][73]:

$$H_{C.L.}(s) = \frac{Y(s)}{U(s)} = \frac{A(s)}{1 + \beta(s) \cdot A(s)} \tag{4.2}$$

where the factor

$$G_L(s) = \beta(s) \cdot A(s) \tag{4.3}$$

is defined as the loop gain. As mentioned throughout this chapter (see for instance par. 4.5.1), an analysis of the amplitude and phase frequency dependence of loop gain G_L reveals several features of the closed loop system. In particular, every kind of eventual disturbances that are superposed to the desired set-point are compensated by the closed loop system, provided that their spectral contents significantly overlap with the frequency interval wherein applies that $G_L >> 1$. In this way also stochastic disturbances, as microphonics detuning (see par. 3.3.1) can be counteracted.

The stability limits of the final system can be also determined (among several different methods, refer to [27][73]) through the loop gain function. In particular, according to the Bode criteria that are further on considered, the stability is achieved by providing positive amplitude and phase margins in $G_L(s)$ in comparison to the loop sign inversion points at gain 0 and phase -180 deg respectively [27]. In addition, it is important to note that an eventual pure delay time τ in the system (as for instance the computational time required by a digital stage) would appear in the loop gain function G_L as an exponential factor, according to the Laplace transforms rule:

$$\mathcal{L}\{f(t-\tau)\} = e^{-\tau s}F(s) \tag{4.4}$$

The additional phase shift induced by the eventual delay tends to decrease the phase margin therefore limiting the system stability. This for instance leads to the need to search for the minimum delay in each digital stage included in the loop, eventually improving its computational capabilities. The enhancement in the stability margin can be then used to achieve larger loop gain values and consequently even better control performances.

Since no compensating action is excited in a closed loop controlled system without a deviation of the controlled variable from the set-point, an ideal and perfect control cannot be achieved. This is not true for a different class of automatic system controls that is sequential or open loop. In particular, the feedforward compensation is a widely used application of open loop controls. It exploits an auxiliary input to the system, properly related to the nominal one, to reach the desired controlled variable behavior.

In order to model and evaluate feedback and feedforward compensation features for the most general linear system with multiple input u and outputs y it is possible to make use of the State Space formalism [74]. The set of n 1st order differential equations that can always describe the system is expressed in terms of matrix multiplication as

$$\begin{aligned} \dot{\bar{x}} &= A\bar{x} + B\bar{u} \\ \bar{y} &= C\bar{x} + D\bar{u} \end{aligned} \tag{4.5}$$

where inputs are collected in the m-units vector $\bar{u}$, outputs in the p-units vector $\bar{y}$ and the n-unit vector $\bar{x}$ represents the systems state variables. Moreover A (n x n) is the *system*

matrix, B (n x m) is the *input* matrix, C (p x n) is the *output* matrix and finally D (p x m) is the *feedthrough* matrix. Then, the relations between controlled variables can be defined accordingly, in particular for the feedforward control case:

$$\bar{u}_{FF} = (1 + G)\bar{u} \tag{4.6}$$

where the inputs $\bar{u}_{FF}$ of the controlled system are related to the uncontrolled ones via a proper *feedforward matrix* G (m x m). Then for the closed loop case, a simplified scheme, known as *state-feedback*, is considered as a reference. The final input of the controlled system depends directly on state variables[25] $\bar{x}$ according to a proper *feedback matrix* F (m x n):

$$\bar{u}_{FB} = \bar{u} + F\bar{x} \tag{4.7}$$

Using (4.6) and (4.7), the final transfer function H(s) for the controlled system in both cases (feedforward and feedback respectively) is computed via a simple recombination of (4.5) after that Laplace transform is applied, and it is given by:

$$H_{FF}(s) = C[sI - A]^{-1}[B + G] + D \tag{4.8}$$

$$H_{FB}(s) = C[sI - A + BF]^{-1}B + D \tag{4.9}$$

Equations (4.8) and (4.9) show that, differently from the closed loop case (H_{FB}), the feedforward control does not modify the plant own poles (here represented as eigenvalues of A matrix) and instead alters the system zeros. The feedforward control, that can theoretically allow the perfect system control, can be applied only to a repetitive and generally well known disturbance. As will be further on presented, this compensation method has been indeed successfully applied to the Lorentz force detuning (LFD).

4.2 OVERVIEW OF LOW LEVEL RF CONTROL SYSTEM FOR TESLA CAVITIES

4.2.1 LLRF FEEDBACK AND FEEDFORWARD CONTROLS

The Low-Level RF (LLRF) system controls phase and amplitude of the accelerating EM field in the superconducting cavities, and it is essential for stable and reliable beam operation. The LLRF includes feedback and feedforward, exception handling and

[25] Therefore state variables and not outputs are fed back through the feedback loop. This is not a critical simplification since outputs are just linear combination of the former ones.

extensive built-in diagnostics with suitable speed and accuracy. Each RF unit in the linac, as described in par. 1.3, has a LLRF controller.

A primary challenge for the ILC activity on LLRF is to achieve a large number of cavities driven by a single klystron. Most of the needed requirements have been already demonstrated over these last years in the LLRF systems, mainly thanks to operation at the FLASH facility at DESY [75] (see par. 1.4) where state-of-the-art technologies for digital control of the operational parameters are used.

The performance requirements for the LLRF are set by the accelerating gradient desired for the cavities and by the stability required for beam parameters such as energy and energy spread, both bunch to bunch and pulse to pulse. Design of LLRF solutions in the ILC activity frame is driven by two main sources of field perturbation inside the cavity:

- *Modulation of the accelerating mode resonance frequency*, leading to cavity dynamic detuning. In this frame, both Lorentz force detuning and microphonics contributions are found. Both these effects have been introduced and discussed in chapter 3. The basic idea is that mechanical deformation of the cavity from its nominal shape induce a shift in the resonant frequency.
- *Beam loading and fluctuation in the beam current*. Several effects are related to the interaction of the accelerated beam charge with the cavity field distribution. Accelerating resonant mode as well as high order modes (HOM) are excited by beam charge, both at the pulsed beam and bunch to bunch time scale. Moreover, bunch to bunch charge oscillation, related to slow fluctuations within the bandwidth of the RF system, will contribute significantly to the final energy spread.

Those several contributions must be finally compared to the tight stability specifications required by ILC to reach the goal value of less than *0.1%* final energy stability in the linac. Current target specifications [1] for the field stability require an accuracy of $7 \cdot 10^4$ for the field amplitude and 0.35° for the phase.

Moreover, as already mentioned, it is mandatory toward a saving in used resources to control simultaneously several cavities with a single controller. This result is achieved implementing a "vector sum" routine that adds, both in amplitude and phase, values probed in each cavity, up to 26 resonators according to ILC specifications [1]. Then the LLRF control unit is designed to control the vector sum of all cavities as it is done when controlling each individual cavity. An effort is needed to correctly calibrate the vector sum result against sources of stochastic fluctuations as microphonics, that can lead to a significant difference between the measured value, eventually perfectly stabilized by the control, and the actual value felt by the beam. About ±10 % in amplitude and ±1 deg in phase accuracy (more critical) is required for the vector sum calibration [26]. Therefore, beside calibration error of the vector sum, also phase noise from master oscillator as well as non-linearity of field detector are among the numerous possible sources of perturbation for the RF field inside the cavity. Besides these figures, exception handling for the LLRF

control system is required to avoid unnecessary beam loss and to allow for maximum operable gradient. Availability and maintainability are also critical considerations.

The most basic function of any LLRF control is therefore a fast feedback loop that measures the cavity array field vector sum and attempts to hold it to a desired set-point. Fast amplitude and phase control of the cavity array field is achieved modulating the signal driving the klystron through a vector modulator. The cavity RF signal is down-converted to an intermediate frequency IF (typically 250 KHz), while preserving the amplitude and phase information. A digital stage performs the needed feedback algorithm and ADC and DAC converters link the analog and digital parts of the system. A general overview of a typical LLRF control unit is shown in Fig. 4.4.

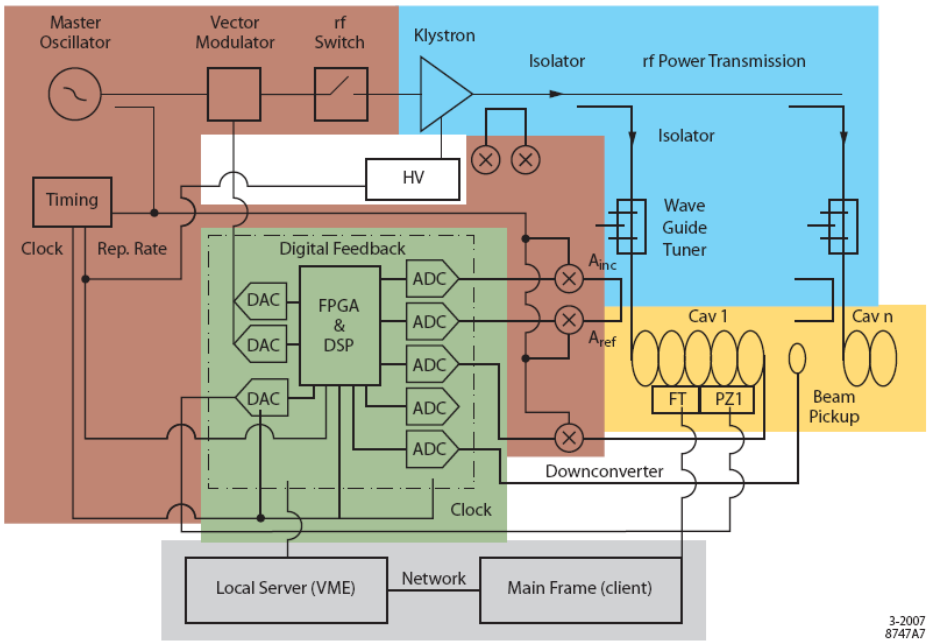

Fig. 4.4 – basic functional diagram of the LLRF control system using digital feedback control [1]

The digital signal processing stage (DSP) executes field vector calibration, sum and elaboration and it is implemented using a dedicated FPGA based electronics (the current reference board, named as SIMCON, is described in par. 4.4.2). Digital detection of field vector components, real (in-phase, I) and imaginary (quadrature, Q), is achieved by a calibrated oversampling of each cavity probe down-converted signal. As a reference, the 250 kHz signal is oversampled at 1 MHz yielding 4 samples per period, corresponding to a phase shift of 90 deg between each pair, and representing I, Q, -I and –Q components respectively. Each pair of consecutive samples therefore undergoes proper rotation in 90 deg steps and scaling, a complex scaling factor is used for each channel, to compensate for phase (cable lengths over all) and gradient differences in each cavity. Both operations are implemented on I&Q components using matrix multiplications. The scaling factor therefore is in the form:

$$M_j(t_k) = \begin{pmatrix} a_j & -b_j \\ b_j & a_j \end{pmatrix} \tag{4.10}$$

where:

$$a_j = g_j \cdot \cos\left(\Phi_{off}\right)_j ; b_j = g_j \cdot \sin\left(\Phi_{off}\right)_j \tag{4.11}$$

for an amplitude correction g_j and a phase correction Φ_{off}. Contributions from every controlled cavity are then summed up to form the vector sum I and Q components that are compared to a set-point table to generate the loop error complex signal. The feedback algorithm used then simply applies a proportional gain, in the form of a proper gain table, to the error signal, a low pass filter is also implemented for loop regulation against sensor noise. The overall schematic architecture of the loop controller digital stage is presented in Fig. 4.5.

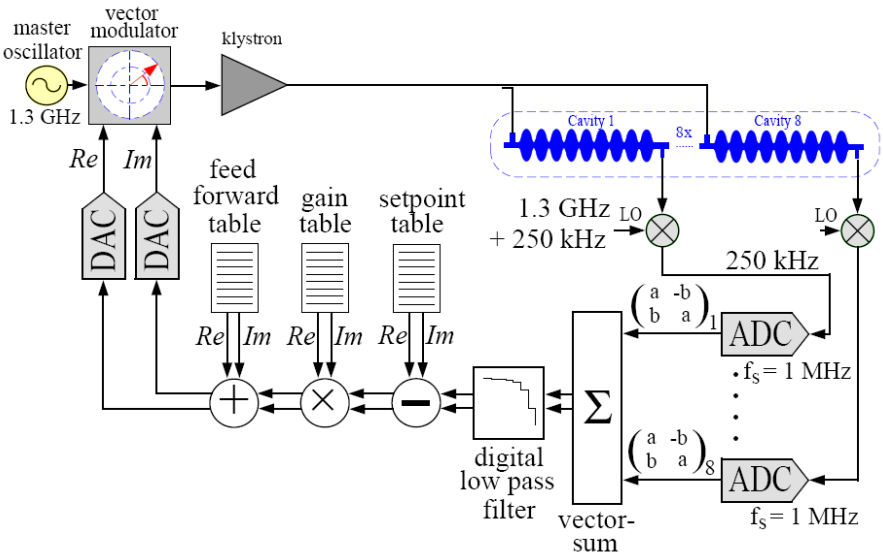

Fig. 4.5 - schematic representation of the LLRF loop controller [26]

Additionally, the closed loop is completed with a calibrated feedforward control that provide optimum compensation of repetitive perturbations induced by the beam loading and by dynamic Lorentz force detuning. At the current state of art of LLRF control, adaptive feedforward feature is moreover applied to improve the compensation performances. An external control block, residing on local server (see next par. 4.2.2), acquires calibrated data during each pulse and executes parameters identification processing between pulses. Estimated cavity parameters are considered as actual values for the needed cavity parameters and they are applied to create the control tables for the following pulse. The new control tables modify the setup and again new parameters are estimated. This iterative processing quickly converges to the desired state of the cavity,

assuming repeatable conditions for successive pulses. Moreover a beam-based feedforward can eventually further improve the controller performances.

The set-points for cavity fields as well as gain and feedforward values, are implemented in the controller memory as tables in order to accommodate the time-varying gradient and phase during the cavity filling. Tables dimensions are related to the RF pulse structure and are currently composed of 2048 samples for 1 MHz sampling frequency. During the RF filling phase the cavity has to perform an "on resonance" filling. Therefore the corresponding section of the set-point table contains a modulated phase that tracks the varying resonance frequency of the cavity and an exponentially raising amplitude, exactly as expected by the natural cavity filling behavior in the resonance condition. Initial phase and asymptotic amplitude are determined to fulfill condition for a final filling field value which should equal the required flattop one. Instead constant values, and equals to the desired gradient and phase, are present in the flat-top section of the set-point as expected.

Finally, as a reference, a simulation of the typical action of the LLRF control during RF pulse is presented in the Fig. 4.6, where also open loop response for the same parameters is visible.

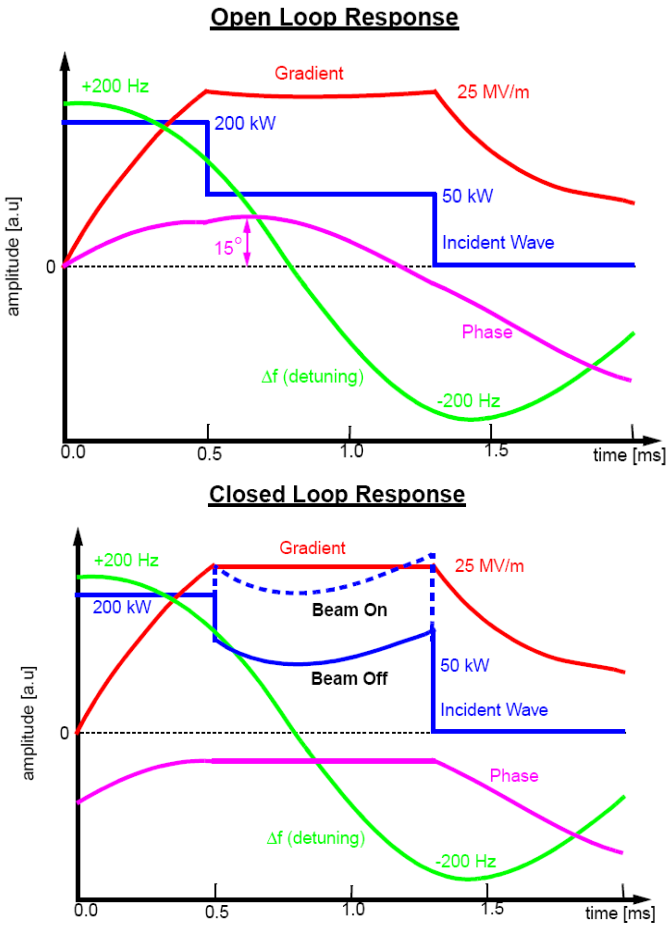

Fig. 4.6 – cavity field, incident power and detuning with (up)and without (down) LLRF control loop [76]

The total delay time of the control loop shown in Fig. 4.5 determine the maximum achievable loop gain and therefore the resulting capability to compensate for field instabilities. Recent results showed the possibility to even lower the loop delay down to less than 1 μs and, during a LLRF test with beam at FLASH, a loop gain value slightly higher than 300 has been reached for the first time, a milestone in the field control, corresponding to completely erasing all beam loading effects on the flattop phase of the RF pulse [77].

Finally, from a more general point of view, each LLRF subunit must also interface itself to several other level of control and diagnostic as RF power distribution, beam transfer control, machine protection, sector and global energy and phase regulation. It must allow for fast trip recovery and built-in diagnostic, support high degree of automation and sophisticated exception handling.

4.2.2 SIMCON FIRMWARE AND HARDWARE

Several generation of digital equipment and code have been developed, to accomplish LLRF control of TESLA cavities, among an international cooperation of Warsaw University of Technology (PERG/ELHEP group), Lodz University of Technology. Poland, and DESY. The present achievement is a complete platform, named SIMCON that stands for "SIMulator-CONtroller", that includes both software and hardware components. The SIMCON platform in its present development (revision 3.1) will be shortly reviewed here. Both aspects are anyway still subject to further revisions and improvements [78].

Since few years, LLRF control solutions developed for TESLA cavities refer to Field Programmable Gate Array (or FPGA) technology [79][80] for both digital signal processing and controller logic implementation and to VME bus [83]. The FPGA technology basically consists of many logic-modules, which are placed in an array-structure. The channels between the logic-modules are used for routing. The array of logic-modules is surrounded by programmable I/O modules and connected via programmable interconnections. This freedom of routing allows every logic-module to reach every other logic-module or I/O-module. As a results huge number (up to more then 1000) of user pins are available, routing and connections for data path are totally programmable and very high complexity and massively parallel architecture are possible, therefore providing the low latency needed for the feedback algorithm.

The large set of features that compose the LLRF control, schematically represented in Fig. 4.5 and described in the previous paragraph, have been coded in the form of a parameterized structure of functional blocks in a VHDL[26] language based firmware [81]. A cavity simulator algorithm has been also developed and coded in VHDL for the SIMCON

[26] VHDL stands for Very-high-speed-integrated-circuit (VHSIC) Hardware Description Language, it is commonly used as a design-entry language for field-programmable gate arrays and application-specific integrated circuits in electronic design automation of digital circuits.

firmware. It includes both electrical and mechanical cavity models that implement a State Space representation of the relations between instantaneous cavity detuning and I and Q components of cavity field gradient. Simulator and controller components are meant to interact continuously during operations according to the adaptive feedforward scheme described in the previous paragraph. Experimental test of adaptive feedforward implementation has been recently and successfully carried out by FLASH LLRF group [82]. Clock generation and distribution as well as timing management functional blocks are also included in the SIMCON code. VME-bus [83] hardware transmission protocol is used for communications between the controller and the external local server. Data flow then is based on an universal and parameterized communication interface for FPGA chips applications named Internal Interface or II [84][85] that has been in-house developed within the collaboration.

Revision 3.1 of the SIMCON hardware layer [86], realized by ELHEP Warsaw group for the VUV-FEL and FLASH LLRF, is presented in Fig. 4.7. It consists of a single low latency PCB board designed for a 6U VME-bus standard EURO crate. The core component is a Virtex2Pro 30 FPGA device by XILINX [79] that has 30816 Logic Cells (CLBs), 136 multipliers with resolution of 18 x 18 bits, 2448 Kbits inbuilt memory (BRAM) and 8 RocketIO transceivers with speed of 3.125 Gbps and 644 available user pins. Moreover the Virtex2Pro chip has 2 embedded PowerPC 405 RISC CPU cores and inbuilt PLLs which allows implementing multipliers, dividers and regulators of the clocks phase signals (Digital Clock Managers, DCM). A second FPGA chip, an ACEX EPIK 100 from ALTERA [80], is installed on the board. It has lower performances then main FPGA and it is specifically in use as VME bus interface and hard-routed to XILINX FPGA and to VME connector.

The SIMCON 3.1 board is also equipped with two 64 Mbits DRAM's blocks, 10 analog input channels with AD6645 ADC up to 105 MSPS at 14 bit and 4 analog output channels with AD9772A DAC up to 160 MSPS 14 bit. SIMCON 3.1 consists of series of ADC's (10 total) and DAC's (4 total) with 14 bits resolution. Digital LVPECL inputs[27], optical links, Ethernet port and JTAG interface are also provided. A picture of the upper side of a SIMCON 3.1 board in its final layout is presented in Fig. 4.7

[27] LVPECL, Low Voltage Positive Emitter-Coupled Logic, is a power optimized version of the Positive emitter-coupled logic (PECL) technology, requiring a positive 3.3V instead of 5V supply. LVPECL is a differential signaling system and mainly used in high speed and clock distribution circuits.

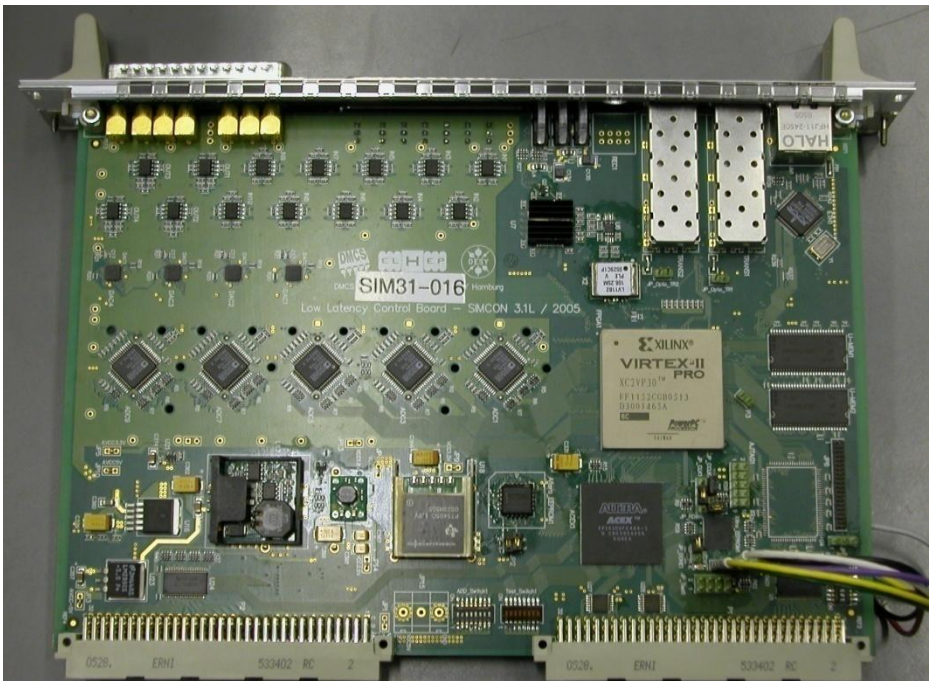

Fig. 4.7 – SIMCON 3.1 FPGA board

The local server for the real-time management of the controller and simulator applications running on SIMCON hardware, resides on an single VME board embedded PC that acts as the VME-bus controller for the rack (the local server does not have critical timing requirements). According to the typical design of a FLASH LLRF control unit, a bus controller hosting SPARC CPU and SUN Solaris OS is used [87]. MATLAB software running on the local server can directly access, through a dedicated library, registers, bits and memory areas in the FPGA using the Internal Interface. The whole LLRF unit can be then integrated in the high level linac control system environment as a server in the network. For the case of the TESLA based demonstrative machines site at DESY, from TTF to FLASH, the Distributed Object Oriented Control System (DOOCS) [88] is in use. A general schematic view of the LLRF control system and its environment is presented in Fig. 4.8.

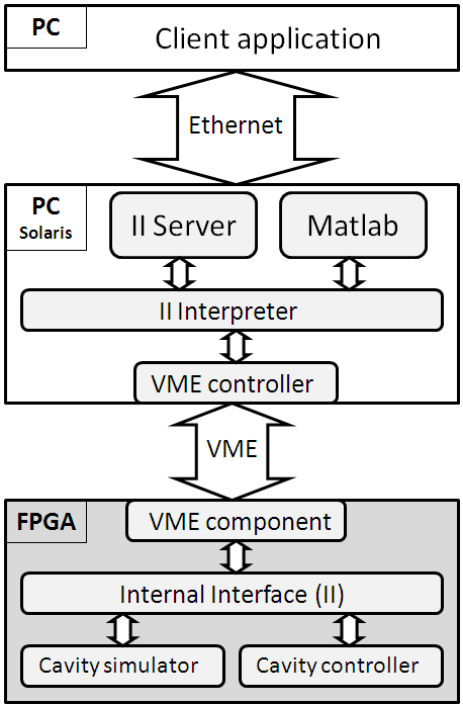

Fig. 4.8 – schematic view of the LLRF control system and its environment

4.3 THE FAST TUNING

The LLRF control system just shown allows achieving, among other requirements, the fundamental condition for amplitude and phase of the accelerating field to be constant during the flat-top duration of the RF pulses, wherein the beam is accelerated by the cavity. Moreover both dynamic detuning, as the Lorentz force detuning (LFD), and low level field controls have been introduced, and the need of a fast and active cavity tuning during the RF pulse now emerges.

This additional need is mainly related to the RF power requirements for the operation of each RF unit, and this ultimately concerns costs and budgeting for the final machine. If the accelerating mode frequency is on its design value the minimum power is required and it is equal to the power transferred to the beam (the power dissipated in the superconducting cavity walls can be here neglected). However, when the accelerating mode frequency is shifted from its design value by Δf_{acc}, additional power is needed to maintain a constant accelerating field. For steady-state conditions the required CW generator power is given by (4.12):

$$P_g = V_{acc} I_b \left[1 + \frac{1}{4} \left(\frac{\Delta f_{acc}}{f_{1/2}} \right)^2 \right] \tag{4.12}$$

V_{acc} is the accelerating voltage of the cavity, I_b is the average beam current and $f_{1/2}$ is the half bandwidth of the accelerating mode resonance. The $\Delta\omega_{acc}^2$ dependence in formula (4.12) led to the common choice (as often in chap. 5 and 6) to refer $\Delta\omega$ to the absolute value of cavity detuning rather than its signed value. The formula (4.12) can be now evaluated considering the dynamic Lorentz forces as the cavity detuning source during the RF pulse. Since also LFD increases as the square of the accelerating field (see par. 3.3.2), the additional power contribution due to dynamic detuning during the RF pulse actually grows *biquadratically* with the accelerating gradient and rapidly becomes critical as the gradient is increased. As a reference, an example of the incident power profile required by the LLRF controller operation in order to correctly drive a cavity that is detuned by the LFD is shown in Fig. 5.19, as a part of the experimental results presented in par. 5.2.3. Significant additional amount of RF power is needed both at the beginning and at the end of the flat-top region and corresponds to the maximum positive and negative detuning value reached by the cavity, given that zero detuning is reached in the middle of the flat-top thanks to a proper pre-detuning.

For gradient values higher than 25 MV/m, i.e. when the induced detuning become significant compared to the 190 Hz cavity nominal half-bandwidth, Lorentz force detuning must be taken into account. According to the reference LFD sensitivity of -0.414 $Hz/(MV/m)^2$ and to ILC pulse parameters [1], a typical LFD of around -600 Hz is expected from pulsed operation at the ILC goal gradient of 31.5 MV/m during the flat-top time window. This value can be compared using formula (4.12) to cavity bandwidth. The result is that, even if the static cavity tune is adjusted accordingly at the beginning of the pulse (via the slow tuner) to reach a zero detuning condition roughly at the middle of the flat-top, the maximum additional power required to drive the cavity results to be about 30 %. If instead average values from test sessions performed at FLASH on module #6 (par. 3.4.2) are considered, the actual sensitivity is -0.471 $Hz/(MV/m)^2$ and this lead to about -700 Hz of detuning and an expected maximum additional required power close to 40 %. These RF power overhead values are intolerably high, taking into account that the microphonics disturbance, here not considered, also contributes to the final additional power needed for cavity field controls. Consider, as a reference, that ILC [1] foresees the use of 560 10 MW RF stations, 26 cavities each, and among several other power margins (i.e. klystron efficiency, waveguide losses), specifications allow only for a 10 % maximum power overhead for the accelerating field low level control.

As a response, since TESLA design report publishing in 2001, the option of an additional, active, control of the cavity tune during the RF pulse time window has been considered, to maximize the RF power efficiency, since the existing passive stiffening of the cavity was not sufficient to permit a proficient operation at gradient close to 35 MV/m and further stiffening improvements are critically limited by cryogenics requirements (see par. 2.3). This led to an activity devoted to the design of a *fast frequency tuner* able to actively keep cavity detuning close to zero or at least inside the cavity bandwidth during the RF pulse with a particular focus on the flat-top phase.

The possibility to counteract a time-varying detuning with a fast frequency tuner relies on the same basic tuning concept already introduced for the quasi-static or slow tuning action. So, since it is technically not feasible to generate a counteracting force distribution which cancels every local deformations of the cavity surface, as for Lorentz forces for example (see paragraph 3.3.2), the RF power overhead reduction is achieved just compensating the induced cavity frequency shift. A time-varying longitudinal force can be applied on the cavity to generate a time-varying frequency shift that can cancel the Lorentz-force detuning during the flat-top phase in pulsed cavity operation. In this case the cavity geometry and therefore the cavity field will be slightly different from that of the unperturbed case but the difference is negligible for the effective accelerating field. On this basis, the search for a suitable fast mechanical actuator capable to realize the needed time-varying deformation of the cavity has started. Theoretical and experimental results that led to the definition of the final actuator model are now presented.

4.4 CHOICE OF THE FAST ACTUATOR

As a starting point, electromagnetic and mechanical parameters of the TESLA cavities presented in paragraph 2.4 allow to consider that the needed dynamical cavity length correction to counteract detuning is expected to be extremely small, close to few microns. This is related to the cavity tuning sensitivity of 315 kHz/mm compared to the LFD shown at the qualifying gradient for ILC (35 MV/m), around -1kHz detuning over the whole RF pulse of which about -600 Hz during the flat-top phase alone.

Since the beginning of the fast tuning development activity the commonly agreed choice has been to search for the optimum actuator among the wide family of piezoelectric actuators. Piezoelectricity based elements are widely used since long time as positioning elements, since they provide nanometer resolution, high dynamic operation (showing up to several kHz bandwidth), high forces (several hundred N) and high reliability. An alternatively option, magnetostrictive based actuators, has been also recently evaluated [28], however, the research on these devices is not as well advanced as on the piezoelectric ones and it will not be considered in the thesis.

Basics of piezoelectricity and results from the R&D activity performed so far on piezoelectric actuators is now presented. Finally the piezo actuators integration in the TTF existing tuner design is briefly described.

4.4.1 PIEZOELECTRICITY BASICS

The piezoelectric effect was discovered by Jacques and Pierre Curie in 1880. The initial observation was the development of charge on a crystal proportional to an applied mechanical stress. Soon thereafter the converse effect, the geometrical strain of a crystal proportional to an applied voltage was also shown. During World War II several

consecutive discoveries led to a new wave of developments and eventual applications. The first findings of unusual piezoelectric properties in refractory oxides (more specifically barium-oxide, titanium-oxide compositions) were made in 1941, and it was an important step as most commercially available piezoelectric elements today are still oxide based. The next key step was to understand the mechanisms of piezoelectricity in these materials. Several publications around 1945 [89] reported unusual dielectric properties in Barium-Titanate and tried to explain the physical principle on a molecular level. One of the most significant discoveries was the poling process in polycrystalline piezoelectric materials in 1946. Until then the piezoelectric effect was only observed on single crystal materials, which are generally more expensive to manufacture and limited in size. An advancement of great practical importance was the discovery of very strong and stable piezoelectric effects in lead zirconate solid solutions by B. Jaffe and co-workers in 1954 [90]. This initiated several developments and led to an enormous field of applications based on piezoelectric materials. Nowadays, the main reference for piezoelectricity is the corresponding publication by the Standards Committee of the Institute of Electrical and Electronics Engineers (IEEE) [91]. It is the most widely recognized description of piezoelectric ceramic behavior.

Piezoelectricity is currently defined as the property of some materials to develop electric charge on their surface when mechanical stress is exerted on them. An applied electric field produces in these materials a linearly proportional strain. The electrical response to mechanical stimulation is called the direct piezoelectric effect and the mechanical response to electrical simulation is called the converse piezoelectric effect.

Piezoelectricity is the property of nearly all materials that have a non-centrosymetric crystal structure. Some naturally occurring crystalline materials possessing these properties are quartz and tourmaline. Some artificially produced piezoelectric crystals are Rochelle salt, ammonium dihydrogen phosphate and lithium sulphate. Another class of materials possessing these properties is polarized piezoelectric ceramic. In contrast to the naturally occurring piezoelectric crystals, piezoelectric ceramics are of a "polycrystalline" structure. The most commonly produced piezoelectric ceramics are lead zirconate titanate (PZT), barium titanate and lead titanate. Ceramic materials have several advantages over single crystal, especially the ease of fabrication into a variety of shapes and sizes. In contrast, single crystals must be cut along certain crystallographic directions, limiting the possible geometric shapes. PZT have crystal structures, in Fig. 4.9 the ideal, cubic structure is shown. PZT crystallites originally are centro-symmetric cubic (isotropic), then after the application of a sufficiently high DC field (called *poling* process) exhibit tetragonal symmetry (anisotropic structure). This is true provided that temperature is below a critical temperature or Curie temperature T_C (typically between 200 and 300 ° Celsius), when the crystalline structure changes back from a non-symmetrical to a symmetrical form thus losing its piezoelectric properties.

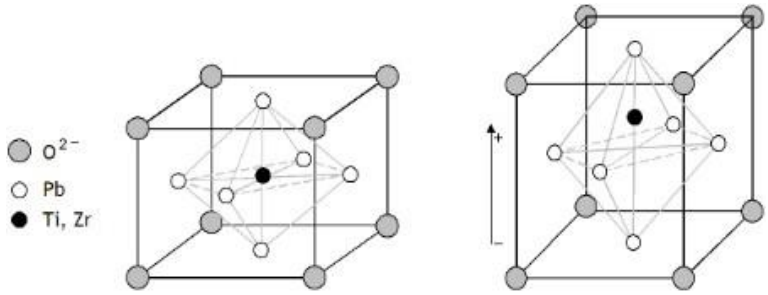

Fig. 4.9 - Single crystal of PZT before (middle) and after poling (right).

Before poling, a piezoelectric ceramic material consists of small grains (crystallites), each containing domains in which the polar direction of the unit cells are aligned. These grains and domains are randomly oriented; hence the net polarization of the material is zero, i.e. the ceramic does not exhibit piezoelectric properties. Poling orients the domains in the field direction and leads to a permanent polarization of the material. The structure is very tolerant to element substitution (doping) by formation of solid solutions. The coupling of electrical and mechanical energy makes piezoelectric materials useful in a wide range of applications.

Piezoelectric effect depends on directions. The reference *direct* axis, called axis 3, is taken parallel to the direction of poling (therefore an *inverse* direction is defined accordingly as opposite to axis 3). Axes 1 and 2 are defined arbitrarily in order to form a direct coordinate system with axis 3. 4, 5 and 6 represent shear movements around axes 1, 2 and 3 respectively. Based on this coordinate system, the piezoelectric effect can be described in a simplified way by matrix coefficients. For actuators, the coefficients "d" (coupling coefficients, 3 x 6 matrix) and "s^E" (stiffness coefficients, 6 x 6 matrix) are commonly used. In fact, piezoelectricity can be considered the combined effect of the electrical behavior of the material:

$$D = \epsilon E \tag{4.13}$$

where D is the electric displacement, ϵ is permittivity and E is electric field strength, and Hooke's Law:

$$S = sT \tag{4.14}$$

where S is strain, s is compliance and T is stress. These may be combined into so-called *coupled equations*, whose strain-charge form is:

$$\{S\} = [S^E]\{T\} + [d_t]\{E\} \tag{4.15}$$

$$\{D\} = [d]\{T\} + [\epsilon^T]\{E\} \tag{4.16}$$

where d represents the piezoelectric constants, and the superscript E indicates a zero, or constant, electric field; the superscript T indicates a zero, or constant, stress field; and the subscript t stands for transposition. The strain-charge equations for PZT like materials may also be written as:

$$\begin{bmatrix} S_1 \\ S_2 \\ S_3 \\ S_4 \\ S_5 \\ S_6 \end{bmatrix} = \begin{bmatrix} S_{11}^E & S_{12}^E & S_{13}^E & 0 & 0 & 0 \\ S_{12}^E & S_{11}^E & S_{13}^E & 0 & 0 & 0 \\ S_{13}^E & S_{13}^E & S_{33}^E & 0 & 0 & 0 \\ 0 & 0 & 0 & S_{44}^E & 0 & 0 \\ 0 & 0 & 0 & 0 & S_{44}^E & 0 \\ 0 & 0 & 0 & 0 & 0 & S_{66}^E = 2(S_{11}^E - S_{12}^E) \end{bmatrix} \begin{bmatrix} T_1 \\ T_2 \\ T_3 \\ T_4 \\ T_5 \\ T_6 \end{bmatrix} + \begin{bmatrix} 0 & 0 & D_{31} \\ 0 & 0 & D_{31} \\ 0 & 0 & D_{33} \\ 0 & D_{15} & 0 \\ D_{15} & 0 & 0 \\ 0 & 0 & 0 \end{bmatrix} \begin{bmatrix} E_1 \\ E_2 \\ E_3 \end{bmatrix} \tag{4.17}$$

$$\begin{bmatrix} D_4 \\ D_5 \\ D_6 \end{bmatrix} = \begin{bmatrix} 0 & 0 & 0 & 0 & d_{15} & 0 \\ 0 & 0 & 0 & d_{15} & 0 & 0 \\ d_{31} & d_{31} & d_{33} & 0 & 0 & 0 \end{bmatrix} \begin{bmatrix} T_1 \\ T_2 \\ T_3 \\ T_4 \\ T_5 \\ T_6 \end{bmatrix} + \begin{bmatrix} \epsilon_{11} & 0 & 0 \\ 0 & \epsilon_{11} & 0 \\ 0 & 0 & \epsilon_{33} \end{bmatrix} \begin{bmatrix} E_1 \\ E_2 \\ E_3 \end{bmatrix} \tag{4.18}$$

In this equation, the "$s^E \cdot T$" term describes the mechanical compliance of the component, similarly to any mechanical component. The "$d^t \cdot E$" term describes the piezoelectric effect, i.e. strain generated by electrical field. The above equations are especially useful for designing piezo applications. However, it must be underlined that they represent an approximation since piezoelectric behavior is affected by intrinsic non-linearities as hysteresis, creep and field dependency.

4.4.2 PIEZOELECTRIC ACTUATORS

The constitutive equations (4.15)(4.16) can be finally applied to an actuator. In this case, the important characteristics are the mechanical stiffness (from the "$s^E \cdot T$" term) and the piezoelectric free strain (from the "$d^t \cdot E$" term). All actuators can thus be described in a first approximation by linear equations. The common representation for this behavior is the force-displacement diagram shown in Fig. 4.10.

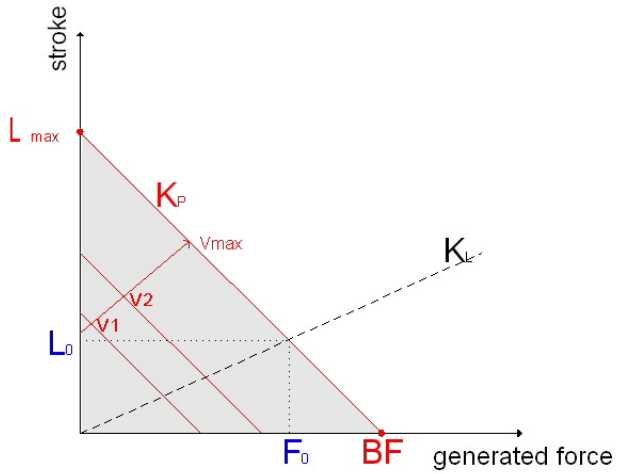

Fig. 4.10 – working area of a piezo actuator

If the actuator operates freely, it will generate a displacement equal to its free displacement, up to its *maximum stroke* L_{max}. If it is operating against a spring k_L, it will generate less displacement, L_0, but more force, F_0, according to the stiffness of the opposing spring k_L (see plot in Fig. 4.10). These parameters also define the operative actuator *stiffness* k_P as the ratio between BF and L_{max}. This can be considered as the "active" stiffness of the actuator and it is completely valid only inside the actuator working range. k_P is, for instance, the stiffness value that must be considered when evaluating the stack performances against a given mechanical structure and maximum mechanical power is reached exactly when k_L equals k_P. If piezo is operating against an infinitely stiff spring, it will generate a force equal to its *blocking force* BF, but no displacement. As a result:

$$L_0 = L_{max}\left(\frac{k_P}{k_P + k_L}\right) \tag{4.19}$$

$$F_0 = BF\left(\frac{k_P + k_L}{k_P}\right) \tag{4.20}$$

Finally, the overall load on the actuator must not, in any moment, exceed its *load limit* value (LL), an additional parameter that is related to the intrinsic ceramic strength. When a static load is applied, as for example for a mass M installed over it, full displacement L_{max} can be anyway obtained at full driving voltage, provided that the applied load does not exceed LL. Simply, the piezo displacement zero-point is shifted according to actuator stiffness. The load limit is not anyway a sharp threshold, because when the overall static preload on the stack approaches LL, a degradation of the maximum stroke performances occurs. As a simple rule to ensure nominal expected performances, the preload should not exceed the value (LL – BF). PZT ceramic based actuators typically perform a maximum generated pressure of 4 MPa and a maximum strain of 0.2 %, moreover, although they can withstand pressures up to 240 MPa without breaking, this value must never be even

approached in practical applications: therefore, with a significant safety margin, a typical maximum pressure of 120 MPa is considered.

It is important to underline that over a larger strain range, when for example the piezo stack is pushed by an external loading force higher than BF, a non-linear behavior is evident and the actual stiffness approaches the higher value k_Y inferred from the Young's module Y of the bulk material (typically around 40 MPa for PZT). Moreover it must be underlined that, despite a classical solid body, piezoelectric ceramic stiffness behaviour is strongly coupled to the electrical boundary conditions. This effect is usually described via the two s^E_{33} and s^D_{33} piezoelectric constants that corresponds to the inverse of the Young's modulus computed, respectively, for electrical short circuit condition and open circuit condition (a factor of 2 is typical for the ratio s^D_{33} over s^E_{33}). An open circuit condition actually corresponds to the piezo current-driving scheme while closed circuit occurs in a voltage-driving scheme, that is widely more used and that will be considered further on.

For what concerns the dynamic behavior, piezoelectric stack, as any other solid state body, exhibits resonant modes. The reference resonant frequency f_0 that is given by manufacturers refers to the bare stack with a fixed end (i.e. the piezo stacks stands on one of the end surfaces), the resulting value is therefore related to the simple spring-mass model formula:

$$f_0 = 1/2\pi \sqrt{\frac{k_P}{m_{eff}}} \tag{4.21}$$

where m_{eff} is, as expected for this case of a rod shaped mass standing on one end, 1/3 of the piezo stack mass. As a reference, a piezoelectric stack can reach its nominal maximum displacement in 1/3 of the period of its resonant frequency, provided that the driving amplifier can deliver the necessary current value. If not actively compensated (for example modulating the shape of the input signal) this displacement is then reached with a significant overshoot. It is important to consider that, when actually installed in its final assembly, if an additional mass M is added and driven by the piezo actuator, the final resonant frequency drops accordingly to the value f:

$$f = f_0 \sqrt{\frac{m_{eff}}{M+m_{eff}}} \tag{4.22}$$

In order to enhance maximum stroke and lower the operating voltage, multilayer actuators are realized from thin layer of PZT material. A multilayer elements is composed of several layers of piezoelectric material, typically about 100 μm thickness, alternating with internal electrodes. Internal electrodes are successively positive and negative. All positive electrodes are connected together by one external electrode on one side of the component; negative electrodes are connected on the other side of the component.

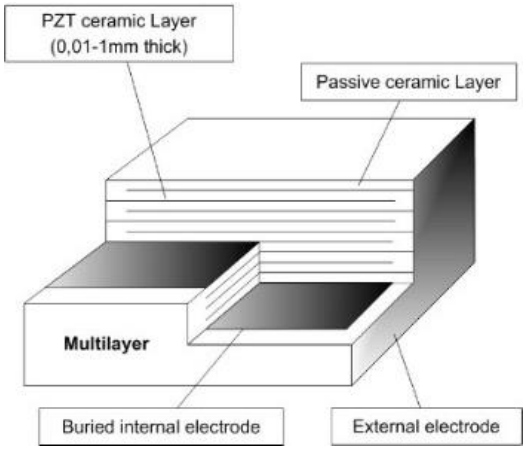

Fig. 4.11 – schematic view of a multilayer actuator

Even if actuators made from bulk material are easier to manufacture using more materials, multilayer ones offer several important advantages. Multilayer components can be operated under higher electrical field up to 3 kV/mm, thus leading to larger static displacement and simultaneously be operated under a lower voltage (100-200 V instead of few kV)). Multilayer stacks are also more resistant to humidity thanks to their embedded electrodes that can be customized with complex electrode designs and eventually multiple functions in the same component. They necessarily exhibit an higher static electrical capacitance between driving electrodes if compared to bulk stacks, capacitance in the order of few μF to tens of μF are likely to occur. Finally, it must be underlined that the effective Young's module for a multilayer actuator is lower than the correspondent value for the bulk material due to the metallic electrodes and the glue interfaces that are present between adjacent layers.

Reliability and life-time are key figures to account for each piezoelectric based actuator. Because of the many different possible applications, there is no readily available model for reliability. This figure would depend mainly on:

– Temperature, cooling: the self heating due to dielectric losses through the dissipation or loss factor tan(δ), specially for high dynamic and frequency operations must be counteracted. As a reference, the thermal heat P generated in the actuator can be evaluated with the following equation:

$$P = \tan(\delta)\, f C U_{PP}^2 \tag{4.23}$$

where tan(δ) is the loss factor, f the frequency of the driving signal, C the static piezo capacitance and U_{pp} is the peak to peak amplitude of drive voltage. Typical values for tan(δ) for PZT materials are about 1-2 %.

- Humidity, contaminants: exposing an actuator to high humidity or contaminants levels can lead to electro-migration and eventually provoke a breakdown in the electrical insulation
- Electrical field: a lower average electrical field during life-time improve reliability. Moreover field value limits exist for actuator operation in both poling (direct) and inverse directions. When an excessive electrical field is applied in the former case discharges through the ceramic severely damage it, instead in the latter case (inverse driving field) the original permanent polarization is lost and polarity is reversed. A typical inverse over direct voltage limit ratio is 20 % for common PZT ceramic.
- Mechanical loading, preload, vibrations: the ceramic stacks should always operate in compression. PZT has a very limited tolerance to tensile stresses, that must be generally limited to the 10% of the actuator load limit. A particular function, especially in the frame of cavity frequency tuning, is given to the mechanical preload in the working conditions. It is widely confirmed in literature [92][91][93] that a sufficient preload significantly prevents actuators from undergo cracks and damages in the ceramic therefore enlarging their operative life-times. An indicative range of preload force is given by manufacturers, namely from 30 to 50 % of the actuator blocking force BF. This range can be also expressed as the 10 to 20 % of actuator load limit LL. Moreover, even if at first order the piezo working area properties are independent from the static load, a second order effect is superimposed. Due to the influence of the load on the polarization of PZT a small increase in the maximum stroke, up to 10 %, is achieved when load is again between 10 and 20 % of the load limit, thus this latter preload force range must be considered as the goal interval to maximize both performances and life-time.

4.4.3 THE FAST TUNER ENVIRONMENT

Apart from the installed tuner, once in a superconducting cavity tuning system in a linac, the piezo actuators will be forced to work in a severe and unusual environment. A detailed analysis of the main aspects of this condition is presented since it will allow to properly define the requested piezo specifications.

First of all, installed actuators will be exposed to γ radiation generated by field emission in the cavities and neutron flux by losses in the accelerated beam. An upper limit for the average dose rate is dictated by the capacity of the cryogenics which can handle an additional heat load of 0.1 W/m corresponding to a dose rate of 10 Gy/h. This means that piezo actuators are requested to achieve an estimated adsorbed dose of about 0.1 MGy per year of operation without critical damages.

Then, actuators are requested to sustain operations in a cryogenic environment therefore both pressure and temperature must be taken into account. Firstly, they will be subjected to an insulation vacuum, usually about 10^{-4} mbar needed for the thermal

insulation of the cold mass inside the cryomodule. Fundamentally, PZT based actuators are almost completely not sensitive to vacuum itself, that instead ensures stacks from being exposed to humidity or eventual contaminants.

Temperature instead drastically affects piezo performances. Each possible tuning system is installed directly on the cavity He tank that is filled with superfluid He at 1.8 K temperature during normal operations. Even if copper strings providing thermal short-circuits are generally installed in order to roughly stabilize the temperature of tuner assembly elements, the heat sink effect barely involves piezo stacks. This is mainly due to the installation constraints, since only two surfaces, both edges of the stacks (usually ceramic, so with poor thermal conduction properties), contribute to the heat flow. As a result, even if when not in use, it is reasonable to assume piezo stacks to reach an equilibrium temperature between 4.2 K to 1.8 K (the entire cold mass is surrounded by the 4.2 thermal shield). But it is anyway expected that even higher temperature would be found locally on the piezo actuators when they are in operation (i.e. driven by a proper voltage). Low temperature applications for piezo actuators, although existing, do not exert significant commercial interest among main manufacturer and this leads to the difficulty to analyze in detail actuator properties and performances at low temperature. Anyway, thanks to several experimental measurements performed at LASA lab as well as in others laboratories involved in the ILC collaboration, as IN2P3 at Orsay and DESY, and thanks to a strong interaction with main piezo actuators manufacturers, a deep understanding of piezo behaviour at cold has been achieved. The effect of temperature on main piezo parameters can be summarized:

- Stroke: a lowering in the stack temperature strongly reduces the maximum stroke that can be achieved by piezo at the same nominal maximum voltage. A reference value of 4.2 K is here assumed since it eases experimental procedures and performances difference between 4.2 K and 1.8 K can be disregarded with confidence. Apart existing differences among different models, there is common agreement in evaluating the remaining maximum stroke at 4.2 K as the 10 % of the full stroke at room temperature.

- Electrical field: at low temperature the PZT ceramic sensitivity to depolarization induced by strong electrical field is strongly reduced. It is therefore possible to operate in an extremely wider bi-polar voltage range than compared to room temperature. The maximum direct (i.e. toward poling direction) driving field sustainable by PZT is doubled when cooled to 4.2 K and a factor of 10 is instead gained for the maximum inverse electrical field. Moreover piezo actuators still show good linearity between these extended voltage limits. As a consequence, it is conceptually possible to extend 4 times the maximum voltage sweep, up to a completely bi-polar operation and so multiply up to 4 times the maximum actuator stroke. Therefore the significant loss in stroke that piezo exhibits at liquid He temperature, compared to warm performances, can be partially compensated and eventually the residual stroke can be raised from 10 % to 40 %.

- Capacitance: the value of the static electrical capacitance between electrodes is strongly reduced at low temperature. Typically, only 5 to 10 % of the room temperature value is shown at 4.2 K.
- Stiffness: both thermal shrinkage of the piezo ceramic itself and stroke temperature dependence affect the actuator stiffness. A significant stiffness increase is shown as a consequence of temperature reduction. The piezo actuator at cold temperature exhibits a stiffness that is roughly 10 times higher.
- Blocking Force, Load Limit: for any practical purpose both the maximum force generated through the piezoelectric effect (i.e. the blocking force, BF) and the maximum sustainable load (LL) can be assumed with confidence to be invariant from room temperature to cryogenic temperature.

According to formula (2.57), only 3 μm of cavity longitudinal displacement would theoretically fulfil LFD compensation requirements. Anyway, to ensure the needed tuning performances, at least a factor of 10 margin in the maximum stroke is required when considering room temperature properties of the actuator. Particularly because the possibility to operate the piezo stack at higher electrical field and therefore with higher voltage, even if possible at cold, must be discarded. The stroke margin must be even higher to take into account also the actual design of the fast tuner installed. Since actuators are not, in any case, directly mechanically coupled to the cavity, an additional margin must be considered because only a fraction of the piezo stroke actually reaches the resonator.

The actuator, apart from the installed tuner, must transfer the largest possible part of its stroke to the cavity. As a first order approximation, referring to the plot in Fig. 4.10, the actual external stiffness of the piezo environment is expected to be significantly dominated by the softer element in the assembly, the cavity, being about 3 kN/mm at room temperature. This means that the actuator stiffness, that means its blocking force once the maximum stroke is determined, should be much higher than that value in order to optimize the transferred displacement. High stiffness actuators allow also, once installed, to optimize the transfer of the displacement induced by the stepper motor to the cavity.

Moreover an additional static loading force could be generated in the system. First of all the cavity itself is longitudinally deformed during operation according to its tuning needs by the slow tuning mechanism. In the worst case (it actually depends on actual tuner design) the actuator is requested to bear completely this force that, considering a worst case of 600 kHz tuning (for a cold cavity) needed to reach the nominal frequency [1], is close to 6 kN (considering cavity parameters in paragraph 2.4). Moreover potentially compressive force on piezo could be generated also by the differential pressures present mainly during the cooldown phase, for example between the He tank and the beam pipe in the cavity. Even these loads can sum up to several kN. Therefore, this load must be withstood not only without any damage but also without any critical lowering in the piezo performances, consequently the load limit is required to be much higher than 6 kN.

A further consideration can be done concerning the rate of displacement required to the actuator in order to compensate for the LFD. The cavity displacement required for the

LFD compensation must be achieved during the flat-top time window of about 1 ms, according to ILC specifications [1]. This results, as previously introduced, in the request of a sufficiently high value of piezo mechanical resonant frequency. It must be considered that two concurring issues would be present once the actuator will be installed in the final assembly: the inertial mass of the setup can lower the resonance value to few percents (10 kg for M and 10 g for m_{eff} means a f/f_0 ratio of 3 %, formula 4.22) while the stack stiffness raising due to temperature induces an higher f_0.

Finally, in order to complete this overview of piezo required specifications, it must be considered that, given the ILC linac repetition rate of 5 Hz, the foreseen period of operation of 10 years and the assumption of 1 piezo pulse each RF pulse, around 10^9 complete stroke cycles must be accomplished by the actuator. Moreover, even actuator size and price should be accounted, in sight of a large scale installation.

On these basis, the detailed required specifications for the fast tuner actuators are summarized in Tab. 4.1. The values shown have therefore been considered as guidelines throughout the whole R&D activity that led to the definition of the final piezo actuator models.

Parameter	Requirements room T	Dimensions
Max stroke - L_{max}	> 40	μm
Blocking force - BF	> 4	kN
Stiffness - K_P	>> 3	kN/mm
Load limit - LL	> 10	kN
Res. freq	> 10	kHz
Life-time	> 10^9	# cycles
Act. Voltage	<= 200	V
Size	20 x 20 x 100	mm^3

Tab. 4.1 – required piezo specifications for the fast frequency tuning

Once these detailed list of required specifications for fast cavity tuning was realized, a deep evaluation of existing commercial piezo actuators available has been performed. The option for a custom made actuator has been discarded since the beginning of this R&D activity since it is mandatory to control costs for the whole tuning assembly in view of a large scale production. Every available information concerning actuators that have been selected and evaluated since 2001, together with their main characteristics, are presented in Tab. 4.3 at the end of the paragraph. Moreover a collection of pictures of some of these different piezo models are resumed in Fig. 4.12 [93][94][95][96].

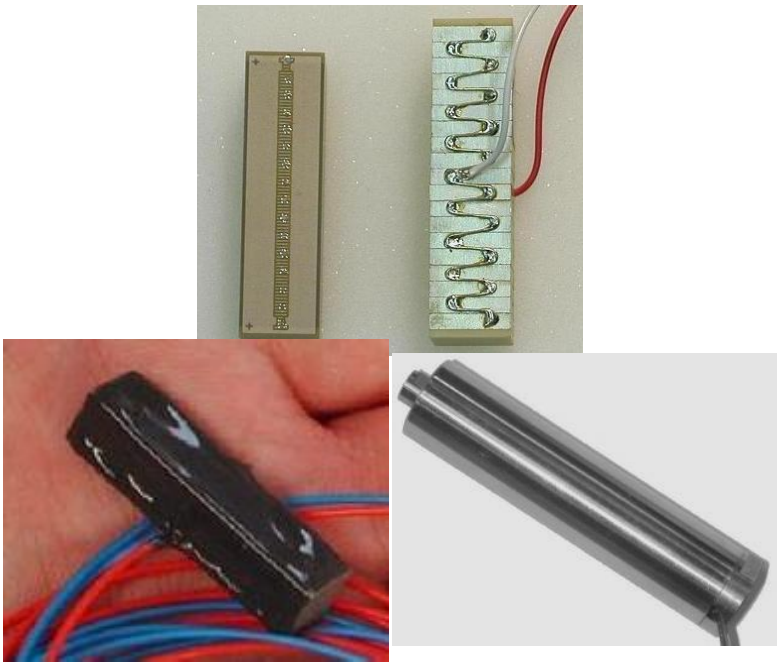

Fig. 4.12 - some piezo actuators: PI_36 (up, left), NOLIAC_40 (up, right), EPCOS_30 (down, left) and PM (down, right)

Over the past years, several experimental measurements have been performed on presented actuator models, mainly for a direct verification of their performances, also in terms of reliability, in a cryogenic environment.

The possibility for the piezoelectric ceramics in use, to sustain the equivalent of 10 years of operation as actuator in an active frequency tuner for ILC superconducting cavities, has been investigated with a dedicated test session at LASA [18]. A PI_36 stack (see Tab. 4.3) has been cooled down and it has been excited uninterruptedly for a month up to its limits, sustaining about $1.5 \cdot 10^9$ cycles of switching up to nearly the maximum stroke, so a good estimate of 10 years of operations. During this test the piezo temperature and current were constantly monitored, some approximations were anyway introduced mainly to overcome actual technical difficulties. Insulation vacuum has been reproduced while, since the lifetime test needs a long period of cool down, the test has been performed in a liquid N_2 bath at 77 K temperature. The equipment used was capable to generate a known loading force on the device under test. During the whole measurement the preload on piezo has been kept between 1 kN and 1.5 kN with an average value of 1.25 kN. A continuous sinusoidal signal with frequency from 117 to 997 Hz and 100 V amplitude has been used as driving signal. A schematic representation of the test equipment realized is shown in Fig. 4.13.

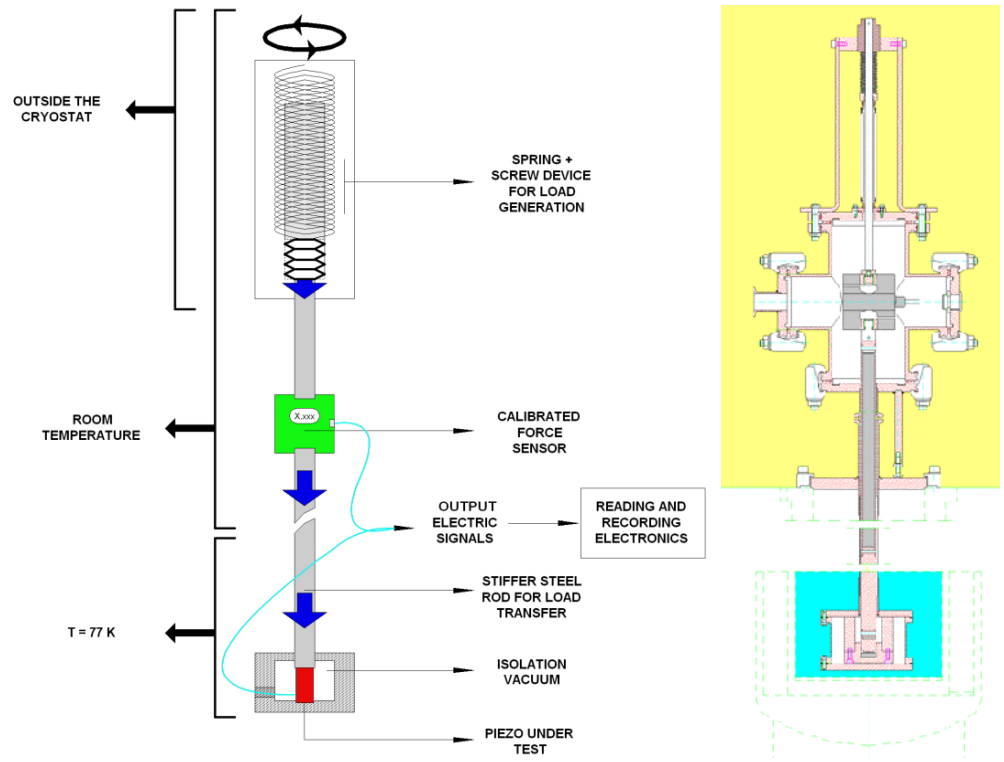

Fig. 4.13 – equipment used for the piezo life-time test at LASA

The life-time test performed confirmed that no significant alteration in the actuator main parameters has been exhibited by the piezo stack after 10 years of simulated operation in a cryogenic environment. Main piezo measurements before and after the test are reported in Tab. 4.2, also the hysteresis figure has been measured and it is shown in Fig. 4.14.

PI_36 life-time test at LASA			
	before	**After**	
Electrical capacitance	13.6	13.56	μF
Resonant frequency	45.94	45.2	kHz
Maximum stroke	40.2	38.3	μm

Tab. 4.2 – comparison of results for the piezo life-time test

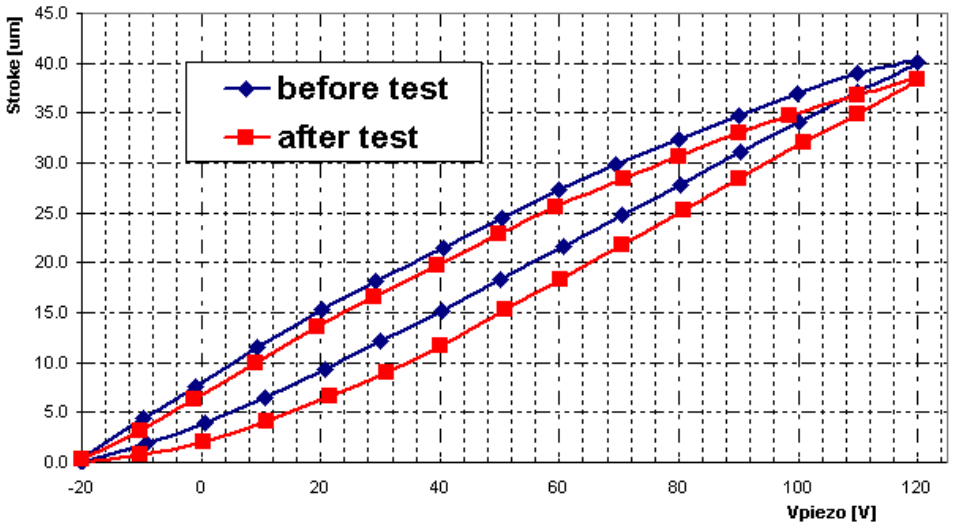

Fig. 4.14 – hysteresis figure for the PI_36 piezo before and after the life-time test

Several direct experiences with piezo actuators have been also performed to investigate the performance degradation due to radiation level. First of all, several hours of operations have been so far collected concerning EPCOS_30, PI_36 and NOLIAC_30 models in CHECHIA, FLASH ACC6 and ACC7 cold tests and other linac activities. None of those revealed any clear evidence of stack degradation due to radiation. Moreover, a dedicated piezo actuator radiation hardness test was performed at CERI – Orleans [97] to check the behavior of irradiated actuator. Four PI_36 actuators were cooled down to 4.2 K and then successfully exposed for 20 h to neutron radiation. The total acquired dose was calculated to be 1.76 - $3.09 \cdot 10^{14}$ n/cm². The only measured effect was finally an increasing in the capacitance value that is perfectly explained by the heating caused by fast neutron beam. This result is coherent to few evidences collected in literature [98] confirming that mild damage to piezo ceramics is expected only at a total dose higher than 100 MGy.

Manufactures		**Noliac**	**Noliac**	**Epcos**	**PI**	**Noliac**	**Piezomechanik**
Model		**SCMA/S1/A/10/10/40/200/60/4000**	**SCMA/S2/A/15/15/70/200/100/9000**	**LN 01/8002**	**P-888.90**	**SCMAS/S1/A/10/10/30/200/42/6000**	**Pst 150/10**
Referred as		NOLIAC_40	NOLIAC_70	EPCOS_30	PI_36	NOLIAC_30	PM
Material		medium soft doped PZT-S1	medium soft doped PZT-S2	PZT-nd34	PZT-PIC 255	medium soft doped PZT-S1	
Case/preload		No	no	no	no	no	Yes / 400N
Length	mm	40 ± 0,5	70 ± 0,8	30	36	30 ± 0,5	64
Active length	mm		68.5		33.84		
Cross section	mm x mm	(10 x 10) ± 0,2	(15 x 15) ± 0,3	6,8 x 6,8	10 x 10	(10 x 10) ± 0,2	
Number of layers			490		300	196	
Average layer thickness	µm		140		113	140	
Young modulus	kN/mm^2	45	47	51	48.3	45	
Stiffness: small range/bulk	kN/mm	67 / 112	90 / 151	80 / 83	103 / 105	95 / 150	25 / 35
Max. stroke	µm	60 ± 9	100 ± 13	40	35 ± 3,5	42 ± 6,3	80
Blocking Force	N	4000 ± 800	9000 ± 1400	3200	3600 ± 720	4000 ± 800	
Load Limit	N	12000	27000		10000		
Resonant .freq. no load	kHz	38		52	40	51	
Density	kg/m^3	$7,7\ 10^3$	$7,5\ 10^3$	$7,75\ 10^3$	$7,8\ 10^3$	$7,7\ 10^3$	
Min. voltage		0	0	0	-20	0	-30
Max. voltage	V	200	200	160	120	200	150
Max speed - unloaded	V/µs			1.6			
Max. charge current	A			20			
Capacitance	µF	8	40	2.1	12.4	5.7	
Loss Factor	tan(δ)	0.017		0.019	0.015	0.017	
Thermal Expansion	ppm/K	-2.5				-2.5	

Tab. 4.3 – collection of piezo properties for models used

4.4.4 PIEZO INTEGRATION IN THE TTF TUNER

At the beginning of the activity related to the dynamic detuning compensation, a prototype of fast frequency tuner has been realized starting from the existing TTF cavity tuner, already described in paragraph 3.2 [62]. The current tuner design has been developed with the insertion of up to two fast piezoelectric actuators. The piezo integration has been obtained avoiding a complete redesign of the mechanical assembly: only one tuner support, opposite to the stepper motor side, has been modified and in place of the existing tuner support rod, a compact titanium frame (piezo fixture), has been designed to host 2 piezo stacks in parallel. This double stack configuration allows to keep a spare actuator for redundancy while, if no replacement is needed, using it as a mechanical sensor. The final design of the TTF piezo tuner is shown in Fig. 4.15.

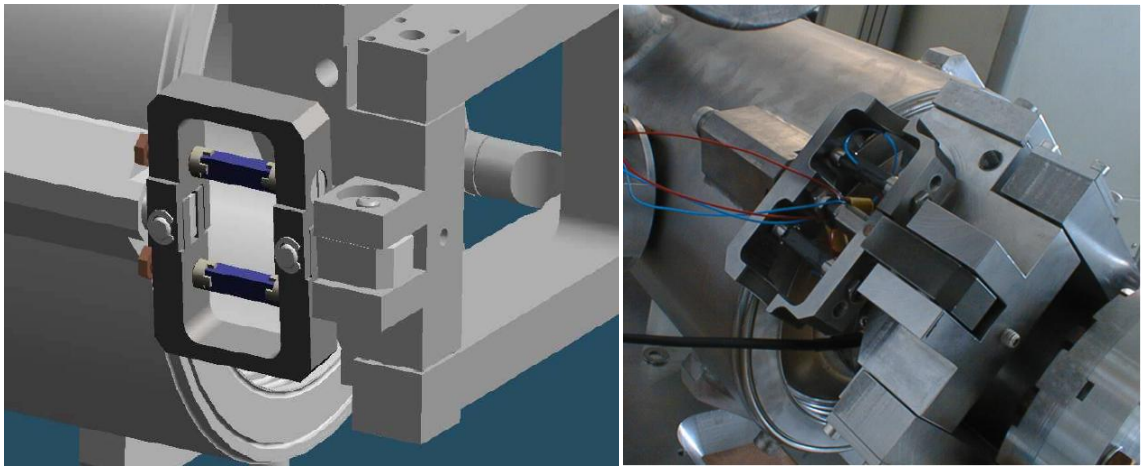

Fig. 4.15 – the piezo frame with 2 actuators installed in the TTF tuner, a CAD model (left) and the first prototype (right)

Each piezo is installed on a screwed holder element that allows displacing the fixture from its nominal position and generating, thanks to the fixture longitudinal stiffness itself, a static compressive force on the actuators.

As a result, the working principle for the fast tuning action can now be schematically represented as shown in Fig. 4.16, to be compared to the similar picture, Fig. 3.2, for the original design of the tuner already introduced.

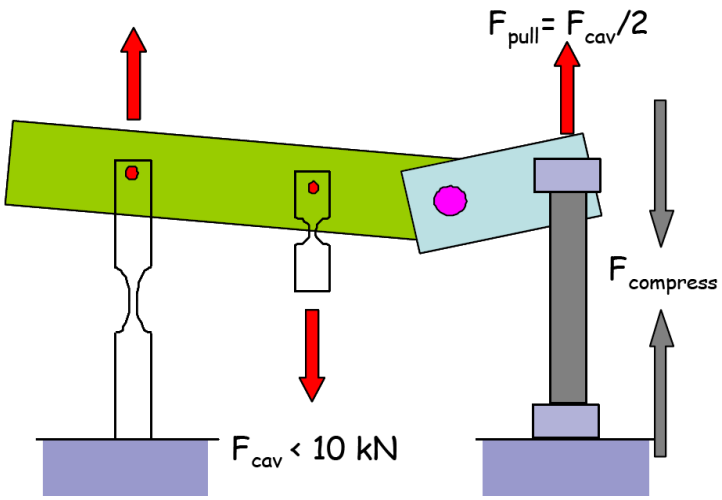

Fig. 4.16 – schematic representation of the fast tuning action in the TTF tuner [99]

The fast tuning action, symmetrically to the slow tuning one, acts through the mechanical leverage of the tuner, having its fulcrum in the tuner support on the stepper motor side and its coupling to cavity roughly in the middle of the leverage. Since the whole tuning setup is designed to push the cavity during normal operation, half of the reaction force F_{cav}, generated by cavity stiffness, acts as an expanding force on the piezo frame. This leads to the important consequence that the only compressive force available for piezo, drastically needed as already shown, is generated by the piezo holder frame itself. So the correct preload value $F_{compress}$ must be set via screwed support during tuner installation so that the final preload $F'_{compress}$, at cold is sufficient to ensure a correct mechanical contact and possibly an optimized life-time. The actual total load F on the piezo is therefore given by following formula, where compressive loads are positive:

$$F = F'_{compress} - F_{cav}/2 \qquad (4.24)$$

The cavity force is determined by the static displacement of the cavity according to slow tuning needs, so F_{cav} value actually depends on the stepper motor position. As a result, the original tuning range of the TTF tuner design in significantly reduced once piezo are installed. Currently, the piezo fixture is stiff enough to allow a tuning range of around 300 kHz, above this value piezo operations could not be guaranteed due to a critical loosening in the piezo fixture.

Although problems related to the operation of this prototypical TTF piezo tuner design are known, it can be considered as widely-know and affordable even if it cannot be the final choice for ILC. Several prototypes have been so far realized during the R&D activity in this field and they have been tested many times on TESLA cavities in a cold environment, both in CHECHIA horizontal cryostat and inside the FLASH linac. Different piezo models have been installed for experimental tests, starting from the 2 EPCOS_30 piezo for the first tests in 2001. Recently, each cavity of module ACC6 at

FLASH has been equipped with a TTF piezo tuner hosting a couple of PI_36 piezo (see Tab. 4.3). A detailed test session of dynamic detuning compensation using installed piezo actuators has been performed on module ACC6 in the CMTB facility at DESY, during which the TTF piezo tuner achieved a complete compensation of the LFD at the accelerating gradient of 35 MV/m. A full report is presented in chapter 5. Finally, also module ACC7 has been equipped with fast tuners but just one piezo has been installed in each fixture, 4 NOLIAC_30 and 4 PI_36. Currently the group at CEA, Saclay Paris, that developed the original TTF tuner design is responsible for the development of a new model with modified design, the Piezo Tuning System or PTS [100]

4.5 DETUNING CONTROL SYSTEM

So far the characteristics of the dynamic detuning of TESLA cavities and the need for a fast tuning have been introduced, together with properties and performances of the reference set of fast actuators, piezoelectric based. It is therefore possible to start considering, from the control theory point of view, which solutions have been designed to make use of the developed fast tuning equipment. Appropriate control strategies that take into account the peculiarities of each sources of dynamic detuning will be now presented, this will lead to the introduction of tuner controller concept. Then electronic equipment, hardware and software, will be revised and the experimental test of separate components of the final controller code will be reported.

4.5.1 CONTROL STRATEGIES

Once the fast actuators have been installed and, through the slow tuner mechanical assembly, are mechanically coupled to the resonator, the final object of the active compensation, i.e. the plant (see par. 4.1), is defined according to the scheme in Fig. 4.17.

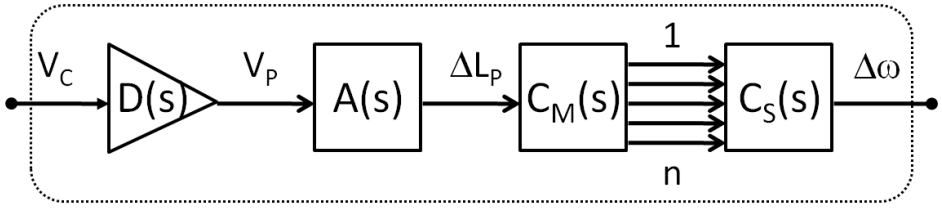

Fig. 4.17 – schematic plant representation for the detuning control system

Laplace transforms of input-output transfer functions are used to represent elements in the chain, as the piezo amplifier and driver, D(s), and the piezo actuator itself, A(s). The cavity representation C(s) instead is composed by its purely mechanical transfer function $C_M(s)$, that determines the excitation of each of cavity n modes induced by piezo dynamic displacement ΔL_P , and by the coupling $C_S(s)$ between each of those n mechanical modes

and the final overall detuning $\Delta\omega$, according to Slater theorem (3.1). The final plant is therefore simply represented by:

$$P(s) = D(s)\, A(s)\, [C_M(s) \cdot C_S(s)] \tag{4.25}$$

As a reference, results of a direct measurements of amplitude and phase of the P(s) transfer function for a TESLA cavity in CHECHIA is presented in appendix A, Fig. a.1.

The Lorentz force induced cavity detuning is, as introduced in par. 3.3.2, intrinsically repetitive and coherently synchronized to the RF pulse, as also confirmed by the several LFD data collected. Therefore, neglecting the small deviations from pulse to pulse due to microphonics, a feed forward (FF) open loop control can be designed aiming to introduce a calibrated time-varying detuning that cancels the effect of the LFD on the controlled variable $\Delta\omega$. Both the Lorentz force detuning effect and its feed forward compensation are presented in the scheme of Fig. 4.18, K(s) represent the Klystron transfer function. The timing information is extracted from the RF pulse signal V_{RF} and provided to the feedforward controller FF(s) in order to achieve synchronization at the used repetition rate.

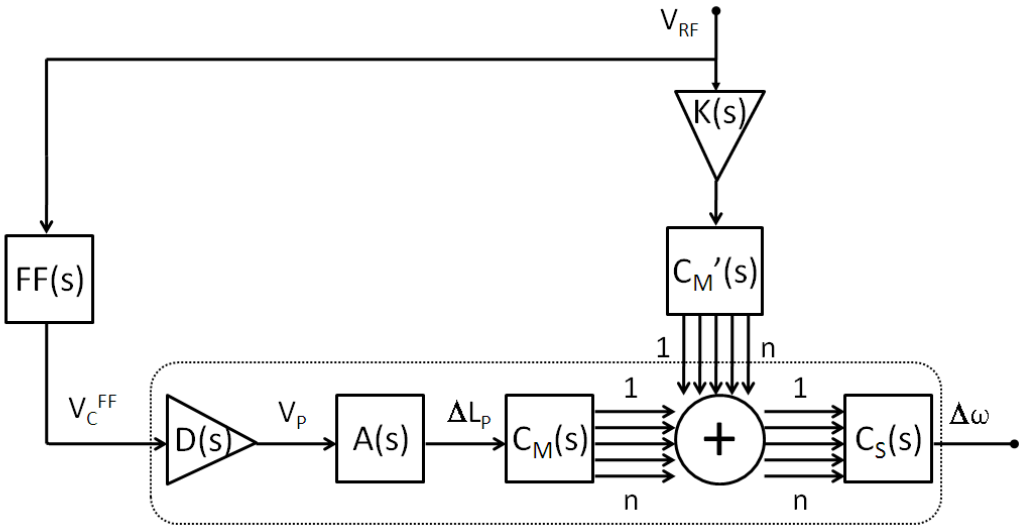

Fig. 4.18 – schematic representation of Lorentz force detuning and its feedforward compensation

It is evident that both the LFD effect and its compensation through piezoelectric actuators, separately act on the controlled variable $\Delta\omega$ through the cavity modes, modeled as two different mechanical transfer function $C_M(s)$ and $C_M'(s)$, thus determining the dynamic properties of both actions. The LFD, in particular, can be modeled as the simultaneous contribution of the excitation of different modes, each one with a different coupling expressed via the $K_{L\,k}$' coefficient. Up to 3 among main cavity modes are, for instance, considered for a correct fitting of LFD data [101] as a consequence of the

peculiar deformation induced by Lorentz forces. The dynamics of this cavity frequency control can be assumed as described by a State Space equation (see par. 4.1):

$$\dot{\bar{x}} = A\bar{x} + B\bar{u}$$
$$\bar{y} = C\bar{x} \tag{4.26}$$

Where the cavity detuning vector $\bar{x}$ includes all contributing n modes, A (n x n) is as usual the system dynamics matrix, B (n x m) is the input matrix and the control input vector $\bar{u}$ (1 x m) can be assumed as composed by the driving signals, V_{piezo}^{m}, one for each actuator included in the control setup. Signal $\bar{y}$ is the final measurement of the cavity detuning $\Delta\omega$ and it is computed from the output matrix C (n x 1). Finally, according to a general control theory result [27], it is possible to assume for the system to be controllable by means of the given control inputs if the its controllability matrix C_0:

$$C_0 = [B\ AB\ A^2B \ldots A^{n-1}B] \tag{4.27}$$

which has n rows and n·m columns has full rank n. This is equivalent to a linear independent finite coupling of the used fast actuators set to each relevant mechanical mode. For practical purposes the coupling factors should be of the same order of magnitude. This can always be guaranteed in principle by use of multiple PZTs. Experience gained so far on active LFD compensation with different actuators and tuner design, see also par. 5.2 and par. 6.8.3 for recent measurements, confirmed anyway that satisfactory compensation can be achieved using a single actuator acting, in contrast with the LFD, locally on the cavity edge and mainly on its length. This results in different but still effective coupling to the various cavity mechanical modes as compared to the Lorentz forces.

For what concerns the exact shape of the piezo driving pulse, several evidences from different sources exist, as for example from free cavity ringings (see par. 5.3.1), confirming that the dominant mode of TESLA resonator, excited by purely longitudinal compression, is typically placed in the range 200 to 300 Hz [101]. As already seen in par. 3.3.2, this is also completely coherent with the dynamic behavior of the LFD disturbance. Finally, the goal for the open loop compensation strategy for the LFD is just to generate a frequency linear drift with a maximum rate in the order of 1 kHz/ms (or 3 μm/ms) during the RF pulse time window. In order to achieve this goal, the chosen strategy has been to roughly replicate the kind of excitation provided by the RF pulse itself, so choosing a single pulse signal with about 1.3 ms rise time. Considering also that the capacitive behavior of the piezo actuators requires to avoid sharp transitions in the driving signal that would lead to undesirable current peaks, a single semi-sinusoidal pulse with a total time width of 2.5 ms is chosen as reference. If, for instance, once the maximum possible amplitude for the driving signal is reached and the resulting detuning slope is still not sufficient, its reference frequency of 200 Hz can be slightly increased, anyway achieving only small improvement (see for example analytical simulations in app. A). Very short pulses as well as significantly steeper rises in the driving pulse would not be in fact far more effective at all for LFD compensation purposes, since the cavity intrinsic mechanical dynamics would dump higher

harmonics included in the signal. This driving signal, with proper timing and amplitude, has been successfully used, among other tests, for the LFD active compensation in ACC6 and at CMTB facility (par. 5.2), ACC7 and for the first Blade Tuner cold test in CHECHIA (par. 6.8.3).

The option of successive harmonic pulses instead of a single half-sin pulse has been also initially considered to enhance compensation efficiency through a resonant amplification. The driving signal is, in this case, made up of few (typically up to four) sinusoidal sequential pulses of a frequency close to the cavity main mechanical mode and starts with larger time advance. This leads to a larger final cavity oscillation, if compared to a single pulse for a given piezo voltage, and can therefore make possible the use of a piezo stack with an inadequate stroke for a single pulse compensation. It has been anyway chosen to discard this option since it could lead to excessive cavity oscillations and finally to instability and beam losses. The presently installed piezo tuners provide in fact piezo stacks with higher margin in performance and the single pulse compensation has been therefore successfully used up to 36 MV/m.

The second wide set of dynamic disturbances have been introduced as microphonics detuning in par. 3.3.1. This detuning source is intrinsically stochastic and uncorrelated although its analysis allows to recognize some contributions, as for example the vibrations induced by vacuum pumps through cryogenic transfer lines. Therefore a closed loop feedback control system must be designed to approach microphonics active compensation and this leads to several additional issues if compared to the LFD case. Cavity detuning signal $\Delta\omega$ can be used as the error signal of the control loop.

Whenever for instance the reference scheme for detuning measurement in CW conditions applies (par. 3.1), detuning can be computed as the cavity phase error and therefore in this case it can be properly fed back to fast actuators according to the scheme in Fig. 4.19.

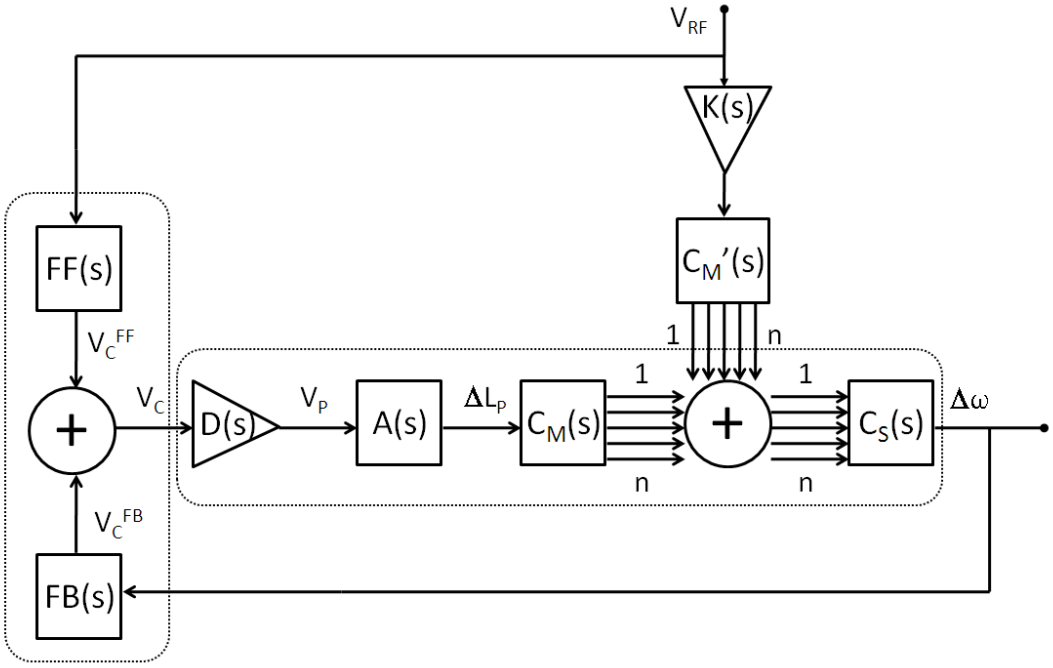

Fig. 4.19 – schematic representation of a simultaneous feedforward and feedback detuning control

The efficiency and the stability of the closed control loop must then be ensured with a dedicated regulator stage FB(s), that together with FF(s) completes the final detuning controller that simultaneously implements feedforward and feedback controls. Few experiences for this peculiar kind of vibration disturbances active suppression have been conducted so far, but successful proof-of-principle measurements exists relying on a digital FB(s) controller implementation in an analog loop. For instance closed-loop microphonics suppression with piezo actuators have been experienced both on a $\lambda/4$ superconducting cavity, although different from TESLA resonator, [102] and on a TESLA copper single cell at room temperature [19]. In both cases the loop controller stage FB(s) is represented by a Digital Signal Processor (DSP) board that implements sophisticated digital filter mainly used to notch out critical resonant frequency from the detuning signal spectrum. For example, Fig. 4.20 shows the analytical model of the loop gain transfer function that has been created from experimental data collected for the $\lambda/4$ test[28], before and after the design of the loop controller. In that case the controller was realized with a digital notch filter followed by an analog filter/amplifier stage (low pass filter with 100 Hz bandwidth and amplification factor of 10). Stability of the final loop is ensured by the Bode criteria.

[28] This analytical modeling has been recently done, after the actual test in INFN – LNL laboratory, for didactic purposes and in order to highlight the effect of the digital controller inserted in the loop.

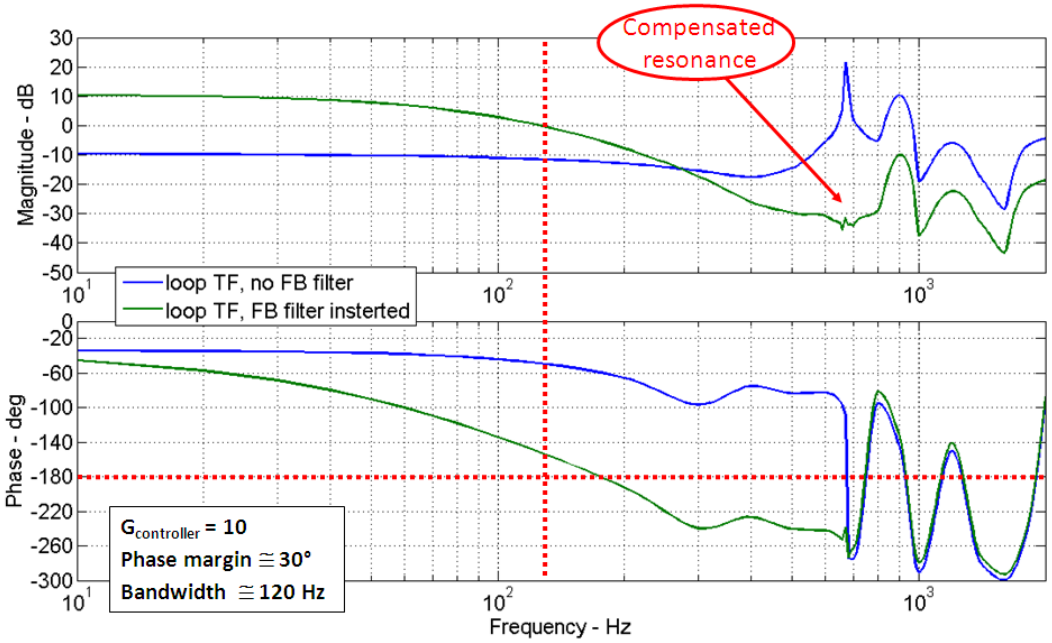

Fig. 4.20 – analytical model of loop gain transfer function for the CW active microphonics suppression of λ/4 cold test at LNL [102][103]

Currently, a different strategy is under development in sight of CW operation of TESLA cavities at BESSY and it is based on the recognition of amplitude and phase of those few frequencies in the microphonics disturbance that bear the larger contribution to the overall detuning [63]. The counteracting signals to piezo actuators are then digitally synthesized with the same frequency but with opposite phase so to cancel the corresponding component in the microphonics. This control system is actually still open loop although frequency recognition can be performed from time to time in order to make the entire process adaptive to slow drifts over time.

For the final implementation in a pulsed linac this classical CW approach to automatic microphonics compensation must be reviewed and redesigned as fully dynamical control (i.e. stationary state control techniques do not apply). In this frame, this actually means to improve accurateness of the actual detuning control, only based on the feedforward counteraction of LFD, including real-time feedback corrections to suppress even the small stochastic oscillations of cavity detuning observed from pulse to pulse. Cavity detuning can be monitored during the RF pulse time window, according to the procedure illustrated in par. 3.4.1. It is anyway mandatory to achieve a real time computation of cavity detuning from RF power probes. A proposal solution in order to accomplish this task is presented in the following paragraph. Finally, detuning data would be used inside a fully digital control system that also integrates the feedforward LFD control, according to the scheme in Fig. 4.21.

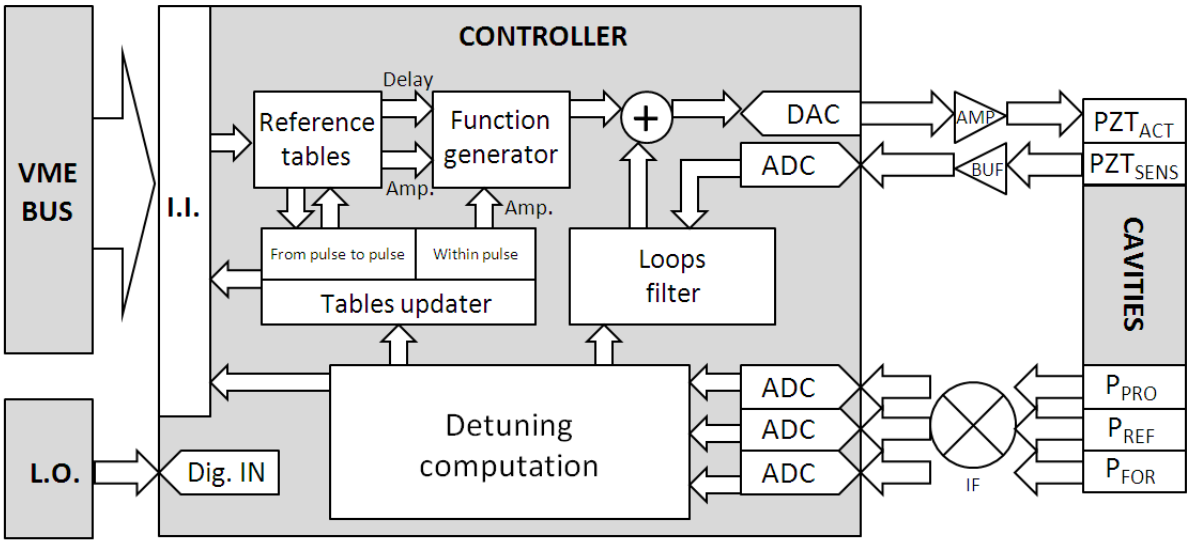

Fig. 4.21 – complete schematic view of the final detuning controller for TESLA cavities in pulsed operations

It is for example possible to assume that the reference sinusoidal shape for the piezo driving pulse is coded in the feedforward table while its final amplitude and time advance parameters are set by the controller. Further details concerning the possibility to successfully control cavity detuning only through amplitude and delay of a fixed pulse shape are given in par. 5.2 and app. A. (see also [28]). The complete cavity tune control system emerging from the schematic representation in Fig. 4.21, would allow to introduce innovative features for the suppression of the detuning during the RF pulse:

- pulse to pulse correction of amplitude and advance of the piezo pulse for the LFD compensation, according to the actual detuning data previously computed. This option could exploit the relatively large time available between pulses in order to complete more complex computations as for example detuning data fitting. A prototypal approach, based on the amplitude parameter of a multi-sinusoidal pulse, has been already successfully tested [28].

- intra-pulse correction of the amplitude of piezo pulse according to the actual detuning data computed during the same pulse. This would not introduce a great improvement due to the significant loop delay that is present in the given feedback loop, completely dominated by the time needed to the mechanical perturbation induced by piezo to propagate up to the final cavity detuning. By different means this delay has been evaluated as about 0.4 ms, as for instance shown in par. 5.3.1 and app. A (and also in [104] among others). Since the time advance of the piezo pulse is set, feedback loop could in principle operate a real-time correction of its amplitude during the pulse, this effect could eventually be positively felt by the cavity when operating with the longer, 1 ms flat-top, pulses foreseen for ILC.

- advanced intra-pulse amplitude correction for a true microphonics compensation involving the signal from a second piezo stack, used as a displacement sensor. Introducing

in the controller design a calibrated piezo-to-piezo feedback loop would eventually allow to monitor and control cavity stochastic detuning indirectly but almost continuously in time, or at least for a given time window before the RF pulse. This control would be eventually superimposed to the piezo pulse already used for the LFD compensation and could in principle lead to the optimum suppression of microphonics oscillations.

The complete controller proposed has not been yet realized and validated. It can be anyway considered as the final goal for the currently ongoing research activity on this topic. Key components needed in the final controller design have been separately developed and tested, this activity and its results so far are reported in the following paragraph.

4.5.2 CONTROLLER CODE COMPONENTS DEVELOPMENT AND TEST

Detuning control strategies presented in the previous paragraph highlighted the features that the final design of a complete digital detuning controller must provide. Namely:

- an advanced pulse signal generator for LFD open-loop compensation purposes.
- real-time cavity detuning computation.
- acquiring and recording of the signal from the spare piezo used as a sensor.
- digital filter to ensure stability to the eventual closed feedback loop.

Prototype VHDL routines for these components have been separately developed and the corresponding experimental tests, recently performed, are reported in this part of the dissertation.

The FPGA SIMCON 3.1 electronic equipment, already developed for the implementation of LLRF controller and described in par. 4.2.2, grants good A/D connectivity and computational performances, so it has been chosen for the implementation of the detuning controller components. This also corresponds to the choice of use homogeneous electronics in view of the final integration of all cryomodule control (LLRF, piezo, stepper motors) and cost reduction.

In 2006 the author and his group at LASA laboratory starts collaborating on this topic, in the frame of a collaboration with DESY and K. Przygoda and P. Sekalski from TUL, Poland [142]. In particular, a complete and functional FLASH LLRF electronic unit has been installed at LASA, this equipment is composed by:

- VME standard EURO crate.
- Universe II chip based VME-BUS controller, equipped with SPARC CPU and Sun Solaris 2.5 OS installed on an external SCSI drive.
- SIMCON 3.1L FPGA board.

The facility is then completed by JTAG connections and VHDL code programming software for both XILINX and ALTERA FPGA chips[29]. The complete assembly is presented in Fig. 4.22.

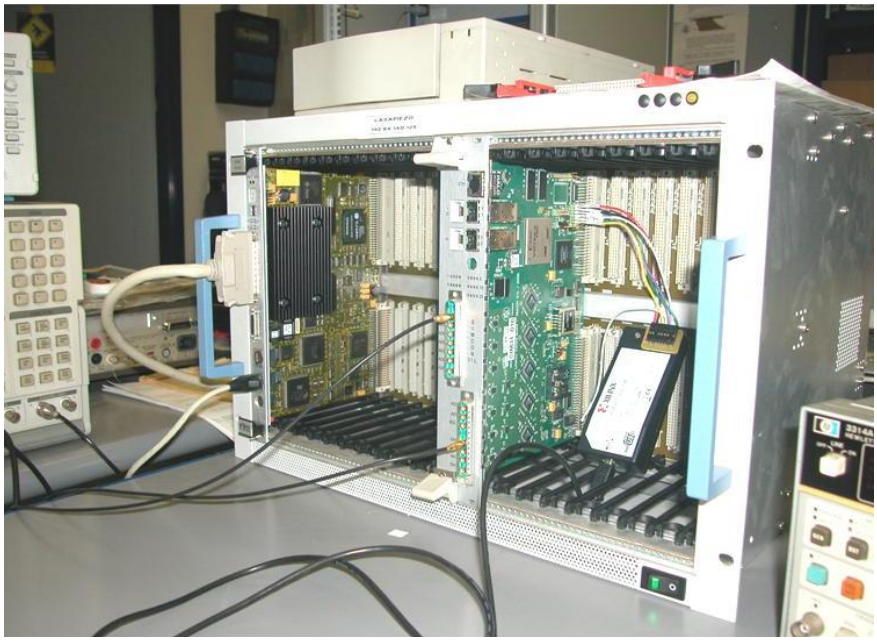

Fig. 4.22 – complete FLASH LLRF subunit installed at LASA, hosting a SIMCON 3.1 FPGA board

A VHDL code for a programmable custom signal generator has been firstly developed by the author and tested. Guidelines for the definition of requirements for the final algorithm have been chosen according to the actual LFD compensation needs and characteristics. After some prototypical version of the code, separately developed and tested both at LASA and at TUL, a final algorithm has been jointly implemented in view of the cold module #6 (ACC6) tests at the CMTB facility, DESY. Its main features at the moment of last ACC6 tests were:

- small resources usage, only about 1 % of the logic resources of Virtex2Pro 30 FPGA chip. In addition, digital input #1 is used for incoming repetition rate trigger signal and all 4 DAC to output the pulse signal.

- sinusoidal signal generation. Fixed sinusoidal shape with real time tunable parameters as number of pulses, delay from the trigger, amplitude, frequency and offset.

- command line user interface to the code. A C++ script runs on the SPARC CPU VME-BUS controller and communicates with the FPGA board through VME bus using the Internal Interface (see par. 4.2.2) [84]. This interface grants real-time and remote access to all the algorithm parameters since the VME-BUS controller is accessible via Ethernet connection.

[29] Mainly ISE Foundation 8.2 from XILINX, MATLAB from The Mathworks and DSP System Generator from XILINX

Finally, this VHDL code, implemented on a spare SIMCON 3.1 board available in the LLRF rack of CMTB facility, has been successfully tested on ACC6 (chap. 5). The code has been successfully used to generate driving piezo signal during almost all the LFD compensation measurements performed [105]. An example of generated piezo driving signal is shown in Fig. 4.23.

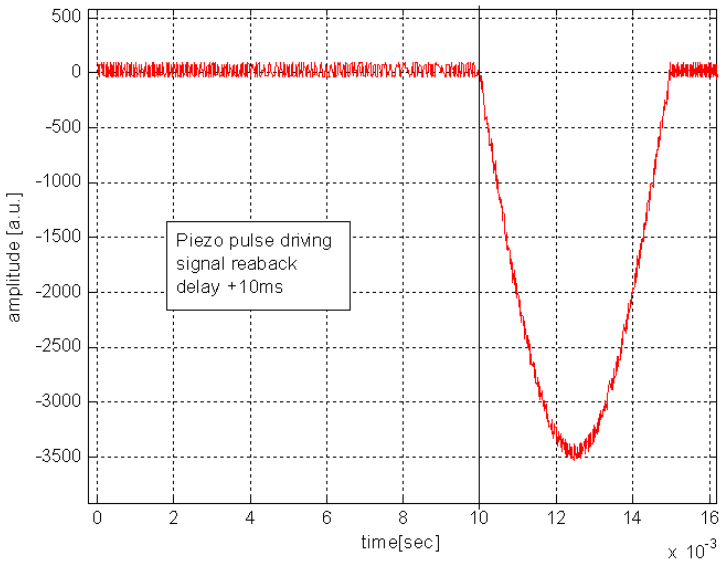

Fig. 4.23 – example of piezo driving signal with custom delay generated with the developed VHDL code

Further developments for this pulse generator VHDL code are currently ongoing, mainly concerning the generation of multiple independent signal outputs (up to 4 for SIMCON 3.1) and the realization of an advanced user interface to the algorithm. An 8 channel setup, including piezo amplifier and signal generator for each channel, has been successfully tested by DESY LLRF group on ACC6 in FLASH [106].

Cavity detuning real-time computation is based on the electromagnetic model of the cavity resulting in formula (2.36) (already introduced in par. 2.1.2):

$$\Delta\omega = -\frac{1}{2\pi}\left(\frac{d\phi_{probe}}{dt} - 2\omega_{1/2}\frac{|U_{for}|}{|U_{probe}|}\sin\left(\phi_{for} - \phi_{probe}\right)\right) \tag{4.28}$$

where U_{for}, U_{probe}, ϕ_{for} and ϕ_{probe} are the magnitude and phase of forward and cavity probe RF power signal respectively and $\omega_{1/2}$ is the cavity bandwidth. The corresponding VHDL implementation [107] is therefore realized through several successive stages according to the scheme in Fig. 4.24.

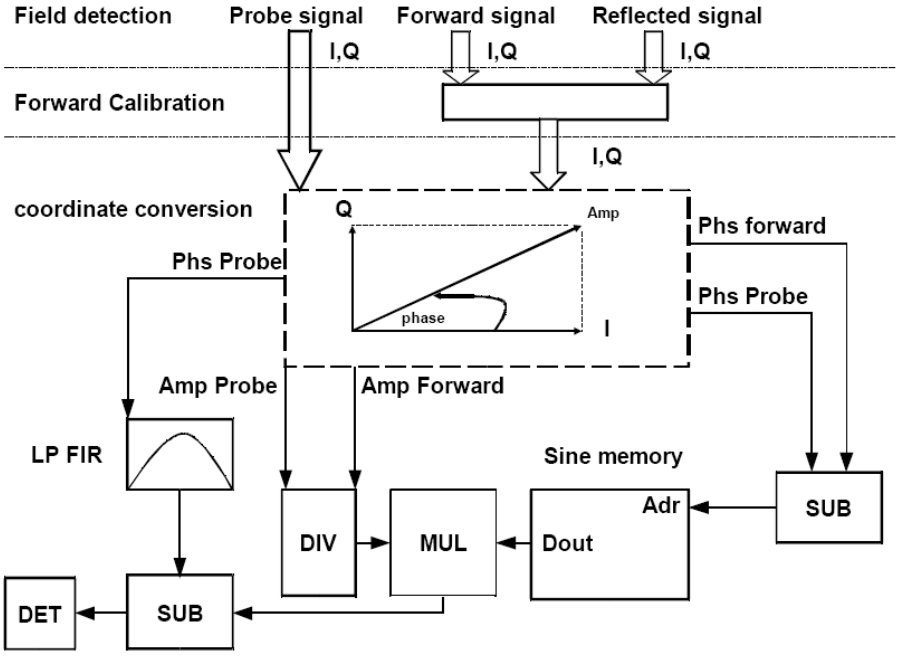

Fig. 4.24 – schematic representation of detuning calculation VHDL implementation

As for LLRF controller, the input signals from RF power probes reach ADC's after down-conversion to 250 kHz intermediate frequency (IF) via nonlinear mixers. Therefore sampling of IF with a sampling rate four times higher gives four samples per cycle. Therefore, two consecutive samples represent a real and imaginary parts of probe, forward and reflected RF power signals. The signals from ADC channels are demodulated using I (in-phase) and Q(quadrature) field detectors. Forward and reflected signals are then properly combined to eliminate cross-talks. This procedure implies a cross multiplication between forward and reflected signals using 4 weighting coefficients named a, b, c and d [69]. Phase/amplitude detector cores[30] are used to obtain phase and amplitude from IQ data (coordinate conversion from cartesian to polar). The amplitude and phase signals are combined together to calculate final detuning value. Dual-port RAM memory block was added for sine values interpolation. The derivative of the probe phase signal is then computed via a proper 32 taps FIR (Finite Impulse Response) filter. Actually the whole system is synchronized using external trigger and strobe signals. The first one informs FPGA that new RF pulse is filling the cavity, it is a 1 μs width square pulse with repetition rate between 2 and 10 Hz. The second one is used for validation of incoming samples from external down-converter and its repetition rate is 1 μs. This code has been developed at TUL by K. Przygoda and colleagues and successfully tested with actual RF power probes data stream during ACC6 and subsequent ACC7 tests in CMTB. For instance, the

[30] Common code cores for polar coordinate detection have been used, they are based on Cordic algorithm and represent a flexible but logic area consuming option.

resulting detuning over the flat-top for cavities 1, 2 and 3 of ACC7 is showed in Fig. 4.25 [105].

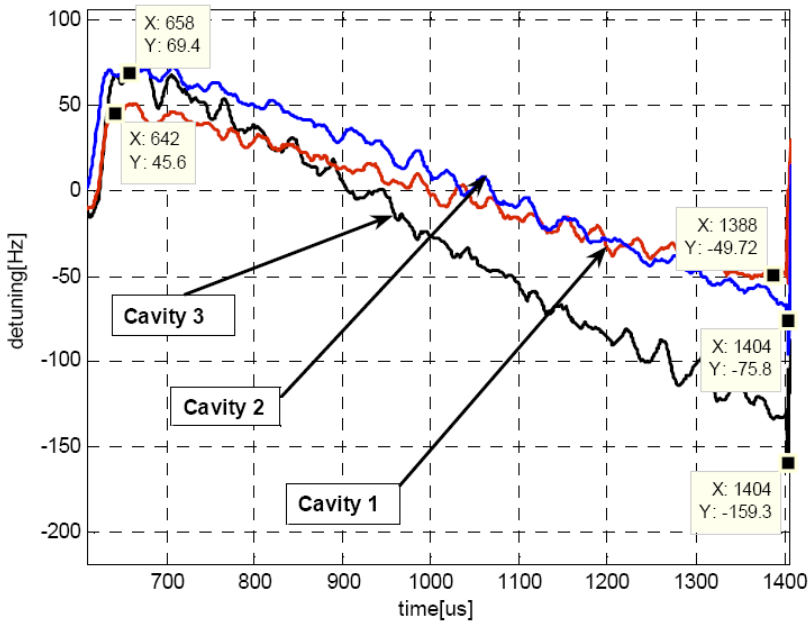

Fig. 4.25 – flat-top detuning of cavity 1, 2 and 3 of ACC7, real-time computed on a SIMCON 3.1 FPGA board

Implemented detuning calculation module so far consumes around 60% of all Virtex2Pro 30 FGPA logic resources. Actually conversion from Cartesian to polar coordinates is the most critical issue for this design and therefore different implementations of this features are under studying to decrease timing and accuracy of the computations. According to this resource consumption, the final design should foreseen the use of 2 SIMCON FPGA boards so that one is fully dedicated to fast detuning computation; optical links provided can handle high data rate communications between boards.

The code for a custom data acquisition (DAQ) feature has been also introduced by the TUL group and then jointly improved and tested during ACC6 tests in CMTB. It uses the provided external DRAM memory chips and it is designed in order to acquire and record signal from sensor piezo stack in the most flexible way using SIMCON board ADC input. The DAQ code finally developed for the ACC6 tests was featuring:

- command line user interface to the code. As for signal generation, a C++ script runs on the SPARC CPU VME controller and communicates with the FPGA board through VME bus and Internal Interface.

- custom number of acquisition channels, up to 10.

- fixed data buffer length of 32500 samples. This values can be eventually modified so to accomplish for different needs, it has been initially chosen as the best trade-off between data analysis needs and resource usage.
- data recording start is synchronized to the board main external trigger, and therefore to the repetition rate.
- custom sample rate or buffer time length. Default value for the sampling frequency is 100 kHz.
- recorded data are saved remotely in a TXT file.

Several data were recorded during experimental test sessions using the proposed DAQ code and used by the author for proposal cavity mechanical investigation, as for instance for the cavity ringings analysis reported in par. 5.3.1 (See, as a reference, Fig. 5. 21 and Fig. 5.25).

Finally, the author explored the feasibility of a VHDL implementation of complex digital filters exploiting the features of the SIMCON 3.1 hardware unit installed at LASA. As already introduced, low pass filtering or dumping of selected critical frequencies could eventually be required when aiming to a stable detuning or piezo-to-piezo feedback loop. Therefore a State Space based (see par. 4.1) VHDL coding has been realized, keeping as a guidelines the minimization of FPGA logic resources used. It is based on iterative accesses to a single 32 bit width, fixed-point architecture, multiply-and-accumulate (MAC) subunit. As usual for FPGA implementation, the maximum achievable clock frequency for the given architecture determines the final sample rate of the filter. Lastly, a MATLAB based user interface running on VME-BUS controller allow to configure by remote the filter algorithm via Internal Interface and to download filter coefficients. A schematic representation of the resulting design is given in Fig. 4.26, only about 7 % of the Virtex2Pro 30 logic resources are required.

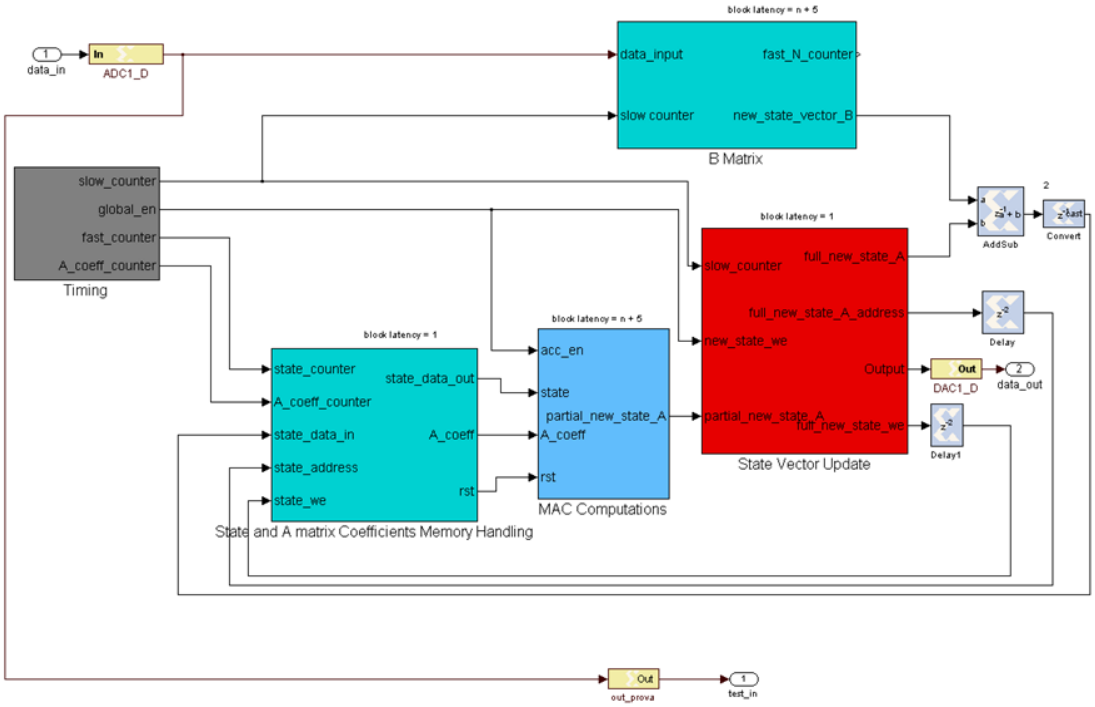

Fig. 4.26 – schematic representation of State Space filter VHDL fully sequential implementation

The developed code has been then implemented and tested with the SIMCON electronic equipment installed at LASA. For example, an 10^{th} order test filter has programmed, then the transfer function between SIMCON board DAC and ADC has been measured with a signal analyzer and compared to its analytical model. Both plots are reported in Fig. 4.27.

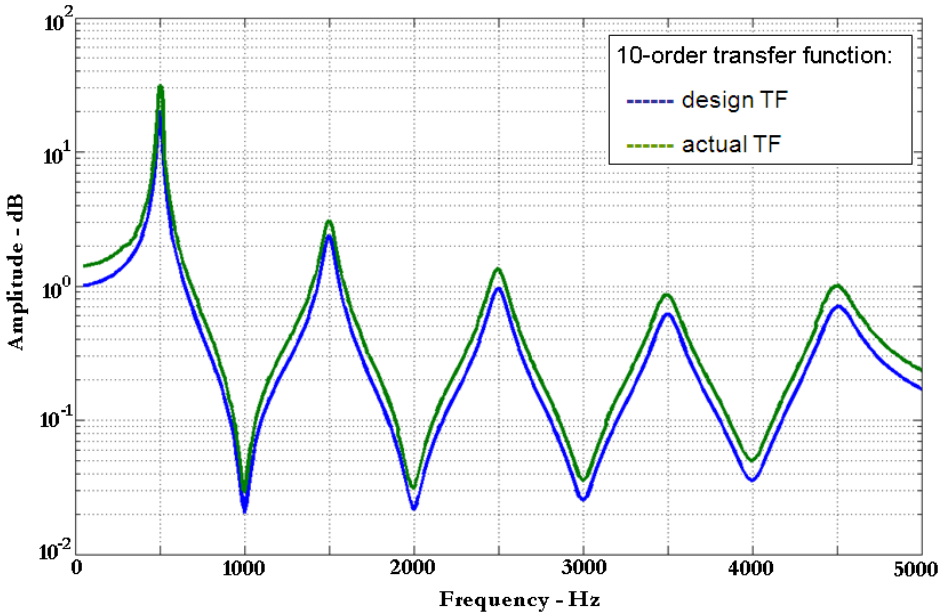

Fig. 4.27 – measurement of an 10th order filter transfer function and comparison with its analytical model

The dependence of the resulting filter sampling frequency from its order has been investigated for the presented VHDL architecture. Results are collected in Tab. 4.4.

State Space Order	**Sampling frequency** [kHz]
64	20
32	100
16	300

Tab. 4.4 – maximum achievable sampling frequency for the VDHL filter implementation of Fig. 4.26

Even for this extremely sequential design, raw results in term of computational capabilities are extremely higher than previously experienced prototype based on DSP processor [19][108] and fully satisfactory in view of TESLA cavities fast tuning needs. It can be considered, as a reference, that a 32nd order filter transfer function would allow to digitally reproduce in great details, or even perfectly compensate for, the dynamic behavior of the detuning variable of TESLA cavity as expressed by its piezo-to-RF transfer function [109]. Anyway fixed-point FPGA structure, although not critical, affects and limits the final filter accuracy if compared to floating-point DSP results; VHDL floating-point emulation cores are available but significantly affect chip area consumption, this option could be anyway considered for incoming revisions of SIMCON hardware hosting more performing FPGA models.

5 EXPERIMENTAL RESULTS ON FLASH MODULE ACC6

From December 2006 to March 2007, DESY FLASH module #6, or ACC6, has been installed for validation testing in the CryoModule Test Bench facility (or CMTB, see par. 1.4). ACC6 is a Type-3 cryomodule (see par. 1.3) assembled in 2006 and equipped with 8 TESLA cavities from two different manufacturer, cavity 1 to 4 from Accel [55], cavity 5 to 8 from Zanon [54] (see par. 2.1.2).

Particular interest was related to the detuning compensation performances of this installed cavity tuning equipment. All 8 cavities were equipped with a TTF tuner (see par. 3.2 and 4.4.4) and for the first time each of those has been equipped with two "2nd generation" piezo actuator, the PI-888 from Physik Instrumente (PI_36) (Tab. 4.3), after several former tests performed just with EPCOS_30 actuators. Piezo actuators installed in each tuner fixture will be further on referred as piezo 1 and piezo 2.

Main goal for the activity on module #6 has been chosen to be the experimental verification of the whole module reliance after at least 10 complete thermal cycle. Therefore the module has been hosted in the facility for long time allowing the possibility to perform several measurements concerning piezo activity and detuning compensation, during three separate test sessions. The former one took place from December 18th to 21st, 2006, then later sessions from January 26th to February 3rd and from February 23rd to 27th, 2007.

On March 2007, module ACC6 has been uninstalled and later on operated on-line in FLASH. Overall results from the test sessions performed on detuning compensation and data analyses are reported in this chapter.

5.1 PIEZO PULSE TIMING ANALYSIS

In order to understand the influence of the timing parameters of the single pulse piezo compensation, a detailed analysis has been performed on module #6 concerning the effect, on cavity detuning, of the advance in time that is set for the piezo pulse, relative to the RF pulse start.

The whole LLRF system of the CMTB, from processing to diagnostic, relies on an high stability external master oscillator (MO) that provides the reference repetition rate trigger signal, usually among 2, 5 or 10 Hz. Then, as previously described in par. 4.5.2 a channel with independent delay or advance from this master oscillator has been provided

for piezo actuator, while the RF pulse start time is kept as fixed[31]. The simple reference scheme is now shown in Fig. 5.1.

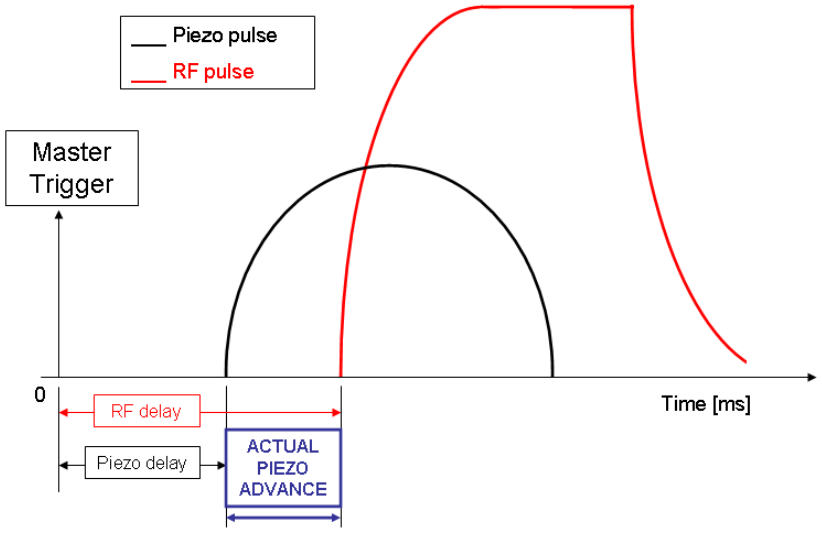

Fig. 5.1 - scheme of the pulses timing for the CMTB measurements

As said above, an analysis of the sensitivity of the whole setup to the timing of the piezo pulse has been performed, applying on the piezo, for safety reason, a signal with an amplitude limited to 10 V. This was just to avoid excessive cavity deformation when the pulse would be set, as expected for this measure, in the "out-of-phase" condition (see appendix A) when the piezo action increases the cavity detuning during the flat-top instead of compensates it. The advance was swept around in a range of few ms and the absolute value of the detuning over the flat-top has been recorded. This measurement has been repeated 3 times with different cavities at 20 MV/m gradient, the resulting data have been summarized in Fig. 5.2. In order to be coherently plotted, since each cavity shows a different sensitivity to detuning, those data have been scaled so that the value of the detuning showed by the cavity without any piezo pulse applied is fixed to unity.

[31] Advance for the piezo pulse was itself limited by the start of RF pulse that was fixed at +2.45 ms from MT, therefore for an advance higher than that a delay is set equal to (rep. rate period) – (wanted advance).

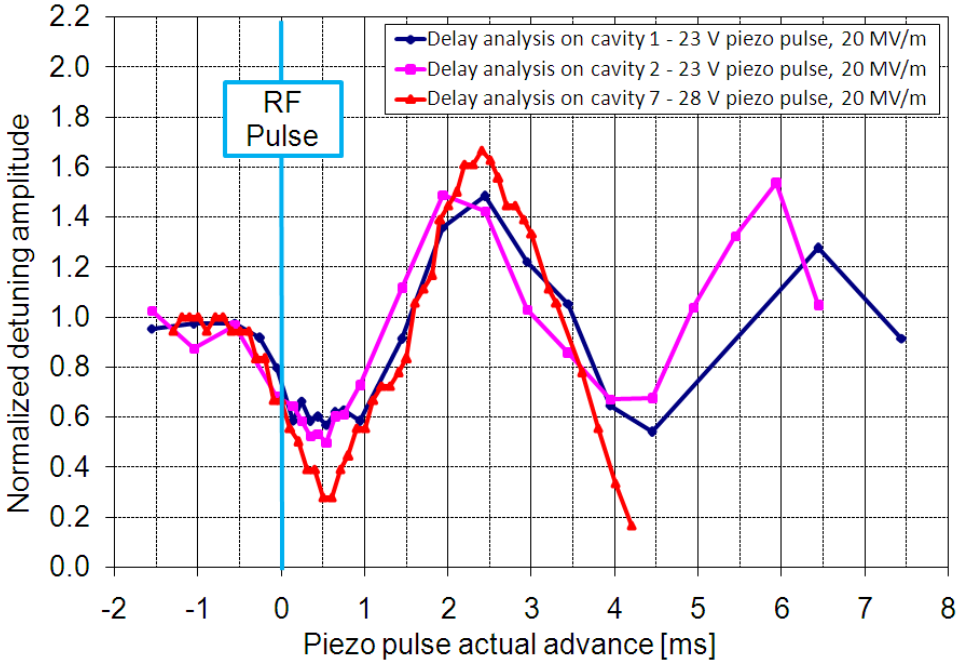

Fig. 5.2 - normalized absolute value of the detuning over the flat-top vs. piezo pulse actual advance

The plot reveals some meaningful aspects and it is completely coherent with expectations. Considering both the theoretical and analytical approaches presented (par. 3.3.2 and app. A respectively), it is expected to observe both compensating and un-compensating effect as a result of a shrinking or expanding slope in the cavity oscillation. When a sufficiently large delay is set for the piezo timing, that is here represented as a negative advance time, the result is that the RF flat-top ends before the start of the piezo pulse, therefore it is expected that detuning approaches the piezo-off value since the piezo action in no more useful at all. Both effects are clearly visible in Fig. 5.2, the latter in particular at the left end of the plot.

A first clear detuning reduction is visible when the advance of the piezo pulse is around 0.6 ms. It is also important to underline that this value can be positively compared to the mechanical propagation time from piezo to detuning, that has been later on estimated in 0.4 ms (par. 5.3.1, appendix A).

Deeper analysis of these results showed that an exact value of *0.64 ms* timer advance can be regarded as the optimum choice for LFD detuning compensation for the three investigated cavities. This first compensation setting will be kept as the first choice for LFD tests and it will be further on referred as "*1st oscillation compensation scheme*" to designate the choice to use the first cavity oscillation induced by the piezo pulse for LFD compensation.

As expected, a second detuning reduction effect is also visible at higher advance time, around *4 – 4.4 ms*. This case perfectly is accordingly referred as the "*2nd oscillation compensation scheme*". This situation is related to the fact that the cavity actually continues to

oscillate after RF and piezo pulses so that a new useful deformation slope can be expected after a complete oscillation. This situation is clearly highlighted in simulations presented in app. A.

Finally, when the wrong slope of the cavity oscillation is synchronized to the RF pulse, the effect is an increasing of the detuning as compared to the piezo-off value. These are usually referred as *"out-of-phase"* conditions.

5.2 LORENTZ FORCE DETUNING COMPENSATION

5.2.1 1ST OSCILLATION COMPENSATION SCHEME

During module #6 tests in CMTB, several LFD compensation measurements have been performed and each cavity have been operated correctly at the maximum achievable gradient. For the former two test sessions only basic feedforward control was available for the SIMCON 3.1 klystron controller[32]. It has been anyway possible to properly set the LLRF controls with a stable closed feedback loop in time for the last test session on module #6. Results from this session are then reported in the last paragraph.

For all reported measurements, the same pulse shape has been used. As previously discussed in chap. 4.5.1, the driving signal has been a *single half sinusoidal pulse 2.5 ms width*.

During the first measurements session a first compensation has been achieved on cavity 3 using results from the timing analysis just shown. Here results are shown.

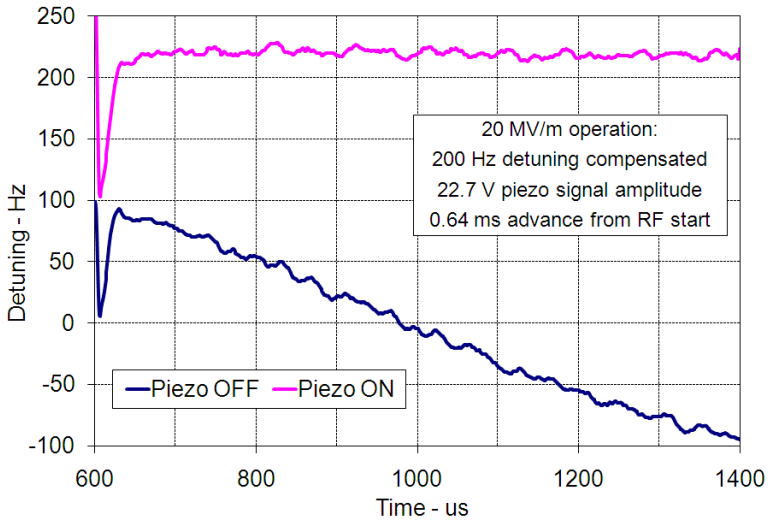

Fig. 5.3 - best LFD compensation result on cavity 3. Details of the used piezo pulse are reported.

[32] This open-loop control on the klystron has been set from the beginning since it's needed for basic pulsed RF tests; closing the RF feedback loop must instead be scheduled in advance since it requires much more time to be put in operation due to the calibration of each channel of the vector sum.

Then, in order to verify differences among cavities, these piezo pulse settings have been applied without changes to all the other cavities in the module. Results in terms of the absolute value of cavity detuning are resumed and shown in Fig. 5.4, they confirmed that the same timing setting can actually be useful, although not optimal.

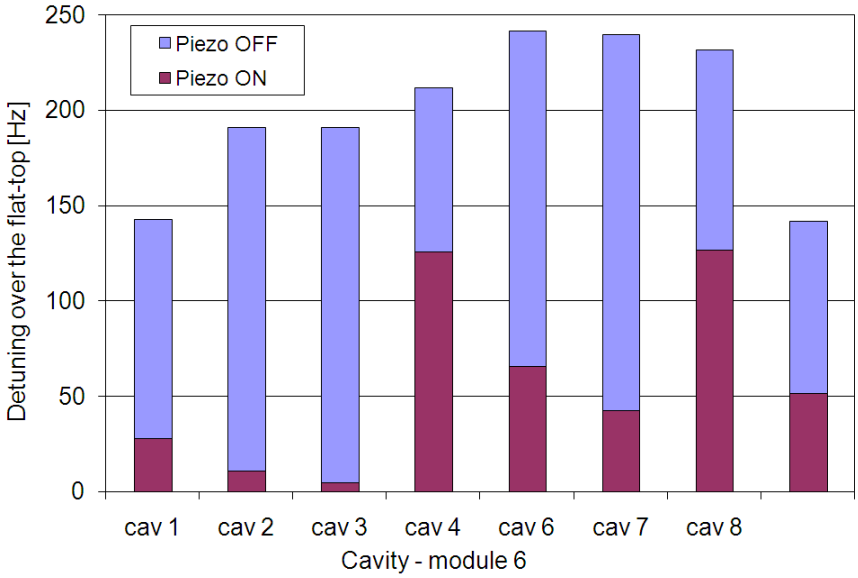

Fig. 5.4 – LFD compensation results when the best pulse for cav. 3 is applied to all cavities at 20 MV/m

Later, obtained results have been used as the starting point for the second test session, where each cavity has been analyzed individually, searching for each specific pulse best settings up the optimum compensation. Moreover the stepper motor position has been set as needed during measurements, so to keep the static detuning as close as possible to zero in any configuration. This is mainly needed for keeping cavities far from quench and at higher gradient simultaneously. It is moreover important to avoid significant lowering of the gradient during the RF pulse otherwise the measured dynamic detuning will be smaller than the actual value.

Moreover, during the second test session, so after 7 complete thermal cycle of the module, two major problems with piezo elements were shown. Piezo 1 of cavity 4, marked as actuator, was completely not responding probably due a failure in the cabling, since both static capacity and impedance are not measurable. Piezo 2 in the same fixture has anyway been used as actuator for that cavity. Instead piezo 1 and 2 of cavity 5, even driven with correct voltage, led to very small response by the cavity. Since those piezo were unfortunately not useful at all for active LFD compensation, cavity 5 was then excluded from further analyses. This has been the first evidence of the effect of successive thermal cycles, in fact the reason was actually found in the critical loss of piezo preload in cavity 5 fixture over time, if compared to the first cooldown configuration, that led to a poor coupling of actuators to cavity[33].

[33] This issue has moreover found confirmation in the historical plot of stepper motor position that reveled a long-time drift in the cavity on-tune position.

All results have been summarized in Tab. 5.2 at the end of the paragraph. Results for the highest gradient for each cavity are highlighted (bold). Some other values, displayed in *italic*, refer to intermediate gradients and corresponding detuning has not been completely compensated on purpose since it has been chosen to rather focus (so spend time) on the top gradient measurement for that cavity.

In order to have a visual feedback of the results, the compensated detuning over the flat-top in each cavity at the maximum gradient condition is here considered. In Fig. 5.5 results for the absolute value of cavity detuning, with and without piezo compensation, are summarized as an histogram.

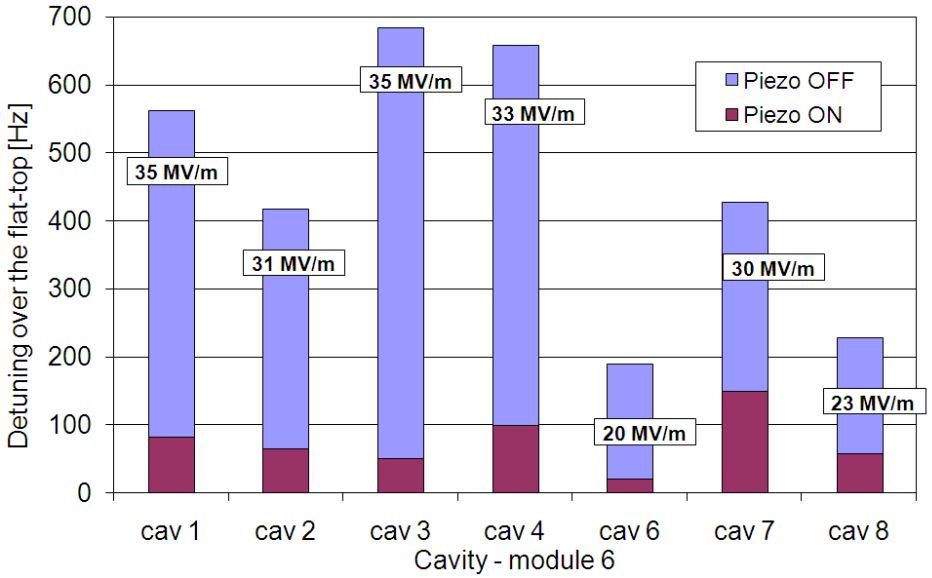

Fig. 5.5 – shown detuning with and without proper piezo pulse settings for each cavity, 1st osc.

Compensating performances vary significantly from cavity to cavity, as a function of individual cavity stiffness and sensitivity to LF detuning. Considering the most sensitive cavity, cavity 3, it can be seen that more than *630 Hz of absolute detuning over the flat-top have been compensated with 78 V pulse on the piezo*. The resulting effects of this active compensation can be seen in the cavity detuning and forward RF power plots that are shown in Fig. 5.6 and Fig. 5.7.

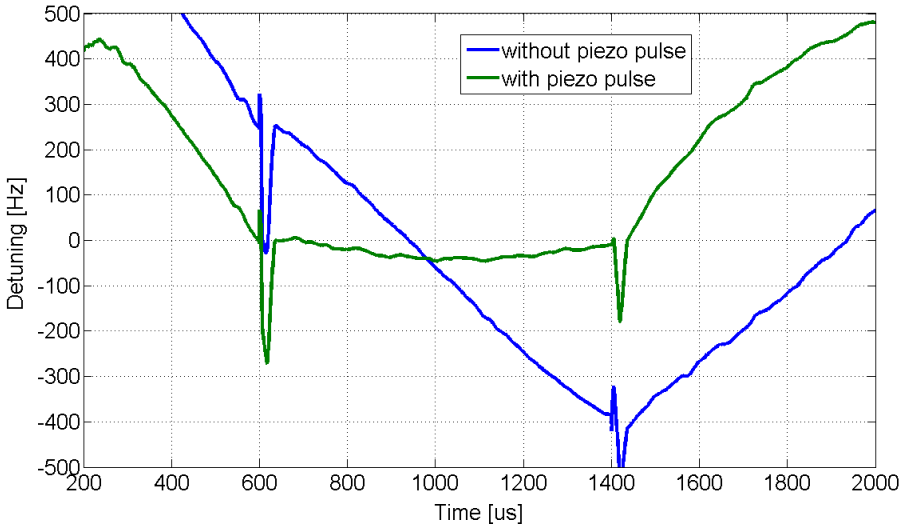

Fig. 5.6 – detuning of cavity 3 in Module #6 at CMTB, operated at 35 MV/m

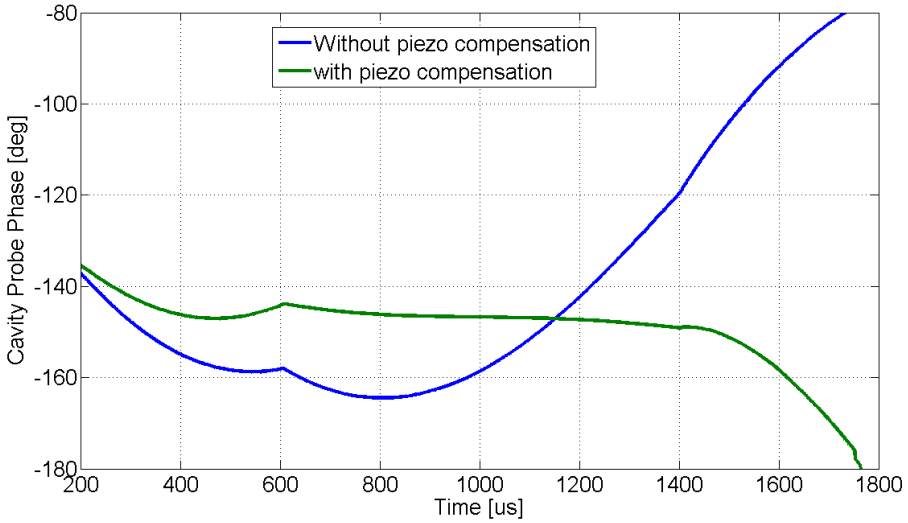

Fig. 5.7 - cavity 3 in Module #6 at CMTB, phase of the forward RF power signal.

These last two plots clearly confirm how the active counteraction from the piezo actuators helps significantly in keeping the cavity on tune, almost zeroing the detuning while keeping the field phase almost flat over the pulse.

The amount of absolute detuning compensated in each cavity has been moreover linearly interpolated as a function of the amplitude of each applied piezo pulse, while using the same pulse shape. Plots for every cavity are now shown, and obtained linear interpolation coefficients have been summarized in. Tab. 5.1.

.

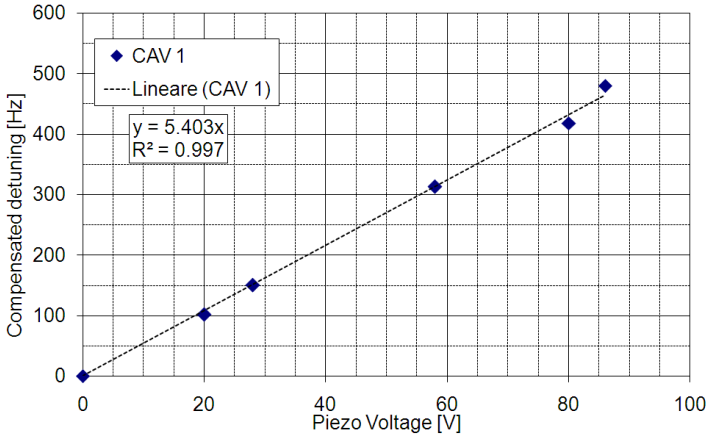

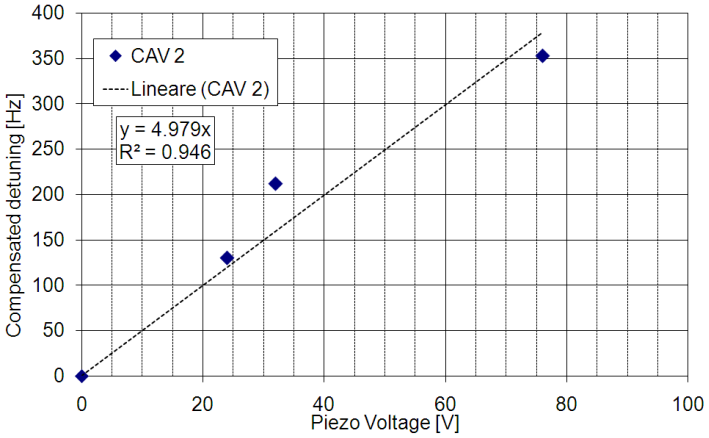

Fig. 5.8a and 5.8b – compensated detuning vs. piezo driving voltage for cavities 1 and 2

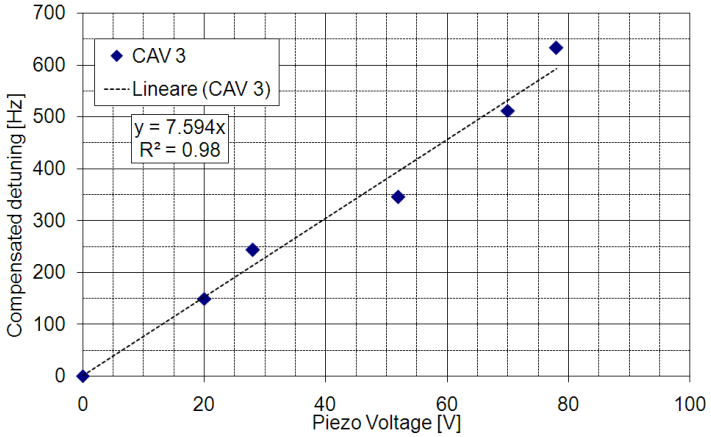

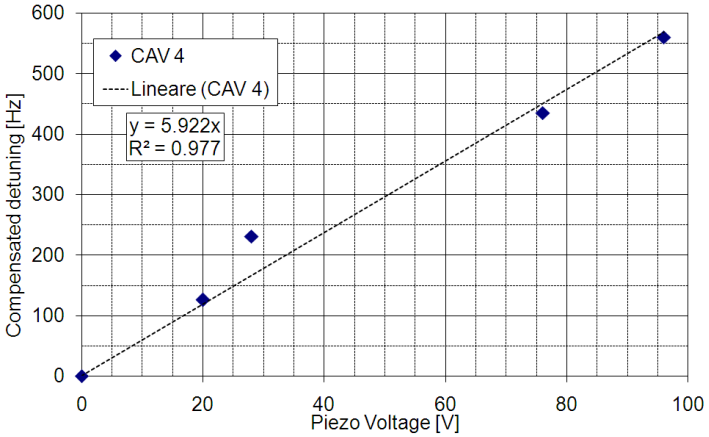

Fig. 5.9a and 5.9b – compensated detuning vs. piezo driving voltage for cavities 3 and 4

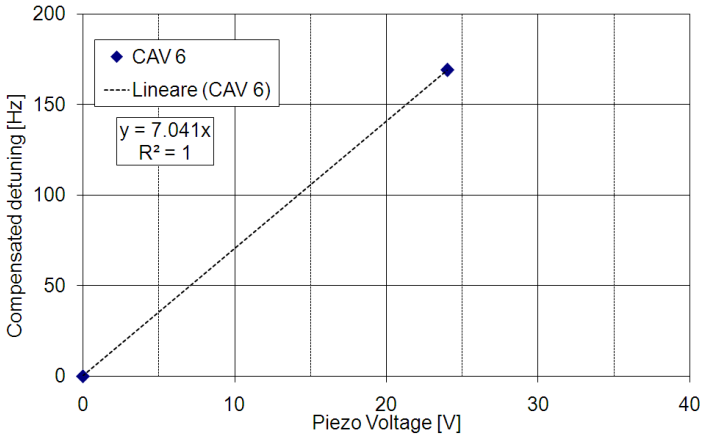

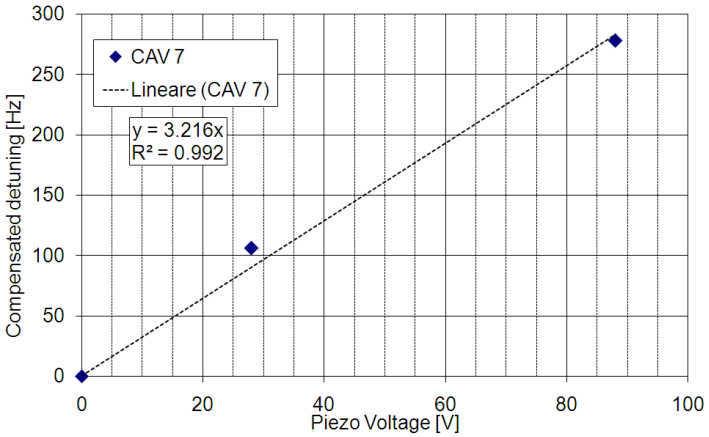

Fig. 5.10a and 5.10b – compensated detuning vs. piezo driving voltage for cavities 6 and 7

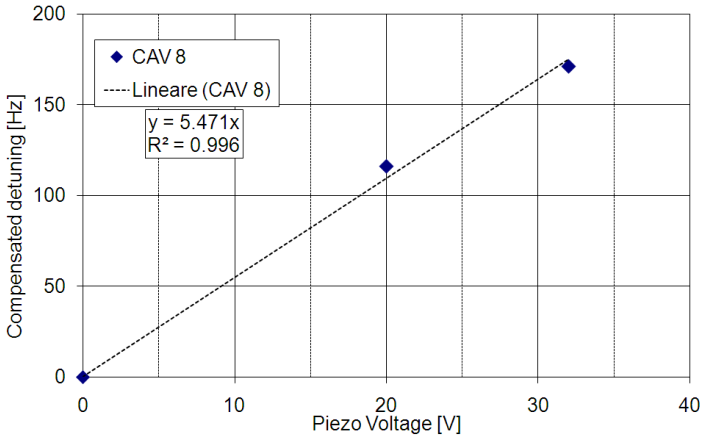

Fig. 5.11 – compensated detuning vs. piezo driving voltage for cavity 8

Fig. 5.8 to 5.11, resulting fit coefficients	
y	**r^2**
5.4	0.997
4.98	0.946
7.59	0.98
5.92	0.947
7.04	-
3.22	0.992
5.47	0.996
Avg.: 5.78 Hz/V:	
Dev. Std.: 1.4 Hz/V:	

Tab. 5.1 - collection of resulting fit coefficients from previous plots

The linear dependence of the compensated detuning over the flat top actually found very good agreement to a linear function of the amplitude of the applied piezo pulse. This can be a key issue in sight of an automatic and adaptive detuning control system and it has been already considered for a proof of principle measurement [28].

Collected data also allow an additional analysis. When the proper piezo pulse is applied to the cavity under test so to compensate the dynamic detuning over the flat-top, an additional static detuning is superimposed as expected. This has been compensated properly driving the stepper motor position. This detuning contribution is always in the increasing frequency direction and it is varying from cavity to cavity as a function of the individual sensitivity to mechanical detuning. Fig. 5.12 shows aggregate results for module #6 and one more time confirms that cavity 7 actually revealed the lowest sensitivity.

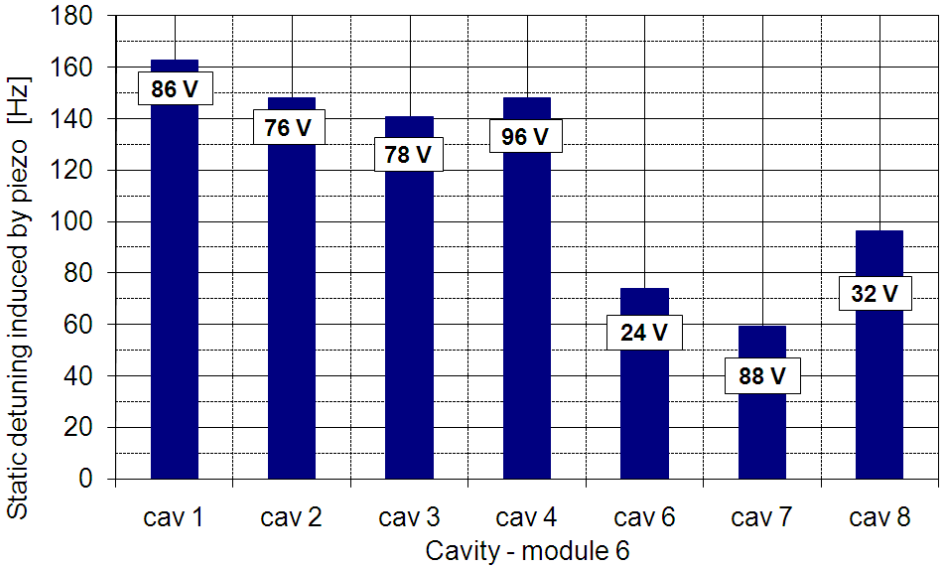

Fig. 5.12 – signed static detuning induced by the piezo pulse for LFD compensation, 1st osc. scheme.

The amplitude of each piezo pulse is also shown in the figure. The detuning values for each cavity have been deduced from the recorded initial and final position of the stepper motor of each tuner, using a value of sensitivity of 0.74 Hz/step (see par. 3.2).

cav	Gradient [MV/m]		FT detuning [Hz]		Static detuning [Hz]		Piezo amp. [V]	Piezo advance [ms]	Compensated dynamic [Hz]	Compensated Static [Hz]	Slow tuner steps
	piezo OFF	piezo ON	piezo OFF	piezo ON	piezo OFF	piezo ON		t from piezo to RF pulse	just with piezo	piezo + stepper motor	final - initial pos.
1	**35**	**35**	**-563**	**-83**	**-24**	**-76**	**86**	**0.64**	**480**	**-52**	**220**
3	**35**	**35**	**-685**	**-52**	**-126**	**-41**	**78**	**0.64**	**633**	**85**	**190**
1	33	34	-472	-54	-78	-32	80	0.64	418	46	-30
3	33	33	-574	-63	-114	-21	70	0.64	512	93	70
4	**34**	**33**	**-659**	**-99**	**-9**	**117**	**96**	**0.64**	**560**	**126**	**200**
1	31	31	-336	-24	-22	-7	58	0.64	313	16	150
2	**29**	**31**	**-418**	**-65**	**62**	**17**	**76**	**0.64**	**353**	**-45**	**200**
3	30	30	-387	-42	53	-1	52	0.64	345	-55	200
4	30	31	-492	-57	-35	59	76	0.64	435	94	180
7	**29**	**30**	**-428**	**-151**	**-83**	**-2**	**88**	**0.64**	**278**	**81**	**80**
1	25	25	-210	-59	31	-10	28	0.64	150	-41	100
2	25	25	-285	*-73*	-19	-28	*32*	0.64	*212*	-10	150
3	25	25	-285	-42	-19	30	28	0.64	243	48	130
4	25	25	-299	-68	47	*264*	28	0.64	231	*217*	*140*
7	24	24	-240	*-146*	*54*	*-18*	32	0.64	*94*	*-72*	*50*
8	**23**	**23**	**-229**	**-58**	**-22**	**-34**	**32**	**0.64**	**171**	**-11**	**130**
1	20	21	-127	-25	-71	14	20	0.64	102	84	140
2	20	20	-165	-35	-132	9	24	0.64	130	141	90
3	20	20	-170	-21	25	-4	20	0.64	149	-28	100
4	20	20	-202	-76	-31	68	20	0.64	126	98	210
5	20	--	-179	--	-120	--	--	--		--	--
6	**20**	**20**	**-190**	**-22**	**-107**	**-24**	**24**	**0.6**	169	**83**	**100**
7	20	20	-149	-43	103	-33	28	0.6	106	-136	100
8	20	20	-156	-40	-7	-8	20	0.6	116	-1	200
1	15	15	-80	--	55	--	--	--	--	--	-40
2	15	15	-107	--	53	--	--	--	--	--	-100
3	15	15	-103	--	84	--	--	--	--	--	-100
4	15	15	-122	--	121	--	--	--	--	--	-150
5	15	14	-112	--	7	--	--	--	--	--	-60
6	15	15	-111	--	54	--	--	--	--	--	-100
7	14.9	14.5	-102	--	17	--	--	--	--	--	-100
8	15	15	-92	--	7	--	--	--	--	--	-100

Tab. 5.2 - summary of results for 1st oscillation compensation scheme

5.2.2 2ND OSCILLATION COMPENSATION SCHEME

The piezo timing analysis previously performed confirmed the possibility of an alternative compensation scheme. It has been referred as "*2nd oscillation scheme*" and it relies on higher values of pulse time advance. This settings have been investigated, although quickly, during the second test sessions on module #6, after the 7 complete thermal cycle.

This settings actually corresponds to wait for a complete cavity oscillation, after the applied piezo pulse, and then use the second correct cavity deformation slope to compensate the LFD. Therefore it requires higher advance time than the previous scheme, as it can be seen from next Tab. 5.3, that summarizes all the data point collected during piezo tests made with this 2nd oscillation setting. The correct piezo pulse advance time has been chosen for each cavity, sweeping around the time range shown by the previous timing analysis, therefore around 4 ms.

Some limitations were unfortunately present for these 2nd oscillation measurements since RF power level control and external signal generator were not available. Therefore the accelerating gradient have been set to a trade-off value of 25 MV/m for all cavities except 5 and 6 that have been detuned. For what concerns the slow tuning, just before the test each cavity has been set to the best tune position so to minimize the static detuning shown. Finally, for these tests the achievable voltage on the piezo was limited to 30 V and this led to the impossibility to completely compensate the dynamic detuning showed over the flat-top. A good compensation has been anyway achieved and better results can be easily reached just rising the driving piezo pulse voltage without any other changes.

Cav.	**Gradient [MV/m]**		**FT detuning [Hz]**		**Static detuning [Hz]**		**Piezo amp. [V]**	**Piezo advance [ms]**	**Compensated dynamic [Hz]**	**Compensated static [Hz]**
	piezo OFF	piezo ON	piezo OFF	piezo ON	piezo OFF	piezo ON			just with piezo	just with piezo
1	25	25	-241	-62	48	10	31	4.7	180	-38
2	25	25	-319	-96	-40	39	31	4.7	223	79
3	25	25	-336	-27	-86	-8	31	4.4	309	78
4	25	25	-356	-43	74	17	31	4.5	313	-57
7	24	24	-240	-96	54	-5	31	4.3	144	-59
8	24	24	-302	-45	-116	-26	31	4.6	257	90

Tab. 5.3 - LFD compensation results with 2nd oscillation scheme

Some considerations can be done concerning showed results. First of all, compensating effect is evident since the lowering of dynamic detuning over the flat-top is clear from data. Even the timing settings are coherent with the need to wait for a complete cavity oscillation since, roughly, 4 ms corresponds to 250 Hz and the detailed analysis performed and discussed in par. 5.3.1 confirms that this can be a good estimation of the main cavity resonance frequency.

Absolute performances in terms of compensated LF detuning seem to be even slightly higher than 1st oscillation scheme results. As a reference, consider the compensated detuning of previous paragraph that have been obtained in a similar settings at 25 MV/m gradient. In the next picture the two data series have been compared, 1st oscillation data have been previously rescaled to compensate for the difference in piezo voltage for some cavities (anyway small, around 28 V instead of 31). This comparative analysis, although meaningful, is not surely conclusive or enough to prove that the 2nd oscillation scheme actually performs better. A dedicated and more detailed test should be performed at different gradient values, for now it is anyway reasonable to assume that at least this setting leads to comparable results.

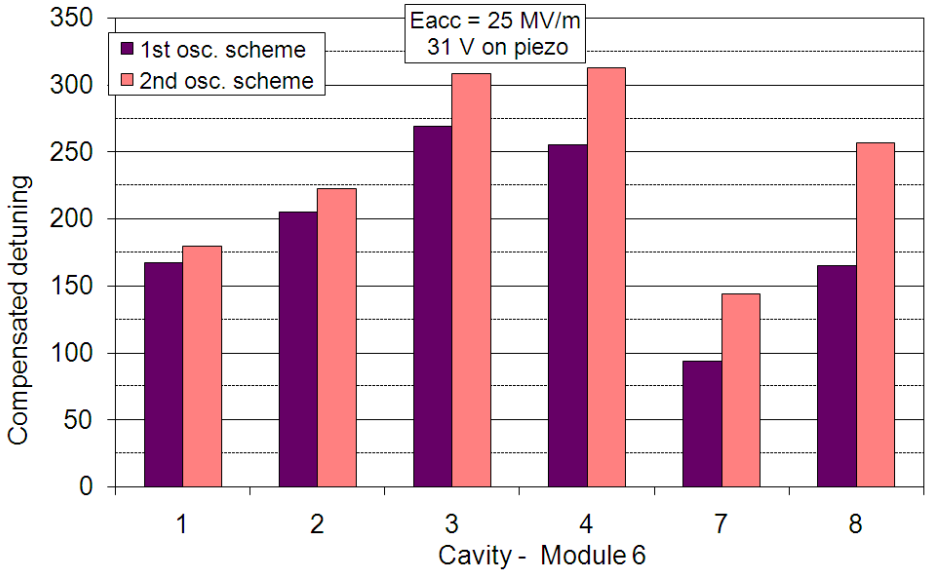

Fig. 5.13 - comparative analysis between 1st and 2nd oscillation LFD compensation results

In the next picture cavity detuning data are shown as an example of the compensation of the LFD with these piezo settings. It is clear from results that, in order to completely null the detuning over the flat-top, additional voltage on the piezo was needed. This is not anyway, as already said, a critical issue.

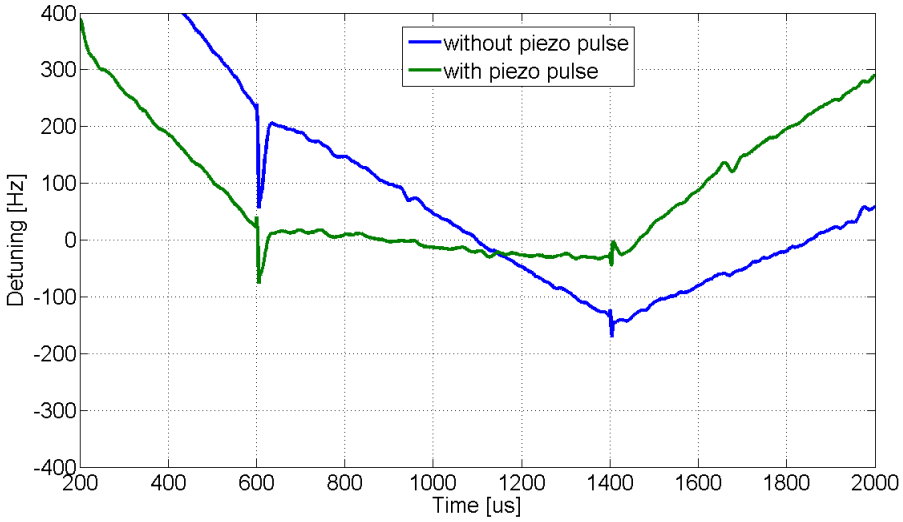

Fig. 5.14 – detuning of cavity 4 in Module #6 at CMTB, operated at 25 MV/m. 2nd osc. scheme

Even the expected absence of additional static detuning generated by the piezo pulse itself is shown. As already underlined, this is maybe the main disadvantage for 1st oscillation setting since, in that condition, driving the piezo pulse forces to search again for the proper cavity tune using the stepper motor.

Moreover, just setting a different time advance value, around the one corresponding to zero additional static generated detuning, it is possible to generate on purpose an amount of static detuning; for example the amount needed to compensated the previously existing one. This peculiar feature has then been confirmed during the measurements whose data has been reported in Tab. 5.4, results are also plotted in the subsequent Fig. 5.15. The result is that a clear lowering of the static value has been obtained without changing the stepper motor position. It is worth going in some more details for this last feature, that is the possibility to easily compensate for a small amount of static detuning just acting on the piezo pulse time setting.

The qualifying and non-trivial issue about it is that in this way *the static and dynamic detuning regulation by means of piezo pulse are actually almost completely independent* since they rely on two different piezo pulse parameters**.** Moreover the behavior of each of these is linear in optimum approximation and this is a favorable condition toward an automatic and adaptive controller.

To investigate this piezo effect, the delay of the pulse has been swept around the optimum value previously identified for LFD compensation. Detailed results are summarized in Tab. 5.4.

Cav.	Gradient [MV/m]		Static detuning [Hz]		Piezo advance [ms]		FT detuning [Hz]		Piezo amp. [V]	Static detuning range [Hz]	Advance range [ms]
	Piezo OFF	piezo ON	max	min	max	min	max	min			
1	25	25	69	-130	4.9	4.0	-87	-78	31	199	900
2	25	25	39	-145	4.7	4.1	-96	-80	31	184	600
3	25	25	37	-197	4.5	4.0	-54	-54	31	234	500
4	25	25	151	-73	4.8	4.3	-74	-69	31	224	500
8	24	24	26	-196	4.7	4.1	-58	-49	31	222	600

Tab. 5.4 – effect of the piezo pulse advance on static detuning with 2nd osc. scheme

As an example, actual data from cavity 4 are showed in Fig. 5.15. It is clear from the plot that the induced variation of the dynamic detuning over the flat-top is almost completely not affected by the delay settings, while the static detuning can be set accurately in a range of roughly 200 Hz.

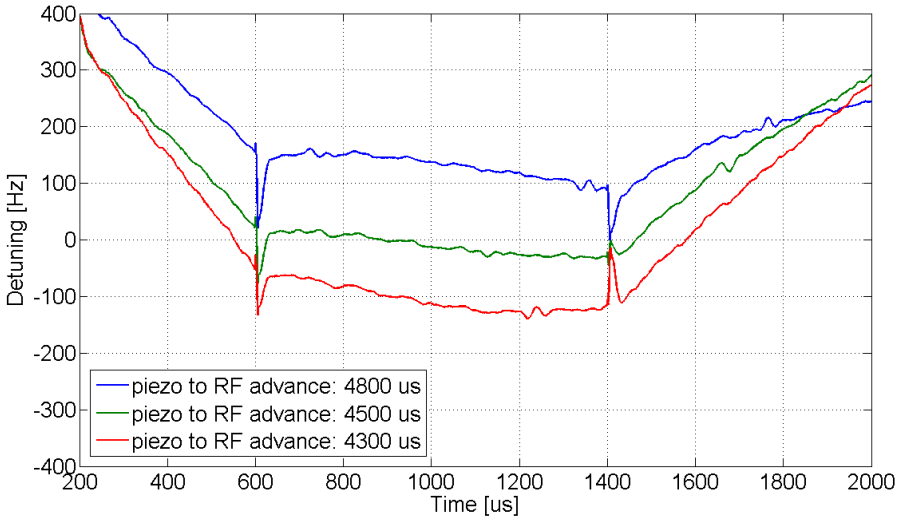

Fig. 5.15 – cav. 4 in Module #6 at CMTB. Control of the static detuning with the piezo pulse advance.

Completely similar curves have been obtained from detuning data of others cavities. The 2nd oscillation scheme that has been proposed here could be considered as promising since at least three qualifying aspects have actually been shown.

- it is possible to decouple the search for the optimum tune of the cavity with the stepper motor from the piezo operations.
- it is possible to compensate for small static variations easily and quickly in the range of about 200 Hz just setting the proper time for the piezo pulse. For example, this

feature can be particularly useful for compensate the effects related to the He bath, like He pressure or level variation, that are typically quicker than the typical response time of the stepper motor.

- Finally, this solution would be highly recommendable in sight of an automatic cavity tune controller since the two key detuning components, static level and detuning over the flat-top, are decoupled one to the other and instead linearly coupled to two different parameters, pulse time advance for the former and pulse amplitude for the latter. This for instance does not happen in the 1st compensation scheme since the amplitude of the piezo driving signal also induce a shift in the static level of the detuning plot. This can be more clearly understood referring to analytical simulations proposed by the author in order to fully understand the active LFD compensation and reported in app. A

To complete the analysis of piezo performances in terms of Lorentz Force detuning compensation it is now possible to superimpose the several measurements performed, in both 1st and 2nd oscillation scheme, to the plot in Fig. 5.2 in order to verify the time coherence among these results.

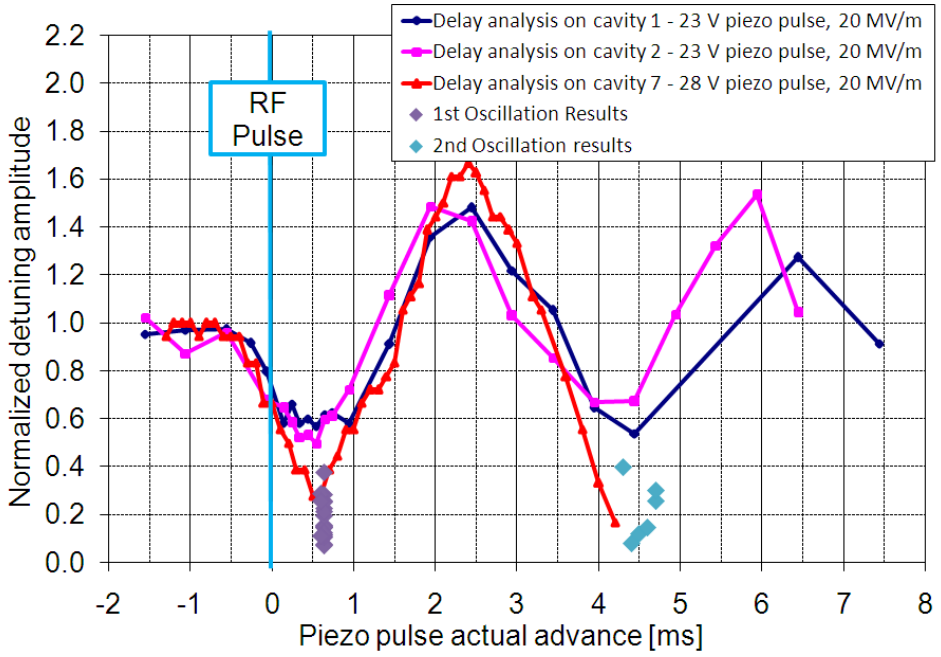

Fig. 5.16 - normalized absolute value of detuning over the flat-top vs. piezo timing, LFD compensation results included

The plot shows a very good correlation between actual LFD compensation data and the pulse time sweep previously performed. As expected, the two compensating scheme, named as 1st and 2nd oscillation scheme, correspond to the minima showed by the delay analysis while the absolute detuning reduction is higher in the former cases since the amplitude of the pulse has been risen as needed.

5.2.3 RESULTS WITH LLRF FEEDBACK CONTROL

Before moving module #6 out from the CMTB facility, the SIMCON 3.1 klystron controller has been finally set so that the RF feedback control loop was operative. This allowed to definitively validate the LFD compensation performances shown so far. This is a key step since the ultimate reference figure for detuning compensation performances must come from the power level needed to operate the module at a given gradient: since the goal is to keep cavities actively close to tune during the RF pulse, a "power saving" effect is expected when using the active piezo compensation.

Once the feedback loop is driving the whole module, cavities accelerating gradient values can no more be set independently one to the other. RF power distribution among cavities of Module #6 has been permanently set according to the final quench limit shown by each resonator during the last Q vs. E_{acc} test performed[34]. As a reference for the relative gradient setting, the values corresponding to the configuration used for the subsequent LFD compensation measurements, are showed in Tab. 5.5.

Cav.	**Gradient** MV/m
1	27
2	29
3	28
4	29
5	18
6	19
7	23
8	23

Tab. 5.5 - settings for cavity gradients in Module #6 after permanent power re-distribution

The relative ratios between cavities have been kept constant throughout the entire test. The absolute value (i.e. the forward power) has instead been set (but just slightly modified) each time. The stability of each RF probe signals is critical for the feedback loop to properly operate, this forced to exclude cavity #8 from the control loop due to a broken bit in the corresponding ADC, leading to unacceptable signal oscillations. Unfortunately, also cavity #7 has been removed from the loop for cabling mismatch in the SIMCON board connector[35]. Therefore, finally, probe signal from cavity 1 to 6 have been considered

[34] This permanent RF power distribution is actually performer directly with variable directional coupler at the waveguide level.

[35] Although these problems on the SIMCON board involved standard components, replace them would have required the complete stop of RF activities on the module and an additional and not acceptable delay in the piezo tests schedule.

in the vector sum of the klystron controller (but cavity 5 actuators were already out of operation for preload loss so that cavity actually remains uncompensated). Before switching on the feedback loop, each cavity probe signal has been multiplied by a proper calibration complex factor so that the resulting vector sum was correctly comparable to the wanted and pre-set amplitude and phase set-points.

The loop-gain has then been set to 25. All data concerning the klystron SIMCON controller have been resumed in next figure, that directly represents the screenshot of the corresponding DOOCS panel. Both actual data (black) and set-point table values (green) are visible on the right. A set-point value of 5.72 for the vector sum amplitude corresponds to an average accelerating gradient of 25.6 MV/m.

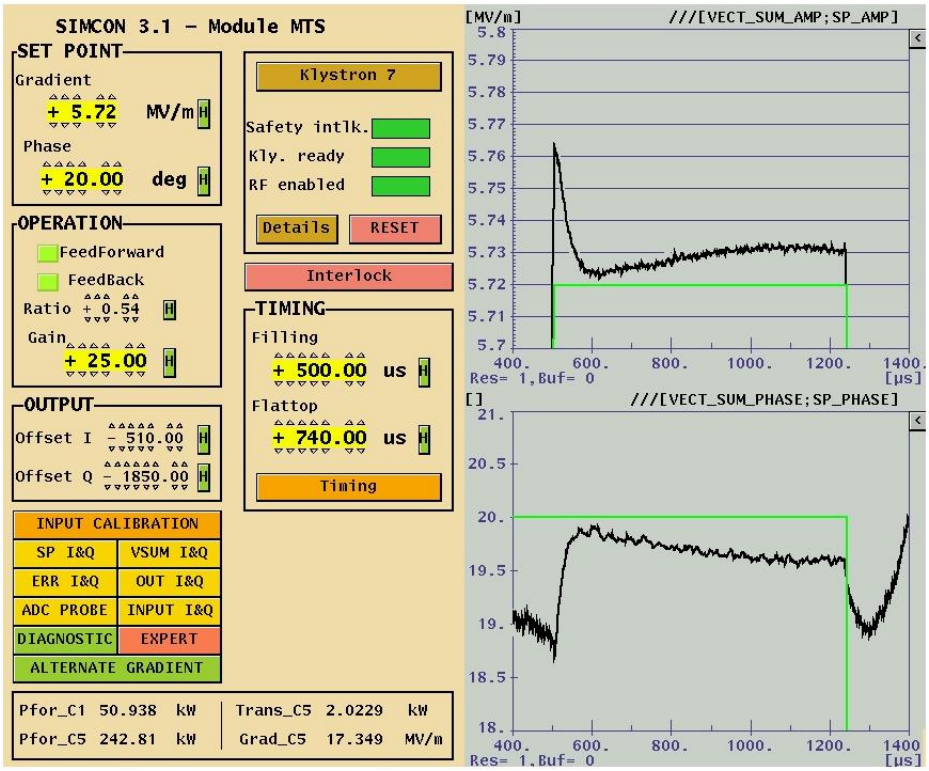

Fig. 5.17 - screenshot of the DOOCS control panel for the SIMCON klystron controller

Since there is the need to operate the whole module in the RF loop, 8 different piezo signals are needed in principle to simultaneously compensate LFD in each cavity, according to its best specific setting. Anyway a trade off must be found between maximization of detuning compensation and resources saving, especially since the analysis previously performed showed that shape and time advance can be the same for every cavity. This is anyway not feasible for the piezo pulse amplitude since it has been shown here that it differs significantly from cavity to cavity.

Finally, both in order to lower used resources and to face the actual availability in terms of signals generators[36], a reference configuration with the use of only 2 independent piezo driving signals, has been chosen to be:

Reference configuration:

- Signal 1 to cavities 1 to 4, high gradient cavities.
- Signal 2 to cavities 7 and 8, medium gradient cavities
- No piezo compensation for cavities 5 and 6, low gradient cavities.

Both the signals have been set according to the previously introduced 1st oscillation compensation scheme. Two alternative configurations have also been considered:

2nd configuration:

- Signal 1 to cavities 1, 2, 4, 7, and 8, high detuning cavities.
- Signal 2 to cavities 3, 5, and 6, low detuning cavities

3rd configuration:

- Signal 1 to cavities 1, 2 and 4, high detuning cavities.
- Signal 2 to cavities 3, 7 and 8, medium detuning cavities
- No piezo compensation for cavities 5 and 6, low detuning cavities.

First of all, the best possible module configuration without the piezo active compensation has been found. This implies the definition of the correct stepper motor position that allows to achieve the highest module set-point before quenching or interlock switching. This results is obtained properly pre-detuning each cavities so that the on-tune condition is reached in the middle of the flat-top. Once the maximum achievable gradient has been reached, data from power readouts and vector sum have been acquired and kept as the reference performance sustainable by the module without piezo active compensation.

Then piezo signals were switched on according to the scheme mentioned above, the amplitude of each of the 2 piezo signals has been set to a proper value to minimize the overall detuning and finally the same power readouts and vector sum data have been acquired. Actual detuning data for the best achieved results, corresponding to the reference piezo signal configuration, are reported in the next picture.

[36] Only two signal generator instruments were actually available during these tests and the FPGA code for multiple signal generation was still under development at the time.

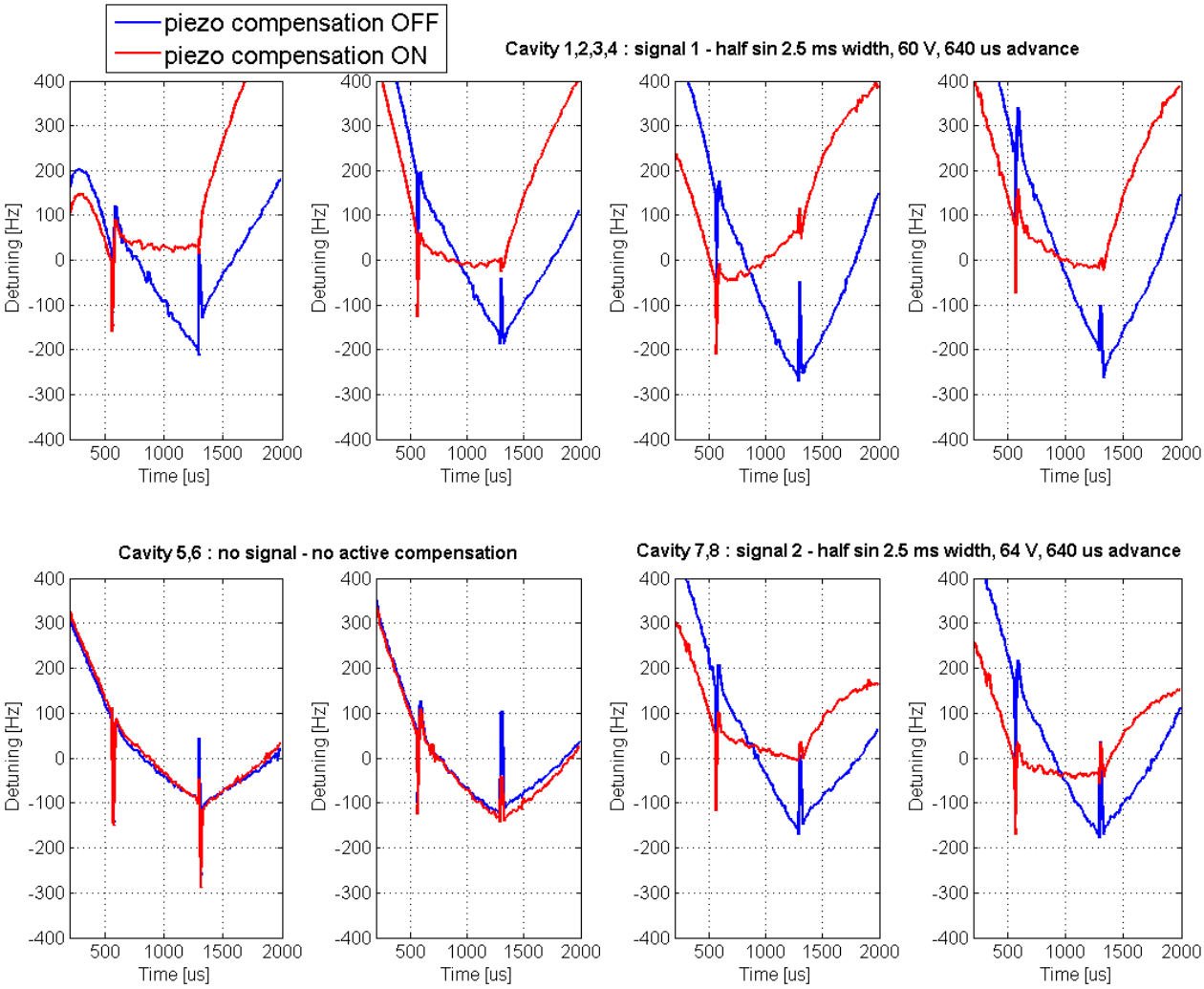

Fig. 5.18 - detuning data from Module #6, with and without piezo compensation, RF feedback on.

It is clear that a trade-off has been accepted among the responses of different cavities driven with the same piezo pulse. For example, cavities 1 and 2 are correctly compensated while for cavities 3 even a clear over-compensating condition has been accepted.

The first results of such active configuration emerge from the forward power readouts analysis. Actual data are compared in the following picture, Fig. 5.19. Since the LLRF controller is now controlling the vector sum of the contribution of each cavity, the shapes of the plotted curves are identical while the amplitude of each one is instead modulated by the permanent power distribution.

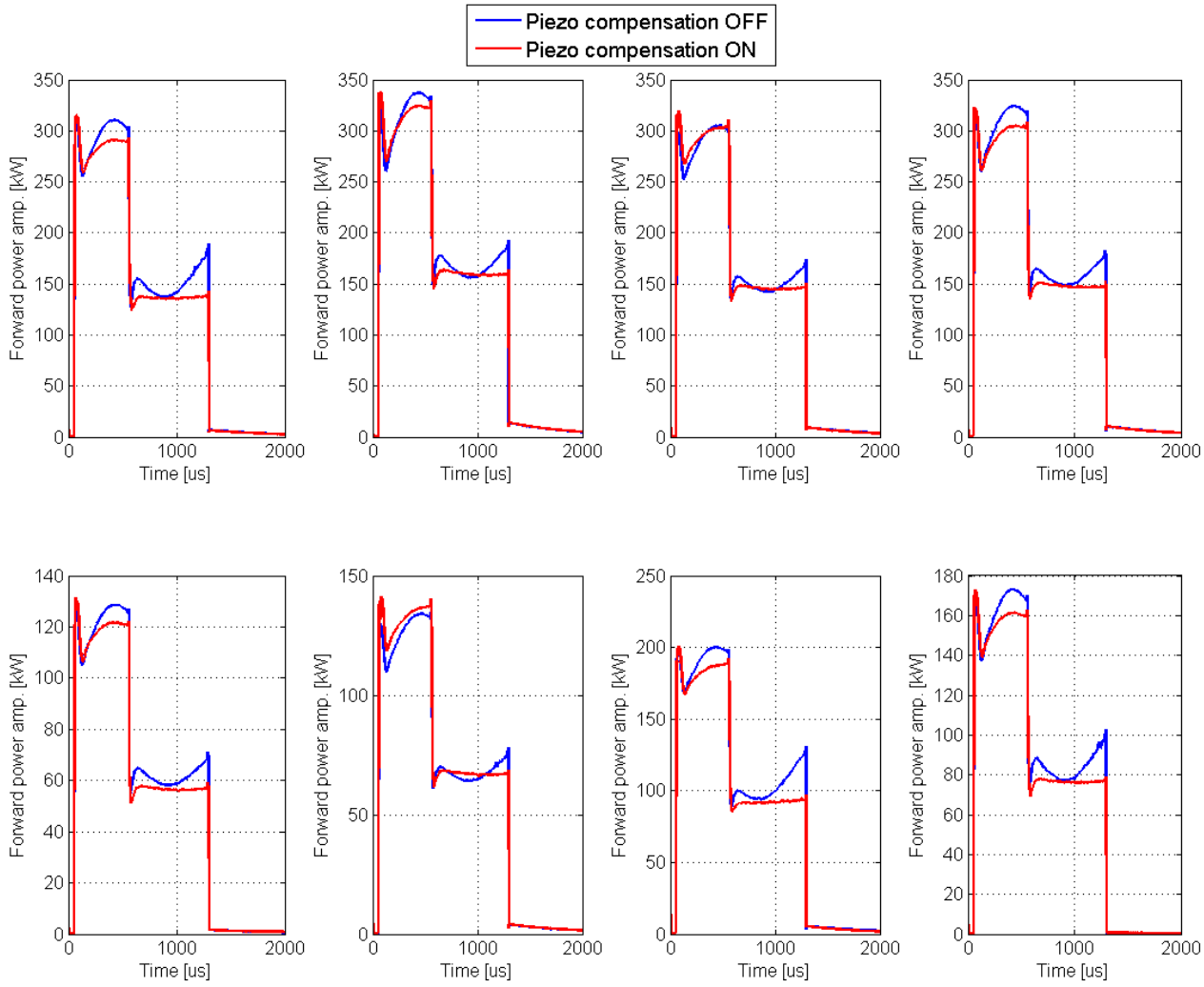

Fig. 5.19 - amplitude of forward power readouts from Module #6, w/o piezo compensation, RF feedback on.

First of all, looking at the blue curves, which refer to the reference condition without piezo, the effect of the RF feedback loop is clear. The instantaneous value of the forward power is corrected via the feedback loop of SIMCON controller in order to compensate for the time-varying tune of the cavities, as expected (par. 4.2). Then, when looking at the red curves, the effect of the piezo active compensation becomes evident. The cavities are kept on tune actively therefore just little time-varying corrections are required to the control loop to follow the specified set-point curves.

Results have been analyzed in order to evaluate the actual improvement achieved with the piezo active compensation. Both the average and the peak values of the forward power over the whole RF pulse have been considered for each cavity. Collected values are summarized in Tab. 5.6.

Cavity	Average Power				Peak Power		
	over the RF pulse		over the FT				
	kW		kW		kW		
	piezo OFF	piezo ON	diff. %	diff. %	piezo OFF	piezo ON	diff. %
1	198.0	186.5	-5.8	-8.9	189.2	144.0	-23.9
2	215.1	210.1	-2.3	-4.2	192.7	163.8	-15.0
3	196.1	195.4	-0.3	-3.1	174.4	150.4	-13.8
4	206.6	196.7	-4.8	-6.2	183.1	152.9	-16.5
5	81.6	77.5	-4.9	-7.8	71.3	59.0	-17.1
6	86.7	88.6	2.2	-0.3	78.0	68.6	-12.1
7	131.5	122.5	-6.9	-10.0	131.0	101.1	-22.8
8	109.7	103.4	-5.7	-7.8	102.6	78.9	-23.1
Avg. ACC6	153.2	147.6	**-3.6**	**-6.1**	140.3	114.9	**-18.0**

Tab. 5.6 – average and peak power results, with and without piezo compensation

An overall power saving during operation has been clearly demonstrated, in particular for what concerns the flat-top region of the RF pulse that has been considered for these active compensation tests. Moreover achieved results are actually even slightly better than values shown in Tab. 5.6: in fact, although the 6.1 % and 18 % reduction in the average and peak power respectively, since cavities have been kept closer to tune the achievable gradient increased accordingly. This can be directly evaluated through the vector sum data with and without the piezo compensation, in Fig. 5.20.

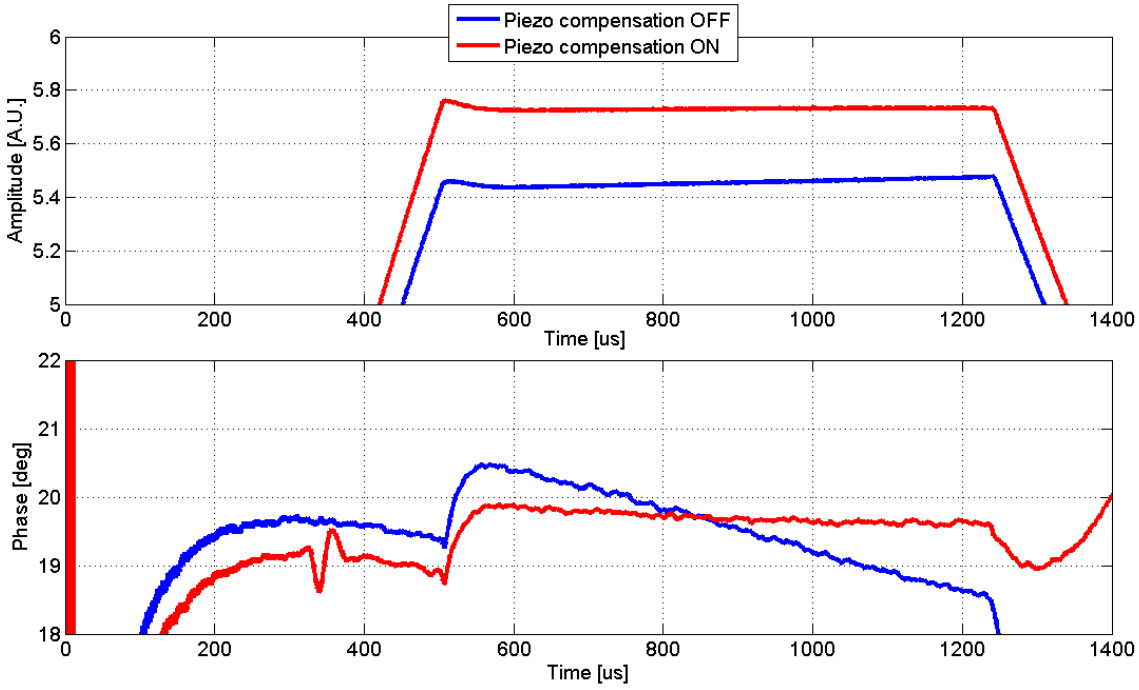

Fig. 5.20 - vector sum data for Module #6 in MTS, with and without piezo compensation, RF feedback on

These data show that, despite the lower forward power value, the average gradient increased slightly from 24.4 MV/m to 25.7 MV/m, corresponding to an improvement of 5.1 %. Using the Lorentz coefficient previously measured for ACC6 in par. 3.4.2 and formula (4.12) it is possible to estimate that this improvement in the accelerating gradient would have instead required + 3% in the peak power if uncompensated, to be compared to the -18% actually achieved thanks to the detuning active compensation.

Finally, the percent variation of the resulting vector sum amplitude and phase during the flat-top have been computed as the ratio between the peak difference over the initial value, to evaluate the effect of the piezo active compensation. Properly interpolating the data plotted in Fig. 5.20 it is possible to deduce that the phase stability over the flat-top improved significantly from 9.6 % to 1.7 %. Instead for what concerns the amplitude stability, the effect is less evident since the performance of the control loop is already good; the computed value moves from 0.73 % to 0.69 %.

Results corresponding to the two alternative configurations considered actually showed very similar results in terms of power balance and stability improvements. This is coherent with the actual situation, where the piezo compensating effect, even if improved with different configurations, gets anyway overcome by the detuning contributions of cavity #5 and #6 that are not compensated at all. It is possible to extrapolate from data of plots in Fig. 5.18 that around 700 Hz of total absolute detuning (positive and negative detuning do not cancel each other) has been left over the module after active piezo

compensation, this value is actually dominated by the about 400 Hz detuning contribution from cavity #5 and #6.

Therefore obtained results confirmed a significant improvement in the module performances especially considering that a very simple compensation scheme has been used, where only 2 different pulses were generated and two cavities were not actively compensated. This also means that considerably high improvement margins are present when going toward a more detailed configuration, as for example where each cavity is compensated with a different piezo pulse, each one with its optimum amplitude at least. It is also clear that the final design of the tuning system must ensure that critical losses of piezo efficiency, as it happened for cavity #5 in ACC6, do not appear. This issue would in fact lead to the impossibility to radically lower the total detuning in the module.

After the successful simultaneous compensation of the LFD for ACC6 presented, although only two independent set of piezo signals were used, the 1st oscillation compensation scheme was used by DESY group to completely compensate the detuning shown by each ACC6 cavity (apart from cavity #5 whose piezo were not operative) when, after tests at the CMTB facility, it was installed in the FLASH linac. In that case the module was operated at a set-point gradient of 22 MV/m and an 8-channel piezo signal generator was available so that the use of a different piezo signal for each cavity was possible [106].

5.3 ADDITIONAL INVESTIGATION OF PIEZO ENVIRONMENT

5.3.1 CAVITY MECHANICAL ANALYSIS

Several key issues of the LF effect and its active compensation (1st and 2nd oscillation timing and sensitivity to dynamical detuning, among others) directly depend on the dynamical mechanical properties of the corresponding cavity. As a starting point to analyze those properties, a proposal procedure to measure the cavity main resonance frequency is now presented. The dominant mechanical resonance is shown by all cavities in different measurements and usually placed in the range 150-300 Hz.

This paragraph will be anyway focused on the possibility to evaluate those mechanical properties through piezo-related measurements. For this purpose, cavity ringings induced by the RF pulse has initially been considered. As already introduced in par. 4.5.2, one of the controller code components that have been developed and tested on a SIMCON FPGA hardware is a data acquisition module (DAQ) with a custom sampling frequency, using on-board ADCs. This setup has been in this case used to record sensor piezo signal right after the RF pulse, so to acquire cavity ringings as felt by piezo stacks. As a reference, resulting data from cavity 3 operated at 35 MV/m are reported in Fig. 5. 21.

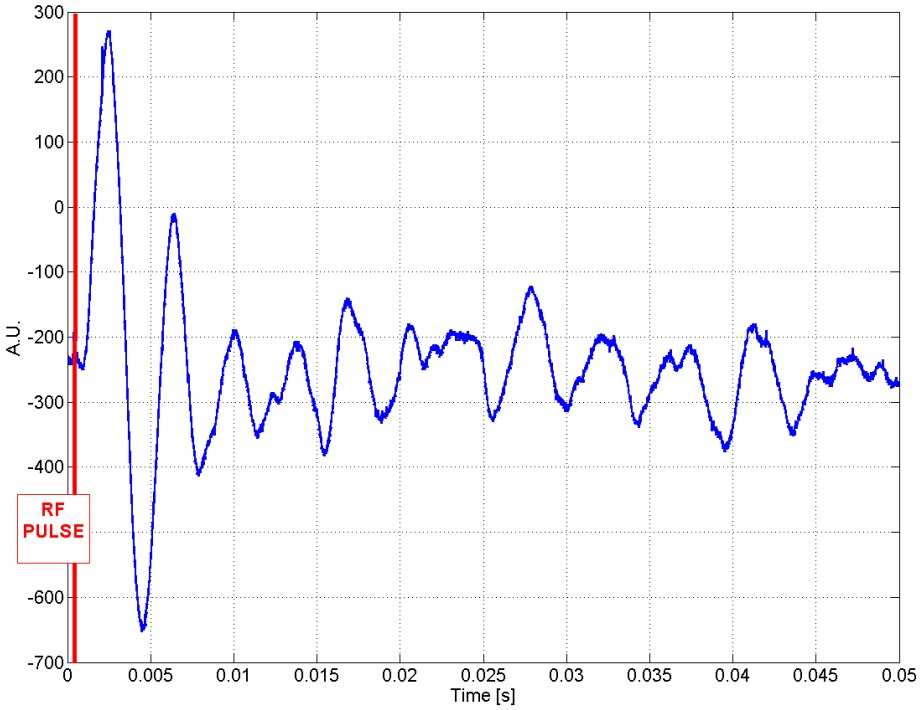

Fig. 5. 21 - sensor piezo signal in cav. 1 at 35 MV/m , after RF pulse

Fast Fourier transform (FFT) has then been used to extract information about the frequency contents of such visible cavity oscillations. Results on a large frequency range are showed in Fig. 5.22, whereas already mentioned, it is possible to recognize how dominating frequencies are clearly located around 250-300 Hz.

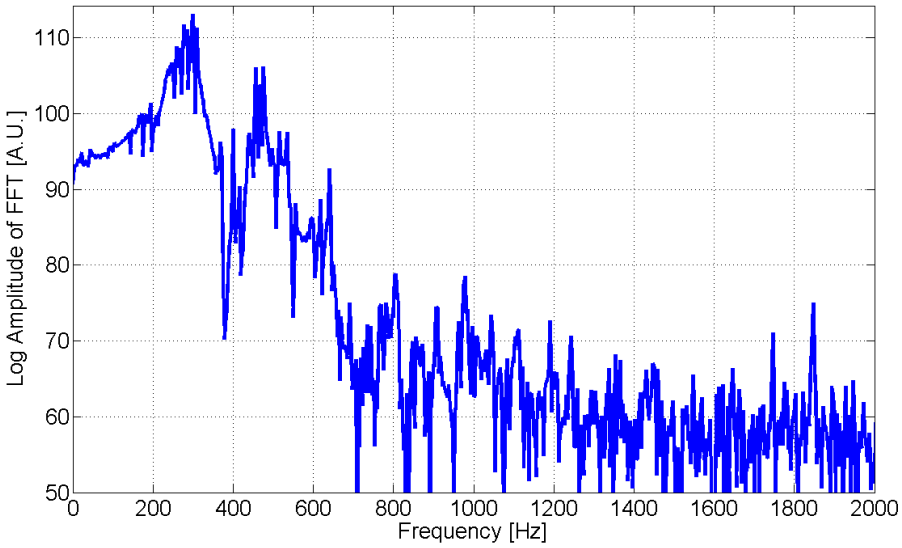

Fig. 5.22 - FFT of sensor piezo signal, cav. 3 at 35 MV/m, log amplitude

Additional manipulation has then been performed on data so to highlight the frequency position of the actual main cavity mechanical resonance. Raw amplitude data from FFT computation have been averaged so to more clearly reveal the peak frequency. A typical resulting curve after data smoothing is presented in Fig. 5.23.

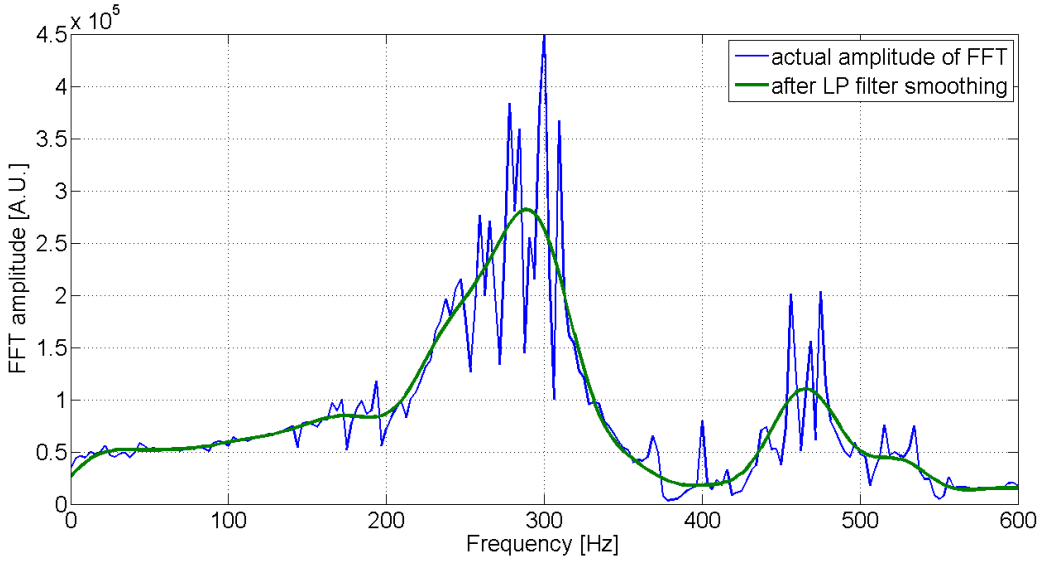

Fig. 5.23 - fit of the FFT of sensor piezo signal, cav. 3 at 35 MV/m

In this way, data from all cavities have been collected and analyzed. In Fig. 5.24 dominant resonances from the 8 cavities of Module #6 are shown, while exact values of each main frequency have been summarized in Tab. 5.7. These last values have been extracted searching for the peak position in each corresponding FFT plot.

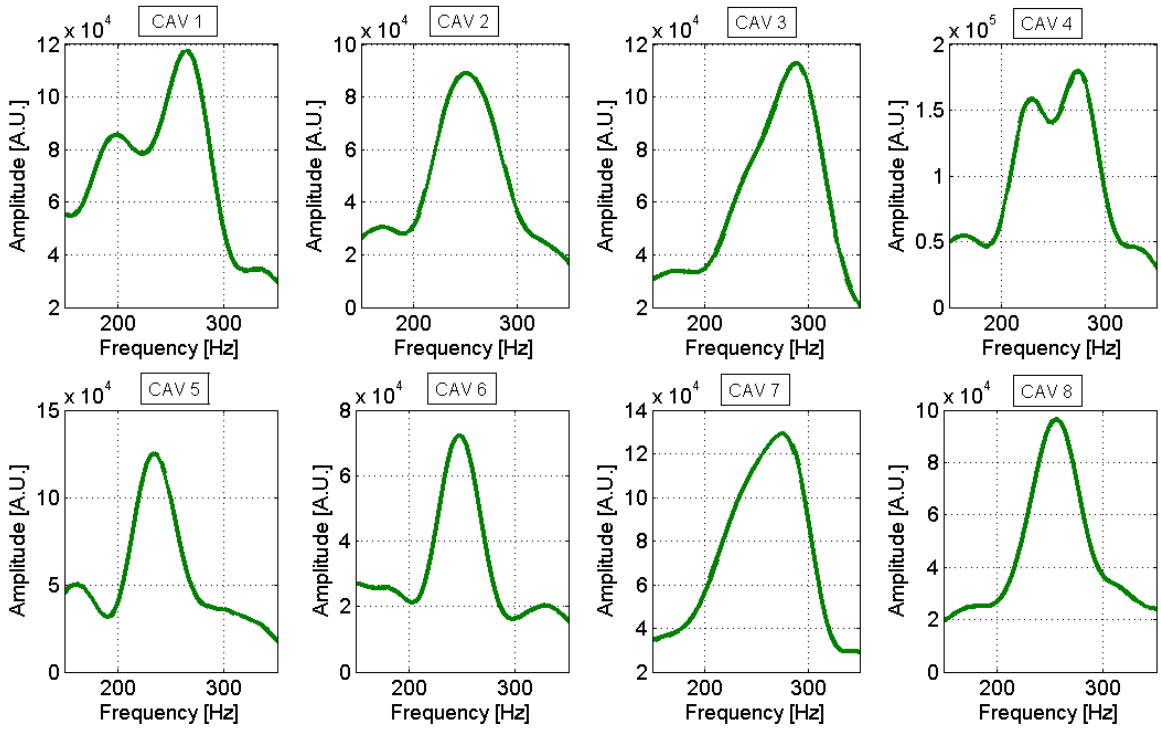

Fig. 5.24 - collection of smoothed FFT of cavity oscillations

Cavity	Main Resonance Freq. [Hz]
1	265
2	250
3	287
4	275
5	234
6	247
7	275
8	256
Avg.	261 +/- 18

Tab. 5.7 – collection of main mechanical resonance frequency values for Module #6

Data show that the main mechanical resonance can be easily identified in this way at least for 6 out of 8 cavities, while for cavity 1 and 4 data seem to show a superposition of two near modes. Since piezo fixture for each cavity of module #6 is installed (see par. 4.4.4) at the He tank end, piezo stacks are consequently close also to the following cavity in the cold mass string. This could lead to mechanical interference between the two near cavities and eventually both cavities resonance frequency appeared in the acquired data, as for plots corresponding to cavity #4 and following cavity #5. These shown resonance

frequency values moreover confirm that the high time advance set for 2nd oscillation compensation (around 4 ms) has been correctly identified with actual cavity oscillation period: on average 261 Hz corresponds to 3.8 ms.

Collected data concerning cavity oscillations allow an additional analysis. In the next plot signal from the sensor piezo in the fixture are shown for both conditions, with and without LFD compensation piezo pulse. Data refer to cavity #3 at 35 MV/m with optimal pulse settings. Both time series are synchronized to the same trigger.

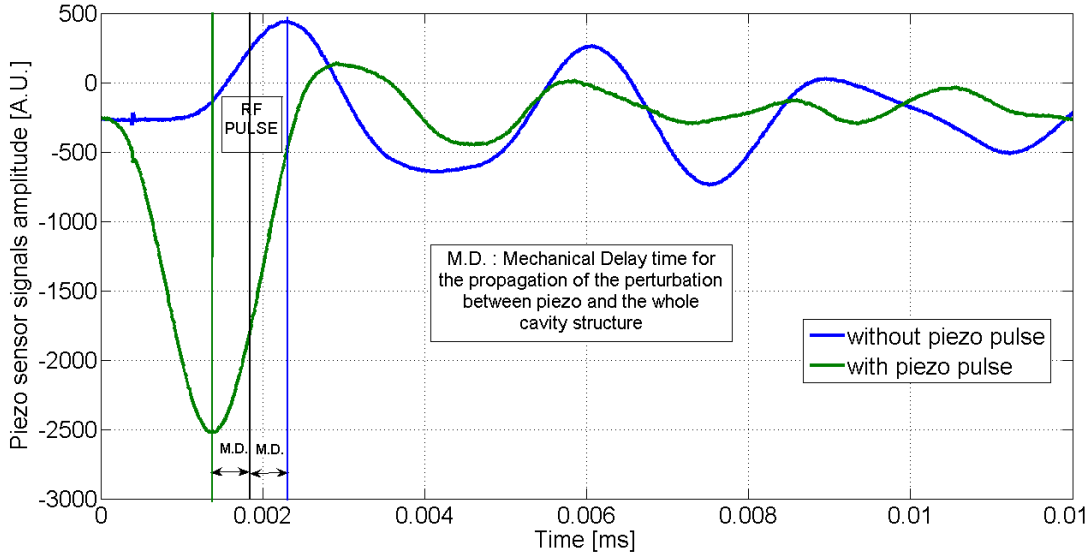

Fig. 5.25 – piezo sensor signal with and without LFD piezo pulse compared, cavity #3

It is now possible to see that piezo active compensation actually leads to a lowering in the amplitude of cavity oscillations also after the RF pulse. Moreover the actual time window between the optimal piezo pulse and the RF-induced first oscillation is a direct evidence of the time needed for mechanical perturbations to propagate between piezo fixture and the whole cavity structure. Half the time distance between those two peaks actually corresponds to roughly 0.4 ms, a value that completely matches the expectation. The shown estimation of the delay time needed to piezo action to propagate also confirms the considerations about the feasibility of a closed loop control of cavity detuning, previously presented in par. 4.5.1. The final bandwidth of the feedback loop would be significantly affected by this mechanical delay and consequently its efficiency on the time scale of a typical TESLA RF pulse. This also validate the choice of an open-loop compensation as the reference approach.

Piezo dual active and sensitive capabilities allowed a further mechanical analysis of the system performed with a standard Signal Analyzer[37], thanks to the possibility to collect a Piezo-to-Piezo transfer function measurements. This was possible since for Module #6

[37] A SRS785A signal analyzer from Stanford Research has been used

two piezo stacks were installed in each piezo fixture, thus both of them has been involved: the actuator excites the system with a low amplitude sinusoidal signal in the frequency range of interest and the sensor one is used to collect the response as a dynamic capacitive displacement sensor.

Amplitude of all collected transfer functions are plotted in the next picture, as a reference also the previously showed FFTs of cavity ringings are visible in the background. The interpretation of such plots is anyway not straightforward. An association between the two series of resonances for each cavity seems possible, even if the Piezo-to-Piezo transfer functions actually revealed many more resonance lines. Certainly for what concerns those last spectra, both the great sensitivity of the piezo stack as a sensor and resolution of the instrument forced the measure to be sensitive to an huge number of secondary resonances on that frequency range, while the free cavity ringings spontaneously select the main ones. This means that actually the Piezo-to-Piezo TF probed the system on a wider length scale, for example interacting also with the nearby cavity in the beam line that is anyway close to each given piezo fixture.

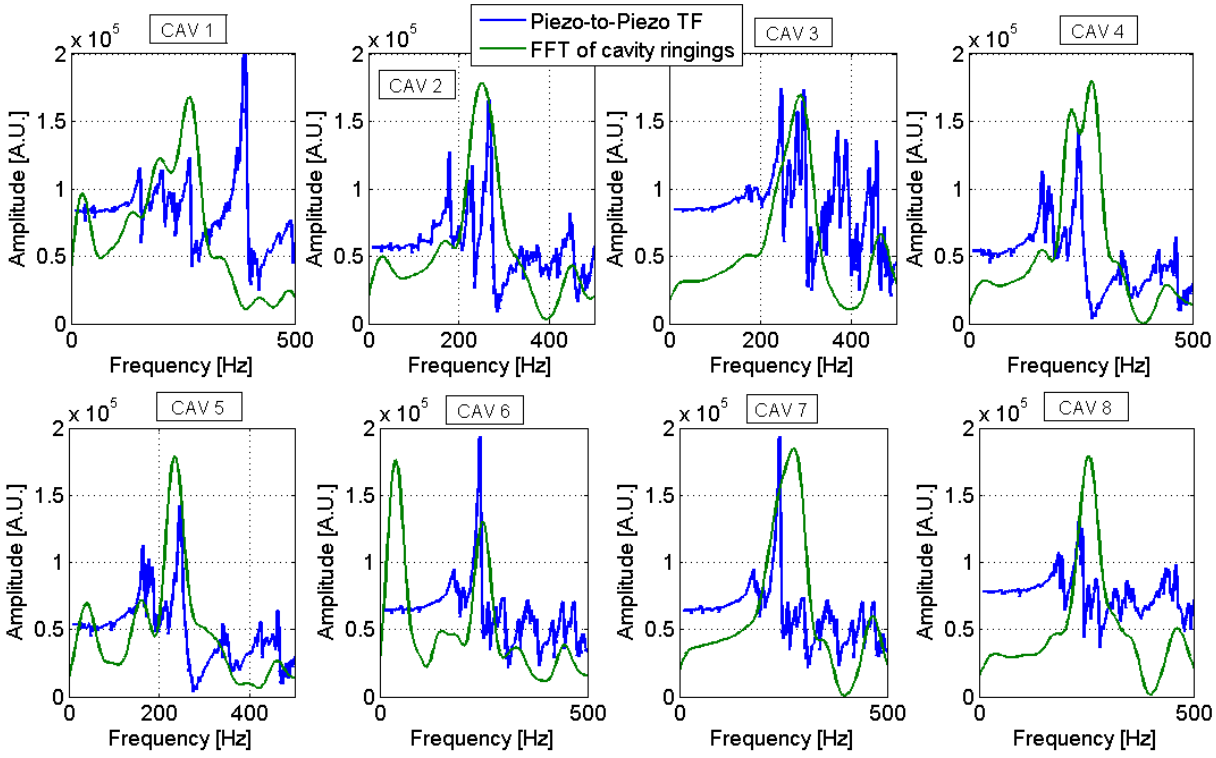

Fig. 5.26 - collection of Piezo-to-Piezo transfer functions

These spectral analyses moreover provide valuable information concerning the preload acting on piezo actuators in their fixture since its value actually determines the mechanical coupling between them during the acquisition of the transfer function. The DC value of each piezo-to-piezo spectrum could be monitored during module operations in order to

eventually prevent critical loosening of actuators, as happened for instance for cavity #5 actuator in ACC6 (actually cavity #5 TF in Fig. 5.26 reveals a DC value clearly lower than the average, although this is not conclusive). A similar mechanical coupling analysis has been performed for example on piezo actuators of the coaxial Blade Tuner during cold test in CHECHIA cryostat (see chap. 6.8.4).

5.3.2 CROSS TALKS ALONG THE MODULE

In the previous paragraph the great sensitivity of piezo stacks as mechanical sensors has been underlined. Here this feature has been used to perform a prototype experimental procedure to investigate the propagation of mechanical perturbations along the module, through the cold mass. Also in this case transfer functions have been measured across cavities using a Signal Analyzer. Actuator piezo in cavity #1 (at the beginning of the cryomodule) has been kept as generator of small harmonic perturbations (5 V amplitude on piezo) while signals from piezo sensor in each other fixture have been recorded and considered for analysis.

As a result 7 transfer functions have been collected, from cavity 1 to 2, 3, 4, 5, 6, 7 and 8 and they have then been compared to the transfer function between piezo 1 and 2 in the same fixture of cavity one. The amplitude of this last transfer function has moreover been scaled by a factor of 200 so to be comparable in amplitude with the others, just for plotting purposes. Overall results are showed in the next picture. For reference, the 8 1-meter long cavities of module #6 are almost equally spaced along its length of 12 m.

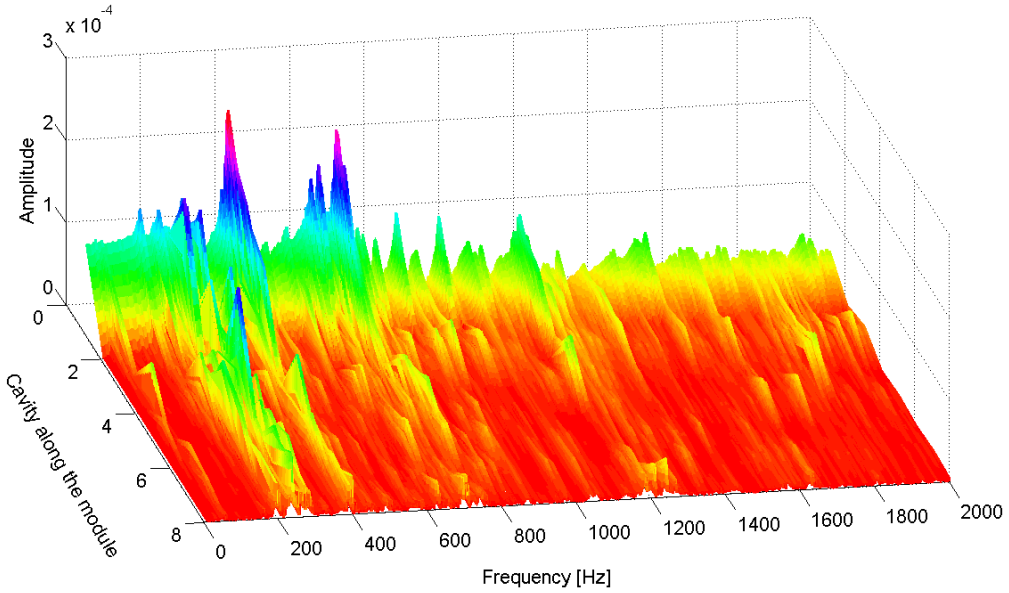

Fig. 5.27 – amplitude of spectra of mechanical resonances along the module cold mass

Out from these overall data, a selected resonance can be analyzed in detail so to recognize its dumping along the module. The main one at around 380 Hz has been chosen for such purpose, a 2D zoomed detail of the previous plot, centered around the selected resonance, is now presented in next Fig. 5.28. The presence of such resonance all along the module and its dumping is then visible in Fig. 5.29, where true amplitude was used for the in-fixture piezo-to-piezo transfer function in cavity #1.

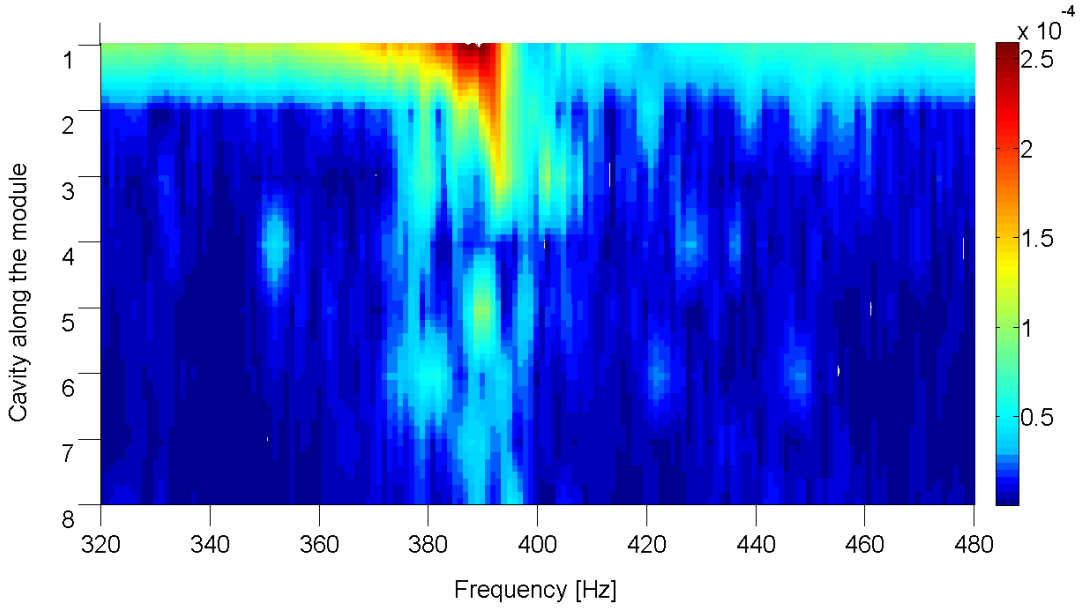

Fig. 5.28 – amplitude of spectra along the module, zoomed around 380 Hz

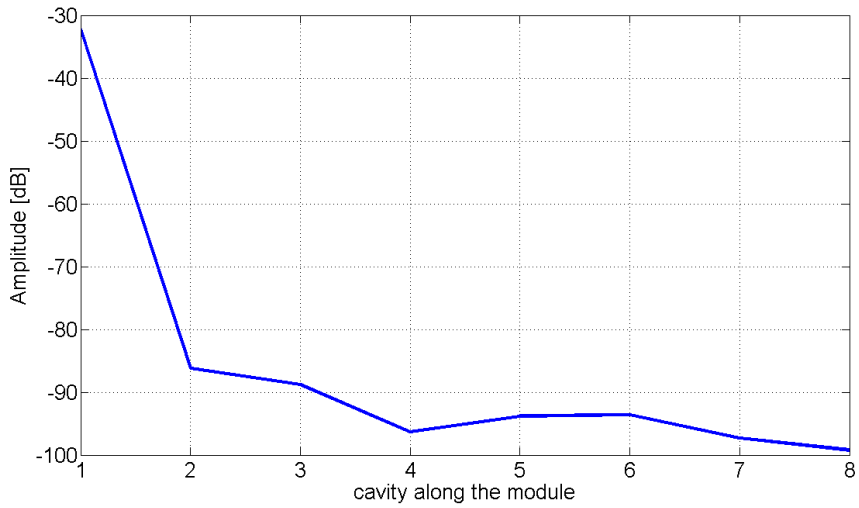

Fig. 5.29 - dumping along the module of the 380 Hz resonance

This results confirmed that the proposed procedure could be used to evaluate the expected issue of mechanical cross-talks among cavities along the beam line. Showed plots confirm that a single given perturbation induced by piezo can be clearly probed all along the module, thus propagating through the cold mass. This could be eventually critical if extended to the case of a full-module high-gradient simultaneous LFD compensation, when all 8 piezo stacks would be operated almost simultaneously with high voltage pulses. Moreover just a 5 V amplitude sinusoidal signal has been used for this excitation, thus only a fraction of a typical LFD compensation pulse that can approach, as seen, 100 V (for PI piezo).

Besides, it must positively underlined that, as showed in the 380 Hz resonance analysis in Fig. 5.29, a good attenuation factor can be anyway expected, around 50 – 60dB even after few meters. Moreover, the resulting effect of this excitation on the faraway cavity #8 is actually completely comparable, in terms of amplitude, to the deformations induced by the environmental microphonics noise, as visible in next pictures. A time window of the signal from sensor piezo of cavity 8 has been recorded, with and without exciting signal on piezo of cavity 1 (5 V, 386 Hz), therefore microphonics stochastic cavity oscillations are visible and the effect of the excitation is visible both in time and in frequency domain.

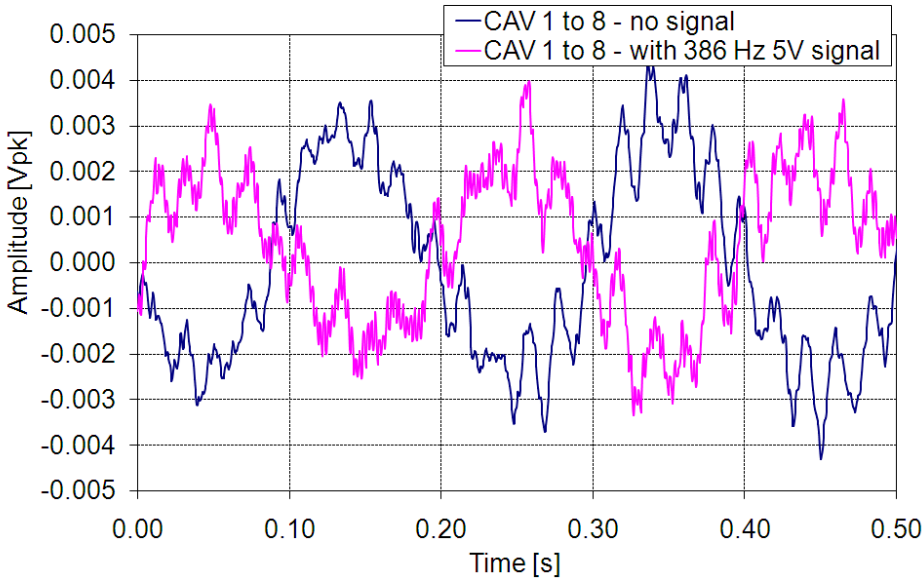

Fig. 5.30 - cav. 8 microphonics with and without exciting signal on cav. #1

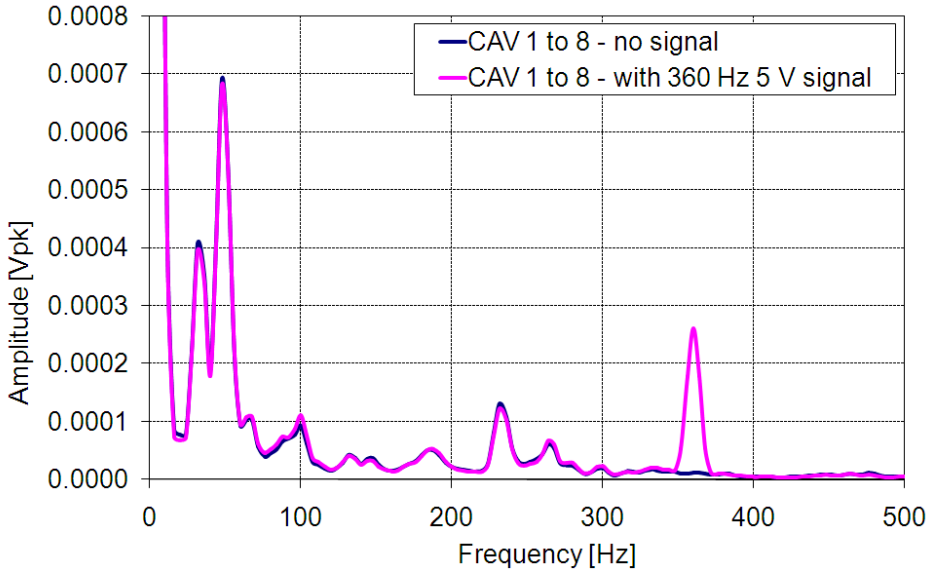

Fig. 5.31 - FFT of cav. 8 microphonics with and without exciting signal on cav. #1

6 THE COAXIAL BLADE TUNER

This chapter is devoted, in its first part, to the deep review of the coaxial Blade Tuner in its original design and to the detailed mechanical analyses of its key components, up to the integration of fast actuators. Then, a Blade Tuner model with revised design that has been recently developed to introduce further improvements, is presented together with results from latest experimental tests.

Several finite elements modeling (FEM) simulations as well as analytical mechanical calculations have been performed to complete the analysis of each part of the coaxial tuner assembly, both for the original and for the revised design. Simulations have been computed for various elements at the reference room temperature of 300 K (RT), all relevant mechanical parameters of the used materials can then be found in appendix B. The main goal of the performed FEM analyses is to evaluate both the longitudinal mechanical stiffness and the stresses during operation for each component, in order to model the behavior of whole tuner.

6.1 A NEW TUNER FOR TESLA CAVITIES

Since 1998 the option of a coaxial tuner for TESLA cavities has been considered in the frame of the baseline design development for the final accelerator.

The design of the TESLA cryomodule, since the release of TESLA TDR [7] in 2001, is driven by the request of a very high filling factor so to reduce the accelerator length or to increase the effective accelerating field. One of the main improvement has been achieved in the interconnection between cavities. The TTF modules have installed cavities with a constant distance of 1384.8 mm, corresponding to a cell-to-cell distance of about 350 mm, exactly $3\lambda/2$ long. This length was actually chosen at the beginning of the linear collider studies only to obtain good cavity separation for the accelerating mode and simplicity in the phase adjustment. As a consequence, the effective accelerating gradient would be 17.8 MV/m only, in case cavities were operated at 25 MV/m, The fill factor, defined as cavity active length over cavity total length, has a low value of 0.75.

The main idea for the new tuner has been originally inspired by H. Kaiser [110] who studied a possible tuner solution for the *superstructure* option in TESLA [111]. This option relied on a different cavity chain layout, realized by means of non-resonantly coupled 7-cell cavities with shorter interconnection distance, corresponding to $\lambda/2$. This special design has been proposed in order to obtain an higher fill factor and simultaneously to increase the number of cells fed by a single input coupler.

Superstructure option has been later on discarded but the search for a minimization of inter-cavity distance remained as the critical point to reduce the accelerator footprint. As a consequence, the present ILC reference layout, as well as for the TESLA design report before it, assumes a coaxial solution since the reduced total cell-to-cell space is incompatible with the actual TTF tuner overall dimension.

Hence the development of a new frequency tuner able to fulfill the expected clearance requirements, has started. This new tuner has been designed to be coaxial with the cavity and, by means of elongation of the helium vessel, to deform the cavity geometry and consequently change the resonance frequency. The tuner assembly is mainly composed of two parts, the movement leverage and the bending rings. Fig. 6.1 shows the complete assembly of the tuner as mounted over the cavity helium vessel. The leverage system provides the amplification of the torque of the stepper motor, dramatically reducing the total movement and increasing the tuning sensitivity. A stepper motor, similar to those in use for the TTF tuner, is rigidly connected to the helium vessel and produces a rotation of the big arm in the center of the tuner. The movement of the big arm induces the rotation of the bending system that changes the cavity length.

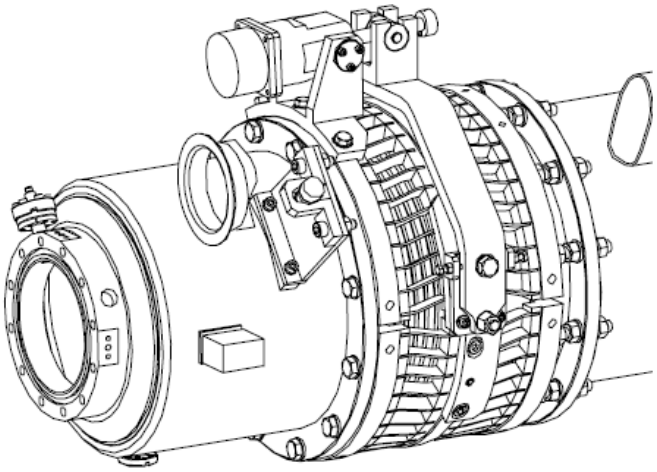

Fig. 6.1 – drawing of the original Blade Tuner (SuTu tuner) assembly

The bending system consists of three different rings: the two external rings, which are rigidly connected to the helium tank, and the one at the center, symmetrically divided in two halves. The big central arm is connected to the bending system in a way to produce the right rotation and the correct axial movement that provides the tuning. The rings are connected by thin titanium plates, or *blades*, that can change the cavity length (compression and tension) as a result of an azimuthal rotation in opposite directions of the two halves of the center ring.

The INFN group of LASA laboratory in Milan is been in charge of its development since the first prototype successfully tested at DESY in 2002, both in CHECHIA and in the superstructures test module inserted in the TTF string.

This prototype model (named as original Blade Tuner or SuTu tuner, from the former SUperstructures TUner) actually represent the reference design for the entire Blade Tuner activity, being the basis of each subsequent model up to the present new Blade Tuner with lighter design. One of the realized tuner prototypes, #IV or SuTu_IV, is shown in Fig. 6.2.

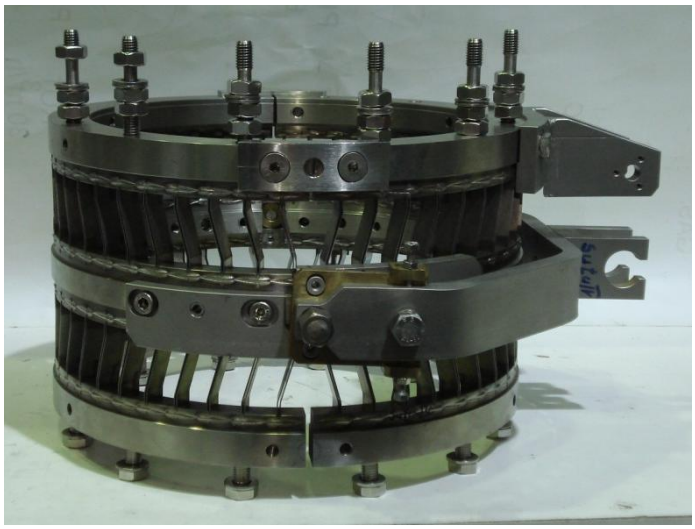

Fig. 6.2 – one of the Blade Tuners used for superstructures tests, the SuTu_IV

In conclusion, the Blade Tuner development activity is currently included in a broad international scenario, wherein different groups are working on competing designs for the final ILC cavity tuner. Beside the prototypes already mentioned in the dissertation, the TTF tuner, its direct development named PTS in charge of the CEA Saclay group [100] and the coaxial Blade tuner, three further proposal are under studying in US and Japan. KEK laboratory [112] in Japan proposed two tuner prototypes, the *Slide Jack Tuner* and the *coaxial Ball Screw tuner*. Finally, a tuner from TJNAF CEBAF upgrade [113], called *Renascence Tuner* is proposed.

All of the proposed tuners might work either directly with TESLA type cavities or need some minor modification, each one has two separate mechanisms for the slow and fast tuning action and in general piezoelectric stack are used for the latter case. Except for the TTF and PTS models, presented prototypes are meant to be installed coaxially to the cavity so to reduce inter-cavity distance. Major differences emerge in the position of active elements of tuners. In fact, while for the European and US design both stepper motor and piezo elements are assembled and work in cryogenic temperature, proposals developed in KEK show different solutions. In the Ball Screw tuner the motor is mounted outside the cryostat and therefore the maintenance is possible, but the piezoelectric actuators are located close to the cavity, in the Slide Jack Tuner both piezo stacks and stepper motors are placed at intermediate temperature inside of the vacuum vessel. Anyway, although KEK proposal are favorable for what concerns maintenance and replacement in case of failure, the price of such solution is the highest (further details on proposed TESLA tuners can be found in [28][114]).

6.2 ORIGINAL BLADE TUNER DESIGN

The working principle of the tuner is based on the deformation of the blades that deform from the rest position (slant of 15° respect to the central axis) to a different configuration producing an elongation or shortening of the tuner itself. This deformation is generated by the rotation of the central rings in respect to the lateral ones. In order to reduce to nearly zero the relative rotation of the lateral rings and to balance the torsional moments, the central rings rotate in opposite directions and the blades are assembled symmetrically respect to the horizontal plane. The rotation of the central rings is obtained through an outer leverage that is directly moved by the stepper motor and, through a connecting plate, induces a displacement in opposite directions of the edges of the central rings. A schematic representation of the kinematics of the tuner in its original design is provided in Fig. 6.3.

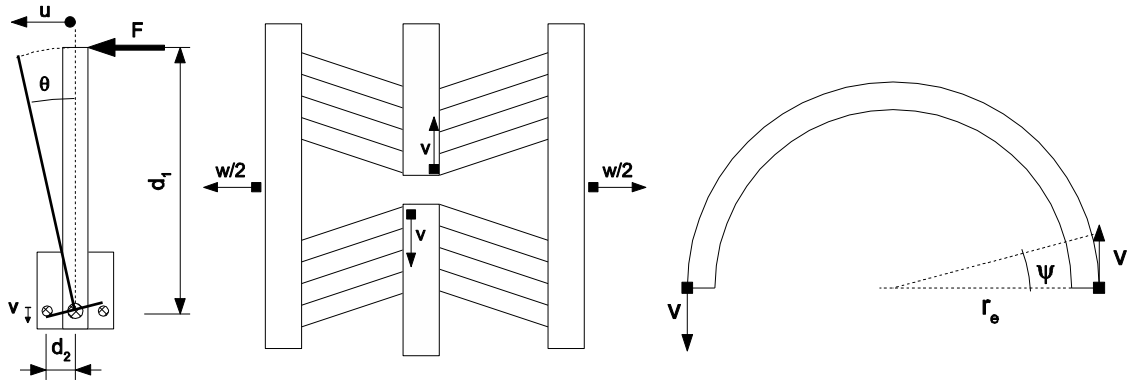

Fig. 6.3 - cinematic description of the Blade Tuner tuning system

Relations among the involved variables are induced from simple geometrical considerations:

$$\theta = \arctan\frac{u}{d_1} \cong \frac{u}{d_1}$$

$$v = d_2 \tan\theta = u\frac{d_2}{d_1}$$

$$\psi \cong \frac{v}{r_e} = \frac{u}{r_e}\frac{d_2}{d_1} \cong \theta\frac{d_2}{r_e} \tag{6.1}$$

Main composing parts of the assembly will be now separately presented and analyzed.

6.2.1 LEVERAGE KINEMATICS

The maximum displacements that can be applied with the leverage is limited either by the contact of the central rings themselves or by the maximum movement of the mechanism itself. In this latter case the limiting part of the mechanism capabilities is the connecting plate between the leverage itsel f and the tuner central ring. This plate has two slot with eccentricity of 1.25 mm as shown in Fig. 6.4.

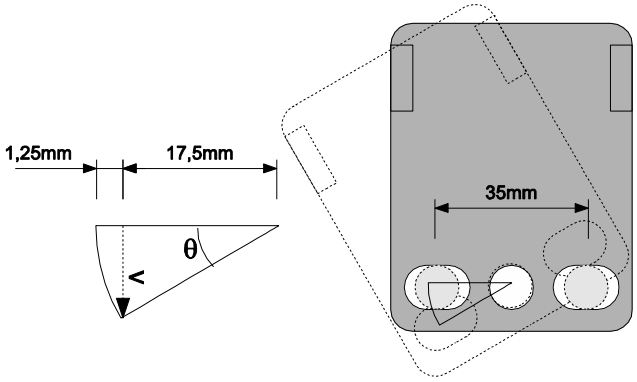

Fig. 6.4 – leverage connecting plate kinematics

Referring to the conceptual schemes of Fig. 6.3 and Fig. 6.4, actual dimensions and limit values for the original design of the Blade Tuner leverage kinematics are resumed in Tab. 6.1.

d_1 mm	d_2 mm	r_e mm	**Max. displacement - Central rings limit central rings distance 7 mm**			**Max. displacements – plate limit plate slot eccentricity 1.25 mm**		
			v_{max} mm	ψ_{max} deg	u_{max} mm	θ_{max} deg	v_{max} mm	u_{max} mm
204.5	17.5	150	3.5	1.34	40.9	21	6.7	82

Tab. 6.1 – dimensions and limits of the Blade Tuner leverage mechanism

The final maximum displacement of the mechanism is actually limited by the contact of the two central rings. Therefore in order to obtain a larger tuning range the geometry of the central rings has to be modified, for example increasing the space between them.

Due to the complexity of the mechanism, a simplified FEM model has been used in order to evaluate the actual stiffness of the assembly. Some parts were neglected and, when possible, the connections have been considered as bonded. The ANSYS finite element model used for analysis is reported in Fig. 6.5, the mesh results are also visible.

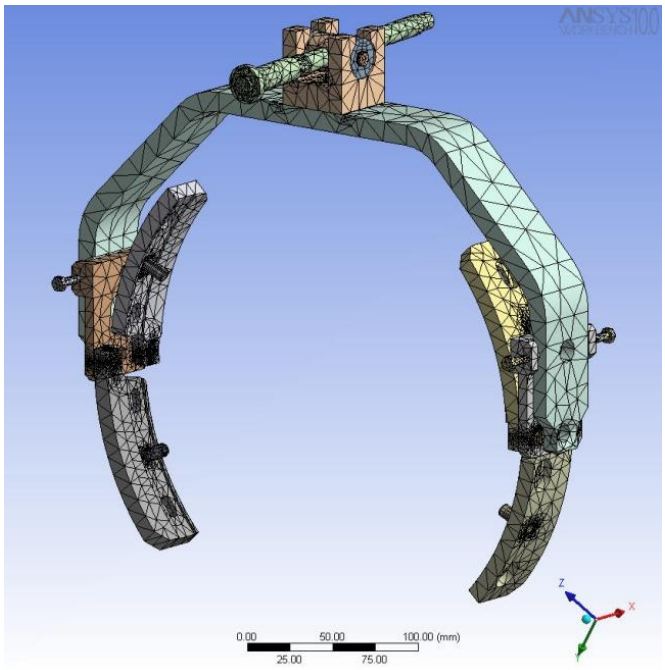

Fig. 6.5 - finite element model of the mechanism

A finite element analysis of the leverage system has then been performed in order to evaluate its stiffness and the maximum stresses. As a reference, an analysis has been performed by imposing a rotation of $\theta = 0.1°$ to the saddles connected to the central rings of the tuner while the driving shaft is constrained at its far end. Considering also the rotation of the central rings in the calculation, the reaction torque at the saddle has been computed and evaluated to be $M_z = 516.4$ Nm.

6.2.2 SINGLE BLADE ANALYSIS

The Blade Tuner core is composed of two parts symmetric respect to a plane, the mechanical analysis can therefore be focused firstly on one of these components. The two parts, called half-tuner, are made of three half rings and two series of blades, positioned symmetrically respect to the central ring. As said, this configuration allows to obtain an axial movement of the lateral rings by means of an opposite rotation of the two central ones. Torsion and shear forces on the helium tank are also minimized. The individual blade properties has been deeply characterized in order to fully understand its behavior under each possible load condition that can occur during operation. The blade original design considered in this paragraph represents the basis also for the revised Blade Tuner model realized as well as for its further developments. Blades used in the original design of

the Blade Tuner are realized in Titanium (Ti) gr. 5 (see Tab. b.2), specific dimensions are reported in the following table, according to the scheme in Fig. 6.6:

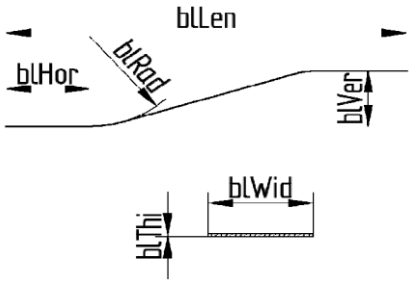

Fig. 6.6 – reference scheme for the blade dimensions

geometry	**material**	**blHor** mm	**blCla** mm	**blVer** mm	**blLen** mm	**blRad** mm	**blWid** mm	**blThi** mm
original	Ti – gr5	12	8	7.5	56	15	15	0.5

Tab. 6.2 – blade dimensions for the original Blade Tuner design

A simple 2D FEM model of a single blade, shown in Fig. 6.7, has been used to analyze blade properties.

Fig. 6.7 – finite element model of a single blade

This model allows to consider only the in-plane deformations, nevertheless an useful estimation of the blade stiffness can be obtained if three analyses with different boundary conditions are performed. Then this information can be used to have a first estimation of the stiffness of the a half-tuner. The three cases, showed in Fig. 6.8, represent the possible behavior of the tuner when all symmetries have already been considered.

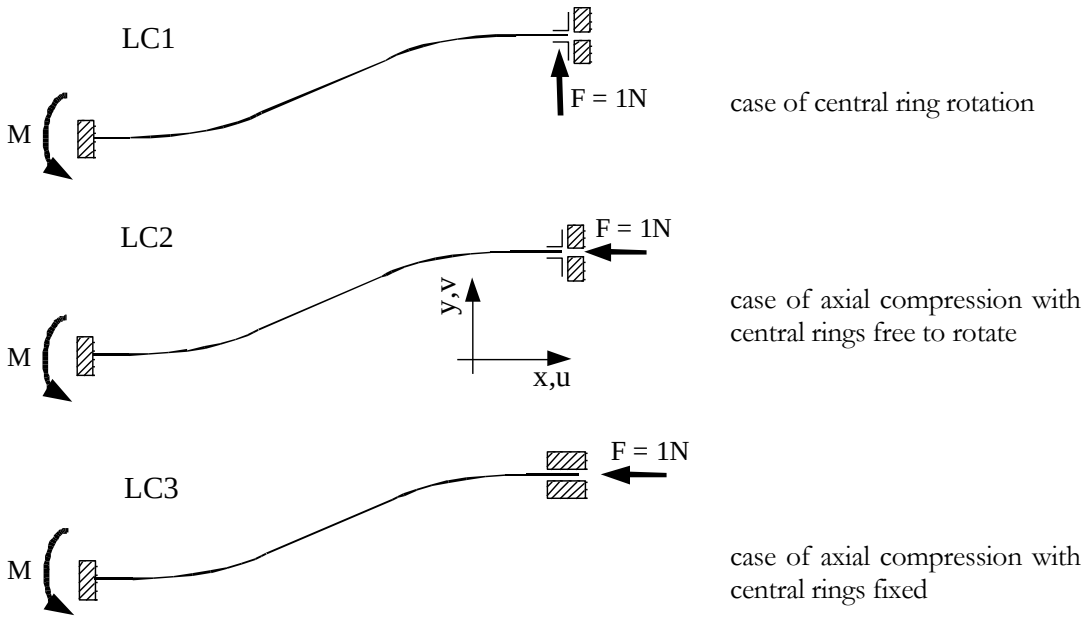

Fig. 6.8 - load cases considered for the analysis of the blade

After performing FEM analysis of the shown model for each of these blade load cases, the following values are obtained:

Load case	Δu (mm)	Δv (mm)	F_y (N)	M (Nmm)
1	-0.075	0.311	1	-20.46
2	-0.0181	0.0749	0	-3.945
3	$-0.297 \cdot 10^{-3}$	0	0.236	0.959

Tab. 6.3 - single blade analysis results

Using computed values referred to a single blade, and considering that 2 x 2 x 23 = 92 blades are used for each half tuner, the following compliance are obtained for the half tuner:

- load case 1: rotation of the central ring without constraints

$$C_{blade}^{mix} = \frac{\Delta u}{F \cdot r_b} = \frac{-0.075}{1 \cdot 140.5} = -5.34 \cdot 10^{-4}\,[N^{-1}]$$

$$C_{blade}^{rot} = \frac{\arcsin\frac{\Delta v}{r_b}}{F \cdot r_b} = \frac{\arcsin\frac{0.311}{140.5}}{1 \cdot 140.5} = 1.58 \cdot 10^{-6}\,[N^{-1}mm^{-1}]$$

$$C_{half-tuner}^{mix} = \frac{2}{92} C_{blade}^{mix} = -2.8 \cdot 10^{-6} \, [N^{-1}]$$

$$C_{half-tuner}^{rot} = \frac{1}{92} C_{blade}^{rot} = 1.71 \cdot 10^{-8} \, [N^{-1}mm^{-1}]$$

- load case 2: compression of the tuner with central ring free to rotate

$$C_{blade}^{mix} = \frac{\arcsin \frac{\Delta v}{r_b}}{F} = \frac{\arcsin \frac{0.0749}{140.5}}{1} = 5.33 \cdot 10^{-4} \, [N^{-1}]$$

$$C_{blade}^{ax-free} = \frac{\Delta u}{F} = \frac{-0.0181}{-1} = 1.81 \cdot 10^{-2} \, [N^{-1}mm]$$

$$C_{half-tuner}^{mix} = \frac{1}{46} C_{blade}^{mix} = 1.16 \cdot 10^{-5} \, [N^{-1}]$$

$$C_{half-tuner}^{ax-free} = \frac{2}{46} C_{blade}^{ax-free} = 7.86 \cdot 10^{-4} \, [N^{-1}mm]$$

- load case 3: compression of the tuner: the central ring cannot rotate

$$C_{blade}^{ax} = \frac{\Delta u}{F} = \frac{-0.000297}{-1} = 2.97 \cdot 10^{-4} \, [N^{-1}mm]$$

$$C_{half-tuner}^{ax} = \frac{2}{46} C_{blade}^{ax} = 1.29 \cdot 10^{-5} \, [N^{-1}mm]$$

where:

- r_b is the mean radius of blades on tuner
- C^{mix} is the axial compliance due to a rotation of the central ring or viceversa
- C^{rot} is the torsional compliance due to a rotation of the central ring
- $C^{ax\text{-}free}$ is the axial compliance due to a axial displacement of the central ring when free to rotate
- C^{ax} is the axial compliance due to a axial displacement of the central ring

6.2.3 HALF AND COMPLETE TUNER

Beside the first simplified analysis shown in the previous paragraph, a more complete FEM simulation of the whole half-tuner has been performed in order to take into account all possible boundary conditions. The 3D model used and its mesh are reported in Fig. 6.9

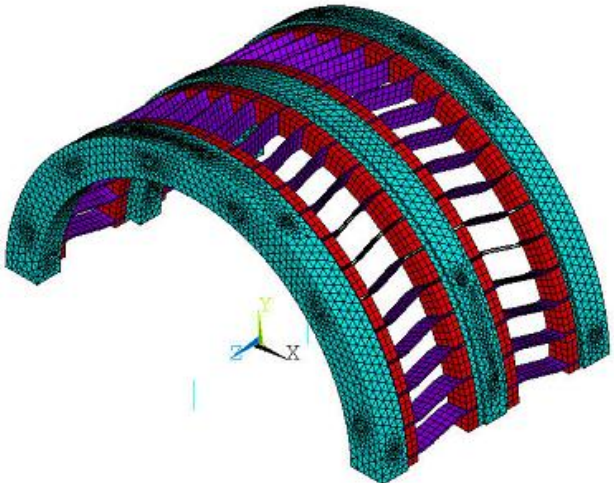

Fig. 6.9 – finite element model of the half Blade Tuner

Given the symmetries of the tuner, generalized displacements have been considered to describe the relative movement of the central ring with respect to the lateral ones. These displacements (two translations and one rotation) are reported in Fig. 6.10. The symbols u, v and w refer to the displacement in x, y and z directions respectively, while accordingly θ, Φ and ψ refer to the rotation around the axis.

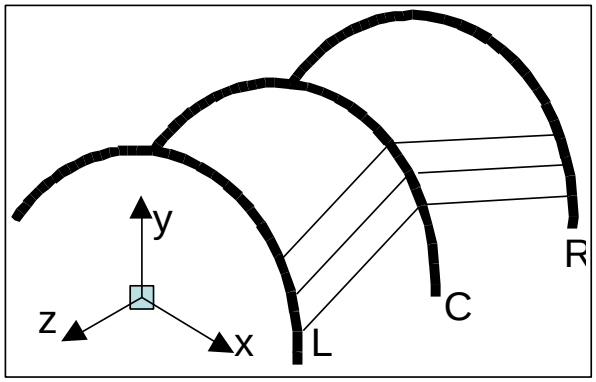

Fig. 6.10 - generalized displacements for the half Blade Tuner analysis

Generalized forces are also introduced and associated to the respective relative displacement as explained in Fig. 6.11.

After performing several analyses with only one generalized displacement active, the following forces-displacements relations, relative to half tuner, have been obtained:

$$\begin{Bmatrix} \hat{F}x \\ \hat{F}z \\ \hat{M}z \end{Bmatrix} = 10^6 \begin{bmatrix} 0.0142 & 0.025 & -0.8403 \\ 0.025 & 0.1642 & -5.450 \\ -0.8403 & -5.450 & 184.4 \end{bmatrix} \begin{Bmatrix} u_{LC} \\ w_{LC} \\ \psi_{LC} \end{Bmatrix}$$

$$(N, Nmm) \qquad\qquad (mm, rad)$$

In these relations Fx, Fz and Mz are opposite to the reactions obtained by the finite element analyses and the symbol ^ is used when half tuner is considered. This matrix is the stiffness matrix of the half tuner when all symmetries are considered. The compliance matrix can be easily obtained:

$$\begin{Bmatrix} u_{LC} \\ w_{LC} \\ \psi_{LC} \end{Bmatrix} = 10^{-6} \begin{bmatrix} 96.51 & -3.614 & 0.3349 \\ -3.614 & 312.3 & 9.211 \\ 0.3349 & 9.211 & 0.2791 \end{bmatrix} \begin{Bmatrix} \hat{F}x \\ \hat{F}z \\ \hat{M}z \end{Bmatrix}$$

and for sake of comparison with experimental data the following relations are found:

$$\begin{Bmatrix} u_{LC} \\ w_{LC} \\ \hat{M}_z \end{Bmatrix} = 10^{-6} \begin{bmatrix} 96.95 & -14.67 & 1.2 \cdot 10^6 \\ -14.67 & 8.316 & 32.998 \cdot 10^6 \\ -1.2 \cdot 10^6 & -32.998 \cdot 10^6 & 3.582 \cdot 10^{12} \end{bmatrix} \begin{Bmatrix} \hat{F}x \\ \hat{F}z \\ \psi_{LC} \end{Bmatrix} \tag{6.2}$$

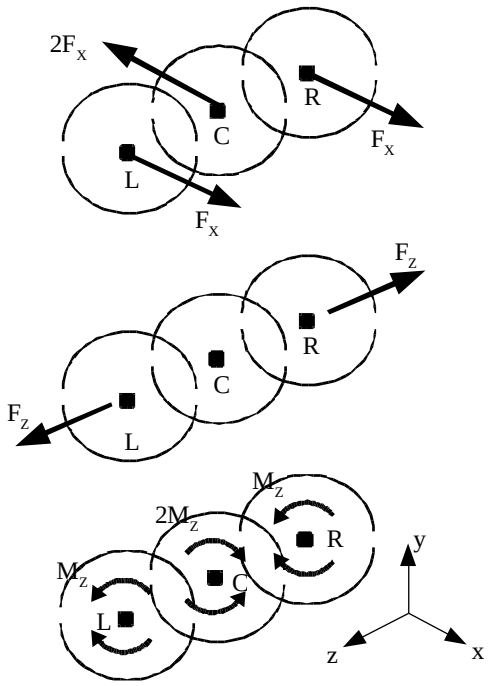

Fig. 6.11 – scheme for generalized forces and relative generalized displacement

Finally, the stiffness matrix of half tuner can be now used to evaluate the behavior of the whole Blade Tuner, considering only blade parts without leverage mechanism. The following assumptions are made:

- only the degree of freedom in the axial direction is considered between the two lateral rings.
- torsion and transversal force in x direction together with their associated displacements are relative to the central ring and are necessary in order to evaluate the behavior of the tuner equipped with the driving mechanism.
- $w_{LR} = w_L - w_R$
- $w_{LC} = w_{CR} = w_{LR}/2$
- $u_{LC} = -u_{CR}$
- $\psi_{LC} = -\psi_{CR}$

To simplify the computation, it is supposed to apply known forces to the tuner, then the only displacement variable that changes is w (the axial displacement) that now refers to the whole tuner, while the other displacements are always referred to half tuner (see Fig. 6.11). In terms of forces, Fx and Fz are now applied to the whole tuner, while the torsion Mz is always applied to the half tuner.

Therefore, given the result in (6.2) and considering a double axial stiffness due to the two half tuner and a double axial compliance due to the double length, the following relations, valid for the whole tuner, are obtained:

$$\begin{Bmatrix} u_{LC} \\ w_{LR} \\ \psi_{LC} \end{Bmatrix} = 10^{-6} \begin{bmatrix} 48.47 & -1.807 & 0.335 \\ -3.614 & 312.3 & 18.42 \\ 0.168 & 4.606 & 0.28 \end{bmatrix} \begin{Bmatrix} Fx \\ Fz \\ Mz \end{Bmatrix} \tag{6.3}$$

6.2.4 STIFFNESS ANALYSIS AND EXPERIMENTAL RESULTS

The tuner total longitudinal stiffness for the different possible configurations and load cases has been computed using the results presented in the previous paragraph. As an example, the computation for the nominal case of a tuner equipped with the leverage mechanism is here presented.

Firstly the relation between the tuner and the leverage rotation is reported (see Fig. 6.3 and (6.1)):

$$\psi_{LC} \cong \theta \, d_2/r_e \tag{6.4}$$

From the principle of virtual work [37], the relation between the torque M_z on the central half-ring of the tuner and the torque M_{Lev} applied at the leverage connection can be determined. When the whole tuner is considered instead of the two half-rings L and C the result is given by:

$$M_{Lev}\,\delta\theta = 4\,M_z\,\delta\psi_{LC} \tag{6.5}$$

From the FEM analysis previously performed on the leverage mechanism (par. 6.2.1), it is possible to define the leverage equivalent stiffness k_{mech} in response to the rotation θ of the saddles connected to central half-tuner:

$$k_{mech} = \frac{2M_z}{\theta} = 591.8\ \text{kNm} \tag{6.6}$$

Therefore, finally, considering results in (6.4), (6.5) and (6.6) it is possible to determine the following relation:

$$M_z = \frac{M_{Lev}}{4}\frac{\delta\theta}{\delta\psi} = \frac{k_{Lev}\theta}{4}\frac{\delta\theta}{\delta\psi} \cong \frac{k_{Lev}}{4}\left(\frac{r_e}{d_2}\right)^2\psi_{LC} \tag{6.7}$$

where, from the geometry of the leverage expressed in (6.1),

$$k_{Lev} = \frac{2d_2}{r_e}k_{mech} \tag{6.8}$$

Relation in (6.7) allows to simplify the matrix expression in (6.3). Therefore substituting the relation for M_z in the tuner stiffness matrix it is possible to compute the tuner longitudinal stiffness for the real case, when the leverage mechanism is installed:

$$\begin{Bmatrix} u_{LC} \\ w_{LR} \\ \psi_{LC} \end{Bmatrix} = C \begin{Bmatrix} Fx \\ Fz \\ \frac{k_{Lev}}{4}\left(\frac{r_e}{d_2}\right)^2\psi_{LC} \end{Bmatrix} \rightarrow \begin{Bmatrix} u_{LC} \\ w_{LR} \end{Bmatrix} = \begin{bmatrix} C_{11}+C_{13}\dfrac{C_{31}\frac{k_{Lev}}{4}\left(\frac{r_e}{d_2}\right)^2}{1-C_{33}\frac{k_{Lev}}{4}\left(\frac{r_e}{d_2}\right)^2} & C_{12}+C_{13}\dfrac{C_{32}\frac{k_{Lev}}{4}\left(\frac{r_e}{d_2}\right)^2}{1-C_{33}\frac{k_{Lev}}{4}\left(\frac{r_e}{d_2}\right)^2} \\ C_{21}+C_{23}\dfrac{C_{31}\frac{k_{Lev}}{4}\left(\frac{r_e}{d_2}\right)^2}{1-C_{33}\frac{k_{Lev}}{4}\left(\frac{r_e}{d_2}\right)^2} & C_{22}+C_{23}\dfrac{C_{32}\frac{k_{Lev}}{4}\left(\frac{r_e}{d_2}\right)^2}{1-C_{33}\frac{k_{Lev}}{4}\left(\frac{r_e}{d_2}\right)^2} \end{bmatrix} \begin{Bmatrix} F_x \\ F_z \end{Bmatrix}$$

By substituting the values of C_{ij}, k_{Lev} and $F_x = 0$ N, $F_z = 1$ kN, the following total longitudinal displacement is found:

$$w_{LR} = 11.95\ \mu\text{m}$$

This w_{LR} value corresponds to a longitudinal stiffness value for the whole tuner of:

$$k_{LR} = 83.7\ \text{kN/mm}$$

For the obtained stiffness value the compliance of the motor and of the bearings have not been considered. Moreover the unavoidable clearance cannot be inserted in the FE analysis, therefore it has been important to verify this value with a dedicated experimental measure.

This test has been performed for the Blade Tuner nominal configuration, therefore with the central ring constrained by the usual leverage mechanism. As a reference, an additional measure has been performed with the central ring constrained by means of two rigid links between the half rings. An axial load was then applied using appropriate weights and the displacements were measured by means of a LVDT sensor[38]. A picture of the experimental setup is shown in Fig. 6.12. A comparison among experimental values and results of both 3D half-tuner FEM model simulations and extension of 2D single blade analysis (par. 6.2.2) is shown in Tab. 6.4.

Fig. 6.12 - experimental compression test on Blade Tuner

[38] Linear Variable Differential Transformers (LVDT) are a class of electrical transformers used for measuring linear displacements. A cylindrical ferromagnetic core, attached to the object whose position is to be measured, slides along the axis of three solenoidal coils [139].

Boundary conditions for the central tuner ring		**Experimental** kN/mm	**2D model** kN/mm	**3D model** kN/mm
No rotation – links installed Translation allowed in axial direction Fx = 0; $\psi_{LC} = 0$		83.3	---	120.2
No rotation No translation $u_{LC} = 0$; $\psi_{LC} = 0$	load case 2	---	155	164.2
Free	load case 3	---	2.5	3.2
Leverage mechanism installed – real case		**25**	---	83.7

Tab. 6.4 – Blade Tuner axial stiffness values for different boundary conditions

A clear evidence from the comparison among experimental and simulated data comes from the fact that the final stiffness value expected from the 3D FEM analysis of the tuner in its nominal configuration is closer to the experimental result of the first case rather than the nominal one. This means that the real leverage and motor assembly is significantly far from an ideal and infinitely rigid boundary for the central ring of the tuner, as is instead the case for the stainless steel links installed for the first case. Finally, the measured value of 25 kN/mm corresponding to the actual Blade Tuner configuration will be considered further on as the reference value.

6.2.5 MODIFIED HELIUM TANK

In the case of TESLA cavities, the helium tank (He tank) must ensure mechanical integrity and stability against external forces allowing the elongation required by the installed tuning mechanism in order to change cavity frequency. In the case of the coaxial Blade Tuner, for these reasons a modified helium tank has been designed and realized placing a bellow in the middle of the tank, below the tuner rings as shown in Fig. 6.13 and Fig. 6.14.

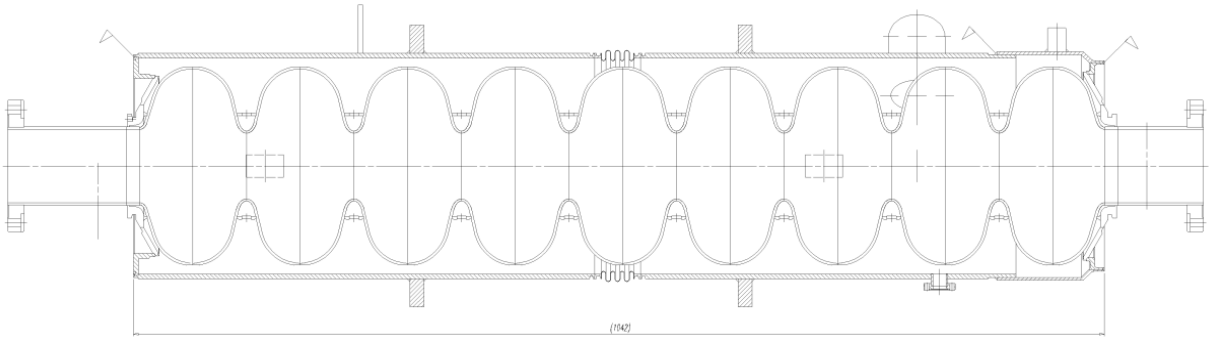

Fig. 6.13 – drawing of the cross section for the cavity assembly with the modified He tank

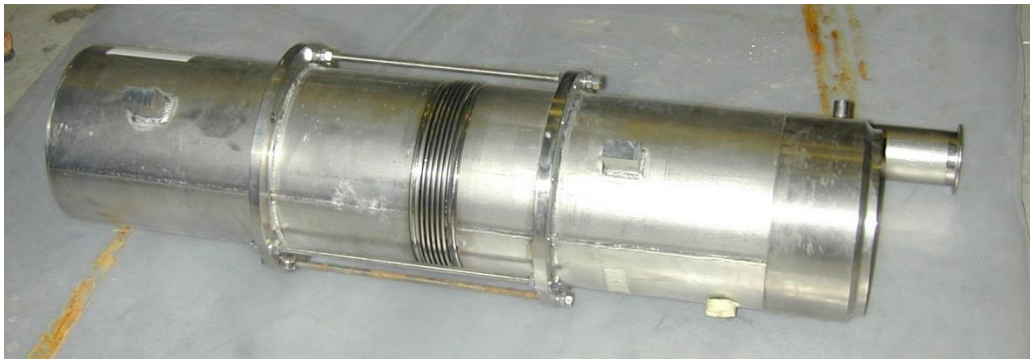

Fig. 6.14 – an actual model of the modified He tank, support screw rods visible between welded rings are temporarily placed to save the bellow from unwanted deformations

In order to evaluate the final longitudinal stiffness for this He tank revised design, FEM have been performed separately for both the vessel, considered as one single part of 1007 mm length, and the bellow. Similarly to every stiffness evaluation through a FE model, resulting value has been obtained imposing a longitudinal displacement of 1 mm at one side and computing the reaction force at the same point. Results for the helium vessel components are k_H = 302.4 kN/mm and k_B = 0.19 kN/mm longitudinal stiffness for the vessel and the bellow respectively. In those cases, FEM analyses were conducted on a 2D model of the element.

An essential role for what concerns the overall longitudinal stiffness of the assembly is then assumed by the two rings that connect the vessel to the cavity, usually named as end dishes or washer disks. For the modified Blade Tuner He tank, the end dishes have been adapted from the original TTF design without a devoted optimization. This issue is today under studying and it is presented in par. 6.9. As a reference, the ANSYS 2D finite element model of the end dish at the coupler side is reported in Fig. 6.15.

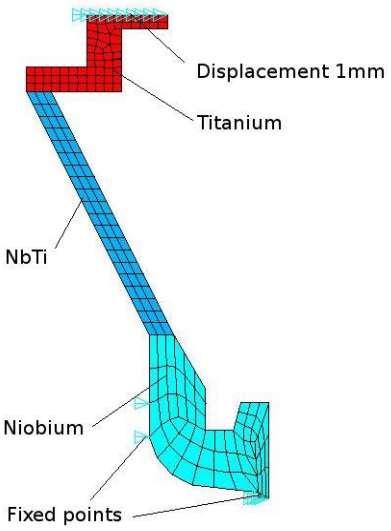

Fig. 6.15 - mesh of the end dish coupler side

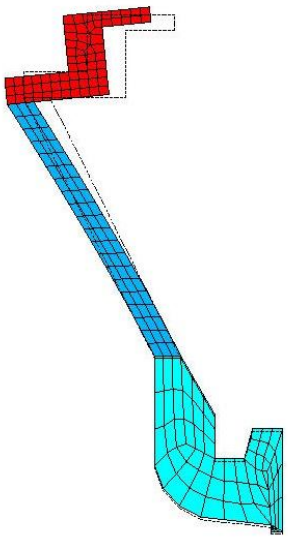

Fig. 6.16 – end dish coupler side deformed mesh

By imposing a displacement of 1 mm at the washer disk connection ring upper face, the structure reacts with a force that corresponds to an equivalent stiffness k_W^C of 24.8 kN/mm. The displacement obtained is shown in Fig. 6.16. A similar analysis, carried out on the end dish at the opposite side, or tuner side, that has a different design, reveled an higher stiffness value k_W^T of 32.2 kN/mm. These two results allowed to estimate the overall longitudinal stiffness k_W of the whole assembly composed by the series of both the coupler side and the tuner side end dishes. Therefore:

$$k_W = \frac{k_W^C \cdot k_W^T}{k_W^C + k_W^T} = 14 \ {}^{kN}/_{mm}$$

In order to check that the vertical displacements of the cavity, when it is installed in a modified He tank with central bellow and coaxial tuner, are compatible with the required alignment precision of 0.5 mm for the cold mass string, some axis-symmetric analyses with non axis-symmetric load have been also performed [115]. The used FEM model replicates the bending due to all dead loads in the system without accounting for additional external solicitations. The coaxial tuner is considered only as a load and the stiffening effect of the four threaded bars is not considered.

Resuming results, analysis revealed that the total dead load (cavity plus helium tank and piezo Blade Tuner) is 598 N and the maximum vertical deflection of the cavity respect to its ends is of 0.115 + 0.144 = 0.259 mm, lower than the specifications required for the alignment of the cells. Finally, also the tensile stress on the bellow has been analyzed. Neglecting the stress concentrations near the welding point, that are not accurately meshed, the maximum stress in the bellow is equal to 6.3 MPa, lower than the admissible value given by the manufacturer.

6.3 PIEZOELECTRIC ACTUATORS INTEGRATION

The original Blade Tuner, so far deeply characterized, have also been successfully tested in 2003 when a devoted superstructures cryomodule has been assembled and tested at the TTF facility. The four Blade Tuners installed completely fulfilled expectations for what concern clearance minimization and slow tuning range [116].

Therefore, the next step in terms of Blade Tuner development has been to introduce in its design the additional fast tuning action required at the high gradients, 35 MV/m, envisaged for the ILC operation. Physical aspects and issues related to cavity dynamic detuning and the need for its compensations have been already introduced in chapter 4.3.

The piezoelectric option for LFD compensation needs have been widely validated thanks to several successful tests previously performed with the TTF fast tuner, as for example FLASH module #6 measurements reported in chapter 5.2. Therefore a piezoelectric actuators based solution has been considered for the Blade Tuner fast tuning action. Anyway, the possibility to host different fast actuating solutions has been considered for the fast tuning integration, among other guidelines as:

- Commercial but affordable piezo elements as the first choice for actuators.
- Flexible actuators accommodation so to preserve the possibility to install piezo of different sizes or even completely different solutions (e.g. magnetostrictive etc. [28]).
- Ensure slow tuner efficiency even against an eventual complete failure of fast actuators.
- Keep the overall design as simple as possible so to reduce the number of additional elements compared to the existing Blade Tuner and lower costs.
- Search for an high axial stiffness for the final assembly so to lower the sensitivity to Lorentz force detuning as remarked in par. 3.3.2, therefore easing fast actuators requirements.

The detailed results obtained by the FEM analyses of the Blade Tuner and its components, discussed in previous paragraphs and which provided accurate information on stresses, deformations and stiffness, have been also used for the integration of the fast tuning elements. Piezoelectric actuators, that represent the reference choice, are subject to several requirements limiting the possible design configurations. First of all, the piezoelectric actuators cannot be subject to tension forces, and bending and shear actions need to be carefully avoided. Moreover, in order to maximize their lifetime, a correct preload range needs to be guaranteed under all operating condition (see paragraph 4.4.2).

In addition to that, the characteristic behavior of piezo operation at cryogenic temperatures, in terms of stroke and preload effects, has undergone a systematic investigation. Some results have been shown in previous paragraph 4.4.

Finally, referring to the typical values of the TESLA type structures in terms of cavity elasticity and tuning requirements (see paragraph 2.4), piezoelectric elements have been integrated by inserting two elements between one of the end rings and the corresponding flange on the He vessel, as shown in Fig. 6.17 and Fig. 6.18 where He tank and cavity are not shown for simplicity. Figures are color-coded by part material: blue denotes Ti, gray stainless steel, yellow CuBe and red brass. The piezo elements are the dark gray rectangular bars acting on the left Ti ring.

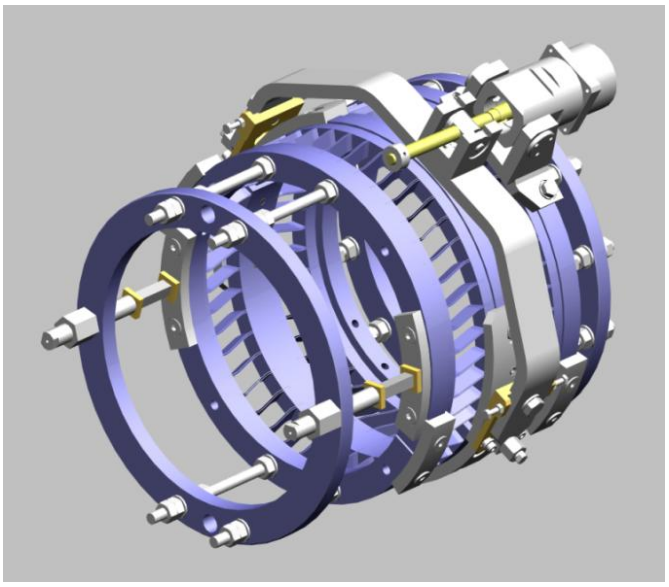

Fig. 6.17 – the Blade Tuner design after piezo actuators integration

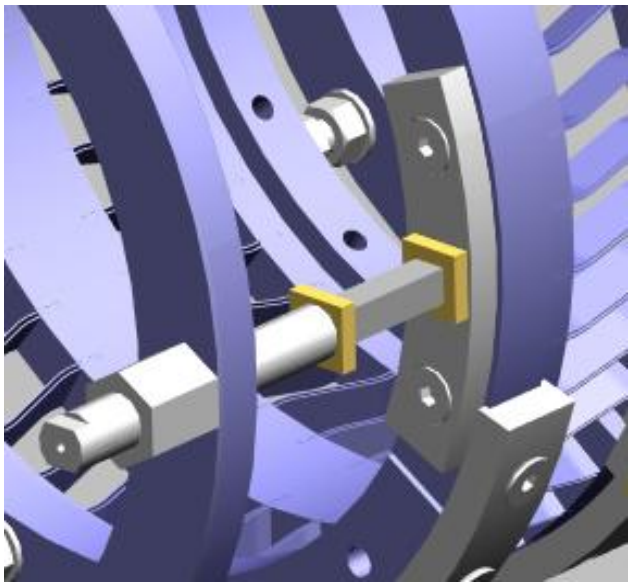

Fig. 6.18 – detailed view of piezo integration in the Blade Tuner

The main idea below this design choice has been to allow the cavity itself, through its axial stiffness, to generate the mechanical preload needed by the piezo actuators (see par. 4.4.2). Moreover, a revised cavity pre-tuning procedure has been studied in order to guarantee a correct range of preload values on the piezoelectric elements along the entire slow tuning range. This procedure allows also avoiding the "neutral" point of the leverage system and requires that the tuner operation always acts stretching the cavity, thus compressing the piezoelectric elements.

The position of the piezo actuators has been carefully chosen in order to avoid possible stresses due to the deflection and vibration of the helium tank. The active elements are kept in position by means of supports as shown in Fig. 6.18: they can accommodate elements of length up to 72 mm and a spherical head can be used in order to minimize shear and bending forces.

In addition to piezo, four threaded bars have been introduced in the design on the upper and lower side of the assembly (see Fig. 6.17). These bars, parallel to the piezo elements accomplish two different tasks. First of all they are needed during transportation, handling and assembly phases to avoid inelastic deformations of the bellow. In this case they are tightly bolted at both ends to provide stiffness to the system. Furthermore, in the operating condition, the inner bolts are loosened by a calibrated distance (less than a mm) and the bars act as safety devices in case of piezo mechanical failure or overpressure conditions inside the helium tank. With respect to the original system used for the TTF superstructures, the leverage system has been rotated to one side, in order to avoid the mechanical interferences with the Invar rod (see 2.4.1) providing the cavity longitudinal alignment in the TTF CRY3 design. The overall final assembly is shown in Fig. 6.19.

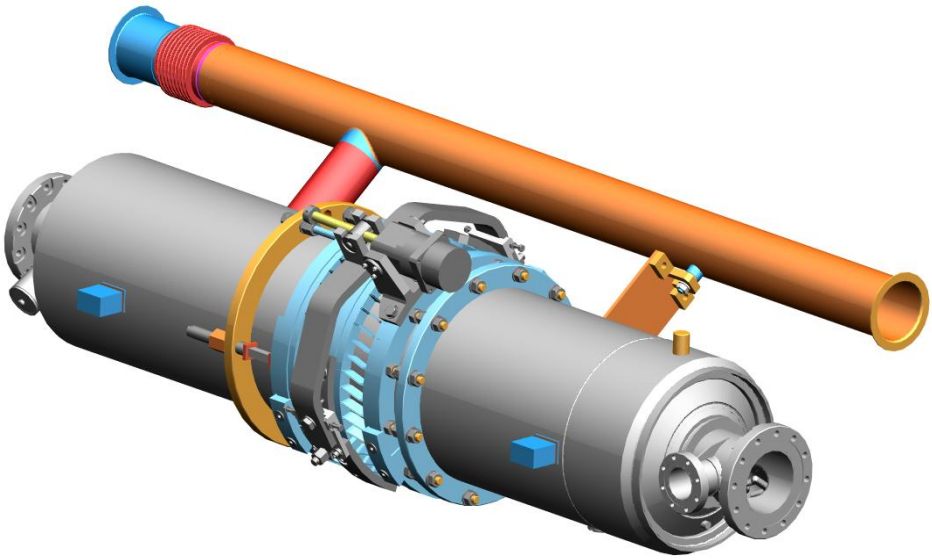

Fig. 6.19 - The cavity dressed with the modified helium tank and piezo Blade Tuner.

Choice of the reference piezo actuator to be installed in the Blade Tuner took advantage of the R&D activity on commercial piezoelectric actuators, described in

paragraph 4.4.3, and of the latest results concerning LFD compensation performances. Finally, two complete Blade Tuner assemblies with corresponding modified He tank have been manufactured and equipped in order to include the piezo active elements. For these first assemblies, 40 mm length piezo actuators from NOLIAC (NOLIAC_40) has been chosen for installation. Properties of interest for this piezo model are reported in Tab. 4.3.

6.4 CAVITY EQUIPPED WITH HELIUM TANK AND PIEZO BLADE TUNER

The behavior of the cavity when equipped with helium tank and tuning system can be now finally analyzed, since it strongly depends from the stiffness of each component. So in this paragraph axial and bending models are developed taking into account all the stiffness values obtained through analyses and simulations presented before. This model of the whole assembly is needed to evaluate the requirements for the piezo actuators and to check that the cavity external stiffness approaches the hypothetical value of 30 kN/mm as desired from the K_L' Lorentz coefficient analysis. Moreover this analytical approach can be applied also to different tuner models.

Firstly, the mechanical characteristics of all involved parts at room temperature are reported. The following analytical models and corresponding computations are strictly valid for the system at room temperature (RT), even if results are considered as valid also for the nominal working conditions at 2 K. This assumption is justified by the fact that it is expected that the stiffness of the core spring element in the system, the cavity, is not varying significantly from RT to 2 K temperature. In addition to this, the effect of temperature lowering on all the other components, from end dishes to tuner, is moreover positive that means that generally leads to an increasing of the stiffness of each component. So, the assumption to keep RT values for system modeling can be considered as the choice to face the worst case for the system. Moreover recent further FEM simulations performed at the FNAL laboratory seem to confirm the former assumption since the longitudinal stiffness increasing of the cavity, from 300 to 2 K, is expected to be limited to 10 % [117].

Part	Material	Axial stiffness	c (mm/kN)	k (kN/mm)	Notes
Helium tank	Ti Gr2	k_H	3.30	302.4	
Blade Tuner	Ti Gr2	k_T	40.0	25	From exp.
Cavity	Nb	k_C	330.8	3.023	
Washer disk	NbTi	k_W	71.4	14	Both disks
Piezo actuator	PIC 255	k_P	4.46	2 x 112	
Tuner bellow	Ti Gr1	k_B	5263	0.19	

Tab. 6.5 - mechanical characteristics of all involved Blade Tuner assembly parts at RT

Then, an axial model with associated displacements and forces is now presented both for slow and fast tuning actions.

In the slow tuning phase the stepper motor applies a deformation to the blades in order to tune the cavity to the right frequency. It is supposed that the Blade Tuner applies a displacement δ_t to the system: with this assumption the cavity will be stretched and the helium tank compressed. Globally the system remain in equilibrium and the axial stiffness model is shown in Fig. 6.20.

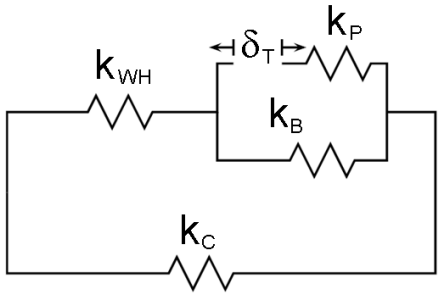

Fig. 6.20 - axial model for the slow tuning action of the Blade Tuner assembly

From simple considerations the expression of the total stiffness k_{WH} of the series composed by helium tank and both end dishes can be found:

$$k_{WH} = \frac{k_W k_H}{k_W + k_H} = 13.38 \text{ kN/mm}$$

Then, from equilibrium and congruence:

$$\begin{cases} \delta_C = \delta_T + \delta_{WH} + \delta_P \\ \delta_B = \delta_T + \delta_P \\ F_C = k_C \delta_C \\ F_{WH} = k_{WH} \delta_{WH} \\ F_P = k_P \delta_P \\ F_B = k_B \delta_B \\ F_{WH} = -F_C \\ F_{WH} = F_B + F_P \end{cases}$$

Solving the consistent equations it is possible to obtain the displacement of any part as a function of the tuner displacement:

$$\begin{cases} \Delta = k_P k_{WH} + k_B(k_C + k_{WH}) + k_C(k_P + k_{WH}) \\ F_{P=} - \dfrac{k_P[k_C k_{WH} + k_B(k_C + k_{WH})]}{\Delta}\delta_T \\ F_B = \dfrac{k_P k_B(k_C + k_{WH})}{\Delta}\delta_T \\ F_{WH} = -\dfrac{k_P k_C k_{WH}}{\Delta}\delta_T \\ F_C = \dfrac{k_P k_C k_{WH}}{\Delta}\delta_T \\ \delta_P = -\dfrac{k_C k_{WH} + k_B(k_C + k_{WH})}{\Delta}\delta_T \\ \delta_B = \dfrac{k_P(k_C + k_{WH})}{\Delta}\delta_T \\ \delta_{WH} = -\dfrac{k_P k_C}{\Delta}\delta_T \\ \delta_C = \dfrac{k_P k_{WH}}{\Delta}\delta_T \end{cases}$$

Finally, the axial force that every part has to withstand as a response to a tuner displacement of 1 mm are reported in Tab. 6.6, while the displacements are reported in Tab. 6.7.

Part	**Force for a δ_t = 1 mm (kN)**
Helium tank / End dishes	-2.435
Blade Tuner	-2.623
Cavity	2.435
Piezo actuators (total force)	-2.623
Tuner bellow	0.188

Tab. 6.6 - axial forces for a tuner displacement of 1 mm. Tensile forces are positive

Part	**Displacement for a δ_t = 1 mm (mm)**
Helium tank / End dishes	-0.182
Blade Tuner	1
Cavity	0.806
Piezo actuators	-0.013
Tuner bellow	0.988

Tab. 6.7 - axial displacements for a tuner displacement of 1 mm. Elongations are positive

In the fast tuning phase the piezoelectric actuators move in the order of some microns in order to opposite to the Lorentz force detuning. It is supposed that both the piezo

actuators in parallel apply a displacement δ_p to the system, with the assumption that the cavity is stretched and the helium tank compressed. Neglecting the dynamic effects, the resulting axial stiffness model is shown in Fig. 6.21.

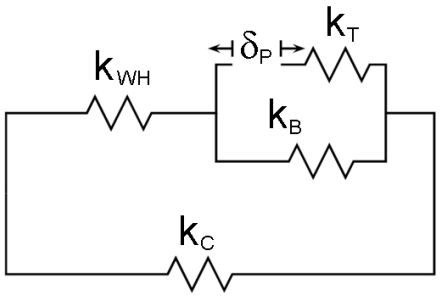

Fig. 6.21 - axial model for the fast tuning action of the Blade Tuner assembly

Following the same analytical procedure of the previous case, except for the δ_t in δ_p and k_p in k_t substitutions, results can be found from equilibrium and congruence and then solving the consistent equation. The axial force that every part has to withstand for a piezo displacement of 1 μm are reported in Tab. 6.8, while the displacements are reported in Tab. 6.9.

Part	**Force for a δ_p = 1 μm (N)**
Helium tank / End dishes	-2.229
Blade Tuner	-2.401
Cavity	2.229
Piezo actuators (total force)	-2.401
Tuner bellow	0.172

Tab. 6.8 - axial forces for a piezo actuators displacement of 1 μm. Tensile forces are positive

Part	**Displacement for a δ_p = 1 μm (μm)**
Helium tank / End dishes	-0.167
Blade Tuner	-0.096
Cavity	0.737
Piezo actuators	1
Tuner bellow	0.904

Tab. 6.9 - axial displacements for a piezo actuators displacement of 1 μm. Elongations are positive

Finally, the performed analysis showed that the actual efficiency of the slow tuning action for the Blade Tuner can be estimated in 80.5 % while it is 73.7 % for the fast tuning action. These results are particularly important for piezo actuators specifications since they mean that it must be expected for around ¼ of the available piezo stroke not to be useful for the LFD compensation purposes. Anyway, also considering actuator properties and

requirements presented in par. 4.4, 40 mm long piezo stacks from NOLIAC (NOLIAC_40) that have been chosen for an initial design grant sufficient stroke margin at cold. Moreover an even safer solution, in terms of performances margin, has been considered and it is based on even longer piezo stacks, 70 mm long and 15 x 15 mm cross section from NOLIAC (NOLIAC_70, see Tab. 4.3).

The presented model for the complete cavity system is then also useful to evaluate the cavity external stiffness. According to the schematic representation in Fig. 6.20, the k_{ext} value can be simply obtained computing the equivalent total stiffness for the upper section of the scheme including end dishes, bellow, piezo and tuner. The resulting value is k_{ext} = 8.3 kN/mm, therefore significantly lower than the goal value of 30 kN/mm introduced in par. 3.3.2. It is anyway clear from the mechanical analyses performed, see results in Tab. 6.7 and Tab. 6.9, that the actual main stiffness loss as well as the main tuner displacing action loss are located in the cavity end dishes, that are the softer elements in the whole cavity constraining assembly. This limiting effect is preserved also if, for instance, the stiffness of the tuner mechanism is raised, as visible in Fig. 6.22 where the resulting k_{ext} is plotted as a function of the k_T according to the current system configuration.

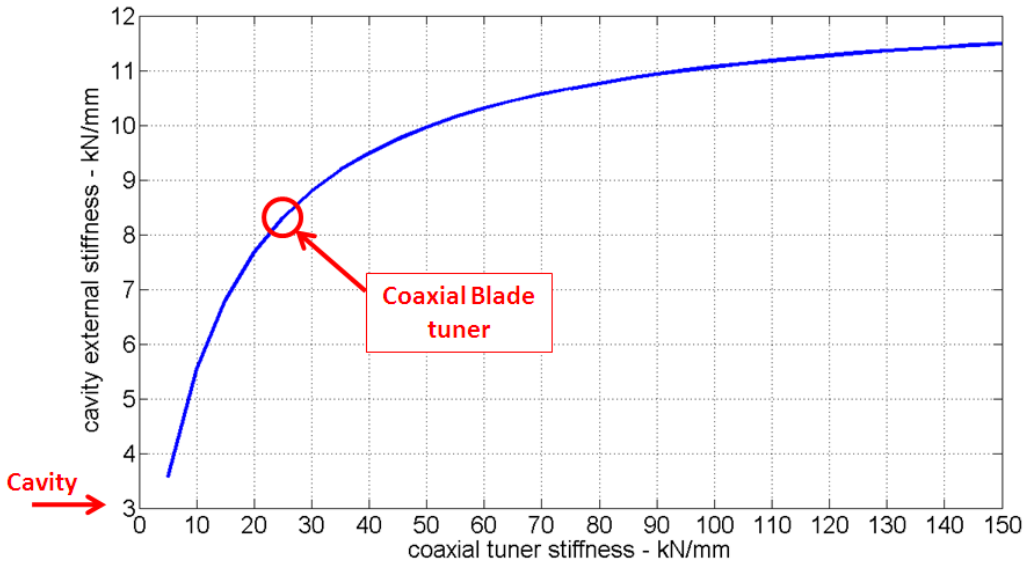

Fig. 6.22 – cavity external stiffness as a function of coaxial tuner stiffness, the current design of the modified He tank and end dishes is assumed

So, even if some limited improvement is possible, analysis confirms that it is not possible to reach an optimum external stiffness value with the current end dish configurations for the coaxial tuner. The role of the end dishes therefore become critical, especially in the case of a coaxial tuner, when the tuning displacement is transferred to cavity through both of them.

As reference, considering for instance the TTF tuner assembly instead of the coaxial one but installed on the same system configuration, the proposed spring model can be

used with the assumption that only the coupler side end dish contributes to the k_{WH} value. So, for a k_{WH} of 22.9 kN/mm the k_{ext} results to be about 16 kN/mm. So, although the estimated external stiffness for the TTF tuner case is almost two times higher than the coaxial tuner case one, the actual improvement in term of dynamic Lorentz coefficient is lower as can be inferred by the plot in Fig. 6.23, where results from K_L analysis in par. 3.3.2 have been used.

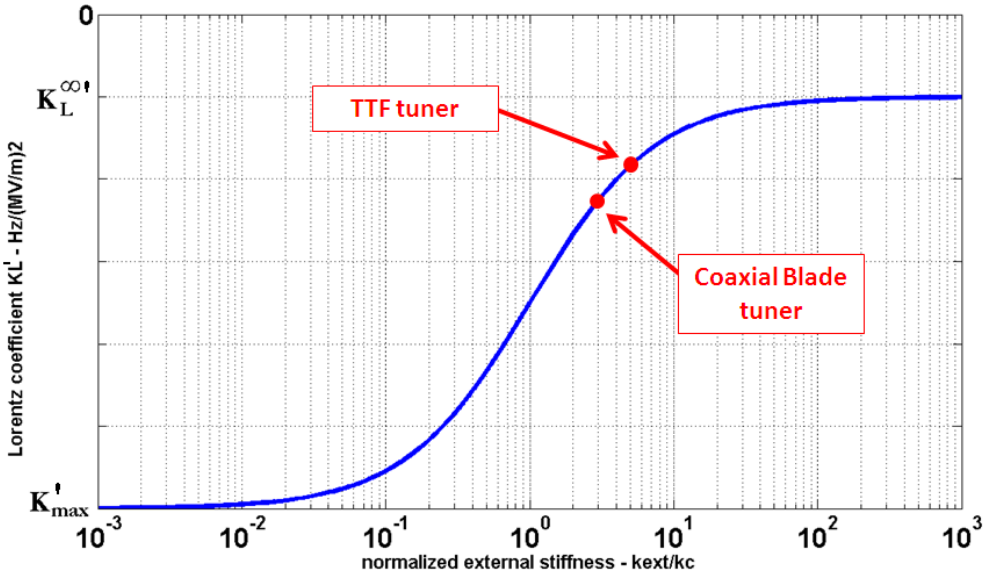

Fig. 6.23 – LFD coefficient as a function of the normalized external stiffness for both the TTF and coaxial tuner solutions

Therefore, it is possible to expect for the coaxial tuner solution to lead to an higher sensitivity to Lorentz force detuning but, in parallel, to ensure an higher fast tuning efficiency than the TTF original solution, that is limited by the same leverage geometry itself.

In conclusion, it is clear that in any case the current helium tank end dish design must be revised in order to reach higher stiffness for the cavity constraining mechanism and to increase tuning efficiency. Therefore, in parallel to the development of the coaxial tuner itself in view of large scale production and costs reduction, the study of a new end dishes design is ongoing. The main result in the frame of the former activity has been the realization and the test of renewed design model for the Blade Tuner. Details on this will be presented in following paragraphs. Instead status and perspective for the latter one are reported in par. 6.9.

6.5 THE NEW BLADE TUNER DESIGN

Since 2003, an activity is ongoing mainly focused on the redesign of the Blade Tuner in view of the long term feasibility of the ILC proposal [1]. Toward this goal all components have been properly engineered and cost, having in mind the perspectives of the large scale production foreseen for the collider (more than 16000 components for the baseline 500 GeV design). The original Blade Tuner as it is shown in Fig. 6.17, has been the starting point of this activity and it allowed several improvements. The whole weight of the original mechanism is approximately 20.5 kg. Each half blade-ring assembly has an array of 23 "packs" of 2 blades on each side, for a total of 184 blades. The blade packs for the two halves of the blade-ring assembly are electron-beam welded in a single pass with a special tooling device, in order to limit any unnecessary loading/unloading procedures of the electron beam welding machine, which leads to an increase in costs and to longer manufacturing times

6.5.1 A SLIM AND CHEAPER DESIGN

On this base, exploration of possible simplifications and cost reduction efforts for an industrial scale Blade Tuner began. Titanium has been chosen as the reference tuner material in the early stage of the design development activity. As for the original Blade Tuner model, this choice grants both thermal shrinkage compatibilities with the materials used for the helium tank and cavity (respectively, Ti and Nb), and good elastic and strength properties, which allow to reduce the stresses in the flexural elements. Later on cheaper structural materials options, as stainless steel, have been considered.

First of all, a conceptual preliminary design has been presented [118]. By lowering the requirements on the ring-blade stiffness a first "lighter" version was devised, which reduces the needed material and the number of machining and weld procedures. A preliminary result of this study is shown in Fig. 6.24, using the same material color coding used for previous Fig. 6.17.

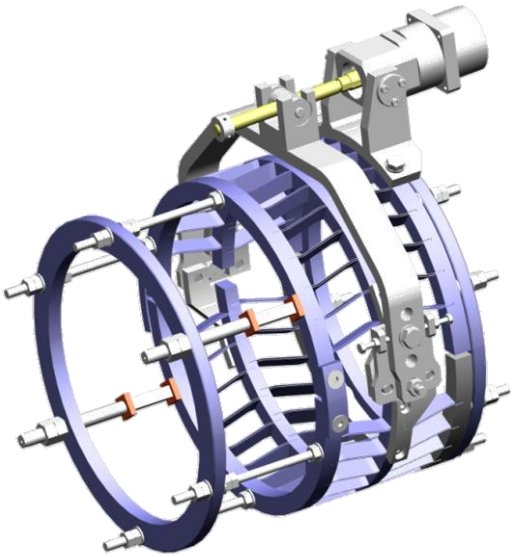

Fig. 6.24 – prototype revision of a lighter Blade Tuner

The width of the Ti rings has been reduced, as well as the number of blade elements. Now the system has an array of 14 "packs" of 2 blades on each side, for a total of 112 blades, with a 40% reduction in the number of blade packs, and a consequent reduction of the assembling time and number of EBW welds. This leads to a corresponding decrease of the nominal stiffness of the ring-blade mechanism that is anyway consistent with the overall stiffness requirement dominated by the other system components, mainly by the helium tank end dishes (see par. 6.4). Fig. 6.25 shows the details of the blade packing into the tuner rings in the two designs.

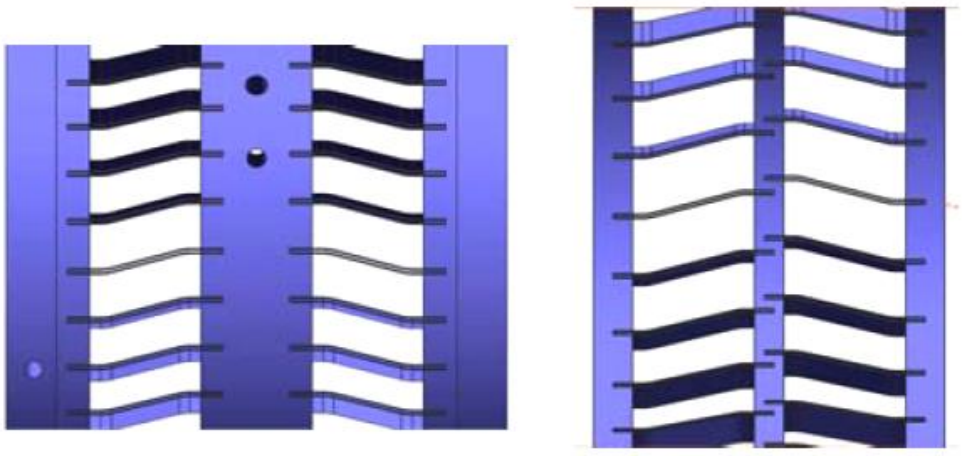

Fig. 6.25 – comparison between the original design (left) and the lighter prototype (right)

In this case the blade position at the central ring is no longer collinear on the two opposing sides, but is assembled in an alternated pattern, allowing welding the two

opposite blade packs in a single EBW seam. The total weight of the tuner is now slightly less than 12 kg, thus allowing a direct 40% decrease in Ti material costs.

For this first concept of revised coaxial tuner, an important modification has been introduced concerning the design of the blades themselves since length and width have been adjusted so to significantly improve the tuning range. The new design make use of longer blades as reported in Tab. 6.10 (see Fig. 6.6 for reference blade scheme). This allows increasing the displacement induced on the cavity to 1.5 mm instead of 1.1 mm as for the original design.

geometry	**Material**	**blHor** mm	**blCla** mm	**blVer** mm	**blLen** mm	**blRad** mm	**blWid** mm	**blThi** mm
original	Ti gr.5	12	8	7.5	56	15	15	0.5
new	Ti gr.5	12	8	**10**	**66**	15	**16**	0.5

Tab. 6.10 – blades dimensions for the revised Blade Tuner design

Several FEM analyses have been performed also on this blade design in order to fully characterize the behavior in terms of load limits and stiffness. Two main issues are considered as limiting the compressive load on the blades. Firstly, buckling is a typical failure mode that is addressed for slender elements like tuner blades, it is related to both material used and shape. It is characterized by a sudden failure when the object is subjected to a compressive force and an equilibrium configuration different from the original exists. This occurs at stress level lower than the ultimate compressive stresses that the material is capable of withstanding. Therefore a safe and lower load limit must be ensured for the single blade as well for the whole tuner. Moreover internal mechanical stresses in the blade are evaluated through the von Mises criteria [119]. This is widely in use to predict failure by ductile tearing or plastic strains in materials like metals, arising when the corresponding stress limit, given for every material, is locally surpassed. As a reference, both internal stresses and the axial load vs. displacement curve are presented in Fig. 6.26 and Fig. 6.27 respectively for the blade at its the maximum admissible deformation, that has been assumed equal to 70% of blVer (see Tab. 6.10).

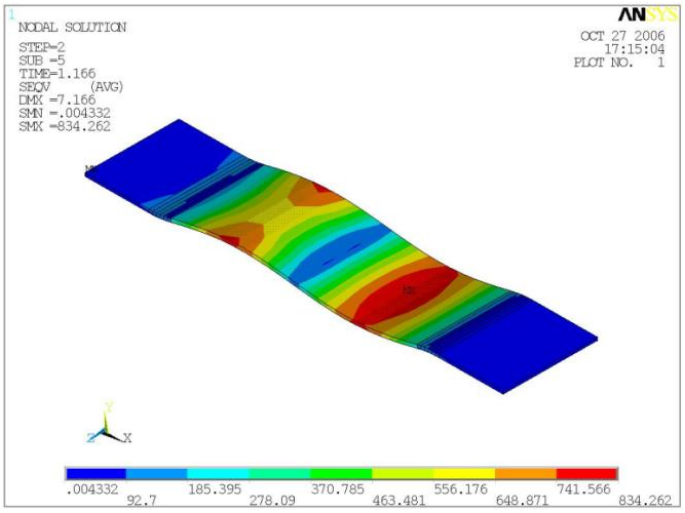

Fig. 6.26 - von Mises stresses on blade after the application of an axial load at the maximum admissible deformation

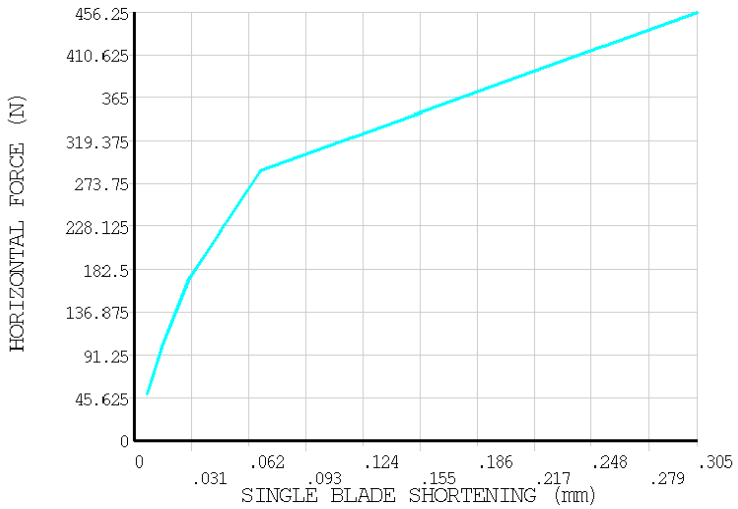

Fig. 6.27 – axial load vs. displacement for the maximum deformation configuration

Analysis allowed to estimate stiffness and main load limits for the new blade design and to compare it to the original one. Final results are reported in Tab. 6.11.

geometry	Material	Limit load stressed state	Max load before plastic strains	Limit load non stressed	Buckling load non deformed state	Limit load final	Stiffness	Tuning range cavity disp.
		N	N	N	N	N	kN/mm	mm
Original	Ti – gr2	786	709	669	427	223	6.49	1.1
New	Ti – gr2	486	456	496	290	162	5.43	1.5

Tab. 6.11 – summary of FEM analyses for a single blade with revised design

These information finally lead to the final choice of the blade distribution along the tuner circumference, always keeping as a reference the main guidelines of simplification and welds reduction previously introduced. Because the final cost will depend from the machining operations, a total number of 96 blades are used. They are grouped in 6 packs of 4 blades each for each half ring collinearly welded on the central ring, thus allowing a 75% reduction of welds and a simplification of machining operations respects to the original configuration. This will simplify the machining operations without a noticeable weight increase.

In parallel to the development of the design of the tuner blade assembly, a key improvement has been also introduced concerning the leverage mechanism originally present in the Blade Tuner. The original driving system is composed of a stepper motor that, by means of a leverage arm, moves the two central rings pulling one side and pushing the other one such to have a perfect symmetric system. This solution, although it ensures high tuning sensitivity and a perfect symmetrical behavior, is cumbersome and expensive. In particular the friction between rotating and translating parts makes them a weak point that has to be solved in a radically way in order to reduce non-linearities. Therefore a simplified driving system has been designed, reducing drastically the number and complexity of parts.

Finally, the revised design solution, with the chosen configuration of the new Blade Tuner rings and blades is presented in Fig. 6.28. The simplified driving system is also visible, mainly composed by the motor with its harmonic drive and a CuBe screw. The axial movement of the nut is directly transferred in the rotational one by the central rings.

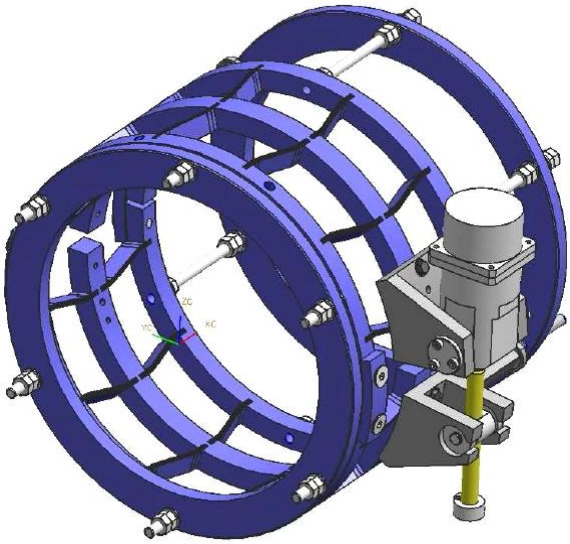

Fig. 6.28 – the new design of the Blade Tuner with the revised driving system

Although this arrangement simply push away the two central rings at one side, therefore losing the complete symmetry, finite element computations and experimental test proved the effectiveness of the solution. The experimental test was performed in LASA laboratory by using a simplified mechanism in substitution of the motor. The displacements recorded at the free rings showed a correct axial movement with negligible rotational or translation effects. This result has also been confirmed by FEM computations performed on the new tuner geometry. In particular Fig. 6.29 shows the axial displacements at the maximum possible deformations blades, corresponding to the tuner longitudinally expanded up to its maximum position.

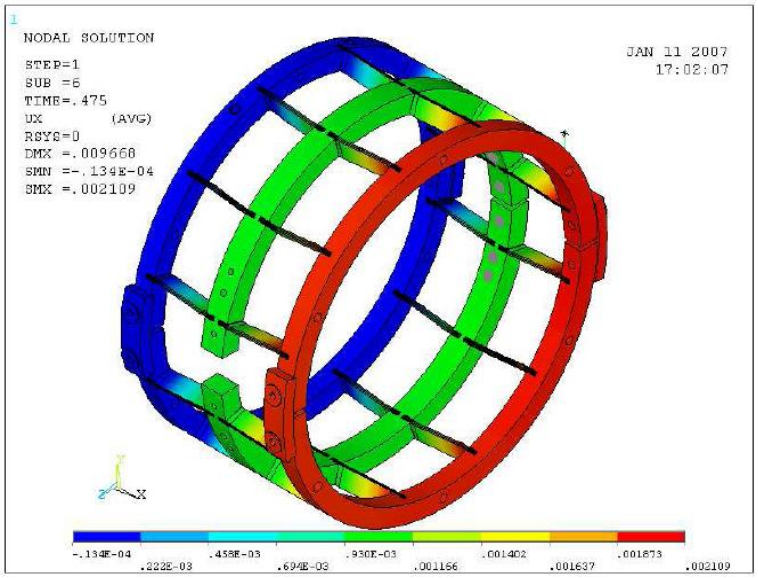

Fig. 6.29 – computed axial displacements for revised Blade Tuner design with lateral motor

The maximum axial force on the motor in this configuration, evaluated in 400 N is fully compatible with the motor and harmonic drive used as of today. The only apparent drawback of the new design is the lowering, due to the lack of the de-multiplication factor of the leverage, in the tuning sensitivity by a factor of about 7. Nevertheless the value corresponding to the proposed configuration, that can be expected to be at most up to 2 Hz per motor step, can be considered as fully consistent with the experience gained with TTF/FLASH operations.

The modifications presented for the Blade Tuner and based on the new blades shape and distribution, lighter rings and lateral motor without leverage, have been summed up in a new proposal design, slimmer and cheaper in comparison to the original design.

The use of a coaxial tuner open different possibilities to optimize the geometry of the helium tank and of the cavity end group. In particular the revised tuner design presented is lighter and more compact than the previous one. Positive consequences are a lower impact on the deflection of the cavity and a larger free space for the positioning of the cryomodule elements such as the invar rod. All this has been obtained maintaining the compatibility with the old design, so that this new version can be installed in the already made helium tank only by means of simple adapters. A comparison of the old and new tuner design is shown in Fig. 6.30. It is clear that the space in the upper part of the helium tank is almost all free, giving an easy access to the positioning of the invar rod.

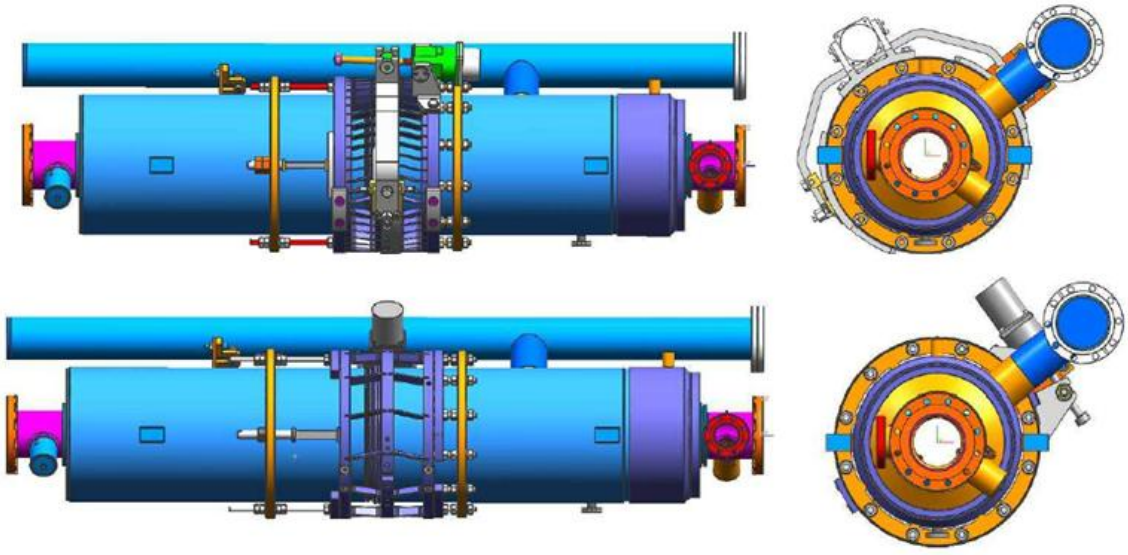

Fig. 6.30 – original and revised design Blade Tuners installed on a modified He tank, lateral (left) and frontal (right) views.

6.5.2 MATERIALS AND MANUFACTURING

Mainly for the steadily increasing price of the bare titanium, the option of replacing few key elements in the tuner with cheaper material has been recently considered. In

particular a tuner version made by stainless steel (SS) and INCONEL has been designed. This would represent a significant cost reduction in view of a possible future use of a steel He tank when the technology will allow solving the problems in welding titanium to stainless steel. A standard AISI 316 alloy is used for the tuner rings while stronger alloy, INCONEL 718, has been chosen for the realization of blades. FEM analysis have been performed also in this case and the results are summarized in Tab. 6.12 and compared to previous results.

geometry	**Material**	**Limit load stressed state**	**Max load before plastic strains**	**Limit load non stressed**	**Buckling load non deformed state**	**Limit load final**	**Stiffness**	**Tuning range cavity disp.**
		N	N	N	N	N	kN/mm	mm
Original	Ti – gr2	786	709	669	427	223	6.49	1.1
New	Ti – gr2	486	456	496	290	162	5.43	1.5
New	Inconel 718	824	693	804	519	268	10.2	1.5

Tab. 6.12 - FEM results for INCONEL single blade with new design compared to previous results

Analysis confirmed that INCONEL blades have higher stiffness and load limit if compared to the titanium solution. The former parameter moreover, although positive for the tuning operation, leads to an higher torque required to the stepper motor for a given displacement of the central ring. A factor of 2 resulted from analysis, therefore a force of 800 N has been foreseen as the maximum axial force on the motor. This value is compatible with motors and harmonic drives in use as of today. To complete the analysis of the presented stainless steel option for the new Blade Tuner it must be considered that, until homogeneous He vessels will be available, the different thermal contractions between tuner assembly and Ti or Nb parts must be addressed. Despite this additional issue, the saving with SS can be evaluated, as of today, to about 1000 euro absolute for the single tuner prototype and to 5% [120] relative for the large scale production, although this latter cost reduction effect will steeply increase over next years.

For all those considerations and analyses shown, both the titanium and the stainless steel options have been developed and realized for qualification. The final technical drawings for the two models have been delivered to manufacturer (Zanon, Schio, Italy) on January 2007. One model for each version has then been manufactured and finally they both were ready for assembly and test on June 2007. The two realized tuners are presented, after assembling, in Fig. 6.31 (to ease notation, Blade Tuner models with revised design will be further on referred also as "Slim_SS" and "Slim_Ti").

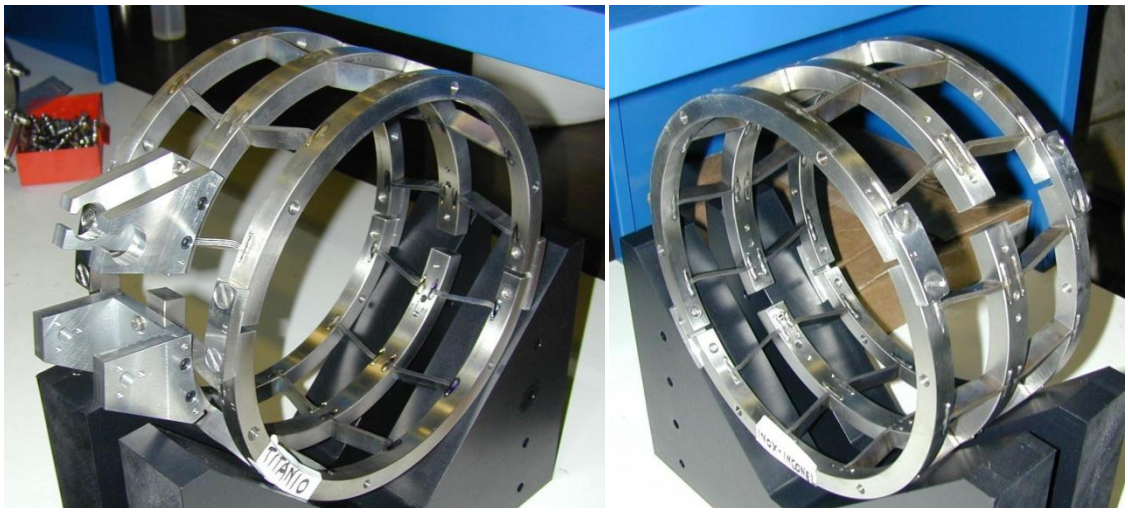

Fig. 6.31 – manufactured and assembled Blade Tuners with revised design, titanium model (Slim_Ti, left) and stainless steel model (Slim_SS, right)

6.6 NEW DESIGN BLADE TUNER MECHANICAL TEST AT LASA

Before the cold test, preliminary measurements have been performed at LASA laboratory using the dedicated tuning facility that hosts a Nb single cell TESLA cavity. Both INCONEL and Ti (also referred as Slim_SS and Slim_Ti respectively) model of the new design Blade tuner have been tested, together with a Superstructure tuner model (SuTu_IV) that has been considered as the reference version.

During tests, load button sensors were also installed for force measurements while micrometer gauges were used for relative displacement. The complete setup for the first installation of the Slim_Ti tuner is shown in Fig. 6.32. Gauges were placed only at the piezo side of each tuner since the other flange is fixed to the table by means of a rigid constraint. For each tuner installed, 4 gauges have been placed on the moving side of the tuner, 2 of them were always set in the proximity of each piezo support while the remaining 2 were set around the ring. The number of turns performed by the motor CuBe screw has been measured and assumed as the input variable for the measurements.

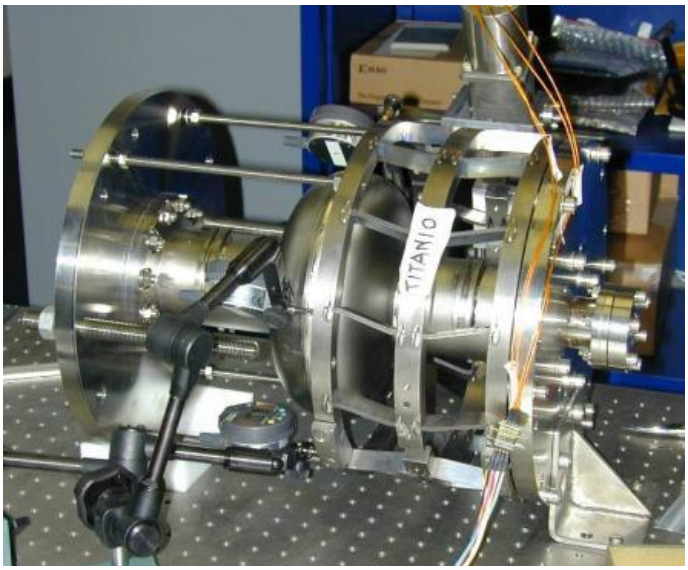

Fig. 6.32 – Slim_Ti tuner installed in test facility

The first performed test investigated the unloaded cinematic performances of each tuner model. A comparative displacement result is shown in Fig. 6.33, were the average readout of the "piezo" gauges is considered. Gauge readouts were anyway completely consistent all over the tuner ring.

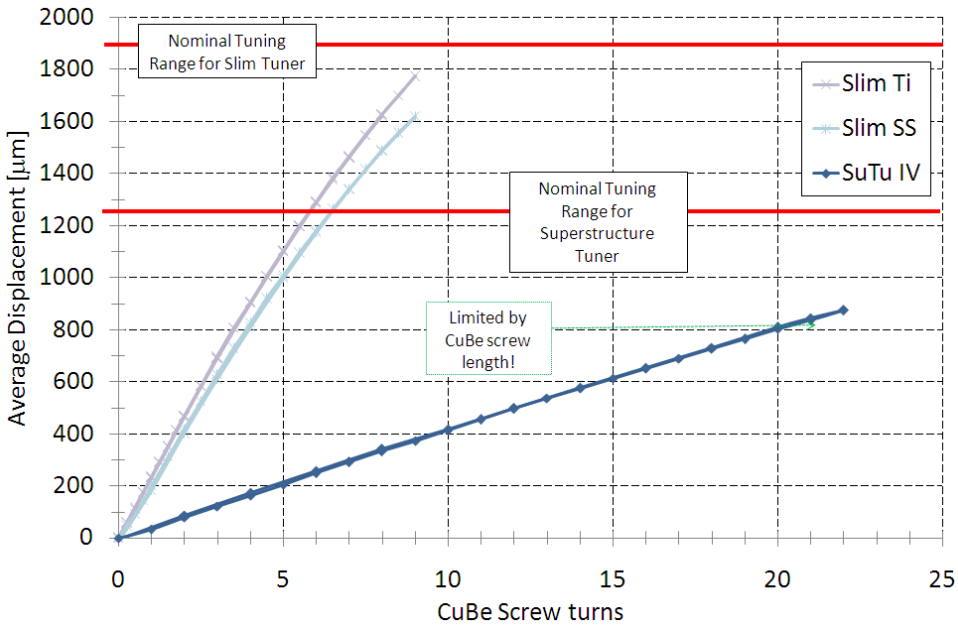

Fig. 6.33 - displacements vs. screw turns curve for the unloaded case

All tuners behaved as expected, even if the tuning range for the SuTu_IV tuner was actually limited only by the length of the CuBe screw.

After this first tests, an external constraint has been added in order to reproduce the static load transferred to the tuner through piezo. With the use of an appropriate combination of spring washers coupled to the force sensor available, the external stiffness (i.e. the stiffness of the tuner constraining mechanism) in its real environment has been reproduced (~3 kN/mm, dominated by cavity stiffness). When higher loads were needed for the test, the combination of spring elements has been changed to increase the overall value. The exact external stiffness for each data series has been anyway measured and it is shown. Loaded and unloaded displacement results are reported in Fig. 6.34 and Fig. 6.35.

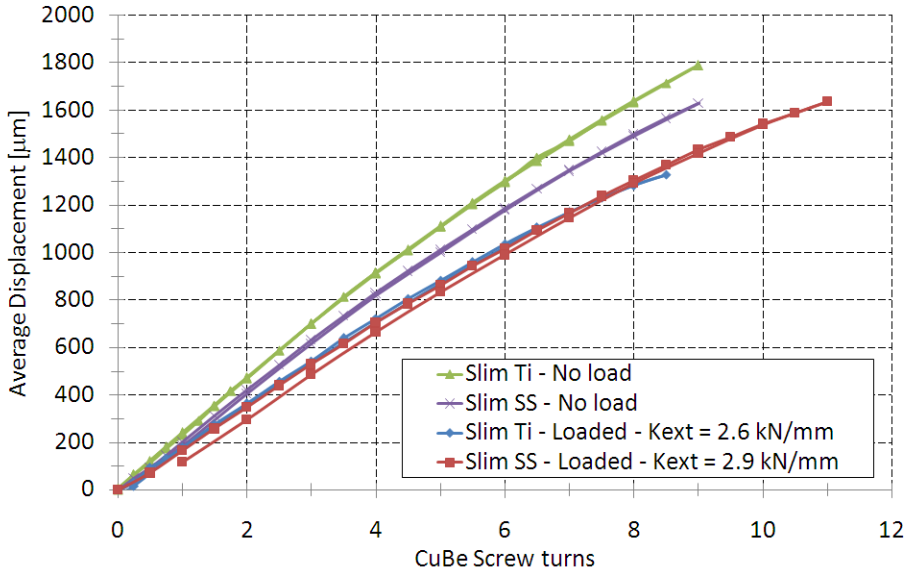

Fig. 6.34 – loaded vs. unloaded curves for new design Blade Tuners

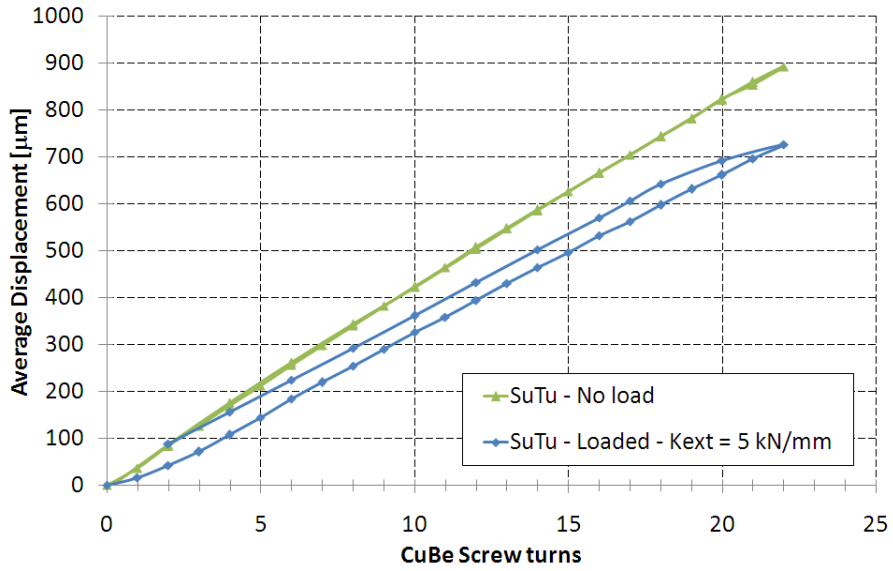

Fig. 6.35 - loaded vs. unloaded curves for SuTu_IV tuner

New design tuner models showed similar loaded responses, and the loaded test successfully confirmed the expected hysteresis lowering in comparison to the SuTu_IV model, in which non-elastic deformations are more likely to occur due to the leverage kinematics itself.

Buckling of few blades appeared for both new design tuner models at high load level. Slim_SS tuner anyway proved to be able to sustain higher load level, repetitively performing an acceptable load limit of 6.15 kN. Maximum load capability is actually limited almost completely by the blades placed closer to piezo holders that bear the main part of the generated force. As a reference, buckling deformation experienced by those blades in the Slim_SS loaded test is shown in Fig. 6.36.

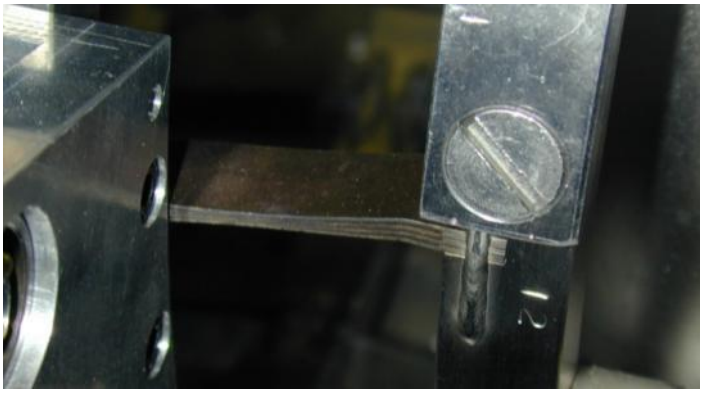

Fig. 6.36 – buckling of most sensitive blades for the Slim_SS tuner over load limit

The SuTu tuner instead was loaded and moved up to a total load of 8 kN and no buckling appeared, due to the considerably higher number of blades. In Fig. 6.37 the generated force is plotted against the total tuner elongation for all tuners.

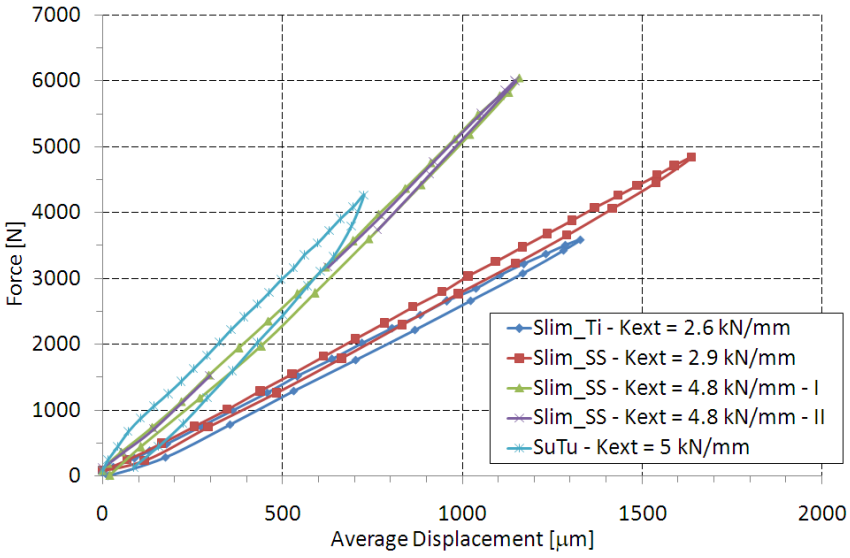

Fig. 6.37 - compression force vs. displacement curves

For the SuTu tuner, a second measurement has also been performed with a static preload added via the piezo screw rods, in order to reach higher load values. Results are visible in Fig. 6.38.

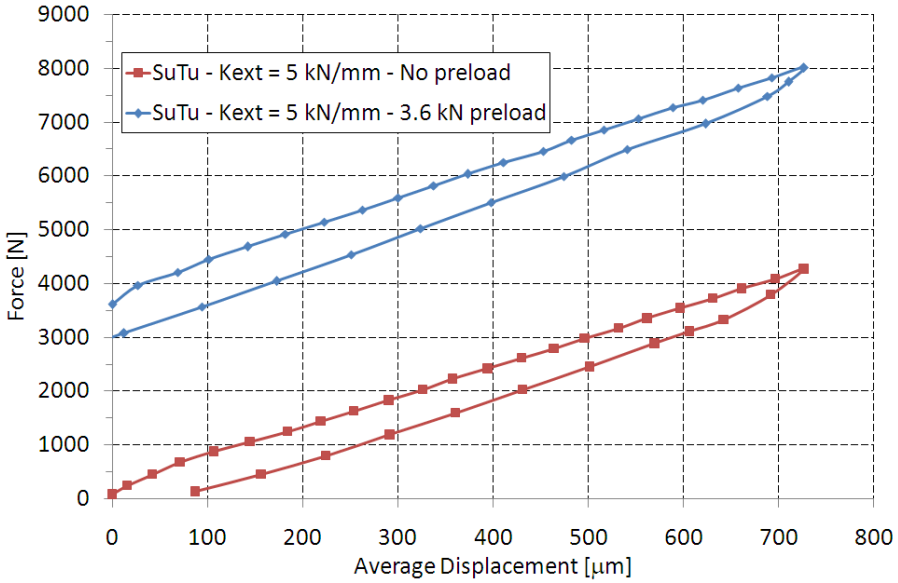

Fig. 6.38 - compression force vs. displacement curve for the SuTu_IV tuner

Finally, to complete the analysis of acquired data, for each CuBe screw turn the difference between unloaded and loaded displacement of each tuner has been computed. This is an estimation of the passive compression (shortening) of the tuner itself at a given load value, therefore allowing to estimate the stiffness of each tuner. Results are shown in Fig. 6.39.

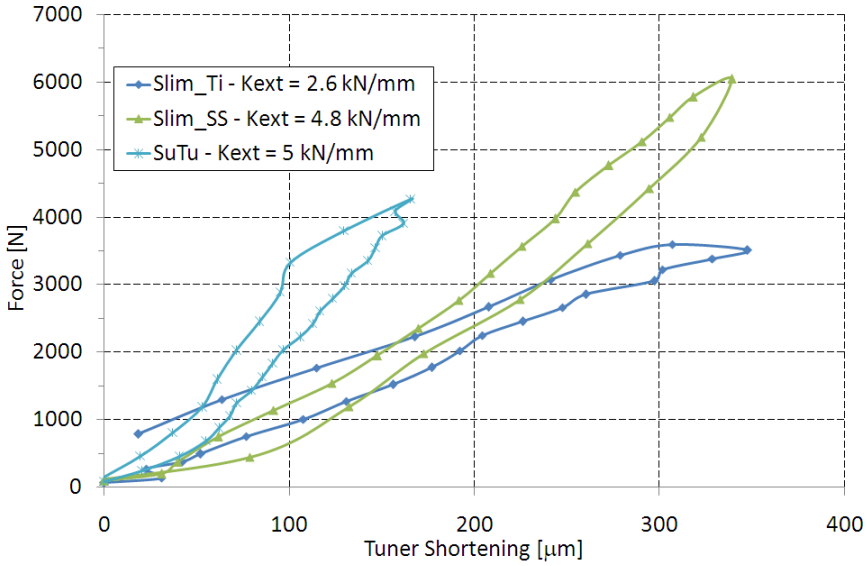

Fig. 6.39 - compression force vs. shortening curves

These curves reveal that the stiffness of each tuner has its minimum value for small shortening (max blade angle) and then reaches its typical value over the full range. Therefore, interpolating over 0 - 25 % of max compression for minimum stiffness and over 25 - 75 % for mean stiffness, the results are:

$$Slim\_Ti: K_{mean} = 11\ kN/mm\ ;\ K_{min} = 9.5\ kN/mm$$

$$Slim\_SS: K_{mean} = 22\ kN/mm\ ;\ K_{min} = 12.5\ kN/mm$$

$$SuTu\_IV: K_{mean} = 32\ kN/mm\ ;\ K_{min} = 17.5\ kN/mm$$

Those values should be compared to a goal stiffness value of 25 kN/mm that can grant the actual piezo-to-cavity displacement ratio of 74 %, that is also the value that has been measured experimentally for the first SuTu tuner.

Numerical FEM simulations have been also performed in order to verify obtained results, both for unloaded and loaded tuner constraints, for the Slim_Ti and Slim_SS (unloaded) and Slim_Ti (loaded) tuners. Results are respectively shown in the following pictures.

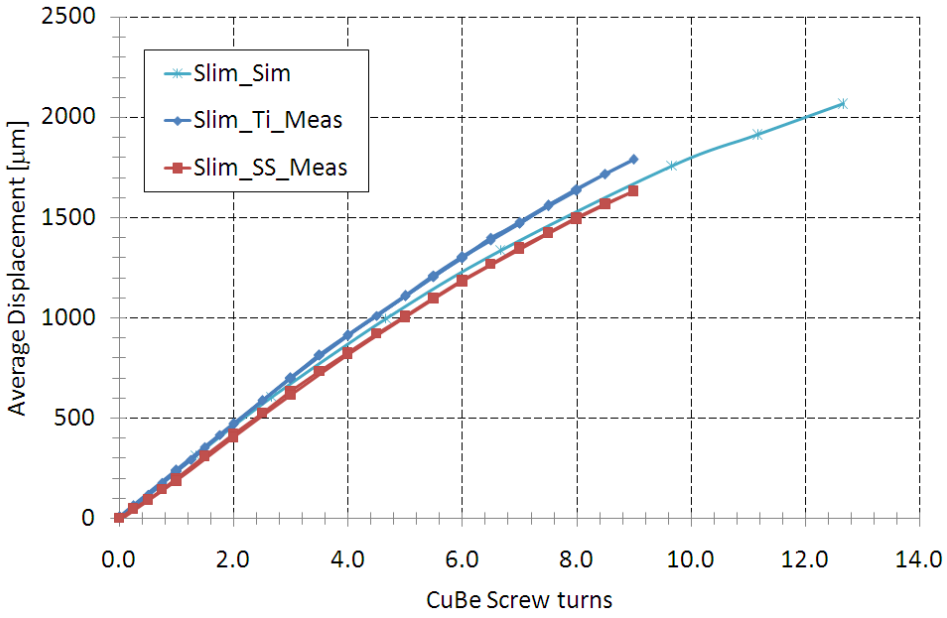

Fig. 6.40 - comparison of experimental and numerical data at the piezo position for the unloaded case

Fig. 6.41 - comparison of experimental and numerical data at the piezo position for the loaded case

6.7 FINAL DESIGN UPDATE AND INSTALLATION PROCEDURE

The results of tests performed at room temperature on available tuner models confirmed that the INCONEL – Stainless steel version of the new design Blade Tuner behaves as expected, therefore it has been chosen for first cold test to be performed in the horizontal cryostat CHECHIA. Some additional modifications in the design have been anyway implemented, consisting of the realization of few additional pieces.

In order to adapt the Slim_SS tuner to the rings design of the old modified He tank available for cold test in CHECHIA[39], 4 stainless steel half rings have been realized to be sided to both the existing outer rings of the tuner. The Blade Tuner 3D model with those additional element installed is visible in Fig. 6.42.

[39] Tuner and He tank sides had different layouts for the screwed holes needed for tuner installation, the existing layout was initially realized in order to host the SuTu tuner.

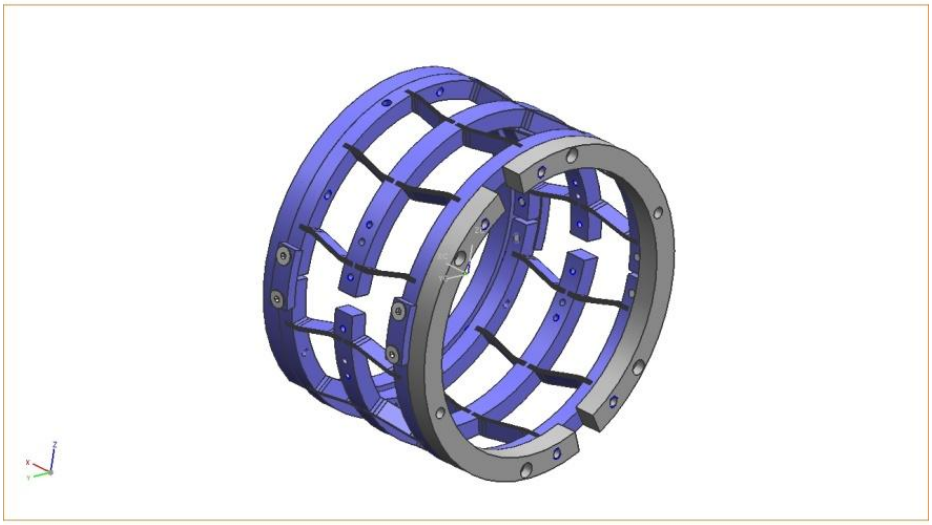

Fig. 6.42 – The additional adaptation rings, in grey, installed for the new design Blade Tuner

Moreover, FEM analysis of the Slim_SS tuner with the additional outer ring installed gave as result an expected increasing of 10 % in the maximum sustainable load limit. Therefore a threshold value of 6.7 kN will be further on considered as the maximum achievable overall load on the tuner.

Finally, each foreseen load case during test, starting from the installation up to the operation, has been considered and simulated in order to estimate, for each single case, the compressive and tensile loads in the system together with the corresponding cavity frequency.

The starting frequency of this analysis is the measured value after the last cavity tuning operation, before the He tank integration. It is assumed and expected that the installation of the tuner itself on the 9-cell cavity would not introduce any further loading and frequency variation, except for the piezo preload. The stepper motor is installed and then kept in the starting point of its tuning range during both installation and cool-down (i.e. no additional motor screw turns before operative conditions are reached).

The analysis relies on results and parameters of the mechanical spring-mass model already developed for the system and discussed in previous paragraph 6.4. In addition the analysis has taken into account the presence of safety bolts properly installed on the support screw rods, as already introduced. Therefore those bolts are engaged when tensile loads are generated on the tuner. Finally, simple FEM simulations were used to estimate the reactive force of the cavity when subjected to a pressure difference of 1 bar, after evacuating the beam pipe.

The following table summarize analyses results for each foreseen load condition. The peak compressive and tensile loads during cooldown procedure are highlighted. A value of

1.15 bar has been considered for the peak pressure during the liquid He transfer to the He tank[40]. Compressive load values are negative.

	Load case	Temp. cavity K	Pressure beam pipe bar	Pressure He tank bar	Pressure isovac bar	Force tuner kN	Force cavity kN	Force Each Piezo kN	Frequency cavity MHz
1	start	300	1	1	1	0	0	0	1297.333
2	tuner assembly and piezo preload	300	1	1	1	-2.2	2.2	-1.1	1297.563
3	vacuum in the cavity	300	0	1	1	**-2.9**	2.9	-1.45	1297.913
4	iso vacuum in the cryostat	300	0	1	0	2.7	2.1	0	1298.07
5.1	He injection	300	0	1.15	0	3.3	2.2	0	
5.2	LHe in the tank	4	0	1	0	**4.55**	0.95	0	1299.94
6	superfluid He / min of tuning range	2	0	0.02	0	-1.1	1.1	-0.55	1299.75
7	superfluid He / max of tuning range	2	0	0.02	0	-5.5	5.5	-2.75	1300.1

Tab. 6.13 – analyses and simulation of each tuner load case, from assembling to cool-down

Such analyses have confirmed that it is correct to expect not to exceed the maximum load sustainable by the Slim_SS tuner and that, moreover, the goal frequency of 1300.0 Mhz should be achievable and close to the middle of the tuning range, as designed.

It is also shown that the peak tensile force must be actually considered as the most critical transient situation, since up to more than 4.5 kN of tensile force is expected to act on the tuner. Given that the cavity is already almost not sensitive to this force, since safety bolts transfer it almost completely to the tuner, the mechanical contact with piezo actuators must be anyway preserved and excessive loosening must be avoided. While a definitive solution for this issue is under development, a provisional but effective remedy to allow the first test has been adopted. This is accomplished using two helicoidal springs that have been installed below the piezo holder by the tuner side, as shown in following Fig. 6.43.

[40] This value is although very difficult to predict and to control, some more experience and statistic is needed.

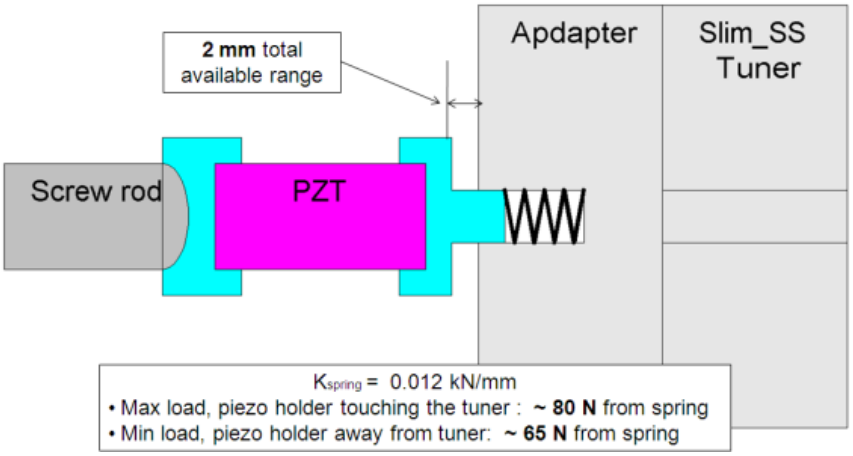

Fig. 6.43 – basic design of piezo holder spring insertion for the new tuner design

Finally, the complete set of new Blade Tuner (Slim_SS) assembly elements, corresponding to the tuner in its final version for DESY cold test, is shown in Fig. 6.44.

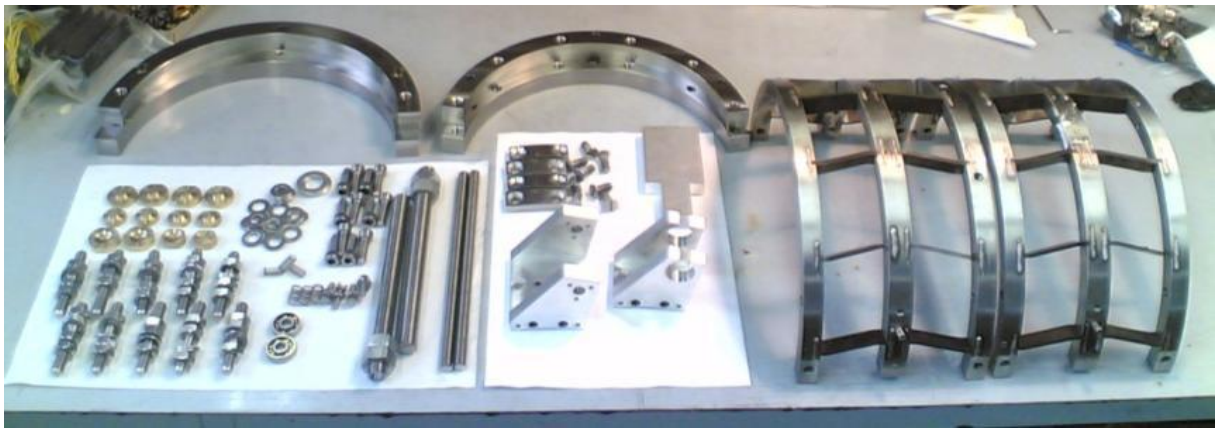

Fig. 6.44 – complete set of Slim_SS tuner elements for the DESY cold test

6.8 NEW DESIGN BLADE TUNER COLD TEST AT DESY

In order to validate expectations for the Slim_SS coaxial Blade tuner, a cold test session has been planned and performed at the CHECHIA horizontal cryostat facility in DESY, previously described in chapter 1.4.

In order to test the coaxial tuner in CHECHIA, the Zanon n°86 cavity, or Z86, has been used. From April to June 2007, the Z86 cavity has been prepared for cold test. End

dish welding has been done at the Lufthansa facility[41] while the modified He tank, with the insertion of a central bellow, has been then installed in DESY. The cavity has moreover sustained the usual DESY acceptance test procedure, including mechanical qualification test and RF test in vertical cryostat. Summary of main Z86 cavity properties and performances, as emerging from those former tests are reported in Tab. 6.14.

Cavity	**Z86**	
Manufacturer	Zanon, I	
Arrival at DESY	22/04/05	
Weight	26.55	kg
BCP sessions	1	
Material removed by BCP	< 10	μm
EP sessions	3	
Material removed by EP	242.1	μm
Baking	800° , 2h	
	127° , 48h	
RRR	296	
E_{acc} , V1	24.5	MV/m
Q_0 , V1	1.8 E10	
Field Flatness , last tuning	97	%
Frequency , last tuning	1297.333	MHz

Tab. 6.14 – summary of Z86 cavity treatments and performances

Finally Z86 cavity was ready for blade tuner installation, and cold tests in CHECHIA have been scheduled and performed in weeks 35 and 36, September 2007. The activity related to the New design Blade Tuner test and its results are presented in this chapter.

6.8.1 COOLDOWN AND WARM UP RESULTS

Starting from September 4th 2007, the installation of the Slim_SS Blade tuner on the full Z86 cavity has been carried through so that in two days the whole setup has been installed in CHECHIA and the test session started.

In order to remove security bars between the He tank rings and install the tuner, beam pipe vacuum has been removed and cavity has been filled with Ar gas at 1 bar pressure. Vacuum in the beam pipe has then been restored right before the insertion in CHECHIA[42]. The first frequency check right before tuner assembling revealed an higher

[41] Lufthansa gmbh, Hamburg. A special EB welding machine is used for end dish integration due the high number of degree of freedom (DoF) needed.

[42] Both operation on beam pipe volume, Ar refilling and vacuum pumping, has been performed in the Halle III clean room.

value, by an amount of around 100 kHz, compared to the last available measure. This frequency difference, between the value reported in Tab. 6.14 and the value measured just before the test, is mainly due to the fact that during bead-pull operation on the tuning machine, when last frequency value has been measured, both bead and its wire are enclosed in plastic tube, introducing a frequency shift of -80 kHz. Additional -20 kHz can be accounted to the Argon gas different dielectric constant with respect to the Air. The He tank welding procedure instead produces a negligible frequency shift, lower than 10 kHz. Anyway, since the initial cavity frequency was higher than expected, a lower preload has been set on piezo actuators, two NOLIAC 40 mm (NOLIAC_40 as referenced in paragraph 4.4.3), in order to reach the correct frequency value for load case 2, Tab. 6.13.

A stepper motor from Sanyo inc. has been installed together with usual TTF gear-box and harmonic drive. Safety bolts on the 4 support screw rods have been installed, 2 on each side of the He tank ring. As foreseen from tuner design the distance between those safety bolts and the outer side of the ring has been set as accurately as possible toward the goal value of 0.6 mm. Unfortunately, this calibrated installation suffered from significant error and the actual distance value could be as high as 1 mm[43]. Finally, a μ-metal foil has been adapted to fit the installed tuner and provide magnetic shielding to the cavity.

The main steps of the tuner assembling and installation in CHECHIA are shown in the following pictures.

Fig. 6.45 – Z86 and modified He tank with support disks and bellow, ready for Blade tuner installation

[43] This issue, actually related to the difficulties experienced during bolts installations by hand, will be overcame using proper devoted tools and solutions under designing.

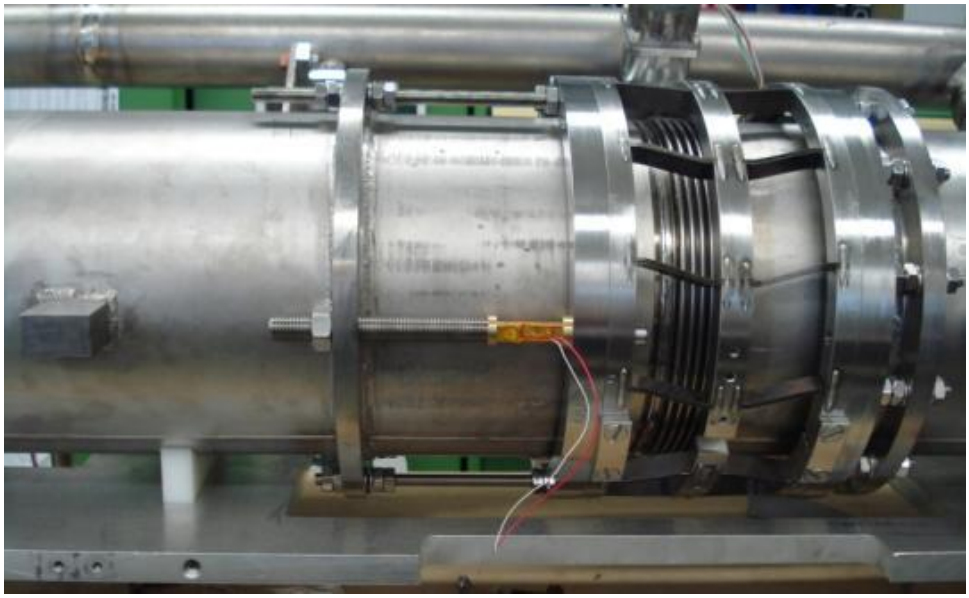

Fig. 6.46 – the Slim_SS Blade tuner completely installed, piezo actuators are in place and preloaded.

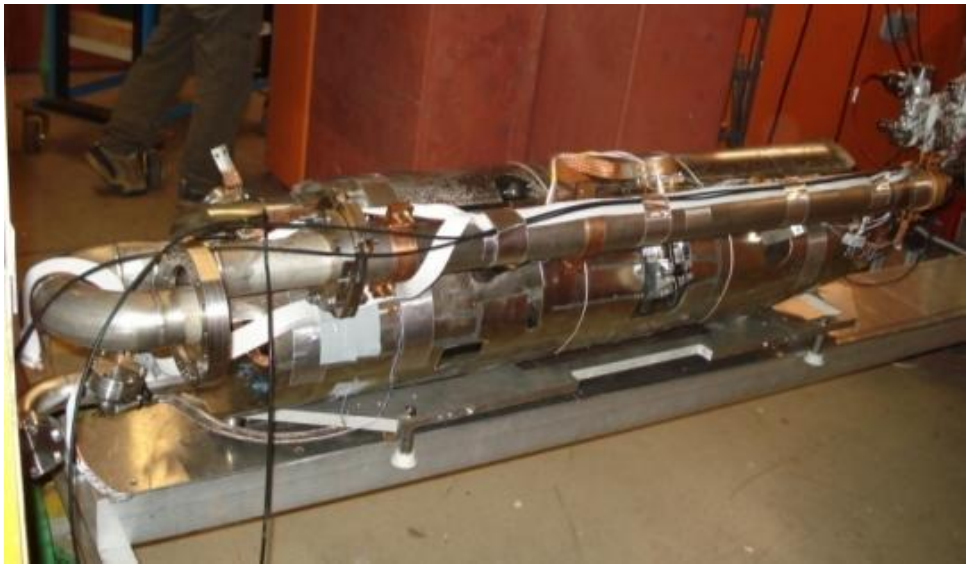

Fig. 6.47 – Z86 right before insertion in CHECHIA, the magnetic shielding is visible around the He tank

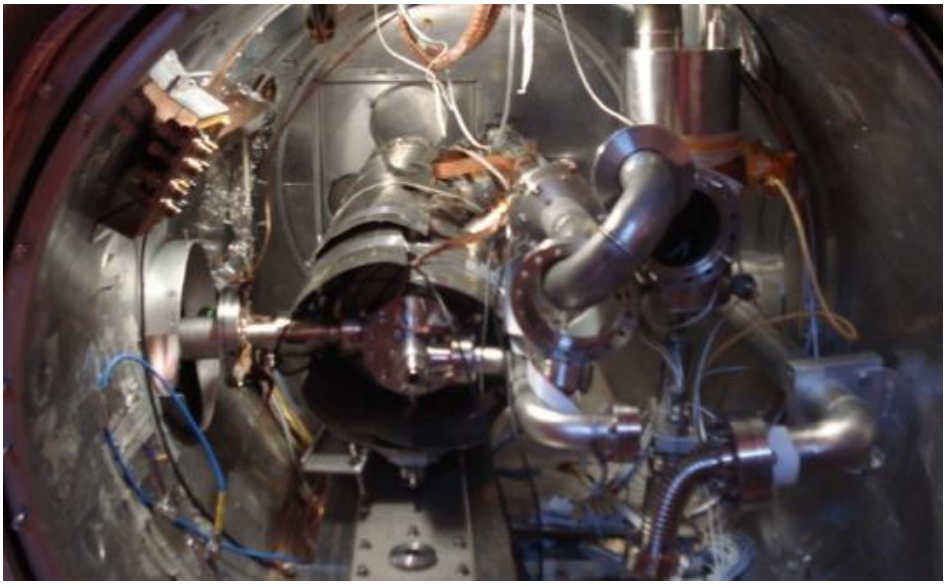

Fig. 6.48 – Z86 installation in CHECHIA completed, before start of cold test

During the entire assembling procedure until the insertion in CHECHIA, both cavity frequency and piezo actuators static capacitance values have been measured (from here on piezo will be referred as "piezo 1", on motor side, and "piezo 2", on the other side). Cavity frequency shift, and therefore its length deformation, has been also monitored to determine the final piezo preload through known cavity stiffness. Finally, after the conclusion of main ancillaries installations (diagnostic cables, coupler, vacuum and liquid He refilling) the DESY usual schedule for CHECHIA cold test preparation has been followed. Therefore, sequentially:

- Isolation vacuum pumping.
- Coupler warm processing: full power pulse, from 20 μs to 1300 μs.
- Start cool-down: liquid He transfer up to 4 K. More than 2.2 bar peak pressure, for about 5 minutes, has been reached during transfer.
- Pumping over liquid He bath: toward superfluid He, 2 K at 30 mbar pressure.

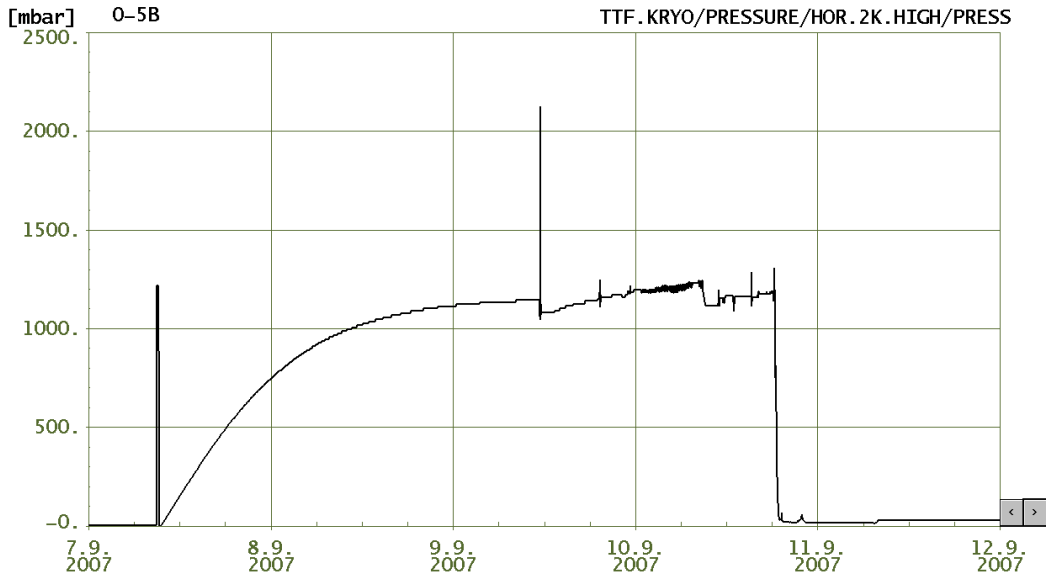

Fig. 6.49 – He tank pressure sensor log, He filling, pumping over He bath and 2.2 bar peak value are visible

– Cavity successfully moved on 1300.0 MHz tune with the stepper motor: +1.25 screw turns.

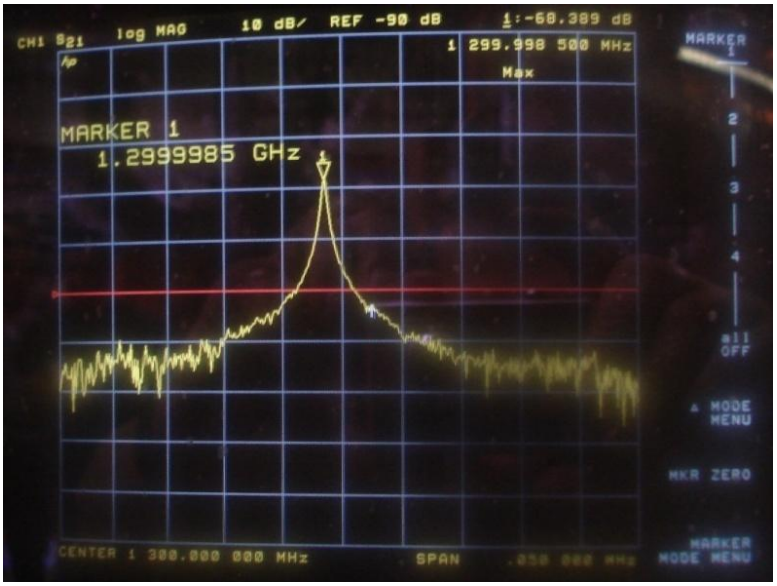

Fig. 6.50 – Network Analyzer screenshot of the tuned cavity frequency measure

– On resonance conditioning.

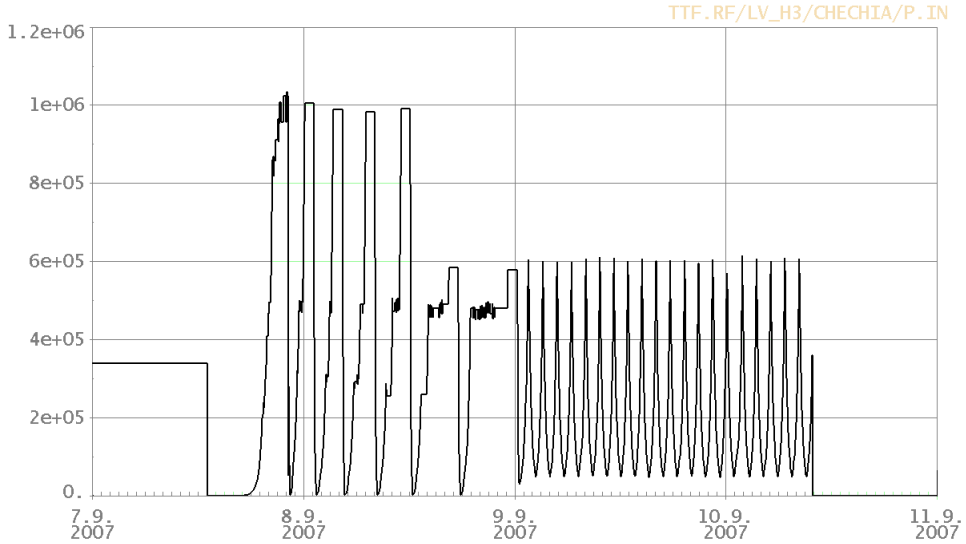

Fig. 6.51 – forward power readout log, warm processing up to 9.9.07 then on-resonance cold processing from 9.9.07 on.

Main results concerning recorded parameters from installation to operative conditions have finally been summarized in the following table.

Status	**Cavity frequency** MHz	**Pressure Beam pipe** mbar	**Pressure He tank** mbar	**Pressure isovac** mbar	**Temp. cavity** K	**Piezo Static capacity** 1 - μF	2 - μF
Start	1297.427	1000 - Ar	1000	1000	300		
Tuner on	1297.445	1000 – Ar	1000	1000	300	9.11	8.81
Piezo preloaded	1297.567	1000 - Ar	1000	1000	300	9.39	9.04
Ready to CD	1297.842	0	*1000*	1000	300	10.23	10.04
CD done, stable 4K	1300.191	0	1200	0	4	3.87	3.34
Pumping 1	1300.135	0	500	0	3		
Pumping 2	1300.045	0	200	0	3		
First 2 K	1299.996	0	30	0	2	3.65	3.1
Stable 2 K, + 1 d	1299.974	0	30	0	2	2.97	2.65
Long run 2 K, + 4 d	1299.978	0	30	0	2	2.25	2.3

Tab. 6.15 – summary of all measured parameters during Z86 preparation and cooldown

As previously reported, a lower preload has been set on piezo actuators due the different cavity initial frequency. The preload can actually be estimated observing, from Tab. 6.15, that around 120 kHz frequency displacement has been forced on the cavity via the screwed piezo support rods, corresponding to less than 0.6 kN preload for each actuator (approx. one half of the goal value).

Also the final cavity frequency, when stable operation conditions were reached, resulted to be higher than expected from previously presented computations, that were mainly based on the amount of information collected at DESY over different CHECHIA cooldown operations, but with a different tuner. The final frequency revealed to be higher by an amount of 230 kHz, three main contributions to this frequency shift can be extrapolated from data:

1) *70 kHz less than expected* for the frequency increasing due only to vacuum in the cavity, +280 kHz instead of +350 kHz.

2) *320 kHz more than expected* for the frequency increasing due to 300 K to 4 K cooldown, +2.35 MHz instead of +2.03 MHz.

3) *20 kHz more than expected* for the frequency lowering due to 4 K/1bar to 2 K/20 mbar cooldown, -210 kHz instead of -190 kHz.

Nevertheless, although higher than expected (-70 +320 -20 = +230 KHz difference), cavity frequency remained below the 1300.0 MHz threshold at the lower limit of the tuning range, therefore the nominal operating frequency has been successfully reached.

Finally, on September 11th 2007, Z86 cavity was ready for tuner and piezo cold test, performing a more than 23 MV/m accelerating gradient, in pulsed operation with full 1.3 ms RF pulse length.

6.8.2 TUNING RANGE RESULTS

After stable 2K He bath conditions were reached, the measurement of the Slim_SS tuning range has been performed, using a vector Network Analyzer to measure the cavity resonant frequency while moving the tuner stepper motor.

All collected points concerning the tuning range are shown in the following plot, in Fig. 6.52. The tuner sensitivity, namely the frequency shift vs. screw turn, has also been computed from data and reported in next Fig. 6.53.

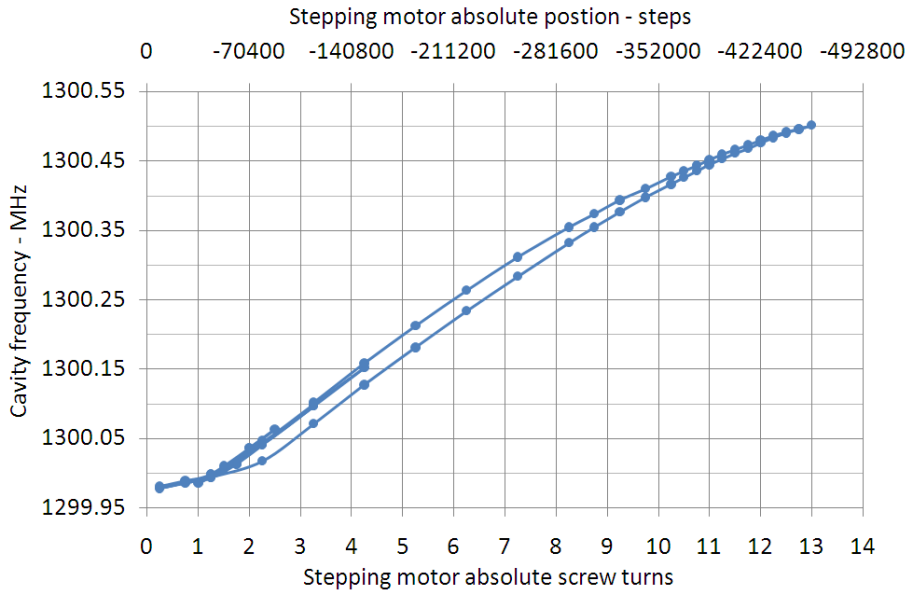

Fig. 6.52 – Slim_SS Blade tuner tuning range, 13 complete screw turns.

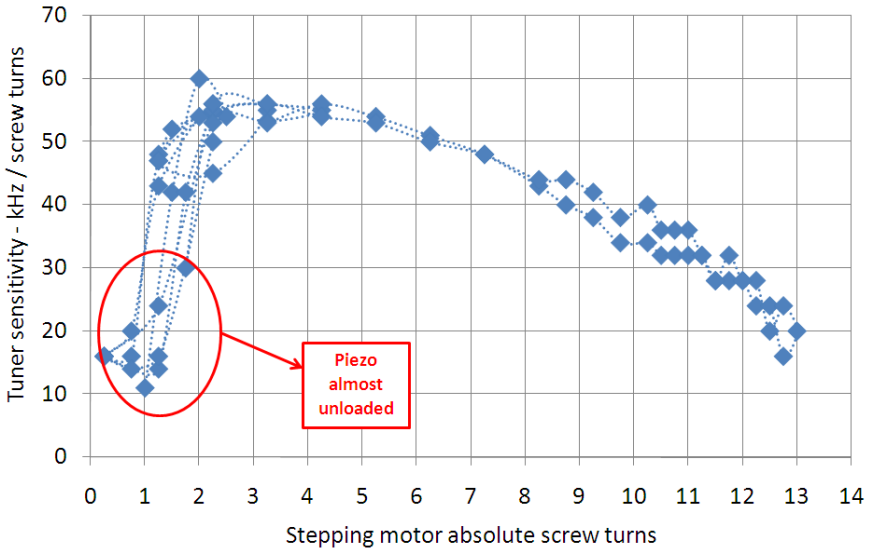

Fig. 6.53 – frequency shift vs. screw turns sensitivity for the Slim_SS Blade tuner

Data confirmed that Slim_SS Blade tuner performed the expected tuning range of 520 kHz, over 13 complete motor screw turns and confirmed the peak sensitivity value of 50 kHz per screw turn expected by tuner design.

The loading force generated by the cavity, that reached a peak value of 5 kN at the higher end of the tuning range, has been successfully borne by the tuner. The smooth and repetitive behavior of cavity frequency around the highest load value confirmed that no buckling occurred to tuner blades.

A visible hysteresis outline is anyway present in the plot of Fig. 6.52, where a peak frequency difference of 30 kHz is present after a complete load cycle, around screw turn # 2. This value actually matches the hysteresis figure shown by the same Slim_SS tuner for the first loaded cycle at room temperature at LASA LAB, shown in Fig. 6.34, where about 0.1 mm of tuner displacement difference can be deduced corresponding to approximately 30 kHz for the cavity. It must be moreover underlined that tuner performances in term of hysteresis reduction has been considerably improved with the new design if compared to the previous design, mainly thanks to the lack of the stepper motor leverage. Shown hysteresis can be anyway justified by the need of a "load conditioning" of the tuner itself, since the installed setup reached those high load values for the first time during this test. It is expected that successive load cycles, unfortunately not performed for lack of time[44], would show a significantly lowering hysteresis. Further confirmations are expected from incoming Slim SS Blade tuner cold tests in BESSY[45]. In this case, the working point hysteresis will be measured beside the full range one, to fully evaluate this tuner issue.

The effect of initial and unexpected frequency offset is even more evident from the data plots presented. Two complete turns were needed from the lower end of tuning range for piezo actuators to be in complete contact with the tuner so to reach the nominal tuner sensitivity. In this range, springs below piezo holder were keeping actuators firmly in place and only slightly detuning the cavity (generated force below 100 N).

6.8.3 LORENTZ FORCE DETUNING COMPENSATION PERFORMANCES

The measure of cavity detuning has already been considered in par. 3.4, where the Matlab scripts for detuning computation have been introduced. In order to evaluate piezo actuators performances, a new set of these scripts have been prepared to be used with CHECHIA test facility. The standard TTF piezo driver board, together with instruments needed have been moreover used for this test. For a detailed description of the apparatus refer to chapter 1.

Before the LFD compensation test started, the cavity has been tuned to the nominal 1.3 GHz resonance frequency using the stepper motor. As told before, this frequency is reached just a little bit further the lower frequency position of the tuning range. Mechanical preload available for piezo in this case is, as said, lower than expected for optimum LFD operations. Actuators were anyway still effective, later on the effect of preload on piezo mechanical coupling has been investigated.

---

[44] Since at each motor position both piezo parameters and piezo-to-piezo transfer function have been acquired, a single complete load cycle took even longer time, almost 1 day.

[45] At the moment of writing, Z86 cavity and Slim_SS Blade tuner were about leaving DESY toward BESSY, where a longer test window is foreseen around beginning of 2008.

In order to determine the correct pulse timing for Lorentz force detuning compensation, a sweep around different pulse timing values has been performed while acquiring resulting cavity detuning. The same pulse used in CMTB module 6 piezo test, single sinusoidal pulse 2.5 ms width, has been set up, also to ease comparison of results.

The results of this piezo timing effect test are graphically summarized in Fig. 6.54.

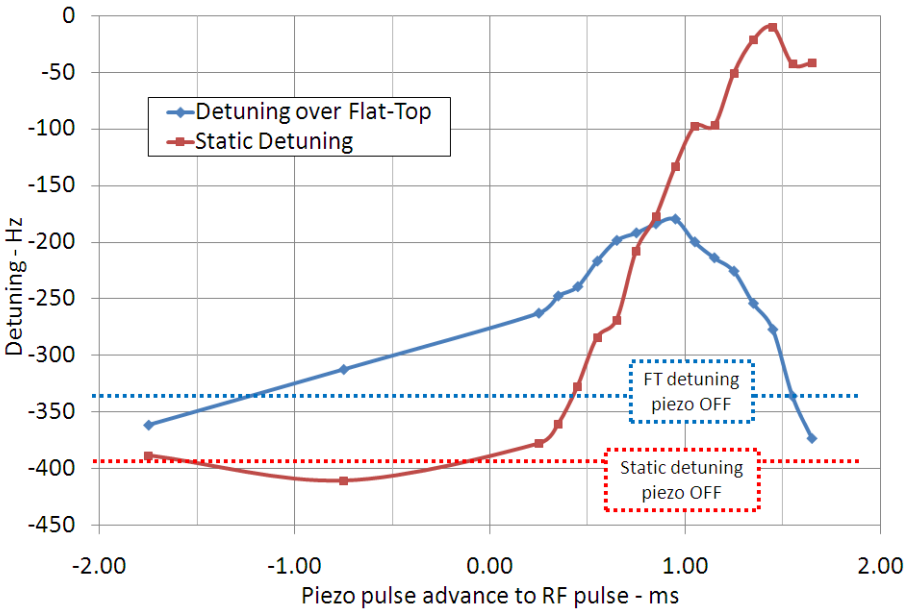

Fig. 6.54 – analysis of the piezo pulse advance effect on cavity detuning, Slim SS tuner cold test

It is possible to recognize in plot of Fig. 6.54 the same pattern already explained for the same analysis performed on FLASH module #6, Fig. 5.2 (except for the sign since the latter plot shows the absolute normalized detuning). Both static detuning and flat-top detuning curves behave as expected, revealing that the best timing setting for the "1st oscillation compensation scheme" requires in this case a piezo pulse advance of *0.85 - 0.95 ms* with respect to the RF pulse. These values are actually comparable to the ones from module #6 TTF piezo tuner analysis, with 0.65 ms advance. For subsequent LFD compensation measurements, an advance value of 0.95 ms has been set.

Assuming that cavity stiffness value, 3 kN/mm, is preserved passing from room temperature to the actual cold environment, the overall preload available for both piezo actuators in the initial test setting, 1.25 screw turns, was lower than 0.2 N. Therefore an additional LFD compensation test has been performed at higher cavity frequency, when available total load was 1.2 kN, corresponding to 2 additional screw turns and a frequency shift of about 100 kHz.

It must be underlined that the expected working point for cavity and piezo actuators at 1300.0 MHz was rather the latter one, as foreseen by load cases simulation already shown. Since, as told before, the initial cavity frequency was 100 kHz higher than expected the piezo preload at the nominal frequency is considerably lower than the designed best

working point. Therefore, to reach this point a further frequency shift must be forced so to allow an higher load on piezo actuators.

The entire Lorentz force detuning shown by Z86 cavity at full gradient, in different load conditions, driving piezo 1 alone, driving piezo 2 alone and even driving both piezo in parallel, has been successfully compensated. Plots of cavity detuning and phase of RF probe data are reported in Fig. 6.55 and Fig. 6.56. They correspond to the best results obtained in the higher piezo load configuration, (i.e. second load case, 1.2 kN total force). Numerical results from all other measurements have then been summarized in Tab. 6.16.

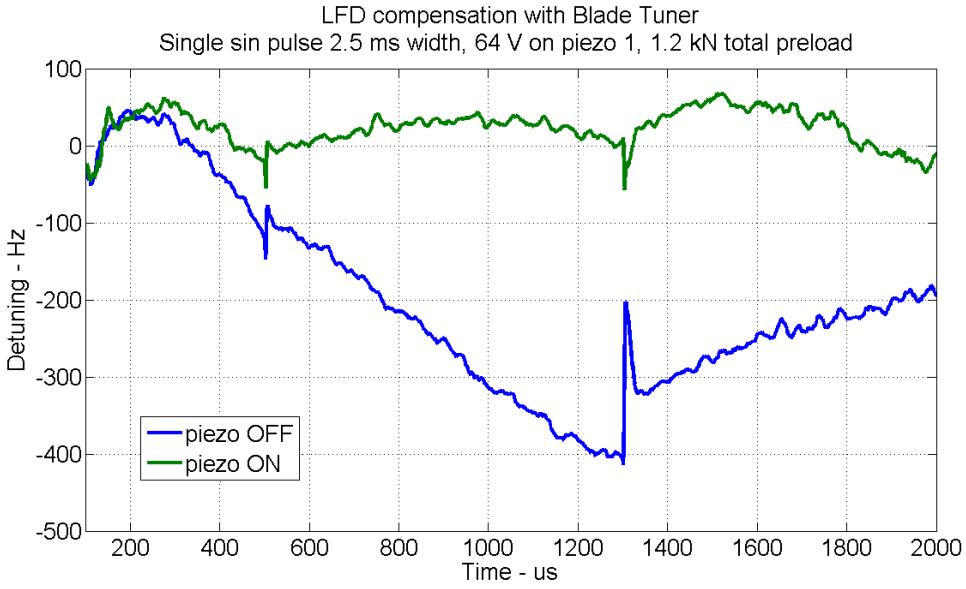

Fig. 6.55 – Z86 cavity detuning with and without piezo active compensation

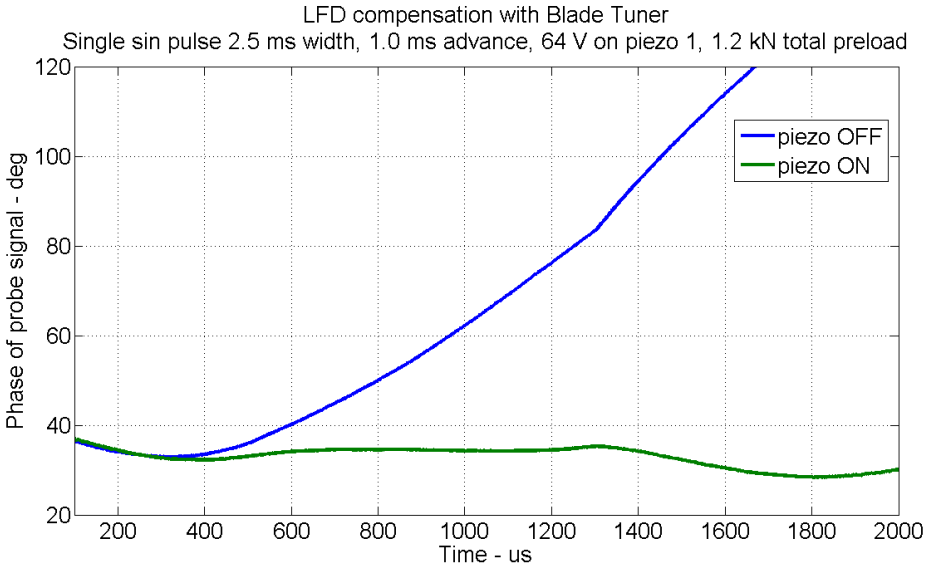

Fig. 6.56 – phase of Z86 cavity RF probe signal, with and without piezo active compensation

Used PZT	Gradient [MV/m] piezo OFF/ON	Cavity freq. [MHz]	Total Piezo load [kN]	FlatTop Detuning [Hz]		Static detuning [Hz]		Piezo amp. [V] V_{max}=200V	Piezo advance [ms]	Comp. FlatTop detuning [Hz]	FlatTop phase stability	FlatTop amp stability
				piezo OFF	Piezo ON	piezo OFF	Piezo ON					
1	23/23	1299.988	0.2	-332	-49	-392	-7	75	0.95	283	+78%	+68%
1	23/23	1300.097	1.2	-308	-46	-326	5	64	0.95	262	+95%	+64%
2	23/23	1300.097	1.2	-308	-60	-326	33	56	0.95	248	+95%	+45%
1+2	23/23	1300.097	1.2	-308	-78	-326	-83	50	0.95	230	+66%	+87%

Tab. 6.16 – all results from LFD compensation measurements on Z86 cavity in CHECHIA

These results are surely encouraging, even if preliminary and collected over a quick test session. Both Lorentz force detuning compensation and clear improvement of RF amplitude and phase values stability over the flat-top time window (or "FT", from 500 to 1300 μs) are visible from reported plots and were obtained with a limited piezo pulse amplitude, especially when actuators are operated in parallel, if compared to the maximum driving voltage of 200 V. Collected data at 1.2 kN load level also revealed that detuning compensation performances are slightly different between piezo 1 and 2, the latter one being more efficient. This behavior was anyway expected. The main contributions come both from the small difference in tuner stiffness, that is asymmetrical by design, and from the piezo preloading procedure itself, right after tuner installation.

LFD values for Z86 cavity without piezo active compensation, as reported in Tab. 6.16, resulted to be slightly over the expectations in comparison to usual TTF operation experiences at the same accelerating gradient, although more measurements on different cavities are needed to confirm this issue. It is anyway clear that both the cavity intrinsic LFD reduction and the lower pulse amplitude needed, confirmed that the whole tuner fast tuning system took clear advantage from the increasing of the mechanical preload when cavity is operated closer to the middle of the tuning range.

In order to have a preliminary evaluation of Slim SS Blade tuner performances, the shown data can be compared to the data set from FLASH module #6 tests. Averaging over the whole module (see Tab. 3.2), the latter tests with TTF piezo tuner, revealed a LFD sensitivity of -0.47 ± 0.05 Hz/(MV/m)^2, compared to Slim SS tuner test results of -0.63 and -0.58 Hz/(MV/m)^2 with 0.2 kN and 1.2 kN preload respectively. Considering the results of the analytical modeling presented in par. 6.4 and the limitations for the test due to the old He tank design, a similar behavior could be expected. It is anyway important that, when the load reaches acceptable values as in the latter case, the K_L' for the coaxial tuner installation is still in the order of most sensitive cavities with TTF tuner installed. For further comparative analyses selected results have been summarized in Tab. 6.17, where ACC6 average LFD compensation results have been scaled for an E_{acc} value of 23 and 25 MV/m to correlate them to the coaxial blade tuner test data. For each case both the amplitude of piezo voltage used for compensation and its ratio with the corresponding maximum nominal voltage (120 V for PI_36 piezo in ACC6, 200 V for NOLIAC_40) are shown.

Test	tuner	PZT used	load	Δω over FT	E_{acc}	V_{piezo} for Δω compensation	V/V_{max}
			[kN]	[Hz]	[MV/m]	[V]	
ACC6 avg.	TTF	1		250	23	45	0.375
ACC6 avg.	TTF	1		300	25	54	0.45
Z86	Blade	1	0.2	332	23	75	0.375
Z86	Blade	1	1.2	308	23	64	0.32
Z86	Blade	2	1.2	308	23	56	0.28
Z86	Blade	1+2	1.2	308	23	50	0.25

Tab. 6.17 – prototypal comparison of LFD results between TTF and coaxial tuner test

Although more tests and statistics are needed about coaxial blade tuner installation and operation at cold, results can be considered as encouraging, principally since the higher LFD sensitivity shown is balanced by an higher piezo fast tuning efficiency in term of driving voltage margins. Moreover a clear improvement on both aspects seems to be confirmed, as expected from design, when increasing the mechanical load on the tuner assembly.

6.8.4 ADDITIONAL PIEZO ENVIRONMENT ANALYSIS

Both the cavity sensitivity to Lorentz Force and the efficiency of piezo detuning compensation revealed some dependence from the mechanical compressive load generated by the cavity and set by the working point in the tuning range. As a reference, the total generated load over the whole tuning range is reported in next Fig. 6.57. The force has been computed taking into account, also for the cold environment, the usual room temperature cavity stiffness value of 3 kN/mm.

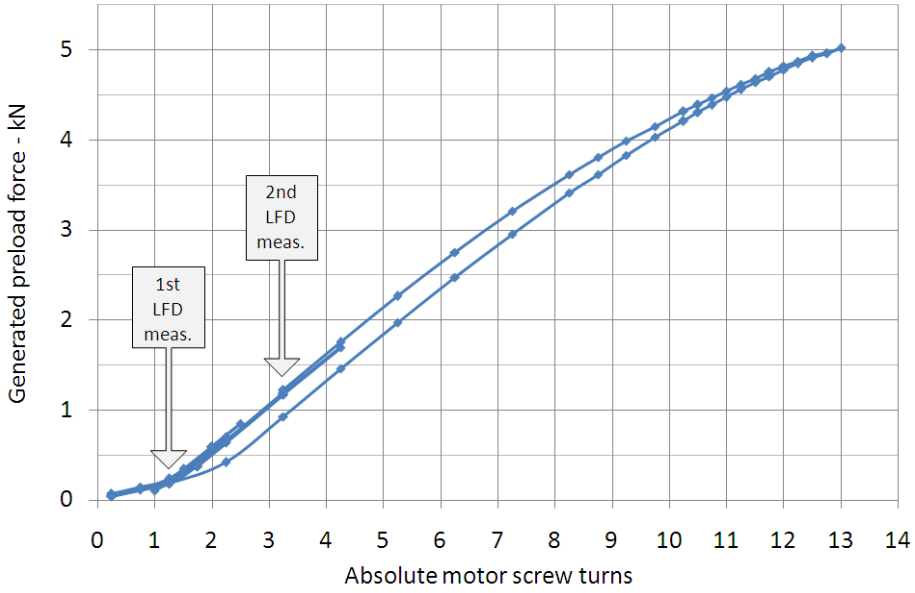

Fig. 6.57 – mechanical load generated over the tuning range on the Slim SS Blade tuner

Moreover, a deeper analysis of the mechanical coupling between piezo actuators and their environment has been performed through the measure of the piezo-to-piezo transfer function. A similar measurements has already been performed previously for the evaluation of cross-talk effects in FLASH module ACC6, see chapter 5.3.2. Now the transfer function has been acquired, using the CHECHIA facility lock-in amplifier[46], in different point of the tuning range, therefore at different preload level. The one corresponding to the highest load is plotted for reference in the next picture, Fig. 6.58.

[46] The instrument used for this measurements was a SRS840 Lock-In Amplifier from Stanford Research.

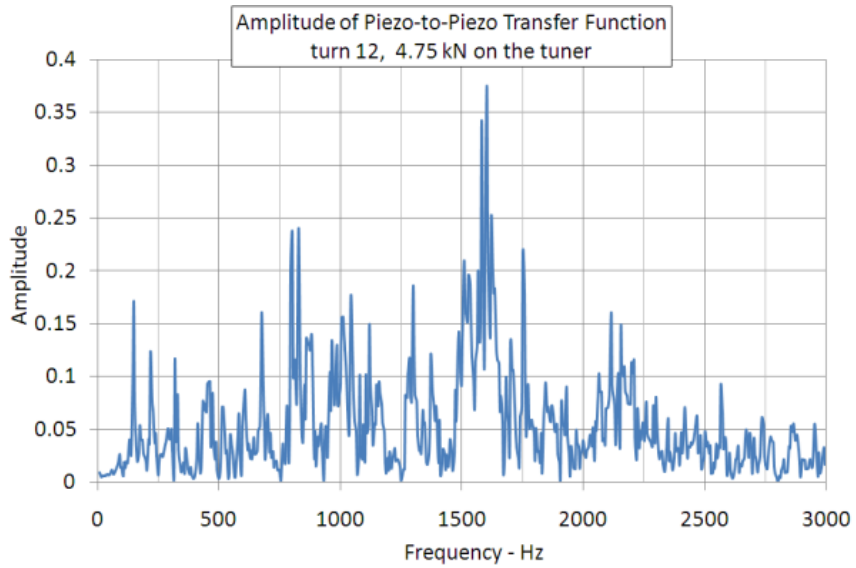

Fig. 6.58 – piezo-to-piezo transfer function amplitude

A first prototype analysis of the collected data is here shown. The average value of transfer function amplitude has been computed over the whole frequency range, the resulting value is then plotted, in following Fig. 6.59, as a function of cavity frequency, that is actually proportional to the applied load.

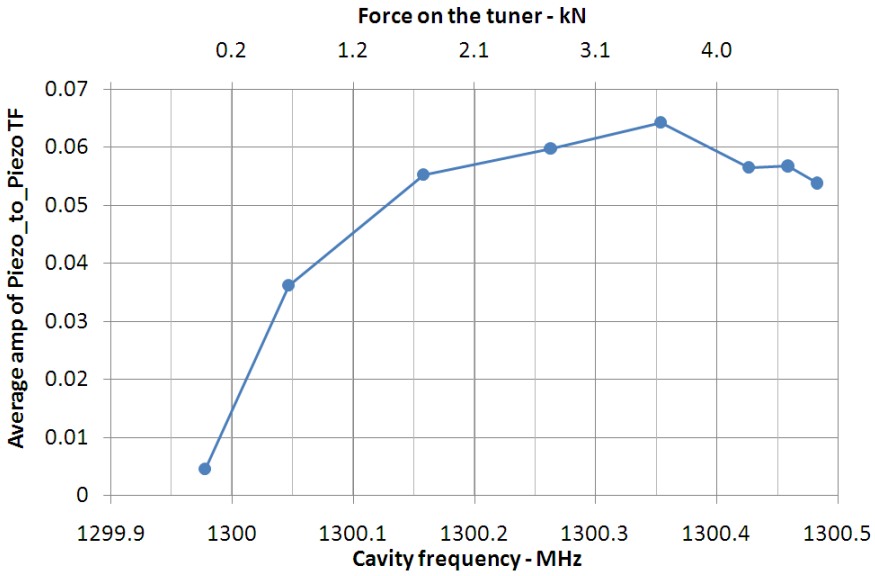

Fig. 6.59 – average amplitude of piezo to piezo TF as a function of cavity frequency

The parameter proposed for the analysis seemed to be correctly related to the efficiency of the mechanical coupling between piezo actuators and their environment, and therefore also between each other. The plot confirmed that the coupling between actuators

gradually improves in the first part of the tuning range, where piezo tests were initially performed, before reaching, as expected, an asymptotic value when the total load generated by the cavity is higher than about 1.5 kN.

6.9 REMARKS AND PERSPECTIVES

Finally, after cold tests performed in CHECHIA, it is certainly possible to confirm that the stainless steel model of the new design Blade Tuner (Slim_SS) successfully fulfilled every expected tasks for the test:

- every tuner component went through the complete cool-down and warm-up procedures without any problem.
- 520 kHz of slow tuning range has been performed in 13 complete screw turns.
- the entire LFD shown by Z86 cavity at the maximum gradient of 23 MV/m has been compensated in different load conditions and with each possible piezo configuration.

These cold test sessions, although rather quick (principal test session lasted from 11th to 13th September 2007), permit to consider the current stage of the Blade Tuner design development as a valid reference design. They also helped in underlining main weak points in the design or performance margins. Most of them have been already pointed out during measurements report in previous paragraphs:

- Unexpected discrepancies in frequency shifts during cavity cooldown, par. 6.8.1.
- Large hysteresis shown over the full first tuning range cycle, par. 6.8.2.
- Higher Lorentz force coefficient than what typically experienced with TTF tuner, although expected from theory. Par. 6.4 and 6.8.3.
- Differences in the coupling strength of the two installed piezo to RF (and so to cavity detuning), par. 6.8.3.

And beside these points:

- Around 24 hours were needed from the end of the cooldown to reach a stable 2 K temperature operations (Tab. 6.15), this is larger than usual time experienced with TTF tuner.
- Degradation of Z86 field amplitude profile from cell to cell, as measured from the field flatness[47] [51] parameter (FF) that moved from initial 97 % to 91 % at 2 K.

[47] Field Flatness values refers to the discrepancies in the RF field amplitude E within cells and it is here defined as $[1-(E_{max}-E_{min})/E_0]$ %.

For the former issue a slower than usual thermal assessment of the tuner assembly is expected to be the cause. Therefore remedy is simply found in using proper copper strings as thermal short-circuits from Blade Tuner components to the helium tank. While this aspect is actually not critical for final cavity operations, the latter one could eventually significantly lower cavity maximum achievable gradient. Although several factors can contribute this final effect, as for example the transportation of the assembled cavity module to CHECHIA, the most critical element has been identified to be the cavity free elongation as response to He tank overpressure during initial phase of the cooldown. As already introduced, 0.6 mm free range should have been allowed between fixed bolts on each safety screw rod and the He tank ring, and such range is needed in order to accomplish for the differential thermal contraction between tuner stainless steel and He tank titanium, 0.5 mm, plus a minor additional range to ensure that piezo stroke is not mechanically inhibited. Even before the start of the cooldown, as said, cavity stretching is induced by the isolation vacuum itself and this tensile force lasts up to the 2 K condition when only 30 mbar pressure is reached in the He tank. Cavity bears the whole force up to the engaging of safety bolts therefore, even in the optimal case, a large deformation, more than 200 kHz in terms of frequency shift, could be induced: a critical deformation for a warm cavity.

Lastly, almost all those issues requires a more intensive experimental investigation in order to be completely evaluated, therefore they will be considered in the next cold test session for the same new Blade Tuner model (the Slim_SS). It is scheduled to take place in BESSY [58] laboratory thanks to the Hobicat horizontal test cryostat in use for the CW RF power test of TESLA cavities.

The important experience of Blade Tuner cold and warm test and the detailed analysis of its results recently led to the definition and realization of a further development in the Blade Tuner design. While preserving the fundamentals of the revised model that has been successfully tested, minor modifications have been considered to further advance its features:

- Blade re-distribution over the tuner circumference. The 4-blades pack that is closer to each piezo position is doubled so that two packs in parallel bear the compressive load exerted on the tuner through each actuator. The overall number of blades is anyway even lowered using 3-blads packs for the remaining position over the tuner circumference (92 vs. 96 blades of the previous design revision) and the blade design is also preserved. This redistribution will modulate the stiffness of the tuner ring so that it is maximized exactly where the forces are applied (piezo sites). This leads to an higher overall longitudinal stiffness for the installed Blade Tuner (see Tab. 6.18), thus achieving improvements for almost all the weak points previously enlisted, specially for what concerns the tuning range hysteresis, the exhibited LFD and the differences between piezo performances.
- Different assembly angle. It has been chosen to increase the clearance between the Blade Tuner and the gas return pipe (GRP) of the cryomodule. This new layout also

slightly but favorably change the piezo position from the edge of the half-ring toward its center.

– Priority to the titanium material option. Lighter and compatible with Nb in terms of thermal shrinkage coefficients, thus completely eliminating the problem of excessive cavity deformation during cooldown. Anyway the experience gained with Slim_SS and Slim_Ti test led to the choice of an increased blade thickness compared to previous design, from 0.5 to 0.8 mm.

All the points enlisted for this latest revision of Blade Tuner design are visible in following Fig. 6.60 where a CAD 3D view of tuner core components and its repositioning inside the cryomodule are presented.

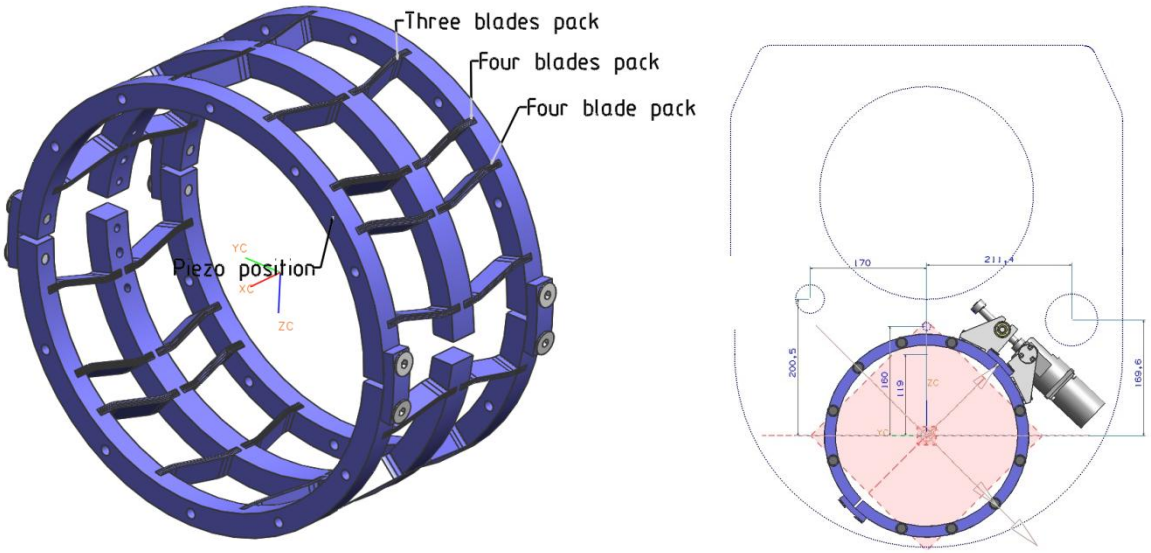

Fig. 6.60 – the final Blade Tuner design (left) and its revised positioning inside the cryomodule

Several additional aspects will benefit of the design modifications introduced in this paragraph:

– Improved compressive load limit, achieved exploiting the same blades assessment previously described.

– the Blade Tuner will, with these further design update, satisfy the ASME code[48] that are required for both XFEL and ILC.

Tab. 6.18 resumes nominal performances expected for this latest Blade Tuner design revision in comparison to both the original SuperStructures tuner and to the Slim_SS tuner tested at CHECHIA results.

[48] Set of codes and standards developed by the American Society of Mechanical Engineers (ASME) for different technical areas and, in particular for this case, for boiler & pressure vessels. For additional information refer to [143].

Blade Tuner Version	Material	Compression load limit [kN]	Stiffness [kN/mm]	Tuning Range [kHz]
Superstructures	Titanium	> 8	25	350
Slim tested	SS/Inconel	6.7	22	520
Slim reviewed	Ti	10	35	550

Tab. 6.18 – nominal performances expected for the final revision of Blade Tuner design.

At present, this final revision of the Blade Tuner design is undergoing last finalization and will be submitted to manufacturer within march 2008. A detailed experimental validation of the first realized model will follow.

In parallel to the definition of the ultimate Blade Tuner, according to considerations in par. 6.4 concerning the requirements for an high cavity external stiffness, the current design of end dishes (also used for Z86 cold tests) is under revision. The different position of the coaxial tuner, with respect to the TTF one, allowed indeed the possibility to introduce an improved design for the end group of the cavity, shortening it and changing its connection to the helium tank. In particular this should lead to a simpler solution, also more effective from the stiffness point of view. A preliminary solution, aiming to rationalize the cavity end cones, has been already studied and it is currently subject to final rationalization. This solution is presented in Fig. 6.61 (the original design is presented in par. 6.2.5). This design, originating from the solution adopted by the SNS and TRASCO cavities [121][122], is kept as simple as possible in order to reduce the overall cost and assembly operations.

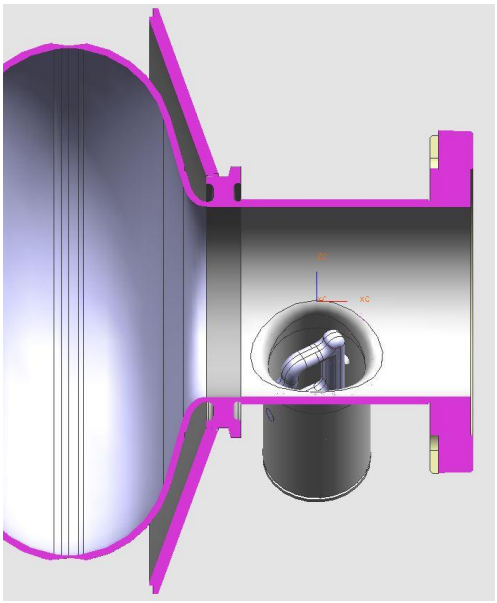

Fig. 6.61 – sketch of the proposed solution for the revised end group

It is also important to underline that the axial stiffness would be significantly higher than that of the old solution, allowing the transmission efficiency of the 90% of the tuner displacements to the cavity, while in the old version the efficiency was only of about 80% as previously shown. Even if the design has to be fully defined, this solution seems very promising in view of a large scale production of cavities for ILC.

In conclusion, both the deep cold test foreseen for the Slim_SS model realized and the manufacturing of the first Blade Tuners with further revised design will outline the path toward the complete experimental validation of this tuning solution for the TESLA cavities. The Blade Tuner latest revision, that fully exploited the performed cold test reported in this PhD thesis, will hopefully become by middle 2008 a solid option for the commissioning phase of XFEL as well as the reference tuning solution for ILC.

Meanwhile, both at LASA and other international laboratories, coaxial Blade Tuner models are currently in use or under development as tuning solution for a range of different accelerating cavities. Firstly, the author's group at LASA developed two coaxial Blade Tuner prototypes for the low-β 5-cell elliptical cavities for proton acceleration, realized by the same group in the frame of the projects for an high power proton accelerator (HPPA) and nuclear waste transmutation (EUROTRANS) [123][124]. One of the tuner prototypes is shown in Fig. 6.62, after assembling on a modified He tank specifically designed and realized.

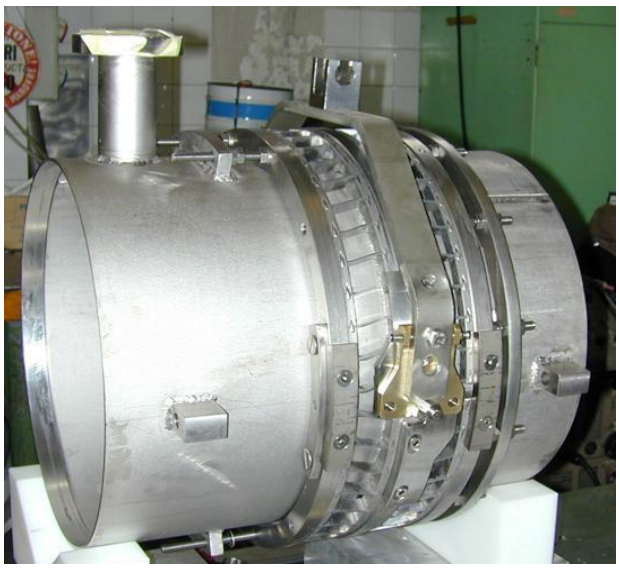

Fig. 6.62 – the coaxial Blade Tuner for the low-β proton SC cavity

In the frame of the ILC collaboration, Blade Tuners models for TESLA cavities are also in use at University of Pennsylvania (UPenn) [125] and at Fermi National Laboratory (FNAL) [126] test facilities. Special design Blade Tuners, derived from the superstructures design, have been moreover chosen for the tuning of the third harmonic accelerating (3.9 GHz) superconducting cavity for new generation of high brightness photo injector under realization at FNAL [127].

Finally, a superstructures design Blade Tuner has been chosen for the tuning of the superconducting 2-cell injector cavity under studying for the Cornell ERL project [128]. In this case, the adopted solution for the cavity fast tuning is similar to the one presented in this dissertation, although smaller piezo stack are in use (about 1 cm length) [129].

7 CONCLUSIONS AND OUTLOOK

This thesis activity has been developed in the frame of the TESLA superconducting particle accelerator technology, the reference choice for both the incoming European XFEL linac under construction at DESY, Hamburg, and the next TeV energy scale e^+-e^- linear collider, the ILC (par. 1.3). The dissertation covers the recent R&D activity and main results within the TESLA technology collaboration, with special focus on the author's contribution on this topic.

In particular, the frame of the presented activity is mainly the effort toward the optimization of the TESLA 9-cell resonator pulsed operations, both in terms of absolute accelerating gradient performances and capital cost saving. In fact, TESLA cavities are extremely sensitive to mechanical disturbances due to their design and to their very high quality factor, typically about 10^{10} (par. 2.1.1). Therefore, in order to achieve the nominal accelerating gradient of 35 MV/m required for the ILC, TESLA cavities must be provided with a fast tuning device (fast frequency tuner) capable to counteract the main detuning source, the Lorentz force detuning or LFD. This issue refers to the interaction between the EM fields in the cavity and the shielding currents on the walls that, through the Lorentz force, is capable to deform the resonator at micrometer level thus inducing a critical shift in the resonance frequency during the RF pulse. Since first proof of principle at DESY in 2001, significant steps have been made and nowadays the use of piezoelectric actuators integrated in the existing cavity slow tuner mechanism is the reference and widely accepted solution. Currently, the TESLA Test Facility or TTF model is the reference piezo tuner design and it is in use at the FLASH linac at DESY. It is realized by means of a leverage mechanism installed at the cavity end, it includes a stepper motor for cavity slow tuning and up to two piezo.

The issue of measuring and characterizing the cavity detuning during pulsed operation has been firstly considered. With the use of devoted MATLAB routines for the off-line computation of detuning from RF power probes, based on an algorithm originally developed by A. Brandt [69], the author contributes to the experimental characterization of the Lorentz force detuning issue for two 8 TESLA cavities FLASH cryomodule, the ACC6 and ACC7, during their validation tests at the CMTB facility (par. 1.4), DESY. This activity then continued within the development of an advanced detuning control system, based on the FPGA SIMCON hardware developed for TESLA Low Level RF control. The goal is to implement in VHDL code a controller firmware capable to perform an on-line computation of detuning, fast enough to use it for an intra-pulse or pulse to pulse control loop. The author contributes to DESY LLRF and TUL groups in the development and test of prototype sub-routines of the controller code; an on-line detuning computation algorithm, a piezo driving signal generator and a signal filtering stage, are reported in the dissertation.

A range of multi-layer piezoelectric fast actuators, among those available on the market, have been deeply characterized in order to understand their features and limits

when operated in a cryogenic environment, since specifications for this special working range are not provided by manufacturers. This activity, jointly performed within the collaboration among author's group at LASA, IPN-Orsay, TUL and DESY, finally led to the definition of the piezo models to be installed in fast tuners.

The author's contribution to the study of possible detuning control strategies, exploiting installed piezo actuators, has been also reported in the dissertation, both for what concerns the closed loop suppression of stochastic contributions (microphonics) and the feedforward compensation of the repetitive Lorentz force detuning (LFD). The use of a single semi-sinusoidal piezo pulse with proper amplitude and delay for the LFD compensation has been chosen and successfully proved on cavities of FLASH module ACC6, wherein each cavity is equipped with a TTF piezo tuner and two PI piezo (par. 4.4.3). Experimental results, jointly performed by the author and the DESY group, fully confirmed the feasibility of the LFD compensation with a single pulse even at the goal accelerating gradient of 35 MV/m. On the most performing cavity, more than 630 Hz of detuning over the flat-top phase of the RF pulse have been compensated as required by the ILC specifications. Test on ACC6 at the CMTB facility allowed to perform, for the first time, the simultaneous compensation of the LFD on an entire cryomodule operated with the LLRF feedback control. Although several limitations and simplifications were present (par. 5.2), results, in terms of both peak RF power saving and accelerating field stability, were remarkable. Proposals for additional mechanical analyses that exploit the presence of piezo stacks and their duality actuator/sensor have been also presented by the author in this dissertation; they allowed to estimate cavity mechanical parameters, as main modes and perturbations propagation time, and lastly the transmission of harmonic disturbances along the module cold mass.

An experimental analysis of the dependence of the piezo pulse detuning compensation efficiency from its time advance in comparison to the RF pulse has been carried out. This investigation, together with an analytical modeling that has been proposed by the author, allowed to determine the possibility of an alternative use of the piezo single pulse for efficient LFD compensation purposes, referred as 2^{nd} oscillation compensation scheme and here introduced for the first time. It relies on a larger time advance for the piezo pulse in order to wait for an almost complete cavity oscillation before the RF pulse, oppositely to the usual settings (accordingly referred as 1^{st} oscillation scheme) that instead corresponds to synchronizing the RF pulse to the initial part of cavity oscillation. While the compensation efficiency of this 2^{nd} oscillation scheme seemed at least comparable, it led to some additional benefits: the piezo pulse does not induce additional static detuning so that piezo operations can be decoupled by the stepper motor position, and small static detuning variations (in a range of about 200 Hz) can be compensated just varying the piezo pulse timing parameter.

Finally, the experience gained in the field of cavity tuners and dynamic detuning compensation has been applied to the development of the coaxial Blade Tuner option for TESLA cavities, also reported in the dissertation. Since the first detailed report released for TeV energy scale linear collider, the TESLA TDR in 2001, a reduced clearance between successive cavities in the cold string was designed in order to improve the machine active

length and finally reduce linac sections length. This choice led to the first evaluation of a coaxial tuner option as a replacement for the TTF tuner. Since the first prototype the cavity tuning is achieved by means of thin plates, called blades, that transform an azimuthal rotation of a central coaxial ring in a longitudinal displacement of two outer rings, therefore changing the cavity length. As of today the coaxial Blade Tuner is still the reference option for the baseline design of the ILC, and the INFN author's group at LASA is in charge of its design and realization. The recent activity, devoted to the revision of the coaxial Blade Tuner design in view of a large scale production, is reported in the dissertation. Author's contributions are primarily considered; they are focused on the test, choice and integration of piezoelectric actuators for dynamic detuning compensation and on the experimental tests of the recently produced prototype. A TESLA cavity has been equipped with a Blade Tuner prototype and a properly modified helium tank and it has been tested in the horizontal cryostat CHECHIA at DESY on September 2007. The prototype successfully achieved expected tuning range and Lorentz force detuning compensation performances; issues and limits shown will be further investigated in a CW cold test to be performed at BESSY, Berlin. The experience gained with the cold test has been then used for a final revision of the Blade Tuner design that is currently under finalization, realization of first models is expected by April 2008. This Blade Tuner latest revision, that fully exploited the performed cold tests reported in this PhD thesis, will hopefully become by middle 2008 a solid option for the XFEL as well as the reference tuning solution for ILC.

APPENDIX A : ANALYTICAL APPROACH TO LFD COMPENSATION

Even if currently several experimental results have been achieved about the Lorentz force detuning (LFD) compensation, an analytical approach has not been yet performed for this issue. Instead this would lead to the possibility to fully understand the observed behavior of the cavity during LFD active compensation, confirm its current interpretation and eventually analytically search for the optimum piezo pulse shape and configuration.

In this paragraph a prototype of analytical approach is presented. It mainly relies on the possibility to model the overall system under investigation thanks to the measure of a proper piezo-to-RF transfer function. As expected for an harmonic analysis, this measurements implies the acquisition of the ratio of the cavity detuning response over the piezo driving stimulus, for a given range of frequencies. Therefore amplitude and phase of the sinusoidal cavity detuning response are recorded, as a result of a sinusoidal driving pulse on piezo, with given amplitude and phase. This analysis will result in a linear modeling of the system, any non-linearity, like those generated by inelastic mechanical couplings between components, must be avoided.

Piezo to RF transfer functions are acquired using the same reference scheme already described for the static and microphonics detuning measurement in Fig. 3.1, based on a low power CW RF cavity driving signal and phase detection. Unfortunately, a limited number of these measurements have been actually performed during this years on TESLA like cavities at cold, and even fewer are available for this proposed analysis. Therefore a measurements performed in CHECHIA at DESY in 2003 on a TESLA type 9-cell cavity has been here considered, since for that test a dedicated low power and correctly coupled ($\beta = 1$) input RF antenna was installed.

Collected amplitude and phase data concerning the piezo-to-RF transfer function are showed in the next picture, Fig. a.1.

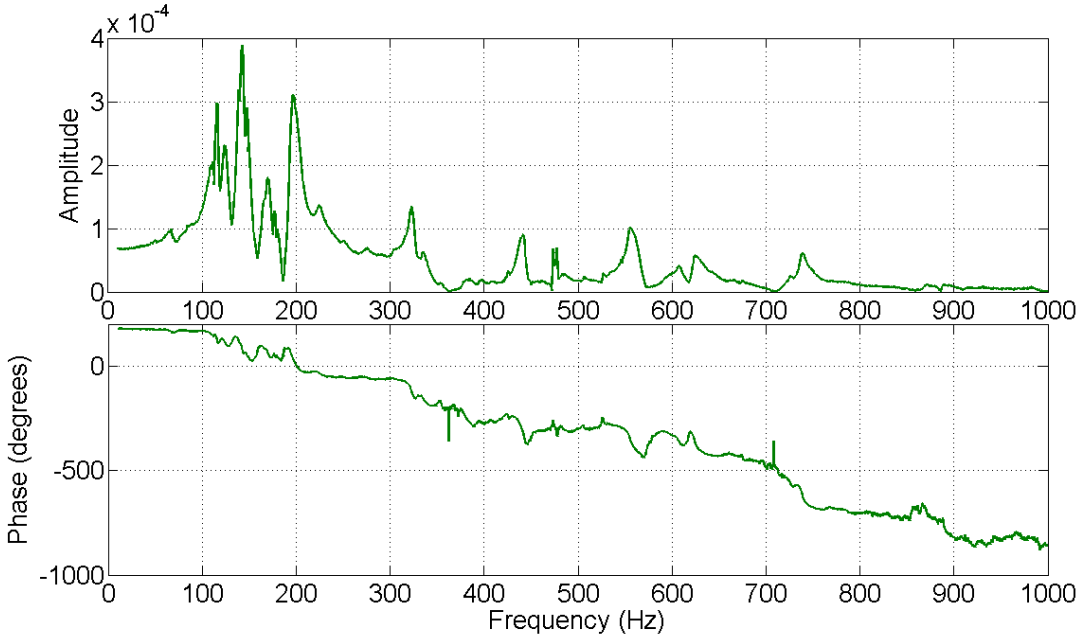

Fig. a.1 - amplitude and phase of piezo-to-RF transfer function of a TESLA cavity in CHECHIA, 2003

Such a measure resumes in two plots several different effects, from pure mechanical resonances to their interaction with the electromagnetic fields inside the cavity, even the coupling of the piezo actuator to the cavity is included. It's anyway easy to recognize cavity mechanical resonances in the amplitude plot, together with a clear delay line aspect of the phase plot (linearly sloping phase). It must be underlined that the actual dominating frequencies in this setup reveal to be placed in a lower range, 100 to 200 Hz, if compared to those showed by cavities in FLASH module #6 (see par. 5.3.1). This mainly means that the time scale of this simulations will differ from the actual LFD response from real cavities and therefore they cannot be directly compared.

The next step is now to use the information in the transfer function to generate an analytical model of the system, as one conceptual block that accepts a piezo driving signal as input and responds with the actual corresponding detuning. Matlab[49] offers some valuable tools to perform such fitting, in particular data have been fitted with a State Space model of a given order (32, that means up to 16 among double poles or zeros) providing that at least the dominant resonances present in the transfer function were correctly interpolated. The result of this analytical fit is showed in Fig. a.2.

[49] Matlab R2006a and its software tools has been used, from The MathWorks company [138].

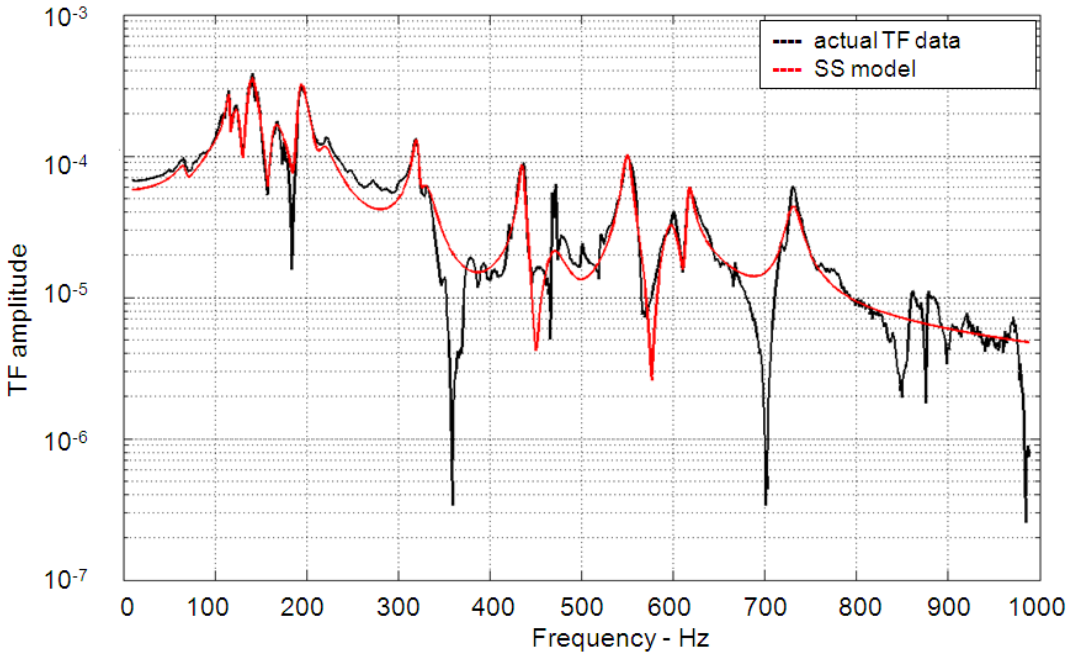

Fig. a.2 - analytical fit of the piezo-to-RF transfer function compared to actual data, TESLA cavity environment

The plot confirms that the fit shows a good correlation, mainly at lower frequencies where dominant elements are placed.

Once such an analytical model of the cavity is available it is possible to analytically compute, using Matlab Simulink[50] tool, the response of this system to a custom input. This step would conceptually corresponds to simply perform the multiplication of the Laplace transforms of both pulse and system, determine the Laplace transform of the output and from this back to time domain. Three pulses have been considered, the reference one is the half-sinusoidal pulse 2.5 ms width since it has been used in the recent LFD experimental measurements reported in this thesis. A square and a triangular pulses have been also prepared for comparison, both of them with the same time length. Input pulses are shown in Fig. a.3.

[50] Simulink is also a Matlab tool, from The MathWorks company too.

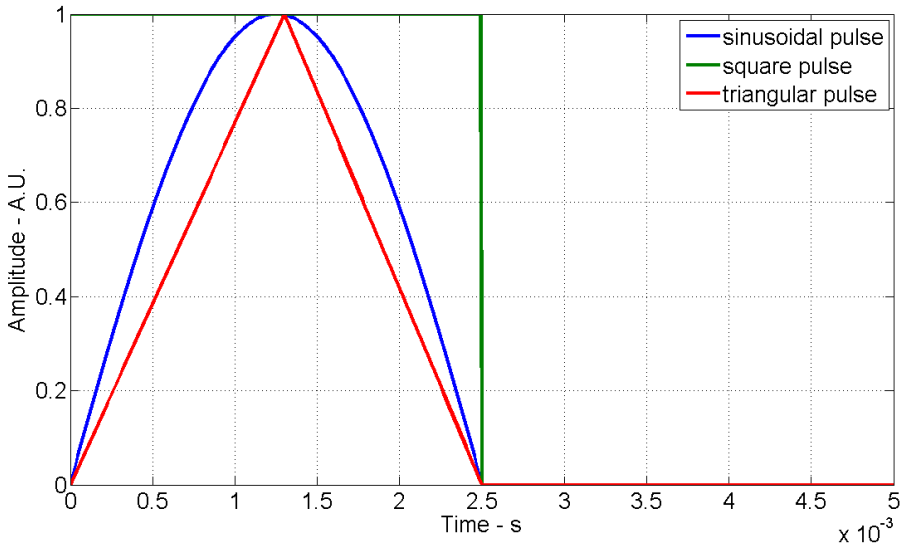

Fig. a.3 - input pulses considered for the analytical LF detuning simulation

Finally, those pulses can be used as inputs to the analytical model deduced from transfer function data in order to collect a simulated time-domain detuning response. Results are showed, in a small time scale, in Fig. a.4.

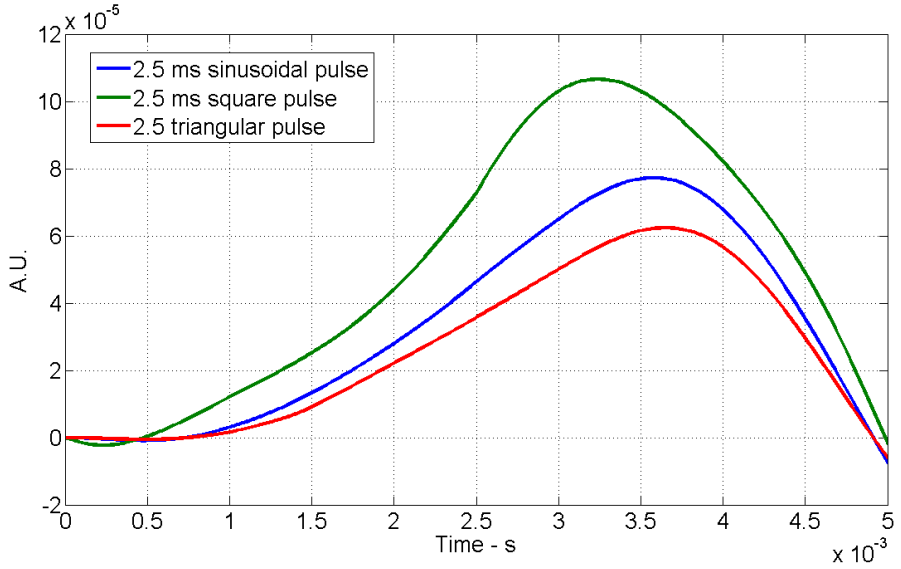

Fig. a.4 - simulated detuning response of a TESLA cavity to different piezo pulses, small time scale

Results confirm expectations, the detuning rise time is higher for the square pulse which is the one that forces the highest current flow through the piezo capacitance. Looking at this simulated response on a larger time scale in the next picture, all the issues related to LF dynamic detuning features and on its active compensation, that previously

arose in experimental tests reported in par. 5.1 and par. 6.8.3, can be actually recognized. The correct interpretation is proposed in Fig. a.5.

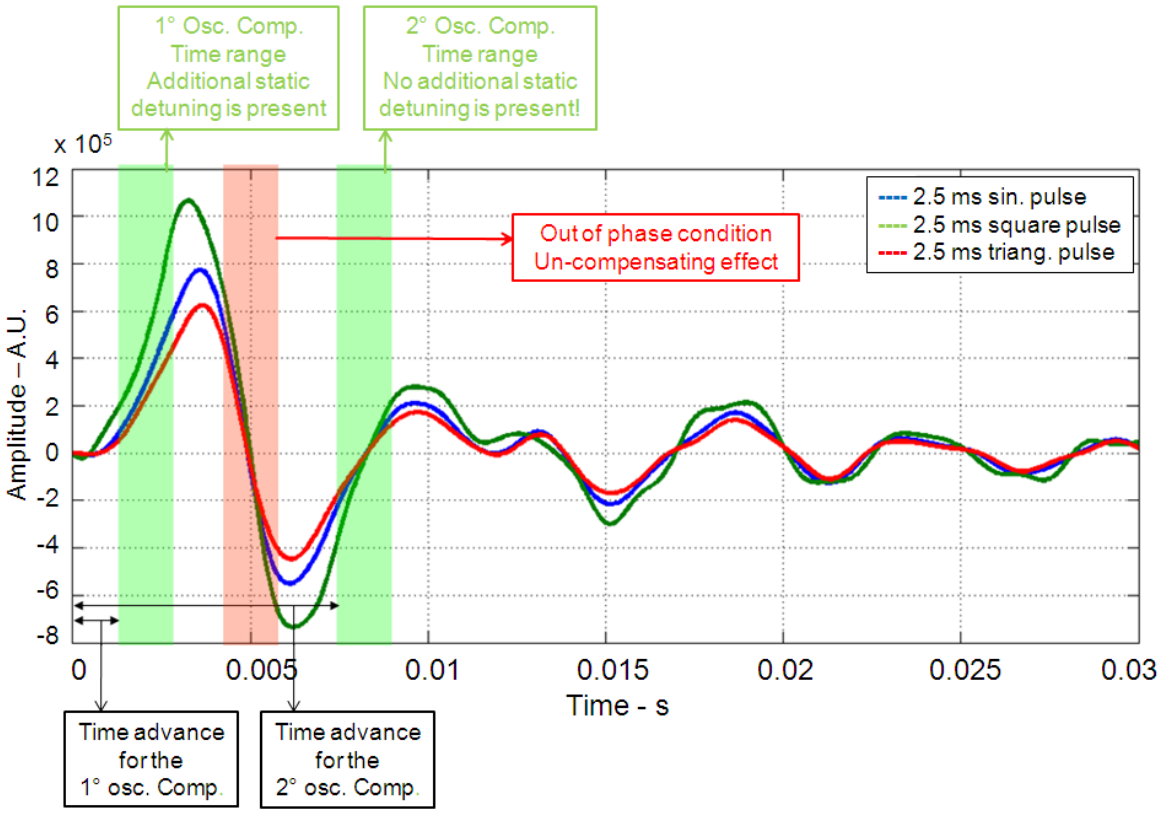

Fig. a.5 - simulated detuning response of a TESLA cavity to different piezo pulses, long time scale

As explained in the picture, both 1st and 2nd oscillation compensation scheme time range (see par. 5.2) can be identified, therefore validating the experimental results previously showed. Even the time advance values seem to be coherent with the experimental setup, provided that the dominating mechanical resonant frequencies in the case of ACC6 cavities were different. Actually those frequencies were higher than the ones of the cavity used to generate simulation data, around 250 Hz instead of around 150 Hz, therefore the time scale of Fig. a.5 should be in principle shrunk in order to be compared to experimental results. Simulation show a time advance values of roughly 1 ms and 7 ms (start of the green time windows) for the 1st and 2nd osc. scheme respectively, instead ACC6 results were, as showed, about 0.6 ms and 4 ms. Therefore a coherent time scale factor of roughly 0.6 seems to be confirmed between data series of the two different setups, a moreover this factor is correctly coherent with the two corresponding periods of dominant mode.

A larger number of piezo_to_RF transfer function measurements are instead available for simplified but meaningful LFD test facilities. Consider as a reference, for this second set, the single copper cell test facility once installed at LASA laboratory and operated at

room temperature. It hosts a single piezo actuator directly coupled to the cavity and the needed RF equipment to perform CW detuning acquisition according to scheme in Fig. 3.1. The setup is showed in Fig. a.6.

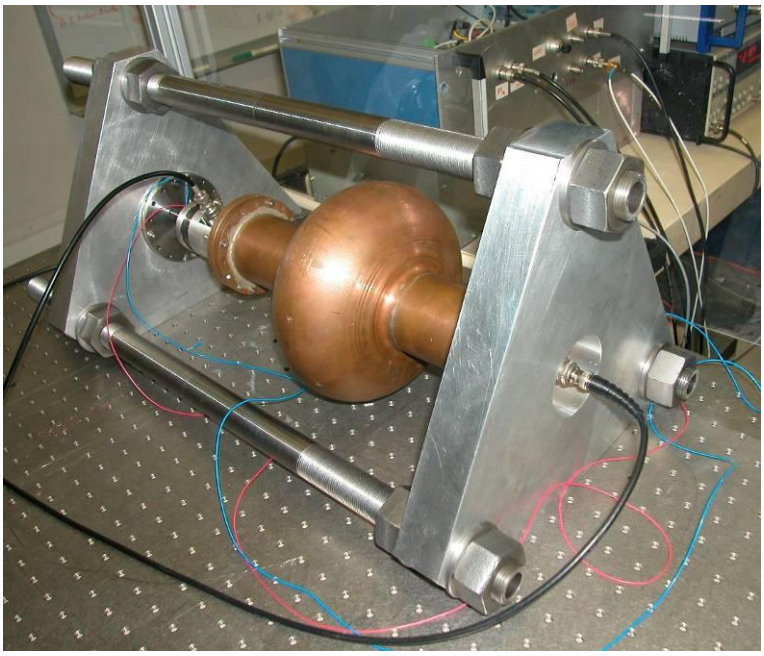

Fig. a.6 - LASA single cell test facility for piezo-to-RF transfer function measurements

Since the system under exam is, in this case, considerably simpler than an actual TESLA cavity setup (made by a larger number of more complex elements) the corresponding piezo_to_RF transfer function is simpler as well, therefore can be fitted with higher precision. Both actual data and fit for the LASA LFD test facility are showed in Fig. a.7.

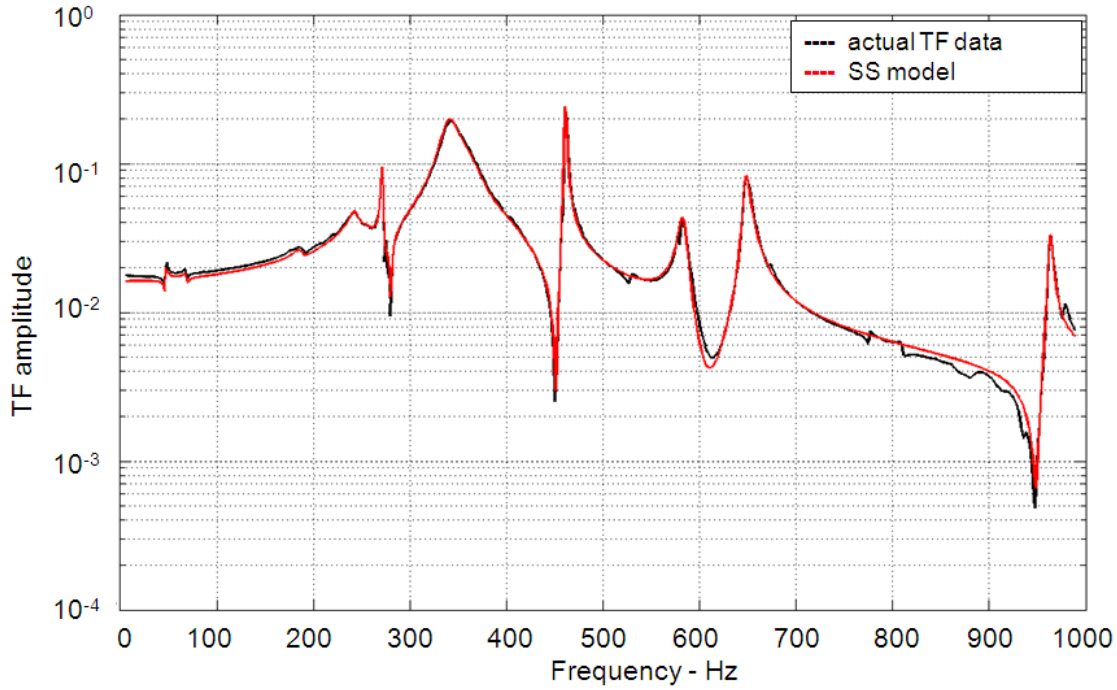

Fig. a.7 - analytical fit of the piezo-to-RF transfer function compared to actual data, LASA LFD test facility

Therefore the detuning response of the system to the same pulses already showed can be computed with higher accuracy, but the dynamic properties are anyway significantly different from the TESLA cavity environment. It can be seen that in this case the dominant frequencies in the transfer function are shifted to higher frequencies as roughly expected by the length reduction of the setup (from 9 cells to 1 cell). Final results for this simplified case are presented in Fig. a.8, the detuning output has been computed for the same three pulses showed before.

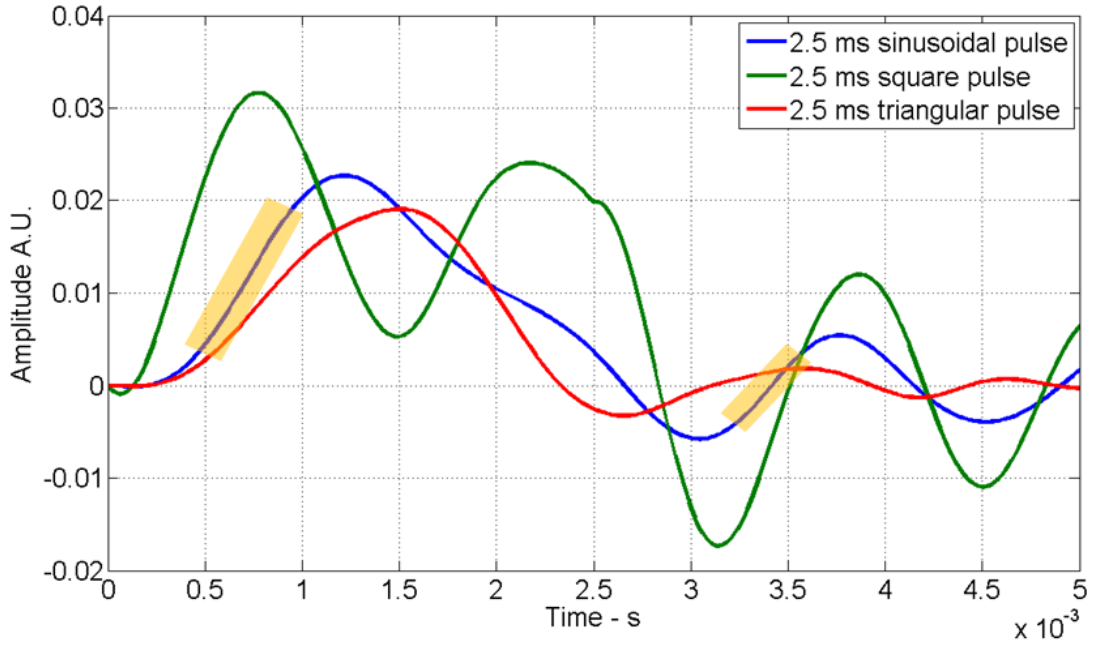

Fig. a.8 - simulated detuning response for the LASA LFD test facility to different piezo pulses

Even if the transient responses are not easily comparable to the TESLA setup ones, also in this case the same time regions are recognizable (highlighted in orange). Considering for instance the response to sinusoidal pulse, blue curve, the 1st oscillation compensation roughly ranges from 0.5 to 1 ms and a 2nd oscillation compensation seems possible around 3.5 ms time advance.

APPENDIX B : MECHANICAL PARAMETERS USED FOR FEM SIMULATIONS

Several results from finite elements modeling analyses (FEM) have been used or at least mentioned throughout this thesis in different frames. In particular, the analyses and development of the coaxial Blade Tuner solution, in charge of the author's group at LASA laboratory and described in chap. 6, made intensive use of FEM mechanical simulations to evaluate the longitudinal stiffness of cavity assembly parts, to estimate internal stresses of tuner elements during operations as well as to understand blades failure modes and load limit. In particular those FEM simulations took use of the ANSYS software from ANSYS Inc., a standard and widely used solution for such analyses [130].

In order to fully understand the setups and results of FEM analyses related to Blade Tuner activity, the type and the main properties of each material involved have been resumed in the following Tab. b.1 and Tab. b.2.

Part	**material**	**specification**
Cavity	Niobium (Nb)	
Helium tank and connection ring material	Titanium (Ti)	Ti Gr2
End dishes	NbTi	
Flanges	Niobium (Nb)	
Bellow	Titanium (Ti)	Ti Gr1
Tuner rings	Titanium (Ti)	Ti Gr2
	Stainless steel (SS)	Aisi 316L
Tuner blades	Titanium (Ti)	Ti Gr5
	Inconel	IN 718
Jaw with pin, operating bracket	Stainless steel (SS)	Aisi 316L
Motor and bearing support	Stainless steel (SS)	Aisi 316L
Connecting plate	Brass	Ot MS58
Stepper motor screw	CuBe	CuBe 1.85Co

Tab. b.1 –constituent material for each cavity and tuner assembly considered in FEM analyses

Material	Parameter	Value	Units
Ti gr1	Young Modulus, E_x	105	GPa
	Density, ρ	4500	kg/m^3
	Major Poisson ratio, ν_{xy}	0.37	-
Ti gr2	Young Modulus, E_x	105	GPa
	Density, ρ	4500	kg/m^3
	Major Poisson ratio, ν_{xy}	0.37	-
Ti gr5	Young Modulus, E_x	113.8	GPa
	Density, ρ	4500	kg/m^3
	Major Poisson ratio, ν_{xy}	0.34	-
Nb	Young Modulus, E_x	102.7	GPa
	Density, ρ	8750	kg/m^3
	Major Poisson ratio, ν_{xy}	0.38	-
Aisi 316L	Young Modulus, E_x	191	GPa
	Density, ρ	7850	kg/m^3
	Major Poisson ratio, ν_{xy}	0.29	-
Inconel 718	Young Modulus, E_x	207	GPa
	Density, ρ	8500	kg/m^3
	Major Poisson ratio, ν_{xy}	0.29	-
NbTi	Young Modulus, E_x	62.1	GPa
	Density, ρ	5700	kg/m^3
	Major Poisson ratio, ν_{xy}	0.38	-
Ot MS58	Young Modulus, E_x	105	GPa
	Density, ρ	8400	kg/m^3
	Major Poisson ratio, ν_{xy}	0.35	-
CuBe	Young Modulus, E_x	127.6	GPa
	Density, ρ	8250	kg/m^3
	Major Poisson ratio, ν_{xy}	0.32	-

Tab. b.2 – young modulus, density and Poisson ration for each material considered in FEM analyses

BIBLIOGRAPHY

1. *ILC Reference Design Report.* : ILC GDE, 2007.

2. *ADA page at INFN-LNF web site.* [Online] http://www.lnf.infn.it/acceleratori/ada/.

3. *ADONE page at the INFN-LNF web site.* [Online] http://www.lnf.infn.it/acceleratori/adone/.

4. *LEP page at the CERN web site.* [Online] http://public.web.cern.ch/Public/en/Research/LEP-en.html.

5. *TEVATRON page at the FNAL web site.* [Online] http://www-bdnew.fnal.gov/tevatron.

6. *CERN LHC web site.* [Online] http://lhc.web.cern.ch/lhc.

7. *TESLA Technical Design Report.* : TESLA, 2001.

8. *JLC page at the KEK web site.* [Online] http://www-jlc.kek.jp/2003oct/index.html.

9. *NLC page at the SLAC web site.* [Online] http://www-project.slac.stanford.edu/lc/home-page_new/nlc-home-intl.html.

10. *ILC web site.* [Online] http://www.linearcollider.org.

11. *TESLA Technology Collaboration web site.* [Online] http://tesla-new.desy.de.

12. **C. Pagani, P. Pierini.** Cryomodule design, assembly and alignment. *Proceedings od SRF05 workshop.* New York, US : s.n., 2005.

13. **J. G. Weisend II, C. Pagani, R. Bandelmann, D. Barni, A. Bosotti, G.Grygiel, R. Lange,P. Pierini, B. Petersen, D. Sellmann, S. Wolff.** The TESLA Test Facility (TTF) Cryomodule: A Summary of Work to Date. *Proceedings of Cryogenic Engineering Conference* . Montréal, Canada : s.n., 1999.

14. *SLAC web site.* [Online] http://www.slac.stanford.edu.

15. *GLC page at the KEK web site.* [Online] http://www-jlc.kek.jp/2004sep/index.html.

16. *X-FEL web site.* [Online] http://xfel.desy.de.

17. *LASA web site.* [Online] http://wwwlasa.mi.infn.it/.

18. **A. Bosotti, R. Paparella, F. Puricelli.** Extreme piezo lifetime test report. : Physick Intrumente technical notes, 2005.

19. **Paparella, Rocco.** Sviluppo di un sistema attivo di controllo delle vibrazioni indotte in cavità superconduttive ad alto campo per acceleratori di particelle. *Master Thesis.* INFN Milano : Università degli Studi di Milano, 2004.

20. **H.Padamsee, J.Knobloch, T.Hays.** RF Superconductivity for Accelerators. : John Wiley & Sons, 1998.

21. **Knobloch, Jens.** Advanced Thermometry Studies of Superconducting RF Cavities. *Ph.D. thesis.* : Cornell University, 1997.

22. **J.H.Billen, L.M. Young.** Report No. LA-UR-96-1384. : Los Alamos National Laboratory, 2004.

23. *Ansoft web site.* [Online] http://www.ansoft.com.

24. *CST web site.* [Online] http://www.cst.com.

25. **C.G.Montgomery, R.H.Dicke, E.M.Purcell.** Principles of microwave circuits. *Radiation Laboratory Series, Vol. 8*. New York : McGraw-Hill, 1948.

26. **Schilcher, Thomas.** Vector sum control of pulsed accelerating fields in Lorentz force detuned superconducting cavities. *PhD Thesis.* : Hamburg University, 1998.

27. **W.S.Levine.** The Control Handbook. : CRC Press / IEEE Press, 1996.

28. **Sękalski, Przemysław.** Smart Materials as Sensors and Actuators for Lorentz Force Tuning System. *PhD Thesis.* : Technical University of Łódź, Poland, 2006.

29. **Onnes, H.Kammerlingh.** The Superconductivity of Mercury. *Nos. 122 and 124.* : Comm. Phys. Lab. Univ. Leiden, 1911.

30. **W.Meissner, R.Ochsenfeld.** Naturwissenshaften 21, 787. 1933.

31. **Lilje, Lutz.** Experimental Investigations on Superconducting Niobium Cavities at Highest Radiofrequency Fields. *PhD thesis.* : University of Hamburg, 2001.

32. **J.Bardeen, L.Cooper, J.R.Schrieffer.** Theory of Superconductivity. *Physical Review, 108:1175*. 1957.

33. **C.J.Gorter, H.B.G.Casimir.** Physica 1, 306 . 1934.

34. **V.L.Ginzburg, L.D.Landau.** Zh. Eksp. Teor. Fiz. [Sov. Phy.-JETP] 20, 1064. 1950.

35. **A.B.Pippard.** Impurities in superconductors. *Proc . Roy. Soc, A203:98*. London, UK : s.n., 1953.

36. **J.Waldram.** Surface Impedance of Superconductors. *Adv. Phys., 13:1*. 1964.

37. **Bathe, K.J.** Finite Element Procedures. : Prentice Hall, 1996.

38. **J.Matricon, D.Saint-James.** Superheating fields in superconductors. *Phys. Lett., 24A:241*. 1967.

39. **H.Piel.** Superconducting cavities. *Superconductivity in Particle Accelerators.* : S. Turner, p. 149, CERN, 1989.

40. **R.Doll, P.Graf.** Superheating in Cylinders of Pure Superconducting Tin. *Phys. Rev. Lett., 19:897*. 1967.

41. **M.Bahte, F.Herrmann, P.Schmuser.** Magnetization and Susceptibility Measurements on Niobium Samples for Cavity Production. *Proceedings of the 8th Workshop on RF Superconductivity.* Abano Terme, Italy : s.n., 1997.

42. **M.Bahte.** Materialuntersuchungen an supraleitenden Niob-Proben mit Magnetisierungs- und Suszeptibilitatsmessungen. *Master thesis.* : University of Hamburg , 1998.

43. **B.Bonin.** Materials for superconducting cavities. *Superconductivity in Particle Accelerators.* : S. Turner, pp. 191–200, CERN, 1996.

44. **K.Saito, P.Kneisel.** Temperature Dependence of the Surface Resistance of Niobium at 1300 MHz - Comparison to BCS Theory. *Proceedings of the 9th Workshop on RF Superconductivity.* Santa Fe, US : s.n., 1999.

45. **B.Aune, R.Bandelmann, D.Bloess, B.Bonin, A.Bosotti, M.Champion, C.Crawford, G.Deppe, B.Dwersteg, D.A.Edwards, H.T.Edwards, M.Ferrario, M.Fouaidy, P.D.Gall,**

A.Gamp, A.Gössel, J.Graber, D. Hubert, M.Hüning, M.Juillard, T.Junquera, H.Kaiser, G.Kreps et al. Superconducting TESLA cavities. *Physical Review Special Topics - Accelerators and Beams, vol. 3, 092001* . 2001.

46. **B.Piosczyk.** Exerimentelle Untersuchungen an supraleitenden Wendelresonatoren aus Niob im 100 MHz-Bereich. *PhD thesis.* : Universitat Karlsruhe, 1974.

47. **R.H.Fowler, L.Nordheim.** Proc. R. Soc. London A 119, 173. 1928.

48. **U.Lauströer, et al.** DESY Report No. DESY M-87-03. 1987.

49. **W.D.Moeller, et al.** High Power Coupler For The TESLA Test Facility. *Proceedings of the 9th Workshop on the RF Superconductivity.* Santa Fe, US : s.n., 1999.

50. **T.Saeki, et al.** Series test of high-gradient single-cell superconducting cavity for the establishment of KEK recipe. *Proceedings of EPAC06.* Edinburgh, UK : s.n., 2006.

51. **P.Schmuser.** Tuning of multi-cell cavities using bead pull measurements. *SRF 920925-10.* : Laboratory of Nuclear Science, Cornell University, 1992.

52. **K.Saito, H.Inoue, E.Kako, T.Fujino, S.Noguchi, M.Ono, T.Shishido.** Superiority of electropolishing over chemical polishing on high gradients. *Part.Accel.60:193-217.* 1998.

53. **K.Saito, T.Higuchi, T.Suzuki, E.Kako, S.Noguchi, M.Ono, T.Shishido.** Water rinsing of the contaminated superconducting RF cavities. *Proceedings of 7th Workshop on RF Superconductivity.* Gif-sur-Yvette, France : s.n., 1995.

54. *Zanon web site.* [Online] http://www.zanon.com.

55. *Accel web site.* [Online] http://www.accel.de/.

56. *Cerca web site.* [Online] http://www.cerca.fr/uk/index.html.

57. *AES web site.* [Online] http://www.aesys.net/.

58. *BESSY web site.* [Online] http://www.bessy.de.

59. **Slater, J. C.** Microwave Electronics. : Reviews of Modern Physics, 1946.

60. **J.B.Encinas.** Phase Locked Loops. : Chapman & Hall, 1993.

61. **A.Mosnier, S.Chel, M.Desmons, B.Hervieu, M.Maurier, B.Phung Ngoc, A.Veyssiere.** MACSE superconducting cavity RF drive system . *Proceedings of EPAC1990.* Nice : s.n., 1990.

62. **Liepe, Matthias.** Superconducting Multicell Cavities for Linear Collider. *PhD Thesis.* : Hamburg University, 2001.

63. **A. Neumann, W. Anders, S. Klauke, J. Knobloch, O. Kugeler, M. Schuster.** Charactherization of a piezo-based microphonics compensation system at Hobicat. *Proceedings of EPAC 2006.* Edinburgh, Scotland : s.n., 2006.

64. **O. Kugeler, W. Anders, J. Knobloch, A. Neumann.** Microphonics measurements in a CW driven TESLA-type cavity. *Proceedings of EPAC 2006.* Edinburgh, Scotland : s.n., 2006.

65. **Jackson, J. D.** Classical Electrodynamics. *2nd edition.* New York : Wiley, 1975.

66. **Tückmantel, J.** Performance of Cavities. *CERN, SL-RF.* 1996.

67. **P. Pierini, C. Pagani, A. Bosotti, P. Michelato, N. Panzeri, R. Paparella.** Characterization of an elliptical low beta multicell structure for pulsed operation. *Proceedings of SRF 2005 workshop* . New York : s.n., 2005.

68. **Simrock, Stefan.** Tutorial on designing the optimal controller. *Proceeding of LLRF 2005 workshop.* CERN : s.n., 2005.

69. **Brandt, Alexander.** Development of a finite state machine for the automated operation of the LLRF control at FLASH. *PhD Thesis.* Hamburg : University of Hamburg, 2007.

70. **Jalmuzna, W.** Design And Implementation Of Universal Mathematical Library Supporting Algorithm Development For FPGA Based Systems In High Energy Physics Experiments. *Master Thesis.* : Warsaw University of Technology, 2006.

71. **Kostin, Denis.** Testing the FLASH Superconducting Accelerating Modules. *Proceeding of SRF2007 Workshop.* 2007.

72. **S.W.Smith.** The Scientist and Engineer's Guide to Digital Signal Processing. *Sec. Ed.* San Diego, US : California Technical Publishing, 1997.

73. **E.Leff.** Introduction to feedback control system. : McGraw Hill, 1976.

74. **K.Ogata.** State Space analysis of control systems. , US : Prentice Hall inc., 1985.

75. *DESY FLASH web site.* [Online] http://vuv-fel.desy.de.

76. **Simrock, Stefan.** LLRF and control lectures. Hamburg : DESY, 2001.

77. *FLASH eLogbook web page.* [Online] http://ttfinfo.desy.de/TTFelog/.

78. **K. Perkuszewski, K. T. Pozniak, W. Jalmużna, W. Koprek, J. Szewinski, R. S. Romaniuk, S. Simrock.** FPGA based Multichannel Optical Concentrator SIMCON 4.0 for TESLA cavities LLRF Control System. *TESLA Report 2006-07.* Hamburg : DESY, 2006.

79. *XILINX web site.* [Online] http://www.xilinx.com.

80. *ALTERA web site.* [Online] http://www.altera.com.

81. IEEE Standard VHDL Language Reference Manual. New York : Design Automation Standards Committee (DASC) of the IEEE Computer Society, 2000. Vol. IEEE Std 1076.

82. **M. Grecki, W. Koprek, at all.** Improvements of the LLRF system at FLASH. *Presentation at the TTF / FLASH Meeting, 26/6/07.* Hamburg : DESY, 2007.

83. **Peterson, Wade D.** The VMEbus handbook. : VFEA International Trade Association, Scottsdale, AZ, 1993.

84. **Pozniak, Krzysztof T.** Internal Interface, I/O communication with FPGA circuits and hardware description standard for applications in HEP and FEL electronics. *TESLA Report 2005-22.* Hamburg : DESY, 2005.

85. **K. T. Pozniak, R. S. Romaniuk, K. Kierzkowski.** Parameterized control layer of FPGA based cavity controller and simulator for TESLA Test Facility. *TESLA Report 2003-30.* Hamburg : DESY, 2003.

86. **K. Pozniak, T. Czarski, W. Koprek,W. Giergusiewicz, R. Romaniuk.** SIMCON 3.0 Hardware Manual. *TESLA Report 2005-20.* Hamburg : DESY, 2005.

87. *SUN Solaris OS web site.* [Online] http://www.sun.com/software/solaris/.

88. *DOOCS web site.* [Online] http://tesla.desy.de/doocs.

89. **Pauling, L.** The Nature of the Chemical Bond. Ithaca : Cornell University Press, 1945.

90. **B. Jaffe, R.S. Roth, S. Marzullo.** Piezoelectric properties of lead zirconate—lead titanate solid-solution ceramics. *Journal of Applied Physics 25.* : American Institute of Physics, 1945.

91. **Standards Commitee of the IEEE Ultrasonic, Ferroelectrics and Frequency Control society.** IEEE Standard on Piezoelectricity. New York : The Institute of Electrical and Electronics Engineers, 1987. Vol. ANSUIEIEE Std 176.

92. **B. Zickgraf, et all.** Fatigue Behaviour of Multilayer Piezoelectric Actuators. *Applications of Ferroelectrics.* : ISAF '94, 1994.

93. *Physik Instrumente web site.* [Online] http://www.physikinstrumente.com.

94. Noliac web site. [Online] http://www.noliac.com.

95. *Epcos web site.* [Online] http://www.epcos.com.

96. *Piezomechanik web site.* [Online] http://www.piezomechanik.com.

97. **M. Fouaidy, G. Martinet, N. Hammoudi, F. Chatelet, A. Olivier, S. Blivet, H. Saugnac, A. Le Goff.** Electromechanical, thermal properties and radiation hardness tests of piezoelectrical actuators at low temperature. *Proceedings of EPAC06.* Edinburgh, Scotland : s.n., 2006.

98. **S. Battisti, et al.** CERN Report 75-18. Geneve : CERN, 1975.

99. **S.Simrock.** Review of Slow and Fast Tuners. *Proceedings of SRF05.* Ithaca, New York, US : Cornell University, 2005.

100. **P. Bosland, Bo Wu.** Mechanical study of the Saclay Piezo Tuner PTS (Piezo Tunning System). *CARE-Note-2005-004-SRF.* : CEA-Saclay, Dapnia, 2005.

101. **K. Pozniak, T. Czarski, W. Koprek,W. Giergusiewicz, R. Romaniuk.** SC Cavity SIMCON User's Manual. *TESLA Report 2005-02.* Hamburg : DESY, 2005.

102. **S. Simrock, G. Petrosyan, A. Facco, V. Zviagintsev, S. Andreoli, R. Paparella.** First demonstration of microphonics control of a superconducting cavity with a fast piezoelectric tuner. *Proceedings of PAC2003* . Portland, US : s.n., 2003.

103. **Paparella, Rocco.** Introduzione ai sistemi di controllo delle cavità risonanti superconduttive per acceleratori di particelle. *Lecture for the Automatic Controls course.* Milan : Politecnico di Milano, 2007.

104. **G.Devanz, P.Bosland, M.Desmons, E.Jacques, M.Luong, B.Visentin.** Compensation of Lorentz Force Detuning of a TTF 9-cell Cavity with a New Integrated Piezo Tuner . *Proceedings of EPAC06.* Edinburgh, UK : s.n., 2006.

105. **P. Sekalski, K. Przygoda, A. Napieralski, W. Jalmuzna, S. Simrock, L. Lilje, R. Paparella.** FPGA-based control system for piezoelectric stacks used for SC cavities's fast tuner. *Proceedings of PAC07.* Albuquerque, US : s.n., 2007.

106. **S.Simrock.** LLRF Development at DESY. *Proceedings of LLRF07.* Knoxville, US : s.n., 2007.

107. **K. Przygoda, R. Paparella.** A novel approach for hardware implementation of a detuning compensation control system for SC cavities. *Proceedings of MIXDES07* . Chiechocinek, Poland : s.n., 2007.

108. **Andreoli, Stefano.** Controllo della frequenza delle cavità superconduttive di TESLA mediante DSP ed attuatore piezoelettrico. *Master Thesis.* Milan : Università degli Studi di Milano, 2003.

109. **Paparella, Rocco.** Development of the control electronics for the coaxial blade tuner. *EPAC06 Special Student Poster Session.* Edinburgh, UK : s.n., 2006.

110. **H.Kaiser.** New approaches to tuning of TESLA resonators. *Proceedings of 9th Workshop on RFSC.* Santa Fe, US : s.n., 1999.

111. **J. Sekutowicz, M. Ferrario, Ch. Tang.** Superconducting superstructure for the TESLA collider: A concept. *PHYSICAL REVIEW SPECIAL TOPICS - ACCELERATORS AND BEAMS, VOLUME 2, 062001.* 1999.

112. *KEK web site.* [Online] http://www.kek.jp/intra-e/.

113. *TJNAF web site.* [Online] http://www.jlab.org/.

114. **M.Liepe, S.Noguchi.** Report on current status for ILC tuner development. *Workgroup 5.* Snowmass : s.n., 2005.

115. **C.Pagani, A.Bosotti, P.Michelato, R.Paparella, N.Panzeri, P.Pierini, F.Puricelli, G.Corniani.** Report on Fast Piezo Blade Tuner (UMI Tuner) for SCRF Resonators Design and Fabrication. *CARE note-2005-21-SRF.* 2005.

116. **J. Sekutowicz, C. Albrecht, V. Ayvazyan, R. Bandelmann, T. Büttner, P. Castro, S. Choroba, J. Eschke, B. Faatz, A. Gössel, K. Honkavaara, B. Horst, J. Iversen, K. Jensch, H. Kaiser, R. Kammering, G. Kreps, D. Kostin, R. Lange, J. Lorkiewicz, et al.** Cold and beam test of the first prototypes of the superstructures for the TESLA collider. *Proceedings of PAC03.* Portland, US : s.n., 2003.

117. **Tariq, Salman.** 1.3GHz Cavity/Cryostat Stiffness Model & Tuning Sensitivity. *SRF Engineering Meeting, 15/2/2006.* Batavia, US : FNAL, 2006.

118. **C. Pagani, A. Bosotti, P. Michelato, N. Panzeri, R. Paparella, P. Pierini.** ILC Coaxial Blade Tuner. *Proceedings of EPAC06.* Edinburgh, UK : s.n., 2006.

119. **R.Hill.** The Mathematical Theory of Plasticity. Oxford : Clarendon Press, 1950.

120. **C. Pagani, A. Bosotti, N. Panzeri.** Improved design of the ILC Blade-Tuner for large scale production. *Proceedings of PAC07.* Albuquerque, US : s.n., 2007.

121. **A. Bosotti, C. Pagani, P. Pierini, P. Michelato, R. Paulon, G. Corniani, J. P. Charrier, B. Visentin, Y. Gasser, J. P. Poupeau, B. Coadou.** Report on a cavity a (TRASCO Z502) fabrication and tests. *CARE Note-2005-001-HIPPI* . 2005.

122. **P. Kneisel, J. Brawley, R. Bundy, I. Campisi, G. Ciovati, K. Davis, K. Macha, D. Machie, J. Mammosser, S. Morgan, R. Sundelin, L. Turlington, K. Wilson, J. Sekutowicz, D. Barni, C. Pagani, R. Parodi, P. Pierini, K. Matsumoto, R. Mitchell, D. Schrage, M. D.** Superconducting Prototype Cavities for the Spallation Neutron Source (SNS) Project. *Proceedings of PAC01.* Chicago, US : s.n., 2001.

123. *CARE web site.* [Online] http://esgard.lal.in2p3.fr/Project/Activities/Current/.

124. *EUROTRANS web site.* [Online] http://nuklear-server.ka.fzk.de/eurotrans/.

125. *University of Pennsylvania web site.* [Online] http://www.upenn.edu/.

126. *FNAL web site.* [Online] http://www.fnal.gov/.

127. **E.Harms, T.Arkan, L.Bellantoni, H.Carter, H.Edwards, M.Foley, T.Khabiboulline, D.Mitchell, D.Olis, A.Rowe, N.Solyak.** Status of 3.9 GHz superconducting RF cavity technology at Fermilab. *Proceedings of PAC07.* Albuquerque, New Mexico, US : s.n., 2007.

128. *ERL page at Cornell web site.* [Online] http://erl.chess.cornell.edu/.

129. **M.Liepe, S.Belomestnykh, E.Chojnacky, V.Medjidzade, H.Padamsee, P.Quigley, J.Sears, V.Shemelin, V.Veshcherevich.** The Cornell ERL superconducting 2-cell injector cavity string and test cryomodule. *Proceedings of PAC07.* Albuquerque, New Mexico, US : s.n., 2007.

130. *ANSYS web site.* [Online] http://www.ansys.com/.

131. **Padamsee, Hasan.** RF Superconductivity 2004. *Proceedings of SRF-2004.* 2004.

132. **E.L. Saldin, E.A. Schneidmiller, M.V. Yurkov.** The Physics of Free Electron Lasers. Berlin-Heidelberg : Springer, 2000.

133. **R. Bandelmann, H. Kaiser, G. Kreps, M. Liepe, C. Martens, A. Matheisen, C. Pagani, H.-B. Peters, D. Proch, J. Sekutowicz, W. Singer.** Nb prototype of the superstructure for the TESLA linear collider. *Proceedings of SRF99.* Santa Fe, US : s.n., 1999.

134. **Sekutowicz, J.** Superconducting Superstructure. *TTF Meeting, June 25/06/97.* Orsay, FR : s.n., 1997.

135. **W.Weingarten.** Superconducting Cavities - Basics. *Proceedings of CAS - CERN Accelerator School on Superconductivity in particle accelerators.* Hamburg : s.n., 1996.

136. *TUL web site.* [Online] http://www2.p.lodz.pl/en/index.htm.

137. *Phytron web site.* [Online] http://www.phytron.com.

138. *Mathworks web site.* [Online] http://www.mathworks.com.

139. *LVDT Wikipedia page.* [Online] http://en.wikipedia.org/wiki/Linear_variable_differential_transformer.

140. *IPN-Orsay web site.* [Online] http://ipnweb.in2p3.fr.

141. *Criotec web site.* [Online] http://www.criotec.com.

142. *TUL web site.* [Online] http://www2.p.lodz.pl/en/index.htm

143. *ASME web site.* [Online] http://www.asme.org/